

TECHNISCHE UNIVERSITÄT MÜNCHEN

LEHRSTUHL FÜR AERODYNAMIK UND STRÖMUNGSMECHANIK

Aerodynamics of Flexible Lifting Surfaces using Fluid-Structure Interaction Approaches

Julie Piquee

Vollständiger Abdruck der von der Fakultät für Luftfahrt, Raumfahrt und Geodäsie
der Technischen Universität München zur Erlangung des akademischen Grades eines

Doktor-Ingenieurs

genehmigten Dissertation.

Vorsitzender: Prof. Dr.-Ing. Volker Gümmer

Prüfer der Dissertation:

1. apl. Prof. Dr.-Ing. Christian W. M. Breitsamter

2. Prof. Dr.-Ing. Kai-Uwe Bletzinger

Die Dissertation wurde am 07.05.2020 bei der Technischen Universität München
eingereicht und durch die Fakultät für Luftfahrt, Raumfahrt und Geodäsie am
19.11.2020 angenommen.

Munich, Germany

Dissertation

Copyright© 2020, Julie Piquee

All rights reserved. No part of this publication may be reproduced, modified, re-written, or distributed in any form or by any means, without the prior written permission of the author.

Acknowledgments

The thesis is the results of my work as a PhD candidate at the Chair of Aerodynamics and Fluid Mechanics of the Technischen Universität München during the period between November 2013 and March 2020. The completion of this dissertation could not have been possible without the contribution of many people. Their participation has been sincerely appreciated and I would like to gratefully acknowledge them with the following.

Above all, I would like to express my deepest gratitude to my supervisor and also my *Doktorvater* Prof. Dr.-Ing. Christian W. M. Breitsamter. I had the opportunity to enroll his group and to learn so much about aerodynamics that I shall be ever thankful. I admire that his door was always open and that he always tried to help whenever he could. I also would like to thank Prof. Dr.-Ing. Nikolaus A. Adams for giving me the opportunity to work in the aerodynamic group.

Then, I wish to thank a lot of my colleagues without whom I would not have been able to succeed. Indeed, I would like to thank my colleagues Dr.-Ing. Mehran Saeedi, Inigo López Canalejo M.Sc. and the others from the Chair of Structural Analysis for helping me with the implementations of the structural part. I am deeply grateful to Dr.-Ing. Benoit Beguin, Dr.-Ing. Anja Kölzsch, Vladislav Rozov M.Sc. and Dipl.-Ing. Maximilian Winter for the countless discussions about aerodynamics. I could always go to them and ask their opinions behind my “Ich habe eine Frage”. Furthermore, I am thankful to Stefan Pfnür M.Sc. and Dipl.-Ing. Marco Stuhlpfarrer for their help in the implementation of the fluid part. The last thanks but not the least, go to Dipl.-Ing. Andrei Buzica and Michael Cerny M.Sc., who helped me with wind tunnel measurements.

I would like to recognize the remarkable work of the colleagues from the workshop, namely Wolfgang Lützenburg, Martin Banzer, Hans-Gerhard Frimberger and the others, for the construction of each experimental model and their support during wind tunnel campaign.

The dissertation would not have been possible without each student, who worked with me. I am especially grateful to Simon Janssen, Lukas Küchle, Marcin Kurzal M.Sc. and Maximilian Schägger M.Sc.. They helped me with various parts of the work. Working with them was a pleasure and gave me more motivation to finish the thesis.

Finally, I am indebted to my friends, my parents and my brother for their encouragement and unconditional support throughout my time at the Chair. I owe a special thanks to Dr.-Ing. Cécile Boudot for her support and Marino Meister without who I would have never start at the Chair.

Abstract

An innovative morphing system is investigated in the present thesis featuring a form-variable wing concept based on a membrane-type lifting surface. This thesis focuses on a wing made of an elasto-flexible membrane material sewn on two rigid spars, the leading- and the trailing edge. The membrane material has the capacity to deform according to its elasto-mechanical properties. The concept changes its geometry under different flow conditions. Therefore, the aerodynamics of such a wing is not fixed but varies with the incoming flow. The main objective of the present thesis is to thoroughly study the concept by means of numerical fluid-structure interaction investigations and conclude about the benefits gained.

The fluid-structure computations are developed for several geometries, namely on airfoils and wings. For each geometry, an experimental model is constructed to perform wind tunnel investigations. Aerodynamic forces, flow field velocities and membrane deformation are measured to evaluate the accuracy of the computations. As the fidelity of the computations are well estimated, further investigations are completed to increase the knowledge on elasto-flexible membrane wing concepts. The influence of different parameters such as the dynamic pressure, the angle of attack, turbulence characteristics or unsteady flow conditions are considered.

Within this thesis, the advantages of an elasto-flexible membrane concept are highlighted by comparing the aerodynamics of the variable geometry to its rigid counterpart. The flexibility of the material and its adaptivity to the free stream allow the membrane to adjust its shape to the pressure distribution. The aerodynamics of the wing shows a pronounced dependency on the angle of attack, the dynamic pressure and the unsteady flow conditions. The camber is accentuated in a positive or negative direction resulting in an increase or decrease of the lifting capacity. The stall onset is postponed to higher angles of attack while the abrupt decrease of the lift is replaced by a gradual loss of it. Non-linear effects are observed due to the non-linear adaptation of the membrane. The laminar-turbulent transition in the boundary layer affects the fluid-structure interaction as well. In this case, the presence of a laminar separation bubble is observed and found to be sensitive to the suction peak at the leading edge. Finally, when the wing experiences a gust, the membrane permits to mitigate the lift at high angles of attack, which shows a great potential for an alleviation of aerodynamic peak loads.

Zusammenfassung

Die vorliegende Arbeit behandelt eine formvariable Flügelkonfiguration mit einer elastischen Membran, die um die Vorder- und Hinterkante des Flügels gespannt ist. Die Profilgeometrie verformt sich somit entsprechend der unterschiedlichen Strömungsbedingungen. Ziel der Arbeit ist es, den Flugbereich durch passiv geregelte Strömungskontrolle zu erweitern und Spitzenlasten auf die Struktur zu verringern. Die Auftriebserzeugung und Strukturlasten sind stark abhängig von der Kopplung zwischen den aerodynamischen und strukturellen Eigenschaften des Flügels, welche wiederum von den Anströmbedingungen und den mechanischen Eigenschaften der Membran abhängen. Diese Arbeit konzentriert sich auf die Implementierung von gekoppelten Fluid-Struktur-Simulationen, um das formvariable Membrankonzept detailliert zu analysieren.

Die Wechselwirkungen zwischen dem Fluid und der Struktur werden im Rahmen dieser Arbeit für verschiedene Konfigurationen, sowohl zweidimensionale Profile, als auch dreidimensionale Flügel simuliert, um allgemeingültige Aussagen über das Konzept von Membranflügeln zu treffen. Zur Validierung der numerischen Studien, werden die Simulationen zunächst mit experimentellen Untersuchungen verglichen. Nachfolgend wird der Einfluss verschiedener Parameter analysiert.

In einem weiteren Schritt werden die aerodynamische Eigenschaften des Membranflügels mit denen eines starren Modells mit gleicher Ausgangsgeometrie verglichen, um die Effekte der Formvariabilität des flexiblen Membranflügels eindeutig zu charakterisieren. Im Gegensatz zum starren Modell verursacht die Oberflächendruckverteilung auf die Membran eine Modifikation der Profilgeometrie und somit auch eine Veränderung der Krümmung. Resultierend verschiebt sich das Eintreten von Strömungsablösung zu höheren Anstellwinkeln und der Auftriebsverlust erfolgt gradueller im Vergleich zu einer starren Geometrie. Nicht-lineare Effekte in den Polen werden aufgrund des nicht-linearen Verhaltens der Membran beobachtet. Eine Transition von einer laminaren zu einer turbulenten Strömung ist für die analysierten Fälle beobachtbar, welche wiederum die Fluid-Struktur-Wechselwirkungen beeinflusst. Es entsteht eine laminare Ablöseblase, die hochsensibel auf die Strömungsbedingungen, unter anderem die Saugspitze an der Vorderkante, reagiert. Letztendlich zeigt die Analyse einer Böeneinwirkung auf die Tragfläche eine Abminderung des Auftriebsanstiegs bei Verwendung von formvariablen Membranstrukturen im Vergleich zu starren Tragflügel. Die Lastminderung und eine verhältnismäßig einfache Anwendung einer passiven Steuermöglichkeit zeichnen das hohe Potential des Konzepts eines formvariablen Membranflügels aus.

Résumé

Dans le cadre de cette thèse, une étude est menée sur une aile dont la forme est variable. L'aile est constituée d'une membrane cousue autour d'un bord d'attaque et d'un bord de fuite. La membrane peut se déformer selon ses propriétés mécaniques. Ainsi, les propriétés aérodynamiques de l'aile ne sont pas fixes mais changent en fonction des conditions de l'écoulement amont. L'objectif principal de cette thèse est d'étudier en détails le concept en exploitant des simulations numériques, mettant en jeu une interaction entre la membrane et le fluide entourant l'aile.

Les simulations sont développées pour plusieurs géométries du type "airfoil" mais aussi sur "des ailes". Chacune des géométries est associée à un modèle expérimental, construit afin de réaliser des mesures en soufflerie. Les forces aérodynamiques, les composantes du vecteur vitesse et la déformation de la membrane sont des paramètres mesurés qui permettent d'évaluer la précision des simulations numériques. Une fois la validité des simulations évaluée, diverses analyses sont entreprises afin d'accroître les connaissances sur le système "aile - membrane". L'influence de la pression dynamique, de l'angle d'attaque, des caractéristiques de turbulence, et des conditions instationnaires de l'écoulement amont sont ainsi des paramètres considérés au long de cette étude.

Dans cette thèse, les avantages d'une "aile - membrane" sont mis en évidence grâce à la comparaison de l'aile à géométrie variable et son homologue non déformable. La flexibilité du matériel et son adaptation face à l'écoulement amont permettent un ajustement de la forme de la membrane par rapport à la distribution de pression. De plus, l'étude montre que les propriétés aérodynamiques de l'aile sont fortement influencées par les conditions de l'écoulement amont. La ligne de cambrure du profil peut être accentuée dans les deux directions, engendrant une hausse ou une perte de portance. Le phénomène de décrochage est quant à lui retardé et décalé vers de plus grands angles d'attaque tandis que la baisse abrupte de la portance est transformée en une baisse graduelle. Une évolution non-linéaire de la portance est également observée résultant du comportement non-linéaire de la membrane. L'influence de la transition entre couche limite laminaire et turbulente est aussi mise en évidence avec la présence d'une bulle de séparation laminaire constatée pour ce profil d'aile. Enfin, le comportement de la membrane face à des conditions de rafale montre un grand potentiel quant à l'atténuation des charges aérodynamiques agissant sur l'aile.

Contents

List of Figures	xv
List of Tables	xxi
Nomenclature	xxiii
1 Introduction	1
1.1 Motivation	1
1.2 State-of-the-Art Technique	2
1.2.1 Morphing Systems	2
1.2.2 Fluid-Structure Interaction Computations	9
1.3 Objectives and Methodology	12
1.4 Outline	13
2 Numerical Methodology	17
2.1 Fundamentals of FSI	17
2.1.1 Monolithic Method	18
2.1.2 Partitioned Method	20
2.2 Dynamics of FSI	22
2.2.1 Fluid Dynamics	22
2.2.2 Structure Mechanics	32
2.2.3 Coupling Conditions	41
2.3 Mesh Generators and Solvers Description	43
2.3.1 Mesh Generator	43
2.3.2 Fluid Solvers	44
2.3.3 Stucture Solvers	45
2.3.4 Outer Coupling Software	45
3 Experimental and Numerical Setups	47
3.1 Membrane Fabrics	47
3.1.1 Membrane 1	48
3.1.2 Membrane 2	48
3.2 Geometries and Wind-Tunnel Models	49
3.2.1 2D Models	49
3.2.2 2.5D Wind-Tunnel Models	52
3.2.3 3D Wind-Tunnel Model	54

3.3	Experimental Setup	56
3.3.1	Force Measurements	57
3.3.2	Membrane Deflection Measurements	60
3.3.3	Velocity Field Measurements	62
3.3.4	Test conditions	63
3.4	Numerical Setup	63
3.4.1	2D Models	64
3.4.2	2.5D and 3D Model	69
4	Comparison of 2D FSI and Wind-Tunnel Data	75
4.1	2D WTB Model	75
4.1.1	Membrane Deflection	76
4.1.2	Flow Field Velocity	77
4.1.3	Lift and Drag	79
4.1.4	Summary and Experimental Consideration	83
4.2	2D WTA Model	86
4.2.1	Membrane Deflection	86
4.2.2	Flow Velocity Field	88
4.2.3	Lift and Drag	92
4.2.4	Summary and Experimental Consideration	93
5	Aeroelastic Behavior of a Membrane Airfoil	97
5.1	Baseline	97
5.1.1	Aerodynamic Forces	97
5.1.2	Pressure Distribution	98
5.1.3	Membrane Deflection	100
5.2	Parameters Dependency Analysis	101
5.2.1	Influence of the Dynamic Pressure	101
5.2.2	Influence of the Turbulence Model	104
5.2.3	Influence of Gust Conditions	108
6	Aeroelastic Behavior of a Membrane Wing	119
6.1	2.5D Model	119
6.1.1	Comparison between FSI and Wind-Tunnel Data	120
6.1.2	Numerical Study	125
6.2	3D Model	133
6.2.1	Baseline	133
6.2.2	Comparison between FSI and Wind-Tunnel Data	142
6.2.3	Numerical Study	146
7	Conclusions and Outlook	157
	Bibliography	161

List of Figures

1.1	The AquaMAV prototype, photo from [82]. (a)-(c) Prototype shown with wings opened (a), swept at 45° (b) and at 90° (c). Prototype viewed from backward (d). CAD illustration of fuselage with internal components (e).	4
1.2	The membrane airfoil/wing prototypes, illustration from [45] and [100].	6
1.3	The NextGen MFX-1 prototype, illustration from [35]. (a)-(b) Prototype showing two morphing configurations with a wing-area change of about 40%.	7
1.4	Morphing membrane wing in the loaded and unloaded case	12
2.1	Description of the partitioned and the monolithic method and their differences. . .	22
2.2	Control volume in cartesian coordinates, [93].	23
2.3	Aerodynamic forces on a NACA 0012 profile	31
2.4	Schematic illustration of the various operations describing a structural analysis. . .	33
2.5	FEM discretization and extraction of a generic element, [34].	40
2.6	Mapping principle.	42
3.1	Description of the Membrane 1 and tensile test results, from [18].	49
3.2	Tensile test process and results for the Membrane 2.	50
3.3	Sketch of the 2D WTB geometry.	51
3.4	Sketch of the 2D WTA geometry.	52
3.5	2.5D WTB model.	53
3.6	Illustration of the adjustable TE of the 2.5D WTA model.	53
3.7	2.5D WTA model installation in the wind tunnel and an enlargement of the construction with the two spars.	54
3.8	Sketch of the 3D WTA elasto-flexible membrane wing model with geometrical characteristics.	56
3.9	3D WTA model mounted in the test section and an enlargement of the construction with the two spars.	57
3.10	Force measurement installation for the 2.5D models.	59
3.11	installation for the 3D models.	60
3.12	Photogrammetry measurement setup for the two-dimensional WTB and WTA models.	61
3.13	Sketch explaining the photogrammetry measurement for the three-dimensional WTA model.	62
3.14	HWA measurement set up for the two-dimensional WTB and WTA models.	63
3.15	2D CFD meshes.	65

3.16 FEM meshes.	66
3.17 Results of the grid independency study for the 2D WTB CFD mesh.	67
3.18 Results of the grid independency study for the 2D WTA CFD mesh.	68
3.19 2.5D CFD mesh.	70
3.20 3D CFD mesh.	70
3.21 Results of the grid independency study for the 2.5D WTA CFD mesh.	72
3.22 Results of the grid independency study for the 3D WTA CFD mesh.	73
4.1 Comparison between FSI results and photogrammetry measurement data: Membrane deflection at $\alpha = 0^\circ, 6^\circ, 10^\circ$ and 15° at $q_\infty = 230$ Pa for the 2D and 2.5D WTB models. The deflection was measured in the middle of the wing span as shown in (a). (b)-(e) illustrate the deflection for the various α	77
4.2 Comparison between FSI results and photogrammetry measurement data: Membrane deflection at $\alpha = 0^\circ, 6^\circ, 10^\circ$ and 15° at $q_\infty = 690$ Pa for the 2D and 2.5D WTB models. The deflection was measured in the middle of the wing span (see Fig. 4.1 (a)).	78
4.3 Comparison between FSI results and photogrammetry measurement data: Membrane deflection for the 2D and 2.5D WTB models at four α and $q_\infty = 230$, and 690 Pa. The deflection was measured in the middle of the wing span (see Fig. 4.1 (a))	79
4.4 Comparison between FSI results and HWA data: Flow field velocity at $\alpha = 6^\circ$ at $q_\infty = 230$ Pa for the 2D and 2.5D WTB models. The velocity was measured in the middle of the wing span shown in (a).	80
4.5 Comparison between FSI results and HWA data: Flow field velocity at $\alpha = 15^\circ$ at $q_\infty = 230$ Pa for the 2D and 2.5D WTB models. The velocity was measured in the middle of the wing span (see Fig. 4.4 (a)).	81
4.6 Comparison between FSI results and force measurement data: C_l - α and C_d - α curves at $q_\infty = 230$ and 690 Pa for the 2D and 2.5D WTB models.	84
4.7 HWA measurement results: Downwash β $^\circ$ at $\alpha = 6^\circ$ behind the 2.5D WTB wing at $X = 1 \cdot c$	86
4.8 Photogrammetry measurement results for the 2.5D WTB model: the deflection was measured in the wingspan at $q_\infty = 690$ Pa. The variable ΔZ represents the difference between the deformed and the non-deformed geometry during the experiments.	87
4.9 Comparison between FSI results and photogrammetry measurement data: Membrane deflection at $\alpha = 0^\circ, 6^\circ, 10^\circ$ and 15° at $q_\infty = 230$ Pa for the 2D and 2.5D WTA models. The deflection was measured in the middle of the wing span as shown in (a). (b)-(e) illustrate the deflection for the various α	89
4.10 Comparison between FSI results and HWA data: Flow field velocity at $\alpha = 6^\circ$ at $q_\infty = 230$ Pa for the 2D and 2.5D WTA models. The velocity was measured in the middle of the wing span as shown in (a). (b)-(e) illustrate the two velocity components.	90

4.11	Comparison between FSI results and HWA data: Flow field velocity at $\alpha = 15^\circ$ at $q_\infty = 230$ Pa for the 2D and 2.5D WTA models. The velocity was measured in the middle of the wing span (see Fig. 4.10 (a)). (b)-(e) illustrate the two velocity components.	91
4.12	Comparison between FSI results and the force measurement data: C_l - α and C_d - α curves at $q_\infty = 230$ Pa for the 2D and 2.5D WTA models.	93
4.13	Photogrammetry measurement results for the 2.5D WTA model: the deflection was measured in the wingspan at $q_\infty = 230$ Pa. The variable ΔZ represents the difference between the geometry during the experiments and the undeformed one. .	95
5.1	Comparison between flexible and rigid geometries: C_l - α and C_d - α curves at $q_\infty = 230$ Pa.	99
5.2	Comparison between flexible and rigid geometries: $-C_p$ distribution on the airfoil and the associated geometry at $q_\infty = 230$ Pa.	100
5.3	Comparison between flexible and rigid geometries: Geometry of the airfoil at $q_\infty = 690$ Pa.	101
5.4	Comparison between FSI results: Membrane deflection and pressure distribution at $\alpha = 8^\circ$ and 15° at $q_\infty = 230$ Pa, 400 Pa and 690 Pa.	104
5.5	Comparison between FSI results: C_l - α , C_d - α and C_l - C_d at $q_\infty = 230$ Pa, 400 Pa and 690 Pa.	105
5.6	Comparison between FSI results: Evolution of the maximal camber f/c - α and X_{Zmax} - α at $q_\infty = 230$ Pa, 400 Pa and 690 Pa.	106
5.7	Comparison between FSI results: C_l - α and C_d - α curves at $q_\infty = 230$ Pa for two fluid models.	107
5.8	Comparison between fully turbulent and transition boundary layer: Membrane deflection and pressure distribution at $\alpha = 0^\circ$ and 15° at $q_\infty = 230$ Pa.	109
5.9	Comparison between fully turbulent and transition boundary layer: Membrane deflection, pressure distribution and C_f distribution at $\alpha = 6^\circ$ and 10° at $q_\infty = 230$ Pa.	110
5.10	Comparison between fully turbulent and transitional boundary layer: turbulent intensity Tu at $\alpha = 6^\circ$ at $q_\infty = 230$ Pa.	111
5.11	Comparison between fully turbulent and transitional boundary layer: Tu at $\alpha = 10^\circ$ at $q_\infty = 230$ Pa.	111
5.12	Comparison between fully turbulent and transitional boundary layer: Tu at $\alpha = 15^\circ$ at $q_\infty = 230$ Pa.	111
5.13	Shape of a “1-cosine” gust with g_0 as the amplitude and λ as the wave length. . .	112
5.14	Schematic visualization of the convective time t^* and the progression of the gust, [53].	112
5.15	Illustration of the response to a “1-cosine” gust with $g_0 = 10$ m/s: u/U_∞ at $\alpha = 0^\circ$ at $q_\infty = 230$ Pa for various convective time t^*	114
5.16	Illustration of the response to a “1-cosine” gust with $g_0 = 10$ m/s: u/U_∞ at $\alpha = 0^\circ$ at $q_\infty = 230$ Pa for various convective times t^*	115

5.17	Illustration of the response to a “1-cosine” gust: Evolution of C_l and C_d at $\alpha = 0^\circ$ and $q_\infty = 230$ Pa as function of the convective time t^*	116
5.18	Comparison of the response to a “1-cosine” gust between a rigid and a flexible geometry: Evolution of C_l at various α and $q_\infty = 230$ Pa as function of the physical time t^*	118
6.1	C_L - α and C_D - α curves obtained for the 2.5D WTA model during wind tunnel measurements, and for FSI and CFD computations at $q_\infty = 230$ Pa.	121
6.2	Comparison between the photogrammetry measurement data and the FSI and CFD results at $q_\infty = 230$ Pa in the middle of the wing for the 2.5D WTA model.	123
6.3	Comparison between photogrammetry measurement and FSI results: The deflection was measured in the wingspan at $q_\infty = 230$ Pa for the 2.5D WTA model. ΔZ represents the difference between the deformed and the non-deformed geometry. . .	124
6.4	Comparison between flexible and rigid wings: Axial component u/U_∞ and vertical component w/U_∞ of the flow field velocity at $\alpha = 0^\circ$ at $q_\infty = 230$ Pa for the 2.5D WTA model.	126
6.5	Comparison between flexible and rigid wings: Axial component u/U_∞ and vertical component w/U_∞ of the flow field velocity at $\alpha = 5^\circ$ at $q_\infty = 230$ Pa for the 2.5D WTA model.	128
6.6	Comparison between flexible and rigid wings: Axial component u and vertical component w of the flow field velocity at $\alpha = 10^\circ$ at $q_\infty = 230$ Pa for the 2.5D WTA model.	129
6.7	Comparison between flexible and rigid wings for the 2.5D WTA model: Evolution of $-C_p$ - X along the wing span at $\alpha = 0^\circ, 5^\circ$ and 10° for $q_\infty = 230$ Pa.	130
6.8	Comparison between flexible and rigid wings for the 2.5D model: Evolution of C_p - X along the wing span at $\alpha = 0^\circ, 5^\circ$ and 10° at $q_\infty = 230$ Pa and visualization of the skin friction lines.	131
6.9	Comparison between flexible and rigid wings for the 2.5D WTA model: Evolution of C_p - X along the wing span at $\alpha = 0^\circ, 5^\circ$ and 10° at $q_\infty = 230$ Pa and visualization of the skin friction lines.	132
6.10	C_L - α and C_D - α and C_L - C_D for various q_∞ and for the CFD computations for the 3D WTA model.	135
6.11	Curvature change at $q_\infty = 520$ Pa and $\alpha = 10^\circ$ for the 3D WTA model.	137
6.12	Curvature change at $q_\infty = 310$ Pa and $\alpha = 10^\circ$ for the 3D WTA model.	138
6.13	Comparison between the membrane deflection obtained for various q_∞ at $\alpha = -5^\circ, 0^\circ$ and 5°	139
6.14	Comparison between the membrane deflection obtained for various q_∞ at $\alpha = 10^\circ$, and 15°	140
6.15	Comparison between the membrane deflection obtained for various q_∞ at several α	141
6.16	Comparison between the flexible case, the rigid case and the force measurement data: C_L - α and C_D - α curves at $q_\infty = 520$ Pa for the 3D WTA model.	143
6.17	Comparison between FSI results and the photogrammetry measurement data at $\alpha = 0^\circ, 5^\circ$ and 10° and $q_\infty = 520$ Pa for the 3D WTA model.	145

6.18 Comparison for the flexible and the rigid cases: Local lift distribution along the wing span at $\alpha = 0^\circ$ and $q_\infty = 520$ Pa.	148
6.19 Comparison for the flexible and the rigid cases for the 3D WTA model: Axial component u and vertical component w of the flow field velocity at $\alpha = 0^\circ$ at $q_\infty = 520$ Pa.	148
6.20 Comparison between flexible and rigid wings for the 3D WTA model: Local lift distribution along the wing span at $\alpha = 5^\circ$ and $q_\infty = 520$ Pa.	150
6.21 Comparison between flexible and rigid wings for the 3D WTA model: Axial component u and vertical component w of the flow field velocity at $\alpha = 5^\circ$ at $q_\infty = 230$ Pa.	150
6.22 Comparison between flexible and rigid wings for the 3D WTA model: Vorticity $\omega_x \cdot c_r / U_\infty$ at $\alpha = 5^\circ$ at $q_\infty = 520$ Pa.	151
6.23 Comparison between flexible and rigid wings for the 3D WTA model: Axial component u and vertical component w of the flow field velocity at $\alpha = 10^\circ$ at $q_\infty = 230$ Pa.	152
6.24 Comparison between flexible and rigid wings for the 3D WTA model: Vorticity $\omega_x \cdot c_r / U_\infty$ at $\alpha = 10^\circ$ at $q_\infty = 520$ Pa.	153
6.25 Comparison between flexible and rigid wings for the 3D WTA model: Evolution of $-C_p \cdot X$ along the wing span at $\alpha = 0^\circ, 5^\circ$ and 10° and $q_\infty = 520$ Pa.	154
6.26 Comparison between flexible and rigid wings for the 3D WTA model: Evolution of C_p along the wing span at $\alpha = 0^\circ, 5^\circ$ and 10° at $q_\infty = 520$ Pa and visualization of the skin friction lines.	155
6.27 Comparison between flexible and rigid wings for the 3D WTA model: Evolution of C_p with X along the wing span at $\alpha = 0^\circ, 5^\circ$ and 10° at $q_\infty = 520$ Pa and visualization of the skin friction lines.	156

List of Tables

3.1	Test conditions considered in the experimental investigations.	64
3.2	Characteristics of the different resolutions of the 2D WTB CFD mesh.	67
3.3	Characteristics of the different resolutions of the 2D WTA CFD mesh.	68
3.4	Characteristics of the different resolutions of the grids for the 2.5D WTA model. .	71
3.5	Characteristics of the different resolutions of the grids for the 3D WTA model. . .	72
6.1	Values of the aerodynamic coefficients obtained for the flexible and the rigid cases at $\alpha = 0^\circ$ and $q_\infty = 230$ Pa for the 2.5D WTA model.	126
6.2	Values of the aerodynamic coefficients obtained for the flexible and the rigid cases at $\alpha = 5^\circ$ and $q_\infty = 230$ Pa for the 2.5D WTA model.	127
6.3	Values of the aerodynamic coefficients obtained for the flexible and the rigid cases at $\alpha = 10^\circ$ and $q_\infty = 230$ Pa for the 2.5D WTA model.	129
6.4	Estimation of the norm error L2 between the FSI and the photogrammetry data for the 3D WTA model.	144
6.5	Values of the aerodynamic coefficients obtained for the flexible and the rigid cases at $\alpha = 0^\circ$ and $q_\infty = 520$ Pa for the 3D WTA model.	147
6.6	Values of the aerodynamic coefficients obtained for the flexible and the rigid cases at $\alpha = 5^\circ$ and $q_\infty = 520$ Pa for the 3D WTA model.	149
6.7	Values of the aerodynamic coefficients obtained for the flexible and the rigid cases at $\alpha = 10^\circ$ and $q_\infty = 520$ Pa for the 3D WTA model.	152

Nomenclature

Latin symbol	Description	Unit
a	Semi-major axis length	m
AR	Aspect ratio	-
B	External forces vector	N
b_u	Semi-minor axis length of the upper-side	m
b_l	Semi-minor axis length of the lower-side	m
c	Chord length	m
c_r	Root chord length	m
c_t	Tip chord length	m
C_l, C_L	Lift coefficient for an airfoil and a wing, respectively	-
$C_{l\alpha}$	Slope of the lift coefficient over α curve	-
C_d, C_D	Drag coefficient for an airfoil and a wing, respectively	-
C_M	Pitching moment coefficient	-
C_p	Pressure coefficient	-
$\underline{\underline{\mathcal{C}}}$	Elasticity tensor	Pa
d	Displacement vector	m
D	Drag force	N
E	Young's modulus	Pa
e_c	Kinetic energy	J
e_i	Internal energy	J
f	Camber	m
f_{lp}	Low-pass filter frequency	Hz
f_{meas}	Sampling rate frequency	Hz
$f(t)$	State of the fluid at time t	-
F_x, F_z	Component of the force F in x and z direction, respectively	N

h_{te}	Height of the trailing edge	m
\mathcal{I}_{FSI}	Intersection domain between the fluid and the structure	-
l	Reference length	m
L	Lift force	N
l_o	Reference length	m
l_{te}	Length of the trailing edge	m
M	Pitching moment	Nm
p	Air pressure	Pa
q_∞	Free stream dynamic pressure	Pa
R	Specific gas constant	J/(kg K)
Re	Reynolds number	-
S	Area	m ²
$s(t)$	State of the structure at time t	-
\mathcal{S}	Surface around the control volume	m ²
t	Time	s
T	Air temperature	K
U_∞	Free stream velocity	m/s
u, v, w	Velocity components	m/s
\mathcal{V}	Control volume	m ³
x, y, z	Space coordinates	m
X, Y, Z	Dimensionless space coordinates (coordinate divided by c)	-
X_{Zmax}	Dimensionless x-coordinate where the maximal deflection occurs	-
X_{sep}	Dimensionless x-coordinate where the flow separation starts	-
y^+	Dimensionless wall distance	-
ΔZ	Dimensionless difference between deformed and non-deformed geometry	-

Greek symbol	Description	Unit
α	Angle of attack	°
ϵ	Angle between the horizontal line and the ellipse axis	°
$\underline{\underline{\epsilon}}$	Strain tensor	-
κ	Turbulent kinetic energy	J
λ	Taper ratio	-
μ	Dynamic viscosity	kg/(ms)
ν	Kinematic viscosity	m ² /s
$\tilde{\nu}$	Effective viscosity defined in the SA model	m ² /s
ν_s	Poisson coefficient for the structure	-
ω	Specific dissipation rate	1/s
ω_x	Vorticity	1/s
Ω	Common domain of the fluid and the structure	-
$\Omega_{\mathcal{S}}$	Common domain of the structure	-
$\Omega_{\mathcal{F}}$	Common domain of the fluid	-
ρ	Density	kg/m ³
$\underline{\underline{\sigma}}$	Stress tensor	Pa
σ_o	Pre-stress	Pa
$\underline{\underline{\tau}}$	Viscous shear stress tensor	N/m ²

Abbreviation	Description
ALE	Lagrangian-Eulerian Approach
BE	Balance Equation
CFD	Computational Fluid Dynamics
CE	Constitutive Equation
CIMNE	International Center for Numerical Methods in Engineering
DARPA	Defense Advanced Research Project Agency
DNS	Direct Numerical Simulation
DLR	Deutsches Zentrum für Luft- und Raumfahrt
FEM	Finite Element Method
FSI	Fluid Structure Interaction
FVM	Finite Volume Method
HWA	Hot Wire Anemometry
KE	Kinematic Equation
LE	Leading edge
LES	Large Eddy Simulation
MAS	Morphing Aircraft Structures
MAV	Micro Air Vehicle
MAW	Mission Adaptive Wing
MPI	Message Passing Interface
NASA	National Aeronautics and Space Administration
NURBS	Non-Uniform Rational B-Splines
SA	Spalart-Allmaras turbulence model
TE	Trailing edge
(U)RANS	(Unsteady) Reynolds-Averaged Navier-Stokes
VAWT	Vertical-Axis Wind Turbine
WTA	Wind Tunnel A
WTB	Wind Tunnel B

Chapter 1 - Introduction

This chapter introduces the objectives and scopes of the thesis. In the first part, the contribution of this work is presented through the description of the motivation. Then, the state-of-the-art technique is discussed to help the reader to understand the context of this work. The state of the art focuses on morphing systems in aerodynamic field for three domains, namely the micro air vehicles, the aircraft and the wind turbines. In each part, the state-of-the-art morphing technique starts from general systems to refine step by step to variable-camber-membrane concepts being the topic of this thesis. The literature study also presents numerical investigations undertaken to predict morphing concepts. At the end of the chapter, an outline describes how the thesis is organized.

1.1 Motivation

Modern engineering is confronted by multi-disciplinary challenges. Nowadays, many problems involve more than one physical effect. Couplings between thermal and stress analyses, structure and noise phenomena, or fluid and structure problems are ubiquitous in engineering and sciences. Multi-physics fluid-structure problems have drawn attention for a long time as they play a key role in many systems. The deflection of wind-turbine blades, the dynamics of parachutes, the self-amplified oscillations of a bridge or a wing, or the dynamics of blood in arteries are all examples of fluid-structure interactions. Despite the high attention, the mutual relationship between both the fluid and the structure parts is not completely understood. High fidelity computations are of great interest as they could provide a better understanding of the reciprocity between the fluid and the structure.

Aerodynamics has always sought to achieve better performance for various conditions. The definition of better performance can be characterized with different criteria. Reducing drag and noise, increasing the efficiency for a certain range of angles of attack and improving the stability

of a flight vehicle are interpretations for better performance in the field of aerodynamics. Another interpretation can be defined by expanding flight envelopes. The latter has been one of the challenges of aerodynamics since the beginning of the aircraft with the Wright Brothers. Several systems have been investigated since then. For example, research on leading-edge and trailing-edge flaps and/or slats started after World War I and kept being developed to enhance lift at high angles of attack.

In the present thesis, a particular concept is considered intending to extend flight operating conditions. Lifting surfaces made of a highly flexible anisotropic membrane are intensively analyzed by means of numerical and experimental investigations. The main objective is to gain more knowledge about the aerodynamics of such a concept and to be able to model it. Therefore, high fidelity computations have been developed involving multi-physics fluid-structure problems. The computations are compared to experimental data to assess the validity and accuracy of the numerical procedure. Several models constructed within this thesis are considered at various conditions to gather knowledge in this domain.

In the following, a state-of-the-art morphing systems and fluid-structure computations are presented. On the one hand, several examples of morphing concepts are described in order to give a clear understanding about the definition of morphing. On the other hand, various applications of multi-physics fluid-structure problems are presented to clarify the current state of numerics.

1.2 State-of-the-Art Technique

1.2.1 Morphing Systems

Many projects have focused their research on how a single flight vehicle can operate in various conditions. In other terms, they have tried to find how the variability and the number of operating conditions for a single flight vehicle can be increased. Many solutions have been proposed with flow control systems. The idea is to act on the flow and changes its topology to enlarge the operative conditions.

Modern aerodynamics distinguishes active to passive flow control systems. The first type acts on the flow by means of an extra power supply whereas the second does not require any auxiliary energy. One term has emerged in active as well as in passive flow control systems: morphing. According to Lexico [2], the definition of the word morph is «change smoothly from one image to

another by small gradual steps, undergo a gradual process of transformation». There is no standard definition to characterize a morphing system in modern aerodynamics. One should understand that behind the word morphing, changes of various types can occur. Morphing can refer to a change in the outer shape or in the inner structure, but it can also involve a change in the noise and the electromagnetic signature. Nevertheless, the main purpose of morphing has always been to increase flight efficiency and/or expand flight envelopes, i.e., a single flight vehicle can be used for various types of missions [73, 95, 29].

In the following, various examples of morphing systems are described to better understand the context of the present thesis. Three categories, namely Micro Air Vehicles (MAVs), aircraft and wind turbines, appear to have a significant interest with respect of the present work.

MAV Field

MAVs are aerial vehicles small enough to be carried by a man. Usually, the vehicles have characteristics such as wingspan less than 0.15m and airspeed less than 40km/h. The operating range of the Reynolds number (Re) is included between 30,000 and 200,000. In this region, a laminar boundary layer affects significantly the aerodynamic performance of the corresponding flight vehicle. A laminar separation bubble can cause a rapid increase of the drag and a decrease of the lift force [66]. Improving the aerodynamic performance by expanding flight envelopes of MAVs has become a new trend. Among others, morphing devices have been popular solutions which have been extensively investigated. In fact, the outstanding flight capabilities of mammals and small birds inspired the research on MAVs suggesting the idea of a shape change during flight.

One example of MAV, which illustrates clearly the idea behind expanding flight envelope through a shape change, is an aerial configuration able to progress in air as well as in water. This capacity enables missions in various environments. The Aquatic Micro Air Vehicle (AquaMAV), presented by Siddall et al. [82], is able to fly in air and directly dives into water from flight to collect water samples. The vehicle has a folding wing able to sweep backwards up to 90° (Fig. 1.1). On the one hand, it allows the vehicle to change its flight behavior in air when it is being partially swept, and on the other hand, it allows it to dive directly into water when it is completely sweptback. Wind and water-tunnel experiments have been conducted, showing the good performance of the AquaMAV. The vehicle produces sufficient lift to balance its weight and, more importantly, decreases its lift and drag when the wing is completely sweptback, allowing the

dive from flight [82].

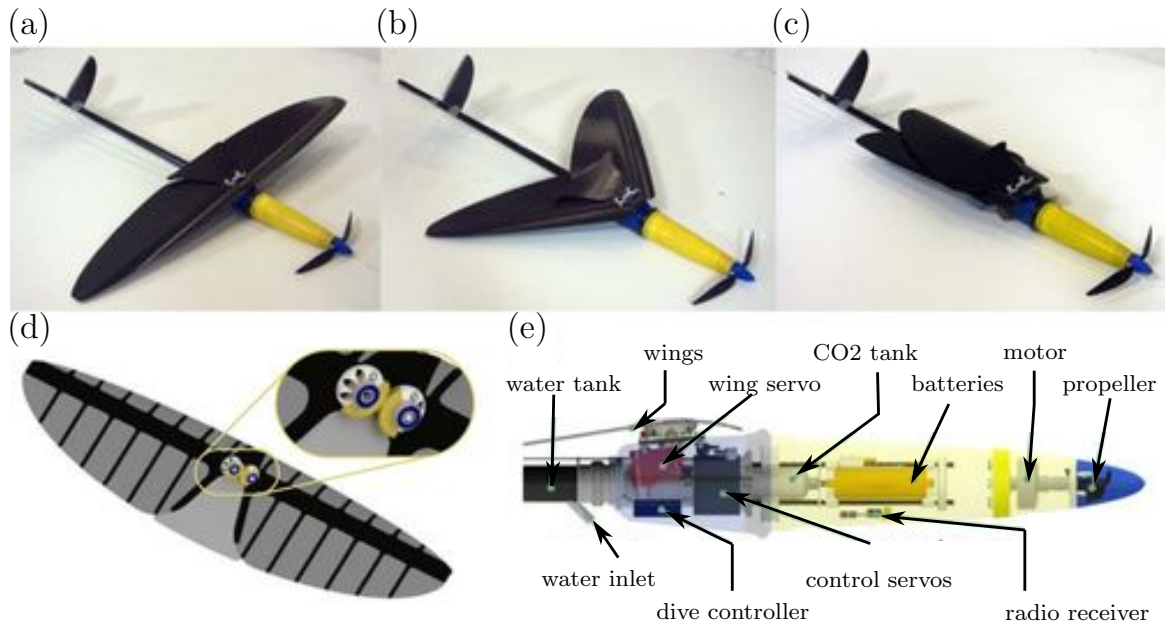


Figure 1.1: The AquaMAV prototype, photo from [82]. (a)-(c) Prototype shown with wings opened (a), swept at 45° (b) and at 90° (c). Prototype viewed from backward (d). CAD illustration of fuselage with internal components (e).

The University of Florida has also been particularly active in MAVs development by means of morphing systems. Since the early 2000s, they have designed and tested several prototypes [37, 45, 47, 57, 58, 56, 84, 98]. Among others, Garcia et al. [37] presented an investigation about a morphing effector which provides a rolling moment on the wing. Two vehicles, one of 0.3m and another of 0.6m, are tested and data is compared to their rigid counterpart wings. The two prototypes are constructed as the following: the leading edge (LE) is built using carbon-fiber weave with carbon battens attached to the trailing edge (TE). An extensible membrane skin is used to cover the skeleton of both wings. The morphing mechanism is similar to ailerons. Rods are sewn onto the wing, in a way that a movement of the rod causes a movement of the membrane. This mechanism appears as an attractive approach in roll control because the flexible nature of the membrane enables an easy asymmetrical alteration of the wings [37].

The flexibility and adaptivity of a membrane could be exploited to change the thickness of an airfoil. If the membrane is used as lifting surface of a wing, the wing shape adapts to both the dynamic pressure and the angle of attack. A deflection of the membrane varies the thickness and, thus, varies the aerodynamic properties depending on the pre-tension of the membrane.

Research on membrane wings is quite common with respect to MAVs. Hu et al. [45] proposed investigations on a flexible-membrane airfoil/wing at low Reynolds number for MAV applications (Fig 1.2a). In their study, four configurations are tested and compared to the rigid airfoil/wing counterpart. The same membrane-airfoil geometry is employed for all configurations, but with a differing number of rigid ribs to adjust the flexibility of the membrane. Aerodynamic forces and flow field measurements are performed to evaluate the aerodynamic characteristics of the concept. The aerodynamic force measurements indicate that a flexible-membrane system offers enhanced aerodynamic performances compared to the rigid wing. The flexibility results in a natural adaptation of the shape of the airfoil/wing to the flow through a softer stabilization of the pressure difference between the upper and the lower side of the wing. Consequences of the shape adaptation are an increase in the lift coefficient, while the onset of stall is shifted to higher angles of attack [45].

More recently, Zhang et al. [100] also considered batten-membrane wings for MAVs application (Fig 1.2b). The wings are constructed on the same basic concept of [45], namely a rigid LE, rigid battens and a flexible membrane as lifting surface. In reference [100], Zhang et al. investigated the influence of the aspect ratio (AR) of the wing and of the cells, with a cell defined as the membrane part of the wing between two battens. The study showed that the bigger AR is, the more significant the difference between rigid and membrane wing is. This implies that the benefits in the increase of lift gained with a membrane wing is more pronounced when the AR is high. Furthermore, a higher cell's AR offers more flexibility and induces an increase in the lift. But when the cell's AR is greater than 2, it leads to TE fluttering inducing a drag penalty at low angles of attack. Therefore, high cell's AR should be avoided in a free-TE membrane wing. The study included also a variation of the pre-tension of the membrane. An overly high pre-tension leads to an incapacity to deform, which implies that the values of the lift are similar to a rigid wing. However, an overly loose pre-tension leads to fluttering phenomenon resulting in poor efficiency [100].

Aircraft Field

The importance of modifying the wing shape was recognized in history with the invention of the aircraft. The Wright brothers identified and understood the importance of adjusting the wing to the numerous varying flow conditions. In 1903, they registered a patent (US. Patent 821.393

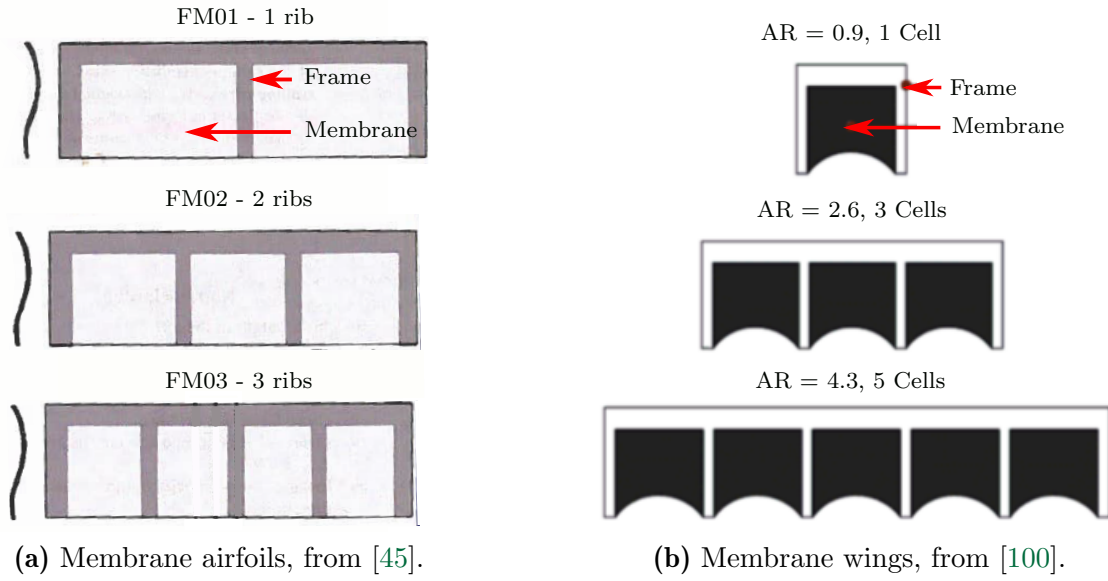


Figure 1.2: The membrane airfoil/wing prototypes, illustration from [45] and [100].

Flying-Machine) referring to wing warping. The wings of the Wright Flyer were made with a thin and flexible membrane able to deform and adjust to the incoming flow. Later, as aircraft had to fly faster, wings had to be more robust leaving the membrane lifting surfaces to stronger structures.

In the last decades, several morphing research programs have been carried out for aircraft. In the 1980s, the Mission Adaptive Wing (MAW) program (National Aeronautics and Space Administration - NASA) had the purpose to investigate the feasibility of variable camber concepts using hingeless LE and TE [20]. Then in the 1990s, The Smart Wing program (Defense Advanced Research Projects Agency - DARPA) focused on developing smart material based control surfaces, which intend to improve aerodynamic performance for a whole flight range [51]. More recently, the Morphing Aircraft Structures (MAS) program (DARPA) permitted to develop active morphing air vehicles able to change their wing shape and the wing area [86].

For example, the Lockheed Martin Morphing aircraft was developed with the capacity to fold itself from a loiter configuration into a dash geometry. The latter reduces the wing area to permit the aircraft to fly at higher Mach number without experiencing aeroelastic instabilities [48]. In 2007, Flanagan et al. [35] proposed a variable wing sweep system developed on the NextGen MFX-1 (Fig. 1.3). The wing consists in an innovative flexible skin, allowing the wing to smoothly change its shape. The wing area and the sweep angle are consequently interdependent. The inter-dependency permits to combine an efficient loiter configuration with a high-speed dash con-

figuration by morphing the wing from a high- to a low-aspect ratio [35].

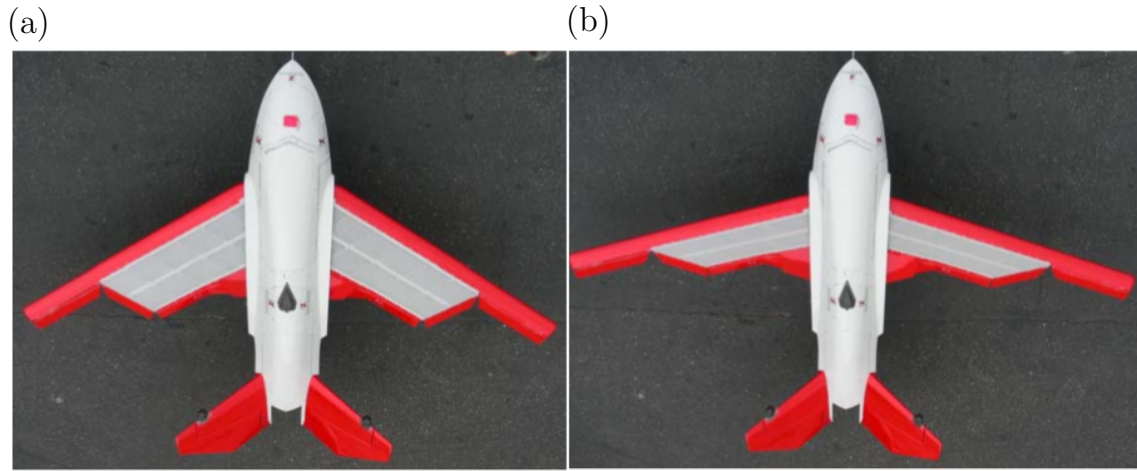


Figure 1.3: The NextGen MFX-1 prototype, illustration from [35]. (a)-(b) Prototype showing two morphing configurations with a wing-area change of about 40%.

Similarly to MAV concepts, camber morphing systems have been investigated to contribute in aerodynamic optimization and enhancement. In the field of aircraft research, variable camber flight vehicles are realized with a deflection of the TE. In 2014, Yokozeki and Sugiura [98] investigated a moving TE with corrugated structures. They employed a Wortmann FX63-137 airfoil to develop the wing model. The morphing TE section is designed from 69% to 90% of the chord length and is connected to a servomotor through a wire placed in the corrugated structure. Activating the motor enables the deflection of the TE to vary the wing camber [98].

Based on the same idea, Zhang et al. [99] developed a variable-camber wing using a flexible TE made with a honeycomb structure surrounded with telescopic tube actuators. Acting on the tubes by changing the internal pressure induces a displacement in the axial direction. The TE is therefore deflected upwards and downwards by introducing a pressure difference between the tubes on the upper side and on the lower side of the TE [99].

Many other examples can be mentioned in the scope of variable-camber flight vehicles. Campanile et al. [24] developed a belt-rib concept and integrated it in an outboard flap of an Airbus A340 aircraft. Woods et al. [97] introduced a fish-bone-active-camber system made with a bending beam, stringers and a skin surface of elastomeric matrix composite. The droop-nose device studied in [96, 65], enables the LE to deform by using actuators and highly anisotropic skins.

Recently, the Technische Universität München initiated research projects on form-variable wings

[19, 18]. One of the concept is made up with an articulated frame structure and an elasto-flexible membrane, which serves as a lifting surface. The structure was developed based on the skeletal form of a pterosaur. It allows large variation of the platform, whereas the flexibility of the membrane results in a camber change. The investigation focuses on the development and analysis of such a morphing membrane wing to gain a detailed understanding of its aero-elastic behavior. Indeed, the shape of the wing is not fixed in advance but results from the interaction between the aerodynamic and the structural forces, all acting on the membrane. The investigations gather wind tunnel data where the forces, the flow field and the membrane dislocation were measured. Furthermore, a self-developed code based on an analytic formulation of the membrane was coupled to the flow solver XFOIL [33] in order to increase the knowledge about the concept. It was found that the geometry and the aerodynamics of the wing are clearly dependent on the flow conditions. The membrane dislocation leads to non-linear polar and permit a delay of the stall to higher angles of attack. It turned up that the natural change of the wing camber with the flow seems to be a promising system to passively control the flow without adding any extra weight.

Wind Turbine Field

The wind energy field has experienced a significant expansion since the beginning of the 21st century [21]. In 2017, the worldwide wind power capacity approached 540 GW, which corresponded to six times more than the production 10 years earlier [1]. This growth highlights the need to produce more efficient wind turbines at lower costs.

One strategy to improve the efficiency of a wind turbine is found in the increase of its size. Higher towers and longer blades can take advantages of faster winds in larger heights [42]. However, longer blades under stronger winds are associated to higher loads and stresses. Therefore, new technologies have been required to enable the feasibility of bigger rotors with a special focus on structural issues and a reduction of fatigue loads from aerodynamic stresses. The new technologies are designated as smart structure or smart rotor control [11, 52]. They are usually based on existing concepts investigated for helicopters. Nevertheless, an increase in weight, in complexity or in moving parts should be restrained as the maintenance still needs to be limited.

Small devices such as microtabs or flaps seem promising [9, 91, 27, 10]. They could be used as discrete devices or as continuously deformable TE. Both systems alter the pressure distribution on the blade and offer an enhancement or a mitigation in lift, which directly affects the aerodynamic

load on the blade [9, 91, 27, 10]. Furthermore, an in-plane system has been investigated with telescopic structure in the span-wise direction of the blade. As documented by Johnson et al. and Van Dam et al. in [50, 92], a prototype has been designed and tested to extract/retract a tip blade out of a root blade. The tip blade are extracted only at low wind speeds (7-9m/s). The larger rotor diameter captured more energy as its area was larger. But the latter resulted in larger aerodynamic loads which induced more bending on the blade root and the tower. The results still showed an increase in the power production from 20% to 50% at low wind speeds.

Flexible materials have proven their capability to improve aerodynamic efficiency in the fields of MAV and aircraft. Hence, an extension of this morphing concept suggests itself to high Reynolds number operating machines. The concept appears to be an interesting solution when it is taken as a part of the blade tip section. Altering the shape of the blade tip area by means of a membrane section without adding additional weight may be a powerful idea.

In 1966, the Princeton windmill research group investigated a first version of a sailwing for a wind turbine. The sailwing consisted in a rigid mast forming the LE, rigid ribs and a sail for the lifting surface. A windmill of sailwings was tested over a one year period using the material Dacron for the sails [87]. At the end of this period the structure appeared to withstand weather conditions such as strong winds, freezing rain and heavy snow storms. It was also found that with its adaptivity, the wing could offer higher lift and a gentler stall behavior than its rigid counterpart. In 1976, the same group tested a smaller-sized family of sailwing rotors and concluded that such a concept was highly competitive in performance compared to its rigid-bladed counterparts [60].

This overview gives various examples of active and passive morphing systems in the MAV, the aircraft and the wind turbine domain. A number of selected examples were presented here in context of the own research, but a lot of other projects have also employed morphing systems being beyond the scope of this section.

1.2.2 Fluid-Structure Interaction Computations

As mentioned previously, modern engineering attempts to spread its expertise by taking into consideration many physical effects in one analysis [23, 17]. During the last decade, the multi-physics fluid-structure area has experienced a considerable growth. Various phenomena have been investigated in order to achieve a better comprehension in multi-physics phenomena. Many examples of fluid-structure interaction (FSI) investigations can be enumerated, ranging from analyzing the

influence of the shape of an airfoil to optimize its performance [97], through calculating the forces acting on a parachute [89, 88], to analyzing the wall shear stress of aneurysms [15].

In the early 2000s, FSI investigations using a coupling between Computational Fluid Dynamics (CFD) and Finite Element Method (FEM) have been performed to model the membrane wing designed by Ifju et al. for MAVs application [84, 57, 56]. The FSI investigations are compared to wind-tunnel test data. The deflection of the membrane with wind tunnel tests is juxtaposed to the one obtained from the computations at two angles of attack, namely 6° and 15° . The correspondence between the two sets of data is close, which encourages the development of such computations [84, 57, 56].

In 2011, Gaspari et al. [30] developed a two-level optimization routine for morphing camber airfoils. The XFOIL code, using a panel method, is employed to provide information about the aerodynamics, whereas a Finite Volume Beam Elements method is applied to calculate the deformation of the structure. A main genetic algorithms finally has exploited the fluid-structure coupling to find the best airfoil change and the best structural configuration to satisfy the requirements of the system.

In 2014, Woods et al. [97] employed a similar coupling to provide information about the fish-bone-active-camber morphing concept. The aerodynamic pressure is found within the XFOIL panel-method code coupled with a boundary-layer code [33], while the deflections of the TE are computed with an Euler-Bernoulli beam-theory-based analysis. These codes are iterated until convergence is achieved for relevant parameters [97]. In the same year, a bio-inspired Mirage Drive propulsion system based on tandem hydrofoils is numerically studied by Augier et al. [8]. An iso-geometric analysis is used to model the hydrodynamics of a 3D full scale of one foil of the propulsion system. The foil is modeled as a combination of the iso-geometric rotation-free Kirchhoff-Love shell and bending-stabilized cable discretized using Non-Uniform Rational B-Splines (NURBS), while the hydrodynamics of the foil is governed by the Navier-Stokes equations of an incompressible flow. The computational results on the foil are compared to experimental tests and a good agreement is found between both sets of data [8].

Bazilevs et al. produced first computational results for a 3D full scale wind turbine using a fully coupled (monolithic method) FSI procedure [13, 14]. Simulations of a NREL 5 MW offshore machine were carried out to better understand the possible displacements of the blade. Such information is of great interest during the design of the machine as it directly affects the loads on

the root of the blade. The fluid is governed by the Navier-Stokes equations for an incompressible flow associated to a residual-based turbulence modeling for moving domains. The structure is modeled with iso-geometric rotation-free shell formulation and NURBS. It was found that the blade mostly displaces in the flap-wise direction up to 6m. Furthermore, gravity affects significantly the bending and the twisting behavior of the blade. The blade experiences high-frequency oscillations leading to fluctuations in the aerodynamic torque [13, 14].

Later, Bazilev et al. [16] extended the study to a Darrieus-type vertical-axis turbine (VAWT). The structural model combines rotation-free Kirchhoff-Love shell and beam/cable elements, while the fluid model uses the same governing equations as mentioned before. The VAWT is entirely computed including its tower and three blades. The tower total height is 9m, whereas the blades are designed with a DU06W200 airfoil profile and are 6m long. FSI computations are carried out considering three initial rotor speeds to better understand the self-starting phenomenon. For low values of the rotor speed, the rotor naturally accelerates, whereas for high values, a dead-band region followed by a lower rotational speed is observed [16].

In 2017, the Technische Universität München initiated a research project on a blade made up with a membrane [76, 74, 77, 75]. The blade geometry is based on the NASA-Ames phase VI wind turbine. It consists of a rigid mast at the LE, ribs along the blade, tensioned edge cables at the TE and a membrane playing the role of the lifting surface. Various environments of multi-fidelity aeroelastic analysis are developed in order to simulate the behavior of the membrane blade. For instance, FSI are developed by using low-fidelity and high-fidelity approaches. In the first case, the fluid state is calculated by means of a vortex panel code, whereas in the second case, the fluid is computed using the Finite Volume Method (FVM). In both cases, the membrane state is found by means of the Finite Element Method (FEM). The membrane blade is investigated in non-rotating and rotating configurations. The performance of the two configurations is estimated by means of the Blade Element Momentum method and compared to a rigid baseline. The study shows that for low wind speeds, the rigid blade generates more power than the membrane blade. However, for higher wind speeds, the trend is reversed: the membrane allows a change of the camber, which positively influences the aerodynamics of the blade.

The membrane concept shows great potential in enabling the blade to extend its working range. Again, the membrane concept by means of its flexibility, could play a role of a passive flow control system and could increase the performance of a machine.

1.3 Objectives and Methodology

Investigations on elasto-flexible membrane wings have already been performed at the Technische Universität München within the works of Beguin and Saeedi [19, 18, 76, 74, 77, 75] (Secs. 1.2.1 and 1.2.2). The present thesis is part of the same topic but allows a new aspect to be explored. In the works of Beguin, the focus was made on experimental investigations performed on a wing designed for aircraft applications. Saeedi focused his work on the development of different FSI methods to analyze membrane wings for wind turbine applications.

The main objective of the present thesis is to investigate elasto-flexible membrane wings for wind turbine application by developing FSI methods (coupling between CFD and FEM) validated with experimental data. The thesis combines numerical and experimental parts on moderate Reynolds number operating machines, which makes it possible to distinguish with the two aforementioned theses [18, 74].

In the present thesis, the wings are made of two rigid spars, namely the LE and TE, and a membrane sewn onto both spars. The membrane acts as a lifting surface and changes its geometry under varying free-stream conditions (Fig. 1.4). Therefore, such a concept appears interesting in the field of aerodynamics and wind turbine as a passive flow control system. The main objective is divided into three milestones.

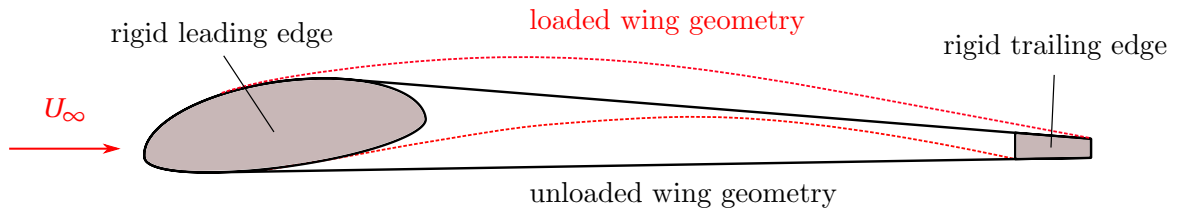


Figure 1.4: Morphing membrane wing in the loaded and unloaded case

The first milestone is to develop approaches allowing the numerical analysis of flexible lifting surface concepts made with membrane fabrics. FSI approaches are used to study the relationship between the membrane and the flow around the wing. FSI are generated by coupling two solvers, namely one calculating the membrane deflection and another one computing the fluid state (coupling between CFD and FEM). However, the accuracy of the FSI computations is to be estimated. Consequently, the computations are compared to experimental data for various models and at

several conditions to enlarge the range of applicability of the couplings.

A second milestone is to numerically investigate the flexible membrane concept. Indeed, it is interesting to understand the benefits gained with such a system. It is well known that flexibility during flight could definitely extend flight envelopes of certain systems. Various airfoil and wings models are consequently computed under several conditions to define the advantages compared to their rigid counterparts.

Finally, the third milestone is to conclude the benefits of flexible membrane wings in the field of aerodynamics and more precisely in the wind turbine field. Indeed, one direct application of the concept is thought to be on a wind turbine blade. The flexibility of the system taken as a part of a wind turbine blade suggests an interesting solution to improve the aerodynamic efficiency of the machine. For which range of angles of attack or wind conditions is the concept interesting? Does it offer a better lift-to-drag ratio compared to its rigid counterpart? Could the flight envelop be extended? The last milestone brings answers to the last questions.

To achieve the latter purposes, the following steps are considered:

- Firstly, FSI approaches are developed to investigate three experimental elasto-flexible membrane models. The FSI approaches are adapted to the models and employed to generate computational results.
- Secondly, experiments are performed to produce a panel of experimental data. The data is compared to the computational results to assess the accuracy of the FSI couplings.
- Then, the flexible membrane concept is investigated at various conditions. A variation of the angle of attack, the dynamic pressure, the turbulence model etc. are considered to explore the radius of application of such a concept.
- Finally, all data is collected to conclude the benefits of a flexible membrane concept in general and more particularly for a wind turbine application.

1.4 Outline

The second chapter of the present thesis presents the numerical methodology. A general description is given about two main methods to develop FSI computations. The words monolithic and partitioned are introduced and explained through this chapter. Then the governing equations are recalled in order to describe the fluid state, the structure state and the coupling conditions

operating at the interface between the fluid and the structure. Finally, Chapter 2 presents briefly the several solvers used in the thesis.

The experimental and numerical set-ups are described in details in Chapter 3. In the first part, the mechanical properties of the membrane fabrics are presented. Then three experimental models are intensively explained and illustrated. The experimental models are tested in wind tunnel facilities and different parameters are measured by means of various technics. Descriptions about the set-up for the force, the membrane deformation and the velocity measurements are given and illustrated by means of detailed pictures. Finally, the numerical set-up modeling the three experimental models is also explained in this chapter.

Chapter 4 presents a comparison between FSI computations and experimental data for airfoil's models. Indeed, the development of the FSI computations are initiated with two-dimensional models to reduce the complexity. The comparison is made for two models introduced in Chapter 3. For each model, the membrane deflection, the velocity of the flow field and the forces are compared between numerics and experiments to assess the precision of the FSI computations. Experimental and numerical considerations are reviewed as well, as they should be taken into account during the comparison.

As the validity and precision of the FSI computations are estimated in Chapter 4, Chapter 5 gives a detailed numerical analysis of a membrane airfoil concept. The chapter is divided into two parts. The first part describes the advantages gained with the flexibility of the membrane in comparison to a so-called rigid counterpart geometry. A meticulous analysis of the membrane deflection and the pressure distribution is given to understand the evolution of the lift and drag coefficient with the angle of attack. The second part considers the variation of several parameters like the dynamic pressure, turbulence characteristics and gust conditions in order to enlarge the knowledge about the membrane concept.

Chapter 6 extends to three-dimensional systems. Two models, presented in Chapter 3, considered to produce three-dimensional flow are investigated in the last chapter. The two systems also add an extra complication in the structure as the membrane deflection is considered in three directions. Computations and experiments are compared to estimate the accuracy of the FSI. Afterwards, FSI results are analyzed in details and placed side to side with rigid data to highlight the advantages gained with the flexibility of the concept. The FSI computations appear in Chapter 6 as an interesting solution to investigate parameters, which are not accessible in the experiments.

Finally, the thesis ends with a conclusion about the elasto-flexible membrane wing systems. All data is summarized and synthesized in order to highlight the major findings concerning the concept and to respond to all the questions raised in the third milestone. The thesis provides at the end recommendations for future investigations on the elasto-flexible membrane wing concept.

Chapter 2 - Numerical Methodology

This chapter presents the methodology employed to perform the numerical computations into three main sections. The first section gives an overview of the fluid-structure analysis. Various expressions defining FSI methods are reviewed. The words monolithic and partitioned, as well as full- and loose-coupling designs are explained. Then a one-way and a two-way FSI couplings are clarified, while a strong-partitioned coupling is defined. The second section reviews the governing equations of FSI problems. The equations governing the fluid are presented, followed by a brief overview of the turbulence modeling in the Computational Fluid Dynamic method of Unsteady Reynolds Averaged Navier Stokes simulations. Next, the equations governing the structure are established followed by a brief introduction to the Finite Element Method. The important variables are defined for the post-processing for each domain, namely the fluid and the structure. The last part of the second section gives an introduction of the boundary conditions on the fluid-structure interface and the two mapping methods employed in the present thesis. Finally, the last section of this chapter gives a description of the various programs used herein.

2.1 Fundamentals of FSI

The topic of FSI analysis have gained popularity in the last decade. Simulations of various phenomena, from daily life to scientific complex problems, may be modeled within a coupling between fluid and structure computational methods. For instance, a pulsating flow of blood circulating in vessels implies deformation of the tissues. This deformation, or more precisely, the wall shear stresses of arterial plays an important role into cardiovascular diseases. As experimental analysis of such a phenomenon remains unattainable, the coupled fluid-structure interaction between the vessels and the blood appears interesting to better understand medical diseases such as aneurysm.

In modern structural design, there is a new strong tendency to build so-called light structures with an efficient load-carrying behavior. However, the design of such structures is a challenging

task as they are more sensitive to vibrations. The fluid around may strongly influence the structure, which may lead to strong deformations. The latter results in a non-negligible interaction between the flow and the structure. The analysis of the interaction becomes mandatory if it has to be verified that the structure can withstand the loads acting on it. Typical examples in civil engineering are thin shells like chimneys and light membrane structures for wide-span roofs or slender bridges.

The last two examples are standard FSI problems where the deflection of the structure is important enough to alter the fluid flow. Such problems are defined as two-way FSI as the reciprocity between the deflection of the structure and the dynamics of the fluid is strong and can not be negligible. In other terms, the coupling is bidirectional. On the contrary, when only one field (fluid or structure) is predominant on the other, such problems are defined as one-way FSI. In other terms, the coupling is unidirectional. In the present thesis, the computational analysis is based on a two-way FSI problem. Therefore, throughout this thesis the term FSI refers to two-way problems.

Regarding the dynamics of FSI problems, the common domain of the fluid and the structure is defined as Ω . Ω is divided into the fluid part $\Omega_{\mathcal{F}}$ and the structure part $\Omega_{\mathcal{S}}$. The fluid-structure interface is defined as $\mathcal{I}_{FSI} = \delta\Omega_{\mathcal{F}} \cap \delta\Omega_{\mathcal{S}}$, being the surface intersection between both parts. The dynamics of the FSI computations is controlled by the conservation laws of the fluid, the structure and the boundary conditions at the surface intersection. The governing equations of both fluid and structure parts are remind in Subsections 2.2.1 and 2.2.2 while the boundary conditions which have to be satisfied at \mathcal{I}_{FSI} are remind in Subsection 2.2.3. To fulfill the conditions at \mathcal{I}_{FSI} , a transfer of information is necessary between the fluid and the structure. The FSI analyses are divided into monolithic and partitioned methods depending on the nature of the exchange of the information. Further information about monolithic and partitioned methods are given in the following sections.

2.1.1 Monolithic Method

Monolithic methods treat the dynamics of $\Omega_{\mathcal{F}}$ and $\Omega_{\mathcal{S}}$ in the same mathematical framework. The coupling is characterized as fully coupled. A single system of equations defines the FSI dynamics, where the governing equations are solved simultaneously by an unified algorithm. Eq. 2.1 is the general form of the FSI system of equations. The diagonal blocks $\mathcal{A}_{\mathcal{F}}$ and $\mathcal{A}_{\mathcal{S}}$ represent the fluid

and the structural internal equations.

$$\begin{bmatrix} \mathcal{A}_{\mathcal{F}} & \mathcal{A}_{\mathcal{F}\mathcal{S}} \\ \mathcal{A}_{\mathcal{S}\mathcal{F}} & \mathcal{A}_{\mathcal{S}} \end{bmatrix} \begin{bmatrix} \mathcal{X}_{\mathcal{F}} \\ \mathcal{X}_{\mathcal{S}} \end{bmatrix} = \begin{bmatrix} \mathcal{Y}_{\mathcal{F}} \\ \mathcal{Y}_{\mathcal{S}} \end{bmatrix} \quad (2.1)$$

The blocks $\mathcal{A}_{\mathcal{F}\mathcal{S}}$ and $\mathcal{A}_{\mathcal{S}\mathcal{F}}$ represent the coupling equations between the fluid and the structure. Boundary and volume conditions are contained in $\mathcal{Y}_{\mathcal{F}}$ and $\mathcal{Y}_{\mathcal{S}}$. The internal governing equations are based on the conservation laws of the fluid dynamics and of the structure mechanics. These equations are defined in a coordinate system which facilitates their resolution.

In classical continuum mechanics, two main points of view are usually exploited: the Lagrangian and the Eulerian point of view. A Lagrangian observer fixes his reference frame to one material domain and follows its movement in space. An Eulerian observer fixes positions or sub-domains and observes the materials which appears at these positions. Both points of view have advantages and limitations. In the Lagrangian point of view, it is possible to track a particle, which allows the consideration of moving boundaries. However, large deformations lead to unstable and inaccurate simulations. In the Eulerian point of view, it is easier to describe the variations of the fluid, but as the material is always subject to change, this does not allow to describe boundaries.

As the monolithic method treats the fluid and the structure simultaneously, the method needs both points of view. Monolithic methods usually use the so-called arbitrary Lagrangian-Eulerian (ALE) point of view to take advantages of both. The ALE point of view consists in having two different domains, namely the reference domain, which is fixed, and the physical domain, which is allowed to move relative to the reference domain. The governing equations of the system are derived in the physical domain and later transformed in the reference domain. A mapping is then required between the two domains to couple one to another.

To solve the system of linear equations in 2.1, iterative solution methods need to be used. For instance, the Conjugate Gradient, the Biconjugate Gradient Stabilized or the Generalized Minimum Residual Method can be mentioned. Then, so-called pre-conditioners are employed to accelerate the convergence of the results like the multi-grid method.

Monolithic methods are difficult to create and to program. But as the equations are solved simultaneously for the fluid and the structure, there are no approximation errors at the surface interaction and no convergence problems due to the transfer of data between the fluid and the structure.

2.1.2 Partitioned Method

Partitioned methods treat the dynamics of $\Omega_{\mathcal{F}}$ and $\Omega_{\mathcal{S}}$ as two sub-problems. The coupling is characterized as loose. The fluid and the structure equations are solved separately with their respective mesh discretization and numerical algorithm. Only the surface intersection is exploited as boundary condition to link the two solvers. Computational tools for these two types of problems are very well developed and already established. The main advantage of partitioned couplings is in the existence of the well developed tools. Two solvers, which have been separately already validated, can be used as fluid and structure solvers for the coupling. Only an outer coupling tool is needed to link the two solvers.

Most of the partitioned methods are employed in a semi-implicit time stepping scheme. Instead of solving both solvers at the same time step, one first solves its problem at one time step and its solution is utilized by the second solver to solve its own sub-problem. Let us define $f(t)$, $s(t)$ and $\Omega(t)$ as the fluid, the structure and the domain state at time t , respectively. A partitioned coupling method, which uses a semi-implicit time stepping scheme, would consist of the two following steps:

$$\mathcal{S}(f(t), s(t), \Omega(t)) \mapsto s(t + \Delta t), \Omega(t + \Delta t), \quad (2.2)$$

where the structure state at time $t + \Delta t$ is found from the fluid, the structure and the domain state at time t . Then, the fluid state at time $t + \Delta t$ is obtained from:

$$\mathcal{F}(f(t), s(t), s(t + \Delta t), \Omega(t), \Omega(t + \Delta t)) \mapsto f(t + \Delta t). \quad (2.3)$$

Indeed, the new solid state $s(t + \Delta t)$ allows a prediction of the velocity of the surface intersection by knowing $s(t)$ and $s(t + \Delta t)$. This velocity is exploited as a boundary condition for the domain $\Omega(t + \Delta t)$ and the fluid state can be solved at time $t + \Delta t$.

The partitioned method is easy to implement, as it only needs to create a platform exchange for the information of the surface intersection. However, this method can not guarantee a good accuracy of the results. Each solver solves its own sub-problem which can lead to errors at the surface intersection. For some applications, the partitioned coupling method can lead to numerical instabilities where the physical parameters do not converge. One solution to improve the result convergence is to iterate many times the same time step, until convergence is achieved. In this

case, the system described by Eqs. 2.2 and 2.3 is therefore as the following:

$$\text{for } i = 1, \dots, N \begin{cases} S(f(t, (i)), s(t, (i)), \Omega(t, (i))) \mapsto s(t + \Delta t, (i + 1)), \Omega(t + \Delta t, (i + 1)), \\ F(f(t, (i)), s(t, (i)), s(t + \Delta t, (i + 1)), \Omega(t, (i)), \Omega(t + \Delta t, (i + 1))) \mapsto f(t + \Delta t, (i + 1)). \end{cases}$$

This approach in improving the FSI convergence computations is also defined as strong partitioned coupling.

The choice of monolithic or partitioned coupling method needs special attention. Fig. 2.1 summarizes both methods and describes their differences. For the partitioned method, the main advantage is that two well established solvers can be used, whereas the monolithic coupling method needs to be implemented. Nevertheless, the monolithic approach does not approximate the force and the deformation at the interface resulting in no approximation errors and an enhanced convergence of the results [17, 23].

Some studies focused on the performance analysis between the monolithic and partitioned approach [31]. For some specific problems, the computational performance of the monolithic approach was twice higher than the partitioned approach. The influence of the domain size in terms of the number of elements was shown on a wave propagation in a straight elastic tube [31]. The computations with the monolithic approach was approximately two times faster than the computations with the partitioned approach. Furthermore, if the length of the tube increases, the partitioned approach fails at some point due to too large displacements, leading both solvers to crash. However, only some specific problems have been investigated and a direct sparse solver using full Newton-Raphson iterations was employed for the fluid solver. One needs to take into account that other solvers might have led to different results [31].

When choosing a method in a new application area, it is recommended to use the monolithic method [17]. The understanding and implementation of the monolithic coupling method will be time consuming. However, the approach is more robust. Many of the convergence problems will be avoided and the performance of the computations will be improved.

However in this thesis, the CFD and FEM solvers were already provided, tested and showed their performance [90, 44]. Therefore, it was decided to adopt a partitioned approach to model the elasto-flexible membrane wing behavior. The two solvers employed at each time step are composed of a fluid solver based on the Reynolds Averaged Navier Stokes (RANS) method, namely the TAU

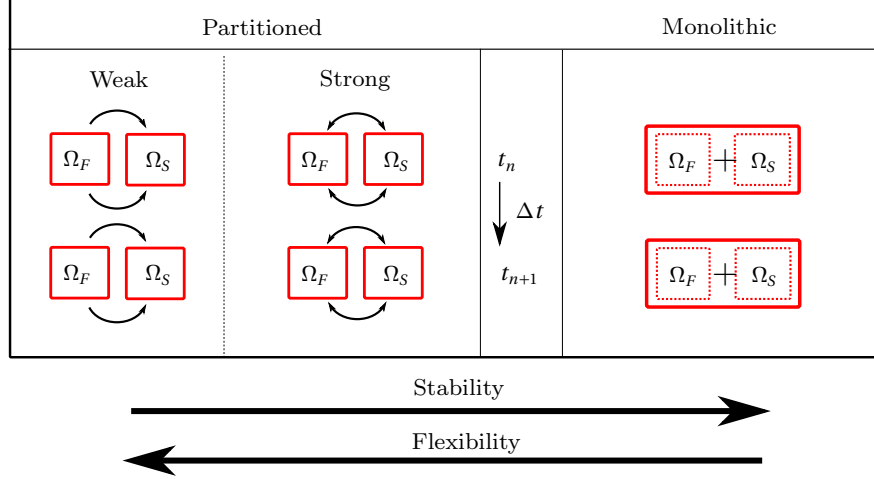


Figure 2.1: Description of the partitioned and the monolithic method and their differences.

code and the CFX solver product of ANSYS, and a structure solver based on the FEM, namely the CARAT++ code and the APDL solver product of ANSYS. All solvers are described and summarized in Section. 2.3.

2.2 Dynamics of FSI

FSI computations are based on the governing equations of fluid and structural mechanics. In the following subsections, the governing equations of both fluid and structural mechanics are reviewed and additional explanations or simplifications are introduced.

2.2.1 Fluid Dynamics

The word *fluid* is usually applied to a substance which cannot resist any force to change its shape. In other words, when a force is applied tangentially to one surface of a fluid, the fluid will experience a continuous deformation changing its shape to conform itself to the applied stress. The spacing between the molecules of a fluid is large and allows movements between each other. On the contrary, in *solid* the spacing is tiny and does not allow movements.

Liquids and gases are defined as fluids. The equations governing their dynamics are based on the conservation of mass, momentum and energy [93, 79, 78, 49, 4]. It is more appropriate to consider a small control volume where the fluid moves to analyze the motion of the fluid. The conservation of mass, momentum and energy is then applied to the control volume and derive five equations

with six variables: the pressure p , the density ρ , the temperature T , and the x, y, z -components of the velocity u , v and w . Then, an additional equation of state is utilized to characterize the fluid and close the system of equations.

In the following, a control volume of a viscous fluid \mathcal{V} is considered with no mass added. \mathcal{S} represents the closed surface of \mathcal{V} illustrated in Fig. 2.2. In the following, the conservation of mass, momentum and energy for \mathcal{V} are reminded. Then two turbulence models in the URANS method are introduced and a description of the variables used for the post-processing of this work is given.

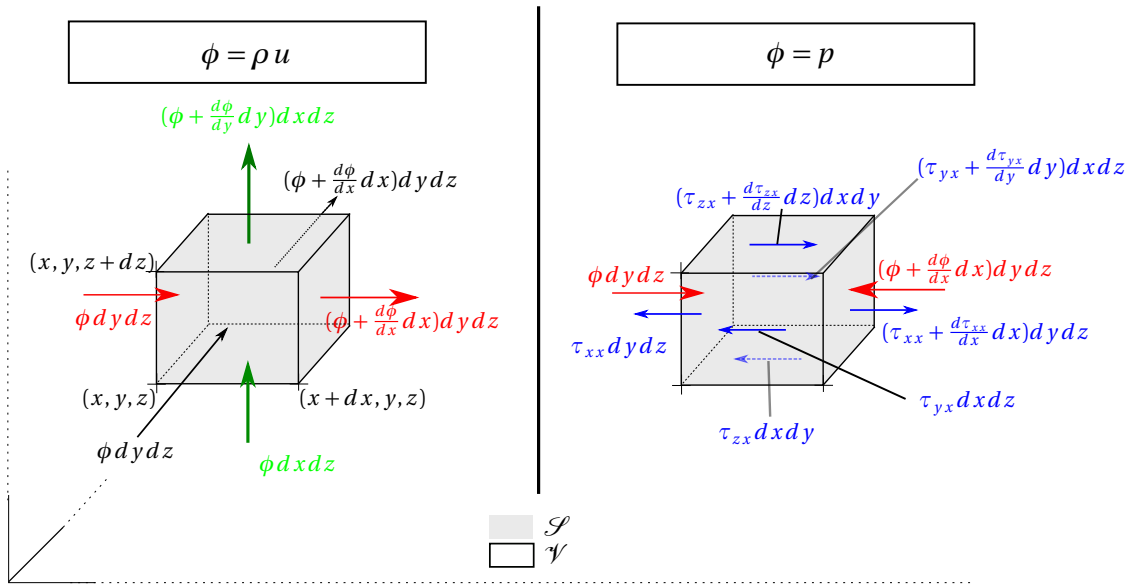


Figure 2.2: Control volume in cartesian coordinates, [93].

2.2.1.1 Governing Equations

Conservation of mass

The conservation of mass states that the variation of the mass of an arbitrary \mathcal{V} is equal to the mass flux crossing the surface \mathcal{S} limited with \mathcal{V} . In other terms, the latter can be described with the following equation:

$$\frac{d}{dt} \int_{\mathcal{V}} \rho d\mathcal{V} = - \oint_{\mathcal{S}} \rho \vec{v} \cdot \vec{n} d\mathcal{S}, \quad (2.4)$$

with ρ being the density, \vec{v} the velocity and \vec{n} the unit normal vector (outward). The minus sign indicates that when the mass decreases, the flux is going outside the control volume. When the

Gauss theorem ($\oint_{\mathcal{S}} \vec{F} \cdot \vec{n} d\mathcal{S} = \iiint_{\mathcal{V}} \vec{\nabla} \cdot \vec{F} d\mathcal{V}$) is used, Eq. 2.4 is transformed to:

$$\int_{\mathcal{V}} \frac{d\rho}{dt} + \vec{\nabla} \cdot (\rho \vec{v}) d\mathcal{V} = 0. \quad (2.5)$$

As Eq. 2.5 is valid for any size of \mathcal{V} , it can be re-written in Eq. 2.6, which is usually known as the continuity equation

$$\frac{d\rho}{dt} + \vec{\nabla} \cdot (\rho \vec{v}) = 0. \quad (2.6)$$

Conservation of momentum

The conservation of momentum is based on the second law of motion stated by Newton. The law states that the variation of the momentum of an arbitrary \mathcal{V} is equal to the sum of the forces \vec{F} acting on it. It can be written as followed:

$$\frac{d}{dt} \int_{\mathcal{V}} \rho \cdot \vec{v} d\mathcal{V} = \sum_{\mathcal{V}} \vec{F}. \quad (2.7)$$

According to [85], the first term of Eq. 2.7 can be re-written as:

$$\frac{d}{dt} \int_{\mathcal{V}} \rho \cdot \vec{v} d\mathcal{V} = \int_{\mathcal{V}} \frac{\partial(\rho \vec{v})}{\partial t} d\mathcal{V} + \oint_{\mathcal{S}} \rho \vec{v} (\vec{v} \cdot \vec{n}) d\mathcal{S} \quad (2.8)$$

$$= \int_{\mathcal{V}} \frac{\partial(\rho \vec{v})}{\partial t} d\mathcal{V} + \int_{\mathcal{V}} \vec{\nabla} \cdot (\rho \vec{v}) \vec{v} d\mathcal{V}. \quad (2.9)$$

At this point, it is convenient to define the material derivative $\frac{D}{Dt}$ as:

$$\frac{D()}{Dt} = \frac{\partial()}{\partial t} + \nabla() \cdot \vec{v} \quad (2.10)$$

$$= \frac{\partial()}{\partial t} + u \frac{\partial()}{\partial x} + v \frac{\partial()}{\partial y} + w \frac{\partial()}{\partial z}. \quad (2.11)$$

The material derivative describes the time-related variation inside an element, when this element moves. Therefore substituting 2.11 in 2.7, the equation can be re-written as:

$$\int_{\mathcal{V}} \frac{D(\rho \cdot \vec{v})}{Dt} d\mathcal{V} = \sum_{\mathcal{V}} \vec{F}. \quad (2.12)$$

The forces acting on \mathcal{V} are divided into surface forces and volume forces. The common volume force is due to the gravity and the surface forces depend on the nature of the fluid, whether it

is considered as viscous or inviscid. The surface forces are consequences of the pressure p acting on the surface of \mathcal{V} and the viscosity of the fluid defined with the tensor $\underline{\underline{\tau}}$. This tensor contains the normal and the tangential stresses inside the fluid. Eq. 2.12 is therefore:

$$\int_{\mathcal{V}} \frac{D(\rho \cdot \vec{v})}{Dt} d\mathcal{V} = \oint_{\mathcal{S}} -p\vec{n} d\mathcal{S} + \oint_{\mathcal{S}} \underline{\underline{\tau}} \vec{n} d\mathcal{S} + \int_{\mathcal{V}} \rho \vec{g} \vec{n} d\mathcal{V}. \quad (2.13)$$

As Eq. 2.13 is valid for any size of \mathcal{V} , it can be re-written as:

$$\frac{D(\rho \cdot \vec{v})}{Dt} = -\vec{\nabla} p \vec{n} + \vec{\nabla} \underline{\underline{\tau}} \vec{n} + \rho \vec{g} \vec{n}. \quad (2.14)$$

Conservation of energy

The conservation of energy is based on the first law of the thermodynamics. The law states that the variation of the internal energy e_i and the kinematic energy e_c of an arbitrary \mathcal{V} is equal to the heat transfer through \mathcal{V} minus the work done by the system. The latter can be re-transcribed as:

$$\frac{d}{dt} \int_{\mathcal{V}} \rho(e_i + \frac{e_c^2}{2}) d\mathcal{V} + \oint_{\mathcal{S}} \rho(e_i + \frac{e_c^2}{2}) \vec{n} \cdot \vec{v} d\mathcal{S} = \int_{\mathcal{V}} (\rho \vec{g}) \cdot \vec{v} d\mathcal{V} + \oint_{\mathcal{S}} (\rho \vec{\mathcal{T}}) \cdot \vec{v} d\mathcal{S} - \oint_{\mathcal{S}} \vec{q} \cdot \vec{n} d\mathcal{S}, \quad (2.15)$$

with $\vec{\mathcal{T}} = -p\vec{n} + \underline{\underline{\tau}} \vec{n}$ being the vector representing the surface forces on \mathcal{S} and \vec{q} being the heat flux through \mathcal{S} . Using the material derivative and as 2.15 is valid for all \mathcal{V} , the conservation of energy can be re-written as:

$$\frac{D\rho(e_i + \frac{e_c^2}{2})}{Dt} = (\rho \vec{g}) \cdot \vec{v} + \vec{\nabla}(\rho \vec{\mathcal{T}}) \cdot \vec{v} - \vec{\nabla} \vec{q} \cdot \vec{n}. \quad (2.16)$$

In the following, the fluid is supposed to be viscous and incompressible. Eqs. 2.6, 2.13 and 2.16 can be simplified considering the density ρ as a constant value. At that point, it is interesting to introduce the Newton fluid model which is often exploited in CFD as air belongs to the newtonian fluid class. In a newtonian fluid the components of the viscous shear stress tensor $\underline{\underline{\tau}}$ can be written as:

$$\tau_{ij} = \mu \left(\frac{\partial v_i}{\partial v_j} + \frac{\partial v_j}{\partial v_i} \right) - \frac{2}{3} \mu \frac{\partial v_k}{\partial v_k} \delta_{ij}. \quad (2.17)$$

where μ is the dynamic viscosity of the fluid and the notation δ_{ij} comes from the tensor $\underline{\underline{\delta}}$, where $\delta_{ii} = 1$ and $\delta_{ij} = 0$ for $i \neq j$. The dynamic viscosity μ depends on the temperature T and follows

the Sutherland's law [49] mentioned in the following:

$$\mu = \mu_{ref} \left(\frac{T}{T_{ref}} \right)^{\frac{3}{2}} \frac{T_{ref} + 110.4 \text{ K}}{T + 110.4 \text{ K}}, \quad (2.18)$$

where $\mu_{ref} = 1.716 \times 10^{-5} \text{ m}^2/\text{s}$ and $T_{ref} = 273.15 \text{ K}$ are the reference dynamic viscosity and temperature.

To close the system of equations, an additional equation of state is needed. It is common to use the ideal gas equation of state [49, 79, 78]

$$p = \rho R T, \quad (2.19)$$

R is the gas constant related to the universal gas constant and the molecular weight of the gas. R differs from one gas to another. For air, $R = 287.1 \text{ J}/(\text{kgK})$.

The ratio γ between the specific heat at constant pressure c_p and the specific heat at constant volume c_v is also sometimes utilized for some parameters. For air, $\gamma = 1.4$ is commonly used.

2.2.1.2 Turbulence models

The system composed by the mass, the continuity and the energy conservation equations are commonly designated as the Navier-Stokes equations. They describe the governing equations of a fluid. In this thesis, the CFD method employed to solve the system is based on the FVM. In the FVM, the domain is divided into several finite volumes and the conservation of flux through these volumes is exploited. The FVM is based on the integral forms of the governing equations presented in the previous subsection. One unknown variable q is approximated by using the conservation of q into each finite volume. The whole domain is solved through a spatial discretization where the approximation of q is done from one finite volume to another, progressing in the flow direction. Terms with divergence inside the governing equations are transformed with the Gauss's theorem to use the integral form on a surface. CFD usually prefers using the FVM instead of the FEM to solve the fluid equations as the conservation of mass, momentum and energy is automatically satisfied in the whole domain [93, 81, 55].

As mentioned in Subsec. 2.2.1.1, the fluid considered in this thesis is supposed to be incompressible and Newtonian. At that point, several quantities can be introduced [78, 4]. The Reynolds number (Re) is a dimensionless parameter which expresses the ratio between the inertial and the

viscous forces in a flow. Re depends on the free stream velocity U_∞ , the kinematic viscosity ν and a reference length L as described in Eq. 2.20. L is a characteristic length of the object, which is studied in the flow. In the present thesis, the root chord c_r of the wing is used as the reference length L :

$$Re = \frac{U_\infty \cdot c_r}{\nu}. \quad (2.20)$$

A viscous flow can be categorized into two regimes laminar or turbulent [78, 4]. In a laminar flow particles move in parallel layers with no disruption between the layers. When the streamlines are followed, the flow seems organized and predictable. The governing equations can be solved numerically and accurately. In an opposite way, particles move randomly in a turbulent flow. When the streamlines are followed, the flow seems chaotic and comprises eddies, swirls and instabilities. Turbulent flows encompass fluctuations which are not predictable. Usually Re characterizes the regime of the flow. A small Re describes a flow where the viscous forces are predominant on the inertial one and the flow is usually laminar. A high Re describes a flow where the inertial forces are predominant on the viscous one and the flow is usually turbulent.

When a flow is turbulent, several length scales are present in the eddies [70]. For reasonable predictions of the flow, all eddy sizes should be solved. Turbulence models are classified into three groups.

- The Direct Numerical Simulation (DNS) includes the computation of all available scales of motion in the flow, from the smallest to the largest eddy length scales. The turbulence is not modeled in this approach.
- The Large Eddy Simulation (LES) consists of computing the large turbulent motion of the fluid, while the smaller eddies are modeled. A filter is exploited in this approach to cut off the large to the small eddies.
- The RANS consists of decomposing the unknowns of the Navier-Stokes equations into a mean and a turbulent fluctuating value. The system of equations has then an additional term defined as the turbulence fluctuation, which has to be modeled to resolve the dynamics of the flow.

The DNS and LES methods need large computational resources. In the present thesis, it is not of interest to resolve the small or large eddies to model the behavior of the flexible wing. Therefore, the RANS method is employed as it is often the case in aerodynamic issues. Two

different turbulence models are employed and both are described in the following.

- **One-equation turbulence model: the Spallart-Allmaras model**

The Spalart-Allmaras (SA) model is based on one equation with central quantity of the turbulent viscosity ν_t [3, 83]. The model was developed in the last decade of the 20th century as a response to the two-equation turbulence model defined as the κ - ϵ model. The motivation was to develop a model for aerodynamic applications using only one transport equation to computationally facilitate the resolution of the flow dynamic. The model describes the transport of ν_t , more precisely of $\tilde{\nu}$ which is the effective viscosity defined as the SA viscosity. $\tilde{\nu}$ is a practical variable introduced to facilitate the calculation near the wall. As there was no exact transport equation to describe the evolution of $\tilde{\nu}$, it was decided to develop a model term by term, which could approximate the transportation of $\tilde{\nu}$. A classical approach was followed with an approximation of a term for production, for diffusion and for destruction by using quantities derived from the mean flow field and ν_t . All the terms were weighted with coefficients and congregated. A final calibration permits to obtain the damping terms. The transport equation of $\tilde{\nu}$ is of the “basic” following form:

$$\frac{D\tilde{\nu}}{Dt} = \underbrace{c_{b1}\tilde{S}\tilde{\nu}}_{production} + \underbrace{\frac{1}{\sigma}\left[\nabla((\nu+\tilde{\nu})\cdot\nabla\tilde{\nu}) + c_{b2}(\nabla\tilde{\nu})^2\right]}_{diffusion} - \underbrace{\left[c_{\omega1}f_{\omega1}\right]\left(\frac{\tilde{\nu}}{d}\right)^2}_{destruction} \quad (2.21)$$

where $\tilde{\nu}$ is related to ν_t with a damping function $f_{\nu1}$ of the viscosity ratio χ described as followed:

$$\chi = \frac{\tilde{\nu}}{\nu} \text{ and } \nu_t = f_{\nu1}(\chi) \cdot \tilde{\nu}. \quad (2.22)$$

The subscript b stands for “basic” and ω for “wall”. To improve precision, additional terms were also taken into account to describe the laminar region. The following terms are added up to 2.21:

$$(1-f_{t2}) + f_{t1}\nabla U^2 \text{ and } -\frac{c_{b1}}{\kappa^2}\left(\frac{\tilde{\nu}}{d}\right)^2, \quad (2.23)$$

where the first term has to be multiplied by c_{b1} serving as a damping function in the production term. Both terms have the purpose to keep the flow laminar and to obtain transition when it is desired. The subscript t stands for “trip”, which means “that the transition point is imposed by an actual trip, or natural but obtain from a separated method” [83]. The model does not predict the transition but tends to describe how is it expected.

- **Two-equation turbulence model: the $\kappa - \omega$ SST turbulence model**

The $\kappa - \omega$ SST turbulence model is based on two equations to solve the turbulence fluctuation [63, 62]. One equation solves the turbulent kinetic energy κ and the other equation solves the specific dissipation rate ω . The $\kappa - \omega$ SST model differs from the $\kappa - \omega$ model as it combines the $\kappa - \epsilon$ and the $\kappa - \omega$ models to yield the best behavior of both. Furthermore, the definition of the eddy viscosity is transformed in the aim of the transport of the principal turbulence shear stress [62, 63].

The idea behind the SST model is to switch between the $\kappa - \omega$ and the $\kappa - \epsilon$ model depending on the proximity to a wall. Near the wall, the representation of the turbulence is done with the $\kappa - \omega$ model whereas in the outer part of the boundary layer, the $\kappa - \epsilon$ model is applied. Nevertheless, the $\kappa - \epsilon$ model has to be modified into a $\kappa - \omega$ formulation to remain consistent. The modeling constants are therefore different and an additional cross-diffusion term appears. Then a blending function \mathcal{F}_1 is introduced to control the activation of both models. The following equations describe the model:

The original $\kappa - \omega$ model:

$$\frac{D\rho\kappa}{Dt} = \underline{\underline{\tau}} \cdot \nabla u - \beta^* \rho \omega \kappa + \nabla \left[\left(\nu + \sigma_{\kappa 1} \nu_t \right) \nabla \kappa \right] \quad (2.24)$$

$$\frac{D\rho\omega}{Dt} = \frac{\gamma_1}{\nu_t} \underline{\underline{\tau}} \cdot \nabla u - \beta_1^* \rho \omega^2 + \nabla \left[\left(\nu + \sigma_{\omega 1} \nu_t \right) \nabla \omega \right] \quad (2.25)$$

The transformed $\kappa - \epsilon$ into $\kappa - \omega$ model:

$$\frac{D\rho\kappa}{Dt} = \underline{\underline{\tau}} \cdot \nabla u - \beta^* \rho \omega \kappa + \nabla \left[\left(\nu + \sigma_{\kappa 2} \nu_t \right) \nabla \kappa \right] \quad (2.26)$$

$$\frac{D\rho\omega}{Dt} = \frac{\gamma_1}{\nu_t} \underline{\underline{\tau}} \cdot \nabla u - \beta_2^* \rho \omega^2 + \nabla \left[\left(\nu + \sigma_{\omega 2} \nu_t \right) \nabla \omega \right] + \underbrace{2\rho\sigma_{\omega 2} \frac{1}{\omega} \nabla(\kappa) \nabla(\omega)}_{\text{cross-diffusion}} \quad (2.27)$$

Eqs. 2.24 and 2.25 are then multiplied by \mathcal{F}_1 whereas Eqs. 2.26 and 2.27 are multiplied by $1 - \mathcal{F}_1$. Near the wall, the function \mathcal{F}_1 is active, permitting the original model to be used, whereas far from the walls \mathcal{F}_1 is equal to zero.

2.2.1.3 Post-processing parameters

Various aerodynamic parameters are defined to analyze the behavior of the flexible wing. It appears important to the author to remind the definition of them to avoid any misunderstanding.

When a body is immersed in a viscous flow, forces and moments are acting on it [79, 78, 4]. The forces and moments are usually caused by pressure p and shear stress τ effects, as it was described by Eq. 2.14. The resultant force, commonly designated as R , can be split into two components, parallel and perpendicular to the flow direction (see Fig. 2.3). The perpendicular component is defined as the lift L , whereas the parallel as the drag D . Both are linked to R with the angle of attack, which is the angle between the free stream direction and the chord of the body. Moments are also exerted on the body. They depend on the point about which the moment is taken. The pitching moment M is depicted on Fig. 2.3.

In aerodynamics, it is important to compare forces and moments between various geometries at several free stream conditions. Therefore, aerodynamics uses dimensionless parameters. The lift and drag coefficient (C_L and C_D , respectively) are obtained by dividing the respective forces by the dynamic pressure q_∞ and a reference area S of the body. The pitching moment coefficient is obtained by dividing the respective moment by q_∞ , S and a reference length l of the body (generally the chord).

$$q_\infty = \frac{1}{2} \rho_\infty U_\infty^2, \quad (2.28)$$

$$C_L = \frac{L}{q_\infty S}, \quad (2.29)$$

$$C_D = \frac{D}{q_\infty S}, \quad (2.30)$$

$$C_M = \frac{M}{q_\infty S l}. \quad (2.31)$$

Furtermore, the pressure coefficient and the skin friction coefficient are defined as:

$$C_p = \frac{p - p_\infty}{q_\infty S}, \quad (2.32)$$

$$C_\tau = \frac{\tau}{q_\infty S l}, \quad (2.33)$$

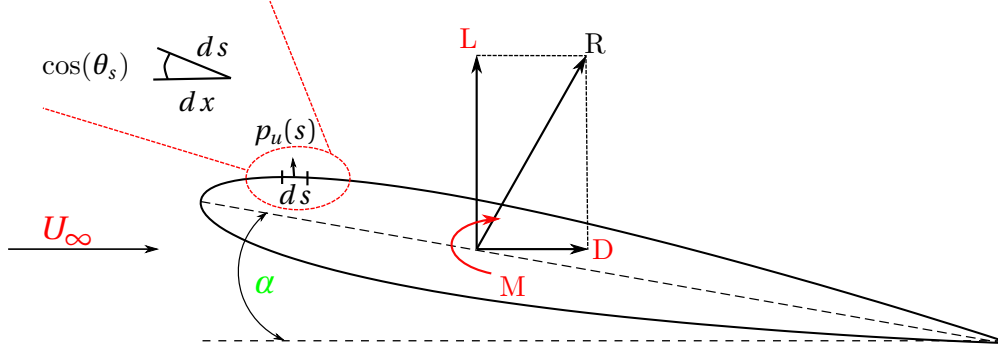


Figure 2.3: Aerodynamic forces on a NACA 0012 profile

with p the static pressure at the considered point, p_∞ the static pressure in the free stream and τ the wall shear stress.

In Chapter 6, the local lift is plotted along the wingspan. The local lift is defined as the following: if an airfoil is considered, the force N is defined as the integration of the pressure $p(s)$ acting on an infinitesimal size ds along the profile. In other words, it is equal to:

$$N = \int_{s_{low}} p_l \cos(\theta_s) ds - \int_{s_{up}} p_u \cos(\theta_s) ds, \quad (2.34)$$

with p_l the pressure acting on the lower side and p_u the pressure acting on the upper side of the airfoil. If the relation $ds = dx / \cos(\theta_s)$ is exploited, the equation becomes

$$N = \int_0^c p_l dx - \int_0^c p_u dx, \quad (2.35)$$

with c the chord of the airfoil. For small angle of attack, the lift is equal to the normal force acting on the airfoil. If the aerodynamic coefficients defined previously are considered, C_L is calculated as followed:

$$C_L \approx \int_0^c \frac{p_l - p_u}{q_\infty c} dx = \frac{1}{c} \int_0^c (C_{p,l} - C_{p,u}) dx \quad (2.36)$$

2.2.2 Structure Mechanics

Structures may be modeled as three-, two- or one- dimensional. A solid is generally a structure where all dimensions have the same order of magnitude in the three coordinates. If one dimension is considerably smaller, the structure is ranged into the surface structure class. The latter can be also divided into plates, shell and membrane elements. To differentiate the last elements, the mechanical properties have to be considered. As an example, while a plate can sustain loading by using its bending stiffness, a membrane can only sustain the loads by in-plane stresses. The bending stiffness of a membrane is reduced to zero.

The equations governing the dynamic of a structure consider the tensor of stresses $\underline{\underline{\sigma}}$, the tensor of strains $\underline{\underline{\epsilon}}$, the displacements \vec{d} , the properties of the structure and the external forces. The equations are based on the kinematic equilibrium (kinematic equation, KE) relating $\underline{\underline{\epsilon}}$ to the displacement, the constitutive relations (constitutive equation, CE) relating the properties of the materiel to $\underline{\underline{\sigma}}$ and $\underline{\underline{\epsilon}}$ and the balance equilibrium (balance equation, BE) relating $\underline{\underline{\sigma}}$ to the external forces. To describe the occurring stress and strain of an elastic body, the three sets of equations need to be exploited [101, 34, 41, 40]. Fig. 2.4 illustrates the different processes to be investigated in order to solve the structural state.

In the following, the BE, KE and CE are first reviewed for a general case before specifying the equations for the membrane theory, as only this class of structures is considered in the thesis. Then, an overview of the FEM is given to introduce the method.

2.2.2.1 Governing Equations

Usually, a solid is considered as a three-dimensional problem. In a cartesian system of coordinates (x, y, z) , the following mechanical variables need to be considered. The tensors $\underline{\underline{\sigma}}$ and $\underline{\underline{\epsilon}}$ describing the stress and strain states, respectively in a material point (x, y, z) , are described as

$$\underline{\underline{\sigma}} = \begin{bmatrix} \sigma_{xx} \\ \sigma_{yy} \\ \sigma_{zz} \\ \sigma_{xy} \\ \sigma_{yz} \\ \sigma_{xz} \end{bmatrix} \text{ and } \underline{\underline{\epsilon}} = \begin{bmatrix} \epsilon_{xx} \\ \epsilon_{yy} \\ \epsilon_{zz} \\ 2\epsilon_{xy} \\ 2\epsilon_{yz} \\ 2\epsilon_{xz} \end{bmatrix}. \quad (2.37)$$

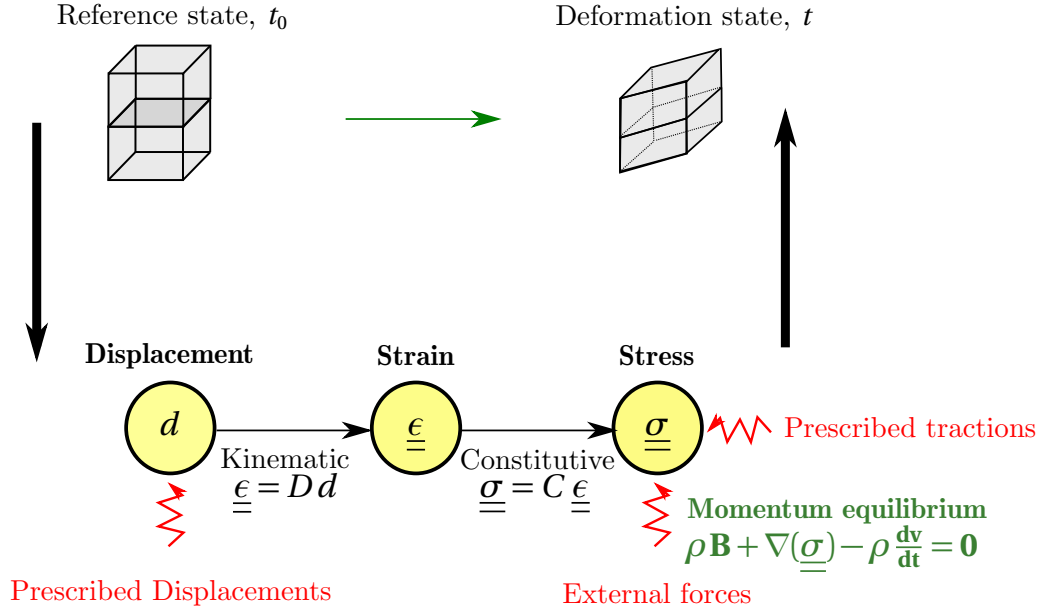


Figure 2.4: Schematic illustration of the various operations describing a structural analysis.

The displacements and the body forces are described at (x, y, z) as

$$d = \begin{bmatrix} d_x \\ d_y \\ d_z \end{bmatrix} \text{ and } \mathbf{b} = \begin{bmatrix} b_x \\ b_y \\ b_z \end{bmatrix}. \quad (2.38)$$

The membrane is considered as a two-dimensional structure. The thickness (h) is considerably small in comparison to the others dimensions. The mid-plane of the membrane is defined as the plane which lies halfway of h . In the continuum mechanics for membrane structures, the following assumptions are made [34, 41, 40]:

- All loads applied to the structure act in the mid-plane direction and are symmetric with respect to the mid-plane.
- In-plane displacements, strains and stresses are assumed to be uniform through h .
- The normal and the shear stress in the transverse direction of the mid-plane are negligible and considered to be equal to zero.
- The structure is considered of the same material, which implies that composite materials are excluded.

Using the assumptions mentioned above, the mechanical variables can be rewritten as:

$$\underline{\underline{\tau}} = \begin{bmatrix} \tau_{xx} \\ \tau_{yy} \\ \tau_{xy} \end{bmatrix}, \underline{\underline{\epsilon}} = \begin{bmatrix} \epsilon_{xx} \\ \epsilon_{yy} \\ 2\epsilon_{xy} \end{bmatrix}, d = \begin{bmatrix} d_x \\ d_y \end{bmatrix} \text{ and } \mathbf{b} = \begin{bmatrix} b_x \\ b_y \end{bmatrix}. \quad (2.39)$$

The three sets of equations, namely the KE, CE and BE are introduced in the following.

- **Strain to displacement relationship: KE**

To describe the mechanical behavior of the membrane in time and space, definitions of how the position of the material point is changing have to be made. The KE allows to describe the position of a specific material point at a specific time during the deformation. In other terms, the KE describes how two points within the solid move relative to each other when external loads are applied.

$\Omega_{\mathcal{S}}$ is supposed to be a deformable body set in a region of the Euclidean space \mathbb{R}^3 . In continuum mechanics, the word *configuration* represents the state of $\Omega_{\mathcal{S}}$ in time. The *reference configuration* normally refers to the initial (usually undeformed) state, namely $\Omega_{\mathcal{S}}(t_0)$, whereas the *current configuration* refers to the deformed state which is investigated, namely $\Omega_{\mathcal{S}}(t)$. We can define a material point as $\vec{X} \in \Omega_{\mathcal{S}}(t_0)$. Its position at the current time is noted as $\vec{x}(t)$. In continuum mechanics, the capital letters are commonly designate to the initial configuration, whereas the small letters to the current configuration. The displacement of a point $\vec{X} = (x, y, z)$ from its initial position to its deformed one $\vec{x}(t)$ is defined with the displacement vector:

$$\vec{d}(t) = \vec{x}(t) - \vec{X}. \quad (2.40)$$

As a common practice, a so-called transformation map \mathbf{F} is defined to describe the transformation between an infinitesimal line element dX to dx . This transformation map is designated to the *deformation gradient* as

$$\mathbf{F} = \frac{dx(t)}{dX}. \quad (2.41)$$

Various measures of the local deformation exist using \mathbf{F} . The Cauchy-Green strain tensors, the Green-Lagrange or Euler-Almansi strain tensors are some examples of how to measure the local deformation (for more details, see [32]). In the scope of this thesis, the membrane material is

the type of material subject to large deformation under small strains. Therefore, the Green-Lagrange strain measurement is applied to describe the kinetics of the local deformation. The Green-Lagrange strain tensor $\underline{\underline{\epsilon}}$ which allows for large displacement and rotation is used in this thesis:

$$\underline{\underline{\epsilon}} = \frac{1}{2}(\mathbf{F}^T \mathbf{F} - \mathbf{I}), \quad (2.42)$$

with \mathbf{I} being the identity matrix.

- **Stresses to strains relationship: CE**

The strains and the stresses intern to a solid are interdependent to each other. Indeed, stresses applied to a solid induce deformations and vice versa. The relationship between both strain and stress is described by the CE. A general relation is described by Eq. 2.43:

$$\underline{\underline{\sigma}} = \underline{\underline{\mathcal{C}}} \cdot \underline{\underline{\epsilon}}, \quad (2.43)$$

with $\underline{\underline{\mathcal{C}}}$ being the so-called elasticity tensor. Eq. 2.43 does not take into consideration the pre-stresses. When pre-stresses are applied, $\underline{\underline{\sigma}}$ can be decomposed into the elastic stresses and the applied pre-stresses. Eq. 2.43 becomes

$$\underline{\underline{\sigma}} = \underline{\underline{\sigma}}_{pre} + \underline{\underline{\mathcal{C}}} \cdot \underline{\underline{\epsilon}}. \quad (2.44)$$

Various material models have been already exploited for the numerical modeling of structures. Membrane materials studied in this thesis are anisotropic materials, which affects directly the matrix $\underline{\underline{\mathcal{C}}}$. Nevertheless, membranes are supposed to be isotropic and to operate in their linear domain in this thesis to simplify the development of the FSI schemes. The St. Venant-Kirchhoff model is employed to model the relationship between the strains and the stresses intern to the membranes. It is an extension of the Hooke's law for large deformation under small strains. The latter and the assumptions made for a two-dimensional case allow to rewrite Eq. 2.44 into:

$$\begin{bmatrix} \sigma_{xx} \\ \sigma_{yy} \\ \sigma_{xy} \end{bmatrix} = \begin{bmatrix} \sigma_{xx-pre} \\ \sigma_{yy-pre} \\ \sigma_{xy-pre} \end{bmatrix} + \frac{E}{1-\nu_s^2} \begin{bmatrix} 1 & \nu_s & 0 \\ \nu_s & 1 & 0 \\ 0 & 0 & \frac{1-\nu_s}{2} \end{bmatrix} \begin{bmatrix} \epsilon_{xx} \\ \epsilon_{yy} \\ 2\epsilon_{xy} \end{bmatrix}. \quad (2.45)$$

- **Stresses to external forces equilibrium: BE**

The momentum of a solid is described following the Newton's second law. It states that the momentum of the solid is induced by the total forces acting on it. This statement is expressed in its integral form, also named as *weak form* as

$$\int_{\Omega_{\mathcal{S}}} \rho \frac{d\vec{v}}{dt} d\Omega_{\mathcal{S}} = \oint_{\mathcal{S}_{\Omega_{\mathcal{S}}}} \underline{\underline{\sigma}} \vec{n} d\mathcal{S} + \int_{\Omega_{\mathcal{S}}} \rho \vec{B} d\Omega_{\mathcal{S}} \quad (2.46)$$

with \vec{v} being the velocity of the solid $\Omega_{\mathcal{S}}$, ρ its density, $\underline{\underline{\sigma}}$ the stresses acting on the surfaces $\mathcal{S}_{\Omega_{\mathcal{S}}}$ of $\Omega_{\mathcal{S}}$ and \vec{B} the external forces acting on $\Omega_{\mathcal{S}}$. The previous statement is valid for all volumes composed into the solid, therefore Eq. 2.46 can be rewritten with a local form

$$\rho \frac{d\vec{v}}{dt} = \nabla(\underline{\underline{\sigma}}) + \rho \vec{B}. \quad (2.47)$$

In the context of this thesis, a steady two-dimensional problem is considered. Therefore, with the assumptions about the membrane material, Eq. 2.47 can be simplified to

$$\begin{bmatrix} 0 \\ 0 \end{bmatrix} = \begin{bmatrix} \frac{\delta}{\delta x} & 0 & \frac{\delta}{\delta y} \\ 0 & \frac{\delta}{\delta y} & \frac{\delta}{\delta x} \end{bmatrix} \begin{bmatrix} \sigma_{xx} \\ \sigma_{yy} \\ \sigma_{xy} \end{bmatrix} + \begin{bmatrix} \rho b_x \\ \rho b_y \end{bmatrix}. \quad (2.48)$$

The governing equations mentioned above are partial differential equations. They describe the local mechanical state of a material point and are valid for all material points. They are qualified as strong forms. Nevertheless, most numerical methods use a discretization principle to solve a problem. The numerical methods approximate variables, in our case the displacement, not locally but on so-called sub-domains. In order to allow the approximation, the domain has to be transformed into a finite problem. The governing equations are not resolved locally but with integral form. The integral form is weighted by selected weighting functions and integrated over the entire domain. As various functions can be used to provide the same results, the equations in their integral form are qualified as weak. In the scope of this thesis, the principle of virtual work is employed to numerically solve the structure state.

- **Principle of virtual work**

The principle of virtual work is to use a *virtual displacement* δx as a weighting function in the balance equilibrium [36, 34]. In comparison to the strong form depicted in Fig. 2.4, the principle of virtual work uses the integral of equation 2.16 times δx . The idea is the sum of the work done by the internal and external forces on the system when it undergoes a δx , is equal to zero when the system is in equilibrium

$$\frac{\delta \mathcal{W}}{\delta x} \delta u = 0, \quad (2.49)$$

$$\Rightarrow \int_{\Omega_{\mathcal{S}}} \frac{\delta}{\delta x} (\mathcal{W}_{int} + \mathcal{W}_{ext}) \delta x d\Omega_{\mathcal{S}} = 0. \quad (2.50)$$

The internal work is equal to the work of the stress forces

$$\delta \mathcal{W}_{int} = (\underline{\underline{\sigma}}_{pre} + \underline{\underline{\mathcal{C}}} . \underline{\underline{\epsilon}}) \delta x. \quad (2.51)$$

δu is directly linked to $\delta \epsilon$, therefore Eq. 2.51 can be rewritten as

$$\delta \mathcal{W}_{int} = (\underline{\underline{\sigma}}_{pre} + \underline{\underline{\mathcal{C}}} . \underline{\underline{\epsilon}}) . \delta \epsilon. \quad (2.52)$$

The external work is equal to the work of the external forces applied to the system:

$$\delta \mathcal{W}_{ext} = \rho \vec{B} \delta x. \quad (2.53)$$

Therefore, Eq. 2.50 takes the following form

$$\int_{\Omega_{\mathcal{S}}} \frac{\delta}{\delta x} (\underline{\underline{\sigma}}_{pre} + \underline{\underline{\mathcal{C}}} . \underline{\underline{\epsilon}}) \delta \epsilon d\Omega_{\mathcal{S}} + \int_{\Omega_{\mathcal{S}}} \frac{\delta}{\delta x} \rho \vec{B} \delta x d\Omega_{\mathcal{S}} = 0 \quad (2.54)$$

Since the last equation is valid for any virtual displacement, it could be simplified by dividing it by δx . Eq. 2.53 is the basis of the FEM method described in the following. It allows to solve the set of equations within finite sub-domains.

2.2.2.2 Numerical Solution Procedure: FEM

FEM is employed to discretize $\Omega_{\mathcal{S}}$. The idea behind FEM is to discretize a domain into finite elements, each composed of nodal points or nodes usually located at the corners or end points [101,

34, 41, 40]. The unknown variables, normally the displacement field, are afterwards interpolated on each node of each element with simple functions. A matrix system is created and needs to be resolved. At the end, boundary conditions are necessary to resolve the problem on the whole domain. Additional parameters can ultimately be calculated according to the interest of analysis (stress or strain).

The first step of the method is to discretize the computational domain $\Omega_{\mathcal{S}}$ into a finite number N of sub-domains $\partial\Omega_{\mathcal{S}_i}$, with $i \in 1, \dots, N$. The sub-domains $\partial\Omega_{\mathcal{S}_i}$ are defined as elements. Most elements are of simple geometries. For a one-dimensional case, the elements are usually straight lines. For a two-dimensional case, they are of triangular or of quadrilateral shape. In three dimension, tetrahedra, pentahedra or hexahedra are considered. Each $\partial\Omega_{\mathcal{S}_i}$ are afterwards divided into nodes. In a quadratic repartition, the nodes are located in the interior of an element (middle of line, or middle of faces) which permits to obtain higher-order solutions. The choice of elements depends on the geometry size and shape of the problem. Most of the time, the choice of elements is based on engineering judgment and experiences. Each element has advantages and disadvantages and a range of applicability. For example, a relatively long and thin piece where two dimensions are much smaller than the other can be modeled as a beam (1D element). If the problem deals with thin structures where one dimension is much smaller than the others, it can be better to use the shell elements (2D element). Furthermore, it is also important to mention that the elements have different degrees of freedom. A beam is for example a 1D element with stiffness in all directions whereas a bar element excludes three rotational stiffness. Therefore, the choice of elements should be done carefully.

The second step is to select basis functions also called shape functions in order to interpolate the unknown variables on the nodes. The shape functions need to satisfy some conditions. We consider the notation f_i^e to refer to a shape function associated with the node i of the element e . The conditions which f_i^e needs to satisfy are as followed [101, 34]:

- **Interpolation condition:** f_i^e needs to be equal to 1 at node i but to 0 at all others.
- **Compatibility condition:** f_i^e needs to satisfy the criteria of differentiation (\mathcal{C}^m) on the element where it interpolates and the criteria of continuity (\mathcal{C}^{m-1}) on the adjacent one.
- **Completeness condition:** f_i^e needs to be able to represent exactly any displacement field or constant strain state.
- **Local support condition:** f_i^e vanishes over any element boundary that does not include node i .

The shape functions are usually polynomials because they are easy to manipulate. The degree of the polynomials depends on the number of nodes on one element and on the dimensions of the problem. A shape polynomial function interpolating a 1D element with a linear repartition of nodes (2 nodes) is a polynomial of degree 1. If a quadratic repartition of nodes is employed (3 nodes), the polynomial is a polynomial of degree 2. If a 2D shell element with a linear repartition of nodes is considered, the polynomial is also a polynomial of degree 1. The numbers of nodes is directly correlated to the number of constants to determined in the shape function, which also determines the degree of the polynomials. In the scope of this thesis, rectangular elements are utilized to solve the displacement of the membrane. The following iso-parametric shape functions are exploited on each element [74]:

$$N_1^e(x, y) = \frac{1}{4}(1-x)(1-y) \quad (2.55)$$

$$N_2^e(x, y) = \frac{1}{4}(1+x)(1-y) \quad (2.56)$$

$$N_3^e(x, y) = \frac{1}{4}(1+x)(1+y) \quad (2.57)$$

$$N_4^e(x, y) = \frac{1}{4}(1-x)(1+y) \quad (2.58)$$

Therefore, the displacement field, the geometry of the deformed and undeformed elements are described as

$$\vec{d}(x, y) = \sum_{i=1}^4 N_i^e(x, y) \vec{d}_i \quad (2.59)$$

$$X(x, y) = \sum_{i=1}^4 N_i^e(x, y) X_i \quad (2.60)$$

$$x(x, y) = \sum_{i=1}^4 N_i^e(x, y) x_i \quad (2.61)$$

$$(2.62)$$

The third step, the FEM method consists of applying the weak form, in our case the virtual work equation, the CE and the KE on each element of $\Omega_{\mathcal{S}}$ (cf. Fig. 2.5). A system of equations is obtained and the boundary conditions are also exploited to solve the system.

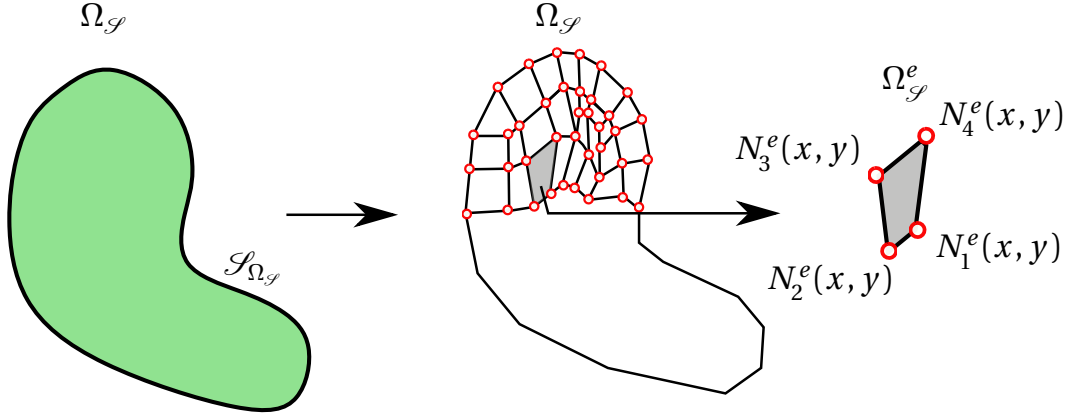


Figure 2.5: FEM discretization and extraction of a generic element, [34].

2.2.2.3 Post-processing parameters

Similarly to the previous section, it appears important to the author to remind the definition of the main parameters used to analyze the structural behavior of the flexible wing.

The initial configuration is designated with a «₀» in subscript whereas the current configuration is designated without any label. The position of membrane elements is analyzed in a cartesian system where (x, y, z) are the coordinates. The small letters (x, y, z) refer to absolute coordinates whereas the capital letters (X, Y, Z) refer to dimensionless coordinates. The dimensionless coordinates are obtained by dividing the absolute coordinates with the wing chord c_r . The deflection of the membrane is defined either with the absolute coordinate or the dimensionless one as

$$z(x, y) \text{ or } Z(X, Y) \quad (2.63)$$

An interesting parameter to analyze the membrane deflection is $\Delta Z(X, Y)$ defined as the difference between the geometry $Z(X, Y)$ at the coordinates (X, Y) and the non-deformed geometry $Z_0(X, Y)$ at the coordinates (X, Y) .

The pre-stress of the membrane is defined as σ_0 and corresponds to initial stress set on the membrane before any incoming flow. The pre-stress is related to the relative elongation by the modulus of elasticity as

$$\sigma_0 = \frac{l - l_0}{l_0} \times E \quad (2.64)$$

2.2.3 Coupling Conditions

2.2.3.1 Conditions at the interface

We recall that the intersection between the $\Omega_{\mathcal{F}}$ and $\Omega_{\mathcal{S}}$ was defined as $I_{FSI}(t) = \delta\Omega_{\mathcal{F}}(t) \cap \delta\Omega_{\mathcal{S}}(t)$. Two main conditions at I_{FSI} have to be fulfilled to perform FSI computations [72]. The kinematic condition requires that the velocity of the solid is equal to the velocity of the fluid at I_{FSI} . For a viscous fluid, the last condition is simply a rephrase of the no-slip boundary condition in the fluid dynamics. Therefore,

$$\forall t \ \& \ \forall x \in I_{FSI}, \vec{v}_f(x, t) = \vec{v}_s(x, t). \quad (2.65)$$

The dynamic condition is related to the Newton's third law of action. It specifies that the normal forces have to be equilibrated at the interface. Therefore,

$$\forall t, \vec{n}_f \cdot \vec{\sigma}_f(t) = \vec{n}_s \cdot \vec{\sigma}_s(t). \quad (2.66)$$

A third condition may be employed in FSI computations, designated to the geometric condition. It stipulates that no holes appear between the fluid and the structure, i.e. no cavitation phenomenon occurs. The domain is time dependent but the geometric conditions $I_{FSI}(t) = \delta\Omega_{\mathcal{F}}(t) \cap \delta\Omega_{\mathcal{S}}(t)$ and $\Omega(t) = \Omega_{\mathcal{F}}(t) \cup \mathcal{I}_{FSI}(t) \cup \Omega_{\mathcal{S}}(t)$ always hold.

2.2.3.2 Mapping solutions: Nearest Element/Dual Mortar Mapping

To resolve the boundary layer of the fluid, the discretization of the domain has to be fine near the wing in the normal and the axial direction of the flow. Usually the fluid discretization is much finer than the structure one, resulting in two different discretizations used for $\Omega_{\mathcal{F}}$ and $\Omega_{\mathcal{S}}$. The latter implies different coordinates where the computations take place. Hence, a mapping has to be employed to allow the fulfillment of Eqs. 2.65 and 2.66: it allows to associate the coordinates of $\Omega_{\mathcal{F}}$ to that of $\Omega_{\mathcal{S}}$ at I_{FSI} , and vice versa.

In the scope of this thesis, a nearest interpolation method and a dual mortar mapping are employed to overcome the discretization issue. Both methods are briefly introduced in the following. To obtain more details about both mapping methods readers are referred to [94].

Nearest Element Interpolation Method

The principle of the nearest element interpolation method is to project one node from one domain ($\Omega_{\mathcal{F}}$ or $\Omega_{\mathcal{S}}$) to its nearest element inside the other domain. Let us define X_f as the fluid node which is projected to the structure element $\Omega_{\mathcal{S}}^e$ and $X_{P,f}$ its projection on $\Omega_{\mathcal{S}}^e$. The value of the force at $X_{P,f}$ is an interpolation of the force at X_f on $\Omega_{\mathcal{S}}^e$. The weight of interpolation depends on the shape functions and the distance between the nodes. In other words, if the parameter u is the unknown and v the known one, the Nearest Element Method can be summerized with the following:

$$u = \sum_{i=1}^{N_u} N_i(X_{P,f}) u_i, \quad (2.67)$$

with N_i the shape functions. The nearest element method belongs to the consistent mapping methods as the consistency, defined as a measure if a constant field is mapped exactly from one discretization to the other, is satisfied.

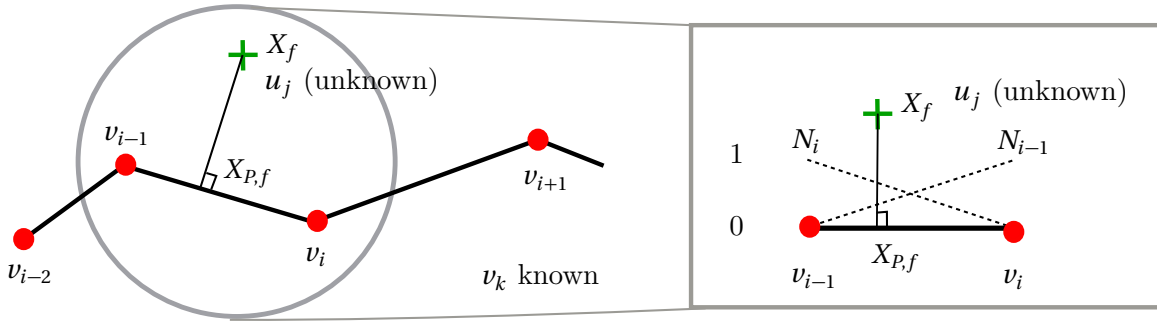


Figure 2.6: Mapping principle.

Dual Mortar Mapping

The Dual Mortar Mapping method is exploited as well. This method is based on the principle of virtual work mentioned in Sec. 2.2.2.1. Indeed, if the parameters u and v are considered, with u the unknown and v the known quantity, the start of the Dual Mortar Mapping is the conservation of the virtual work of u and v as followed:

$$\int_{\Omega_{\mathcal{S}}} \delta x \cdot (u - v) = 0, \quad (2.68)$$

with δx the virtual displacement. Exploiting the definition of u and v with the shape functions,

Eq. 2.68 becomes:

$$\int_{\Omega_{\mathcal{S}}} \delta x \cdot \left(\sum_{i=1}^{N_1} N_i^u u_i - \sum_{j=1}^{N_2} N_j^v v_j \right) = 0. \quad (2.69)$$

The virtual displacement can also be defined with shape function as $\delta x = \sum_{i=1}^{N_1} N_i^u x_j$, using the shape function of the unknown parameter. Therefore, 2.69 can be re-written in:

$$\int_{\Omega_{\mathcal{S}}} [x_i]^T [N_i^u]^T ([N_i^u][u_i] - [N_i^v][v_i]) = 0. \quad (2.70)$$

$[x_i]$, $[u_i]$ and $[v_i]$ are space-independent. Therefore, the following is:

$$[x_i]^T \int_{\Omega_{\mathcal{S}}} [N_i^u]^T [N_i^u] d\Omega [u_i] = [x_i]^T \int_{\Omega_{\mathcal{S}}} [N_i^u]^T [N_i^v] d\Omega [v_i].$$

The latter is of form $C_{AA}[u_i] = C_{AB}[v_i]$ and can be resolved.

The Dual Mortar Mapping is less robust than the Nearest Element Method but provides more precise results.

2.3 Mesh Generators and Solvers Description

2.3.1 Mesh Generator

Two meshes are needed to compute the fluid and structure states of the FSI computations. Two separate mesh generators are exploited to create the fluid and structure meshes, also designated as CFD and FEM meshes, respectively. The two mesh generators are briefly introduced in the following.

- **ANSYS ICEM CFD**

The CFD meshes are generated with ANSYS ICEM CFD [6]. ANSYS ICEM CFD is a mesh generator, which provides a geometry acquisition and a mesh repair tool. It offers the possibility to compute structured, unstructured and hybrid meshes. In the present thesis, structured meshes are created through a multi-block method to compute the fluid state. The definition of the various boundary conditions are also defined as surface during the mesh generation. The resulting mesh is afterwards translated to an input file formatted for the ANSYS CFX solver or the TAU code.

- **GiD**

The FEM meshes are generated with GiD [28]. GiD is an adaptive pre- and post-processor for numerical computations developed at the International Centre for Numerical Methods in Engineering (CIMNE). It is an interactive graphical user interface which allows the definition and the mesh generation of numerical model. The benefit with GiD is that it can be directly linked to CARAT++. Therefore a suitable FEM mesh can be generated and written in the right format for the CARAT++ code. For more information, please refer to the manual guide [28].

2.3.2 Fluid Solvers

The equations governing the fluid states are solved by means of CFD solvers. In the present thesis, it was decided to take the advantages of the CFD TAU code and the solver ANSYS CFX, whose performance were already shown [90, 44]. Both solvers are shortly presented in the following. For more details, please refer to the references given in the thesis.

- **TAU code**

The TAU code was developed at the German Aerospace Center (DLR) Institute of Aerodynamics and Flow Technology [80, 38]. It can be employed to resolve either subsonic or supersonic flows on structured or unstructured meshes. The TAU code includes a partitioning, a pre-processing, a solving, a grid deformation and a grid adaptation modules.

The partitioning module divides the mesh in sub-domains to enable a parallel computing on several processors. The TAU code exploits the Message Passing Interface (MPI) architecture to define the communication between the processors. The pre-processing module generates a dual grid [80, 38, 93] constructed from the original mesh, which is used to solve the URANS equations. The dual approach utilizes the cell-vertex grid metric method. A multi-grid approach is also available to accelerate the convergence of the computations. In the present thesis, the 3w-type multi-grid cycle is applied to run the CFD computations, which means that two coarser meshes are generated during the pre-processing procedure. The solving process uses a FVM approach to resolve the URANS equations. Upwind and central schemes are available for the spatial discretization. Concerning the time discretization, the explicit Runge-Kutta and the implicit Euler schemes are implemented. The grid deformation tool allows moderate changes of the geometry. The displacements are considered as an input and, depending on the ratio between the local displacement and the size of the cell, they are weighed and iterated in each step.

The benefit with the TAU code is that it is possible to combine it with a Python code making the information exchange with the FEM solver Carat++ realizable.

- **ANSYS CFX**

ANSYS CFX is a CFD software that combines a pre-, post-processing and a solver [5] modules. It usually serves to solve the Navier-Stokes equations by means of the FVM with URANS approach. It can model steady-state as well as transient, laminar and turbulent, subsonic, transonic and supersonic flows, etc. Various turbulence models are implemented, which enables the computations to better approach the experiments. In the present thesis, the fluid is considered as incompressible and is model for a transient flow. Two turbulence models (Sec. 2.2.1.2), namely the $\kappa - \omega$ SST turbulence model and the $\gamma - Re_\theta$ transition model coupled to the $\kappa - \omega$ SST model, are used and compared in Chapter 5.

2.3.3 Structure Solvers

- **CARAT++**

CARAT++ solves the equations governing the displacement of the membrane [26]. It is a FEM solver optimized for membrane and shell elements. The dislocation of the structure is calculated in an incremental way based on the principle of solution advancement by continuation. The procedure starts with the unloaded structure and converges to an equilibrium solution under loaded situation by advancing the solution step by step. In the current study, a predictor-corrector method using force control is employed to solve the structural problem. In predictor-corrector methods iterations are performed to calculate the new equilibrium state.

- **ANSYS APDL**

ANSYS APDL is a FEM solver that can perform variety of engineering simulations modeling thermal, magnetostatic or stress problems [7]. The software includes a pre-, post-processing and a solver modules. Geometries can be within the software created, but also loaded. The software proposes a mesh generator to generate structured and unstructured meshes.

2.3.4 Outer Coupling Software

External coupling programs are needed to allow the information exchange between the fluid and the structural solvers. Two programs are utilized in the present thesis and are briefly introduced

in the following.

- **EMPIRE**

EMPIRE is a co-simulation environment developed to solve multi-physics problems [94]. In the present thesis, EMPIRE couples the TAU and the CARAT++ codes. It exploits the Client-Server model, where TAU and CARAT++ are considered as the clients and the program Emperor as the server. The server enables the parallel computation between the clients. In other words, the clients can not communicate directly with each other but only via the server. The benefit with EMPIRE is that it is compatible with Python, making a coupling with TAU possible. For more information about EMPIRE, please see the reference [94].

Basically, a Python script is developed to enable the communication between EMPIRE and the two clients, namely TAU and CARAT++. Within the Python script, the pressure information is received from the TAU code and converted into forces at each nodes of the CFD mesh. Then, the mesh mapping from EMPIRE (see Sec. 2.2.3.2) enables the interpolation of the forces on the FEM mesh nodes. The forces are considered as an input for CARAT++, which computes the associated displacement. During the next step, the displacement is mapped from the FEM mesh nodes to the CFD mesh nodes and Python converts this information into a format readable for TAU. The grid deformation module integrated in TAU generates the new mesh and TAU solves the fluid on the deformed mesh. This is iterated till a convergence on the aerodynamic coefficients or the maximal outer coupling iteration is achieved.

- **ANSYS MFX-MultiFeld**

ANSYS MFX Multi-Feld employs an strong partitioned approach (see Sec. 2.1.2) to couple the ANSYS CFX and ANSYS APDL solvers. The ANSYS MFX Multi-Feld program uses a Client-Server model. It does the mapping and communicates the time and interpolated loads between the two solvers. To ensure robust and reliable results, multiple iterations are performed within each outer time step until each the fluid and the structure achieves a converged state. More information about the ANSYS MFX Multi-Feld can be found in [5].

Chapter 3 - Experimental and Numerical Setups

This chapter explains the experimental and the numerical investigations within four sections. The first section describes the two fabrics employed in the present thesis. The second section presents the various geometries and the associated wind tunnel models. In total, three experimental models are tested in the facilities of the Institute of Aerodynamics and Fluid Mechanics of the Technische Universität München (TUM-AER). Two models can be qualified as two-dimensional or quasi-two-dimensional and the last one as a three-dimensional model. The third section presents the measurement techniques carried out at the TUM-AER. The set up for the force, the membrane deformation and the flow field measurements are described for each model. The last section gives an overview of the FSI computations: After a presentation of the boundary conditions used to establish the computations, the various meshes are described and the grid independency studies are reported and discussed.

3.1 Membrane Fabrics

The wings are made with highly-extensible membrane fabrics serving as lifting surface. Two different fabrics are utilized to construct the various wind tunnel models, each having its own mechanical properties. The mechanical properties are determined within uniaxial tensile tests. The two membranes and the results of each tensile test are described in the following sections.

One side of each membrane is coated with a rubber layer, which ensures air impermeability (see Fig. 3.1a). The coated side is exploited as the external surface of the wing, as the surface is smooth, making the computations easier to implement. Each membrane is chosen because of its mechanical properties: they allow enough deflection but simultaneously can withstand the aerodynamic loads on the wing. It has to be considered that, if the stiffness is too high, the deflection is not “sufficient” and the aerodynamic characteristics are not very different in comparison to a rigid counterpart wing. But if the stiffness is too low, the deformation is too excessive, which precipitates the flow

separation on the wing. Having these considerations in mind, the two following membranes are chosen to construct the wind tunnel models.

3.1.1 Membrane 1

The first membrane, designated as Membrane 1, is a result of Beguin's work [18] provided by the manufacturer Eschler Textile GmbH [39]. It consists of a commercial off-the-shelf polyamide/elastan material coated with a polyurethane cover on one side. The fabric's thickness is equal to **0.5mm** and its mass per surface area to **250g/m²**. As the fabric is anisotropic, the mechanical properties in the weft and in the warp directions are interdependent. Therefore, bi-axial tensile tests are normally required to determine the Young's moduli. Nevertheless, such tests were not carried out in the present thesis. Instead uni-axial tensile tests were conducted to estimate the properties in each direction (cf. [18]). Fig. 3.1b is taken from the work of Beguin and shows the stress-strain curves obtained during the uni-axial tensile tests. The Young's moduli are equal to $E_{warp} = 1.01$ MPa and $E_{weft} = 2.18$ MPa in the warp and the weft directions, respectively. In order to limit the deflection resulting in a change of camber and thickness and not precipitate the flow separation, the weft direction is chosen to be the chord direction of the wing.

3.1.2 Membrane 2

The second membrane, designated as Membrane 2, is also a product of the manufacturer Eschler Textile GmbH [39]. It was selected to construct larger wind tunnel models. Compared to the membrane 1, its stiffness is higher to limit larger deformations induced by higher aerodynamic loads acting on larger wings. But the mechanical properties are still close to the one of Membrane 1. To assess the Young's moduli, new tensile tests are conducted at the Chair of "Metall- und Leichtbau" of the Universität Duisburg-Essen. The tests are illustrated in Fig. 3.2a and the results are described in Fig. 3.2b. The tests consists of stretching membrane samples at strain levels of 10%. The samples are cuts of the membrane with a size of **200mm** in length and **100mm** in width. Membrane 2 is **0.5mm** thick and its mass per surface area is equal to **160g/m²**. In Fig. 3.2b, the stress-strain curve obtained during the tensile tests indicates the Young's moduli being equal to $E_{warp} = 2.2$ MPa and $E_{weft} = 4$ MPa in the warp and the weft directions, respectively. As previously, the weft direction is chosen to be the chord direction to limit the membrane deflection with respect to possible changes in the mean camber line.

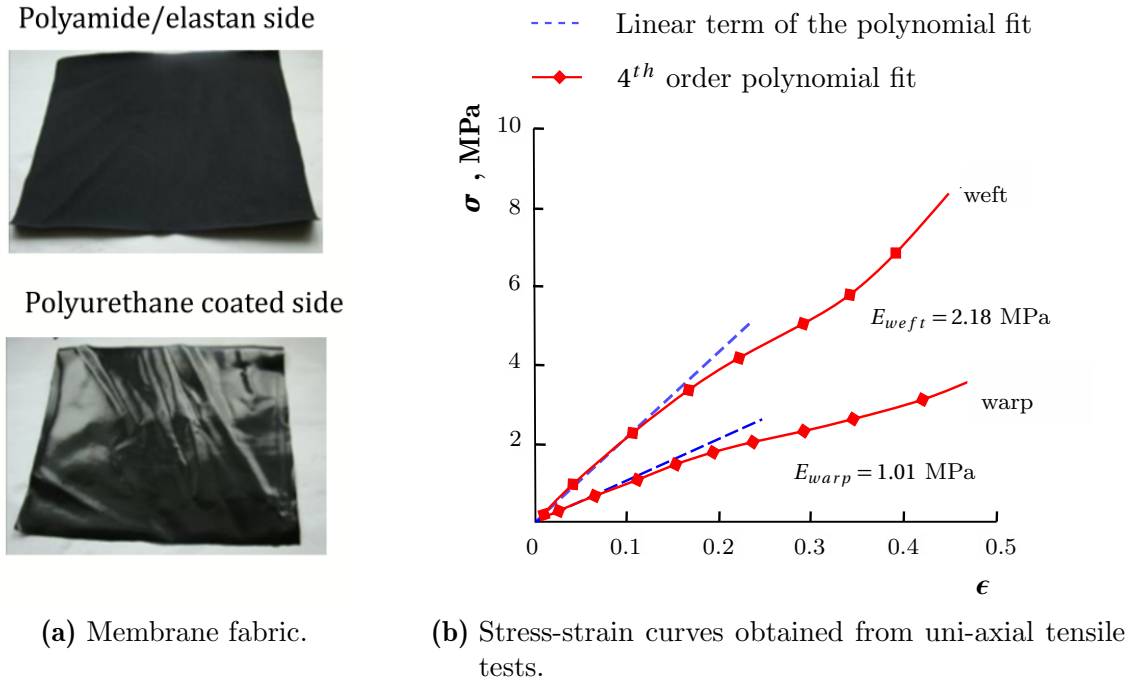


Figure 3.1: Description of the Membrane 1 and tensile test results, from [18].

3.2 Geometries and Wind-Tunnel Models

3.2.1 2D Models

In order to develop the FSI computations, two-dimensional geometries are first considered. Such geometries are easier to implement and the computations associated are not excessively time-consuming. Two different airfoil geometries are developed for numerical and experimental investigations. The two geometries are based on the same construction idea.

The geometries are composed of three main parts, namely a LE, a TE and one of the membranes described in Section 3.1. The membrane is sewed on the LE and the TE, being two rigid spars. The LE is built with an asymmetric double elliptical section. Such a geometry allows to reduce the pressure gradient at the beginning of the suction side [18]. In comparison with a cylindrical-geometry spar, the peak of suction is considerably reduced, which lowers the possibility of flow separation along the chord direction. The TE spar is relatively thick in order to avoid any deflection under aerodynamic loads. It has different forms for all models depending on the size of the wing. The TE can be adjusted in chordwise direction to set a pre-stress on the membrane.

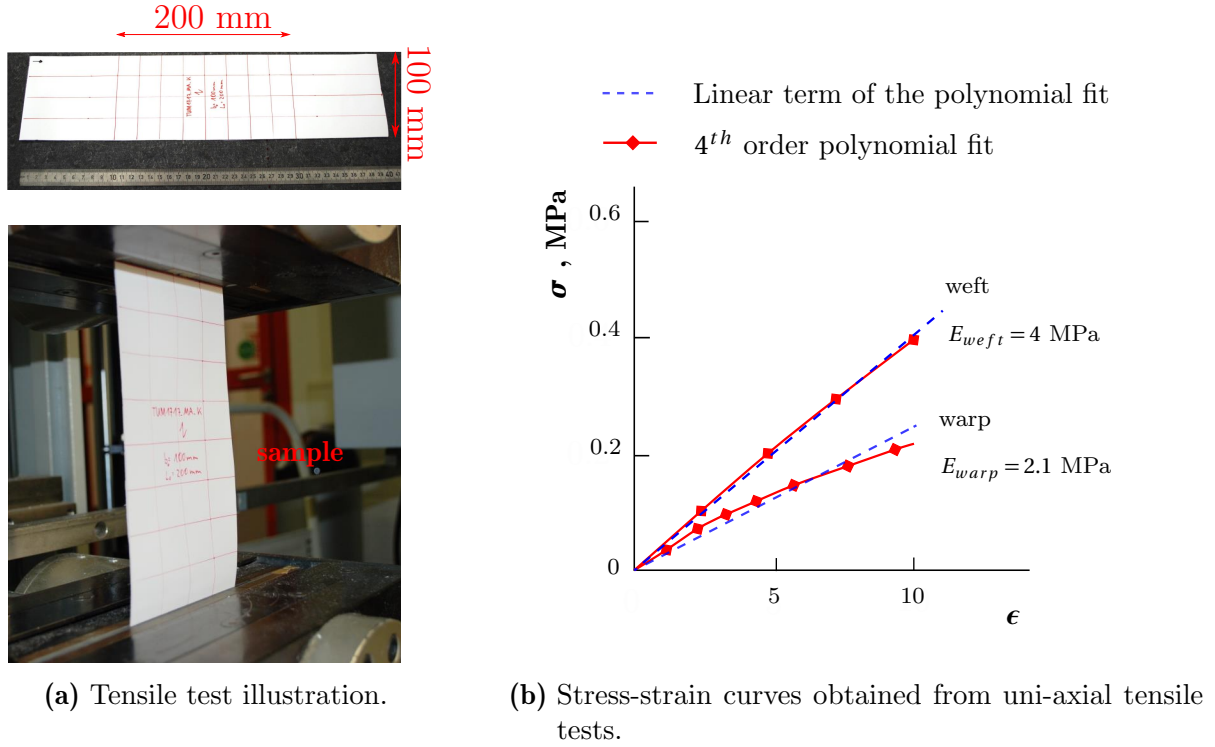


Figure 3.2: Tensile test process and results for the Membrane 2.

The two geometries differ from each others as the first one was developed for the Wind Tunnel B (WTB), whereas the second was for the Wind Tunnel A (WTA) of TUM-AER. Therefore, the first geometry is smaller than the second one. In the following, the two geometries designated as the WTB and WTA geometries are described.

3.2.1.1 WTB geometry

The WTB geometry is a result of the investigations of Beguin [18]. He developed the concept and supervised the construction of the wind tunnel model. Among others, he found out that using an asymmetric double elliptical LE spar allowed a mitigation of the intensity of the pressure peak on the suction side. Furthermore, inclining the asymmetric ellipse allowed to reach a higher lift coefficient as the inclination influence the camber of the airfoil by increasing it. The geometry developed by Beguin is depicted in Fig. 3.3. The main dimensions are designated with the following variables:

- a : semi-major axis of the ellipse (61 mm);
- b_u : semi-minor axis of the upper half ellipse (12 mm);

- b_l : semi-minor axis of the lower half ellipse (8mm);
- l_{te} : length of the trailing edge (28mm);
- h_{te} : height of the trailing edge (8mm).

The airfoil geometry has a chord length (c) equal to 220mm. It can be noticed that a is around 25% of c and b_u and b_l are around 40% and 20% of a , respectively. For more information about the design of the LE spar, the following references can be consulted [18, 19].

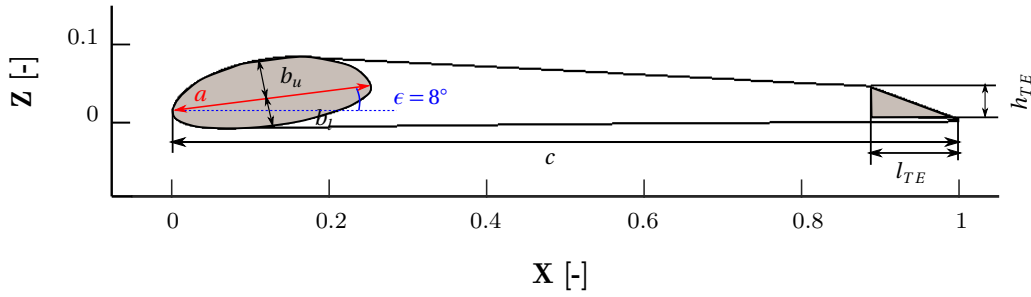


Figure 3.3: Sketch of the 2D WTB geometry.

The setup of the geometry in a numerical model is applied by using the Computer Aided Design (CAD) software CATIA®. This numerical model is used to develop a first methodology and strategy for the FSI computations.

3.2.1.2 WTA geometry

The WTA geometry is designed based on the work of Beguin as well [18]. The idea behind using the wind tunnel A is to increase the size of the wing model. Therefore, a new geometry with a longer chord length ($c_r = 500\text{mm}$) is developed with respect to the principles described previously. The LE is built with an asymmetric double elliptical section with new lengths obtained by conserving the ratio between the lengths a and c , and b_l , b_u and a , namely 25%, 40% and 20%. The WTA geometry is depicted in Fig. 3.4 and the values of the main dimensions are summarized in the following:

- a : prior axis of the ellipse (260mm);
- b_u : second axis of the upper half ellipse (44mm);
- b_l : second axis of the lower half ellipse (31mm);

- l_{te} : length of the trailing edge (40mm);
- h_{te} : height of the trailing edge (10mm).

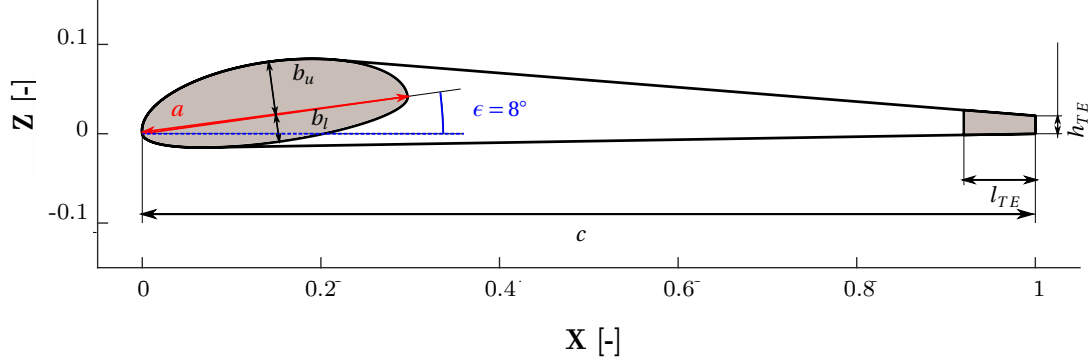


Figure 3.4: Sketch of the 2D WTA geometry.

The setup of the geometry in a numerical model is applied by using CATIA[®] as well and utilized for the FSI computations.

3.2.2 2.5D Wind-Tunnel Models

3.2.2.1 WTB Experimental Model

The experimental model representing the WTB geometry is illustrated in Fig. 3.5. The sectional WTB geometry is extruded to create a rectangular wing. At each tip, an endplate of circular form is placed to limit the 3D flow effects produced by the wing tip flow generating a two-dimensional or a so-called quasi two-dimensional flow situation. The endplates have a diameter of three times the airfoil chord and are made of Plexiglas[®] to provide optical access to the deflection of the membrane. The wing is then held by a support, which is directly mounted on the aerodynamic balance of the wind tunnel.

The experimental wing has an overall span of 564mm and a nominal chord of 220mm, giving an aspect ratio of $AR = 2.56$. The TE can be positioned in chordwise direction to adjust the pre-stress of the membrane by introducing an initial elongation (cf. Fig. 3.6). In the current study, an elongation of 2% of the chord length is set, which corresponds to an initial pre-stress of $\sigma_0 = 43.600$ Pa.

The wind tunnel experiments considered for the WTB model are aerodynamic force measure-

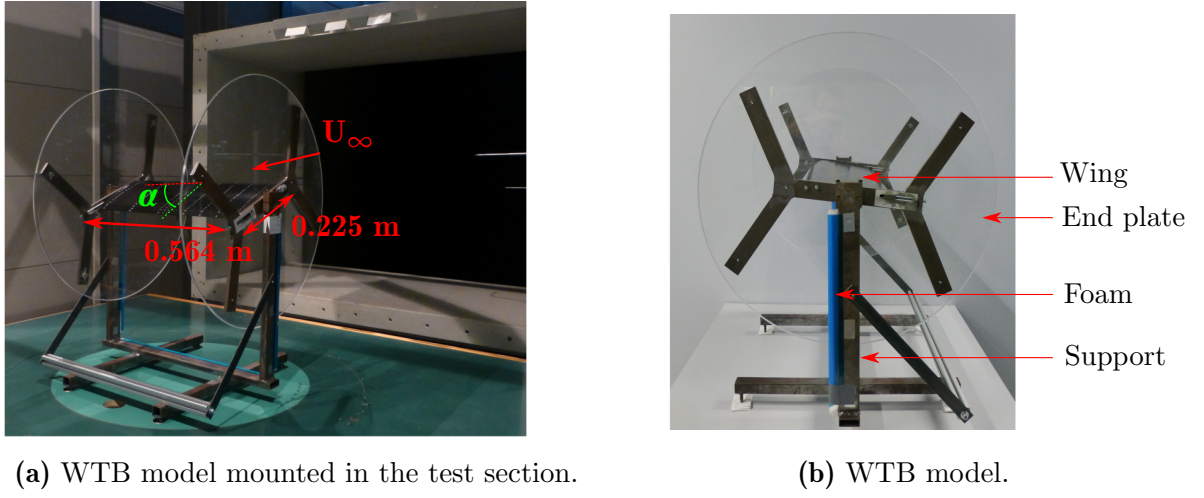


Figure 3.5: 2.5D WTB model.

ments simultaneously conducted with a photogrammetry technique to measure the deflection of the membrane. Finally, a hot-wire anemometry system is also employed to acquire the flow velocity field on the upper-side of the wing and to measure the downwash angle.

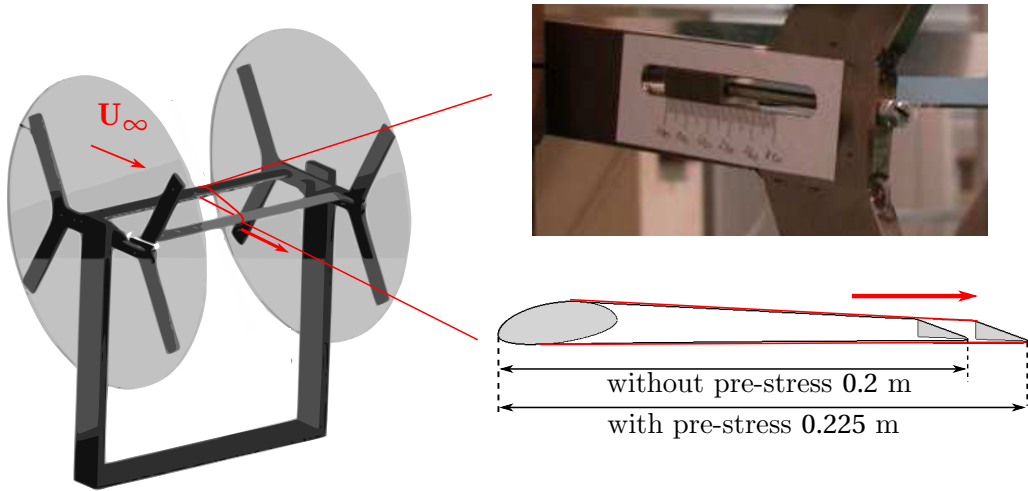


Figure 3.6: Illustration of the adjustable TE of the 2.5D WTA model.

3.2.2.2 WTA Experimental Model

The same principle is applied to construct the WTA model as for the WTB model. The 2D WTA geometry is extruded to generate a rectangular wing and endplates are added at both tips. The endplates are also of circular planform and made in Plexiglas[®]. The TE can be again adjusted in

the chordwise direction to set a pre-stress on the membrane. In the present study, an elongation of 9% of the chord length is set for the current model, which corresponds to an initial pre-stress of $\sigma_0 = 360.000$ Pa. The same measurement techniques are employed as with the WTB model, namely aerodynamic force measurements, photogrammetry technique and hot-wire anemometry.

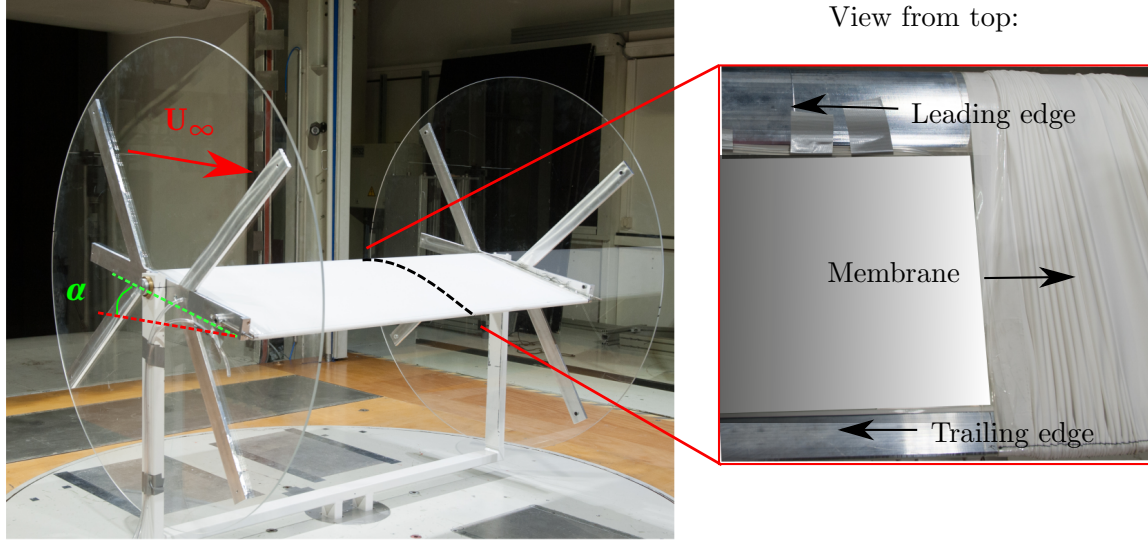


Figure 3.7: 2.5D WTA model installation in the wind tunnel and an enlargement of the construction with the two spars.

3.2.3 3D Wind-Tunnel Model

Altering the shape of a blade at some positions seems an interesting idea to influence the wing loading. The membrane configuration can be thought as a promising system as it is a “without-weight addition” concept. Acting on the tip section may have a more important impact on the loads situated at the root because of the lever arm. Therefore, a half three-dimensional membrane wing is investigated to gain information about such a concept. The following section gives a description of the geometry of the three-dimensional wing and an illustration of the wind tunnel model.

3.2.3.1 Geometry

The wing is tapered to properly represent a three-dimensional flow. It was decided to not use a twist in order to put the focus of the study only on the influence of the membrane. The wing tip

has been designed with a taper ratio of $\lambda = 0.6$, a root chord equal to $c_r = 500\text{mm}$ and a tip chord equal to $c_t = 300\text{mm}$, which results in a wing reference area of $S = 0.564\text{m}^2$ and an aspect ratio of $AR = 3.26$.

The geometry is depicted in Fig. 3.8 and the main dimensions are reported in the following:

- a_1 : prior axis of the ellipse at the root (300mm);
- b_{u1} : second axis of the upper half ellipse at the root (60mm);
- b_{l1} : second axis of the lower half ellipse at the root (30mm);
- a_2 : prior axis of the ellipse at the tip (180mm);
- b_{u2} : second axis of the upper half ellipse at the tip (36mm);
- b_{l2} : second axis of the lower half ellipse at the tip (18mm);
- d_{te} : height of the trailing edge (24mm).

Two sketches describe the geometry of the airfoils defined for the wing root and wing tip (Fig. 3.8): Section A-A represents the airfoil geometry at the root wing (inboard part) and Section B-B represents the airfoil geometry at the tip wing (outboard part). The LE spar is designed according to Beguin's analysis, as it was mentioned in Sec. 3.2.1.1. The TE spar is a cylinder and can also be axially positioned to adjust the pre-stress of the membrane. In the present thesis, an elongation of 10% of the chord length is set on the membrane of the current model, which corresponds to a pre-stress of $\sigma_0 = 400.000\text{ Pa}$.

The impermeability of the configuration is necessary to ensure meaningful results during the wind-tunnel tests. Therefore, two sections made of steel are added at the wing root and the wing tip. The sections have the same geometry as the wing root and the wing tip airfoil (cf. Sections A-A and B-B on Fig. 3.8) and allow to seal the membrane.

3.2.3.2 Experimental Model

The experimental configuration of the three-dimensional membrane wing is represented in Fig. 3.9. The wing is mounted in the test section of wind tunnel A of TUM-AER. A peniche, represented in Fig. 3.8, with the same geometry as the airfoil at the wing root (Section A-A on Fig. 3.8) is placed under the wing to avoid any influences of the boundary layer of the wind-tunnel test section floor. Both, the peniche and the wing, are mounted on a circular plate in the test section, which can be rotated to set the angle of attack α during the experiments. The wing is directly connected to an aerodynamic balance under the wind-tunnel test section floor to measure forces

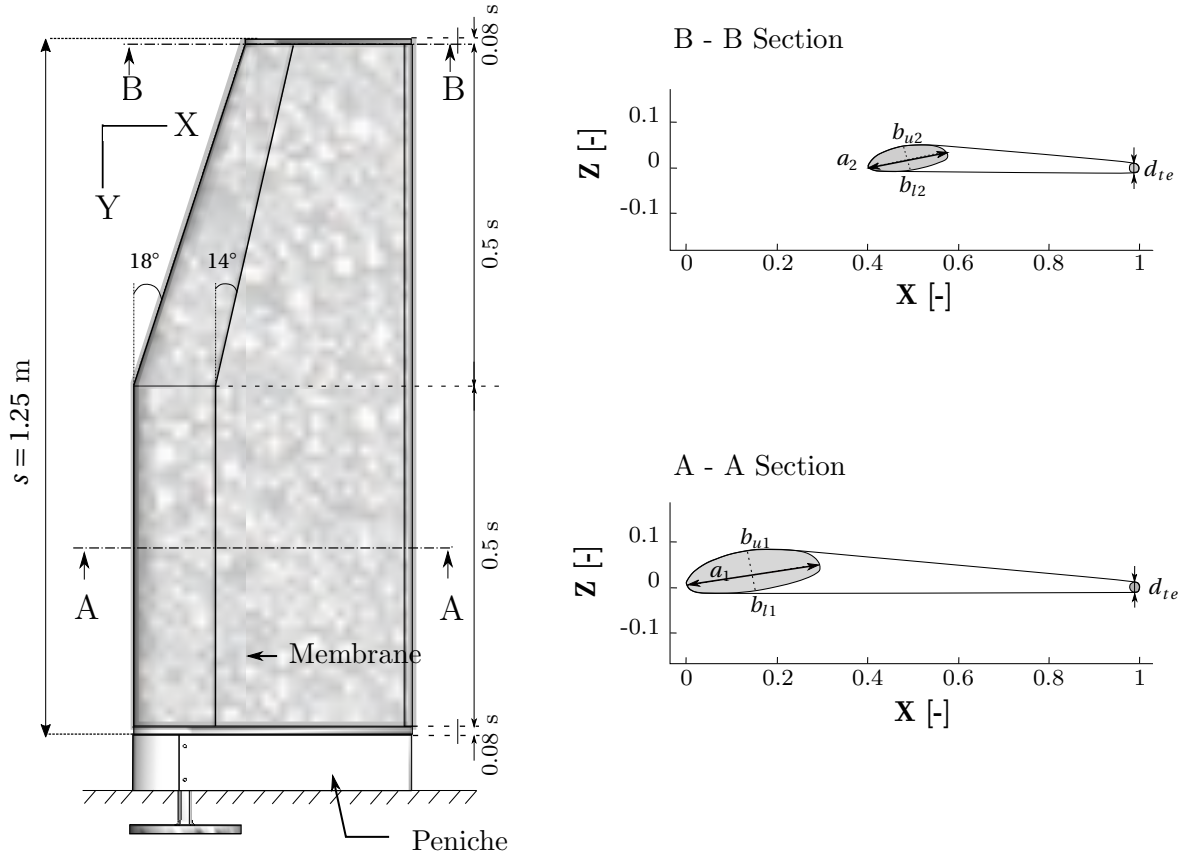


Figure 3.8: Sketch of the 3D WTA elasto-flexible membrane wing model with geometrical characteristics.

and moments. There is no contact between the peniche and the wing, ensuring that the balance measures the forces and moments acting on the wing only.

In addition to aerodynamic force and moment measurements, photogrammetry tests were performed to measure the deflection of the membrane. More information about both techniques are given in the section 3.3.

3.3 Experimental Setup

The experiments were conducted in two Göttingen type low-speed wind tunnel facilities, namely the WTB and WTA of TUM-AER. In both facilities, aerodynamic force measurements are performed while a photogrammetry technique is employed to measure the membrane deflection. Hot-

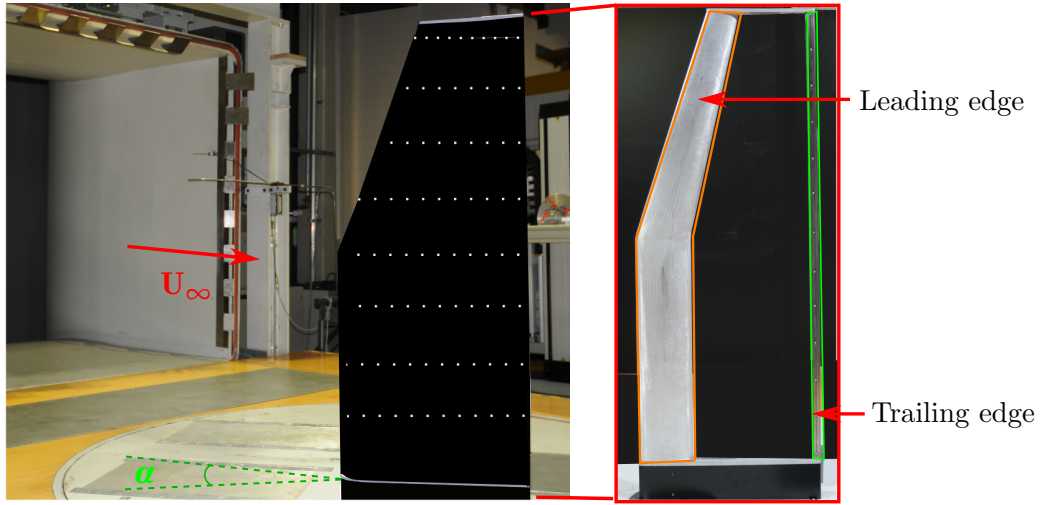


Figure 3.9: 3D WTA model mounted in the test section and an enlargement of the construction with the two spars.

wire anemometry measurements are additionally conducted to obtain information about the flow velocity field.

The WTB of TUM-AER has an open section with a test section size of 1.2m height \times 1.55m width \times 2.8m length. The power of the fan can reach up to 130 kw, which corresponds to a maximal velocity of around 65m/s. Analogously, the WTA has an open section with a test section size of 1.8m height \times 2.4m width \times 4.8m length. The maximal fan power is up to 420 kw, which corresponds to a maximum velocity of 65–75m/s. In both wind tunnels, the turbulence intensity is lower than 0.4% in the three coordinate directions. More details about the facilities are given in [25].

3.3.1 Force Measurements

For all models, the lift and drag forces are measured using an external six-component aerodynamic balance placed under the test section of the wind tunnel. The aerodynamic balance uses strain gauges to measure the loads acting on the wing. The measurements are recorded during a time of 20s and are averaged over this time period. In the following, the force measurement setup is described for all models presented in Sec. 3.2.

3.3.1.1 2.5D Wind Tunnel Models

The two experimental models are placed in the test section of both wind tunnels facilities (see Figs. 3.10). They are directly mounted on aerodynamic balances set under each test section. The two wings are held by a support while endplates are used to suppress wing tip flow effects. Consequently, the force measurements record the forces acting on the wing but also on the group support-endplates.

A dynamic calibration is needed to substract the force contributions of the group support-endplates. Normally, a dynamic calibration is performed by taking the wing off the support, setting a so-called dummy wing in the middle of the model held by the traversing unit. The dummy wing has a similar geometry than the flexible wing to approach the flow topology as close as possible to the original one. There is no contact between the dummy wing and the group support-endplates. Hence, the measured forces are the one only acting on the group support-endplates. A subtraction is then mandatory to obtain the forces acting on the wing only.

A typical dynamic calibration is conducted for the WTB model at two dynamic pressures, namely $q_\infty = 225$ and 690 Pa. However, a dummy wing was not available for the WTA model. Therefore, the dynamic calibration is performed without reproducing a similar flow topology on the group support-endplates. It was intended to conduct a dynamic calibration at two q_∞ , namely $q_\infty = 230$ and 515 Pa, but the vibration of the endplates were too large at $q_\infty = 515$ Pa to enable an accurate test. As the drag of the group support-endplates has a significant influence on the drag of the wing ($\approx 80\%$), a correction needs to be made to assess the drag of the group support-endplates at $q_\infty = 515$ Pa. As the endplates are very similar to blunt bodies, it is assumed that the drag coefficient remains constant in the operating Reynolds number range ($Re < 1 \times 10^6$) (see [46]). If $c_{D,515} = c_{D,230}$ and $\rho_{515} = \rho_{230}$, then

$$\begin{aligned} \frac{D_{S,515}}{q_{515} \cdot A} &= \frac{D_{S,230}}{q_{230} \cdot A} \\ D_{S,515} &= \frac{q_{515}}{q_{230}} \cdot D_{S,230} = \frac{0.5 \cdot \rho_{515} \cdot v_{515}^2}{0.5 \cdot \rho_{230} \cdot v_{230}^2} \cdot D_{S,230} \\ D_{S,515} &= \frac{(30\text{m/s})^2}{(20\text{m/s})^2} \cdot D_{S,230} = 2.25 \cdot D_{S,230} \end{aligned} \tag{3.1}$$

Therefore, the support's drag at $q_\infty = 515$ Pa is assumed to be $D_{S,515} = 2.25 \cdot D_{S,230}$.

3.3. Experimental Setup

Repeated measurements indicated a maximum deviation of $\Delta C_L = \pm 0.02$ and of $\Delta C_D = \pm 0.01$ for the WTB model and of $\Delta C_L = \pm 0.05$ and of $\Delta C_D = \pm 0.01$ for the WTA model representing the uncertainty range. Force measurements are performed at several α for various q_∞ . Table 3.1 gives an overview of the tests carried out in the wind tunnel facilities with the associated conditions.

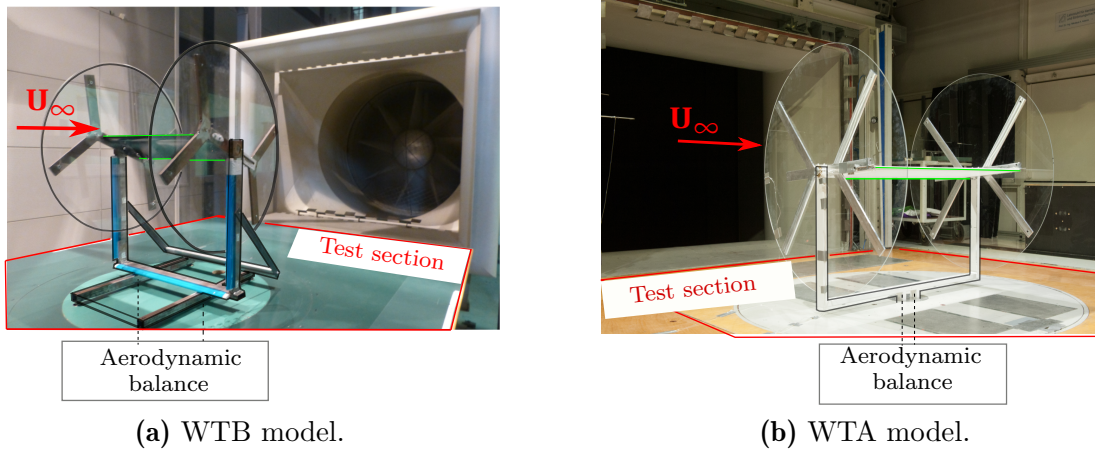


Figure 3.10: Force measurement installation for the 2.5D models.

3.3.1.2 3D Wind Tunnel Model

The experimental WTA three-dimensional model is constructed with a peniche as it was mentioned in Sec. 3.2.3. The peniche is screwed on the floor of the wind tunnel test section whereas the model is directly mounted in an aerodynamic balance of the wind tunnel facility. As it was already mentioned, there is no contact between the peniche and the experimental model. The measured forces are the one acting on the wing only. Nevertheless, the wing is set on a circular plate allowing the adjustment of α . The balance turns with the model providing forces and moments in the wing-fixed coordinate system. Therefore, a rotation of α is mandatory to obtain the forces in the wind tunnel coordinate system. Fig. 3.12 illustrates the setup and the rotation transformation. Repeated measurements showed a maximum deviation of $\Delta C_L = \pm 0.04$ and of $\Delta C_D = \pm 0.004$. Force measurements are performed at several α for various q_∞ . Table 3.1 gives an overview of the tests carried out indicating the specific conditions.

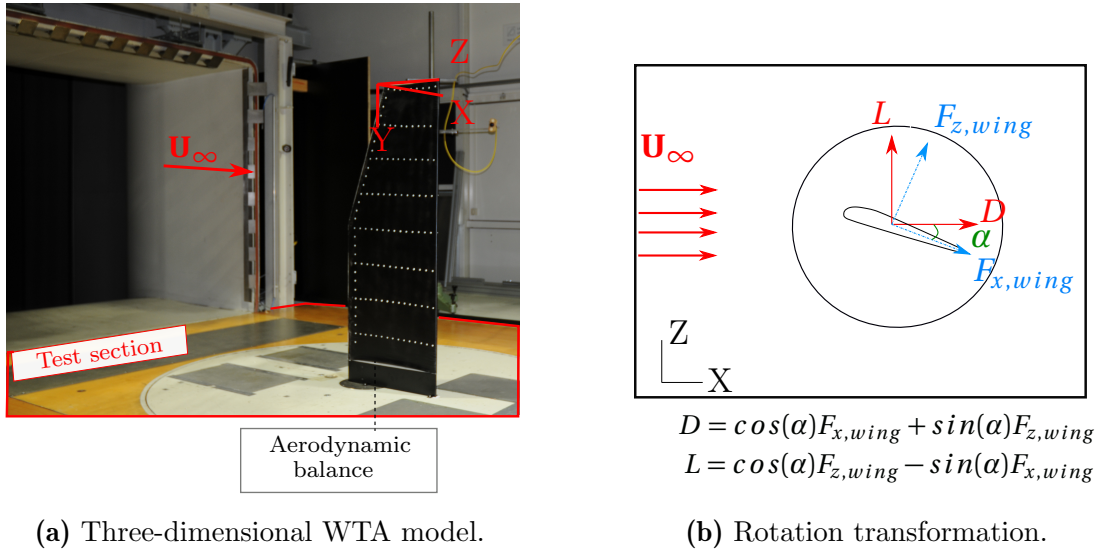


Figure 3.11: installation for the 3D models.

3.3.2 Membrane Deflection Measurements

A photogrammetry technique is utilized to measure the deflection of the membrane. The idea of the technique is based on the following: all the rays of light converge to the perspective center of the camera [59]. Hence, there is a collinearity relationship between an object in space, its image taken by the camera and the perspective center (usually defined as O). In other words, if a point P is considered in the space and P' is its image point in the image plane, then the points P, P' and O are aligned. The collinearity relationship can be exploited to establish equations between the coordinates of P in space, P' in the image plane and the parameters of the camera. Afterwards, the procedure exploits the direct linear transformation (DLT) to rearrange the equations and reconstruct the coordinates of P from the coordinates of P' and the parameters.

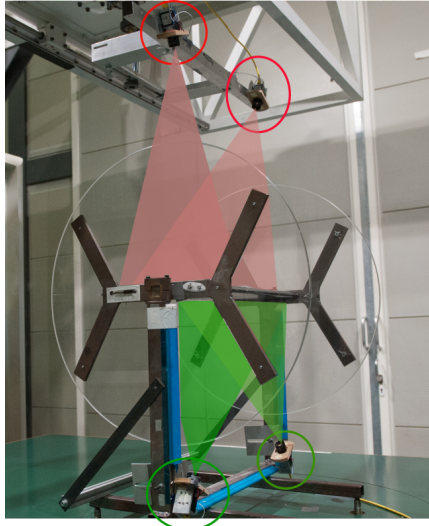
The parameters are composed of interior orientation coefficients, which describe the internal geometric model of a camera, and the exterior orientation coefficients, which are related to the position of the camera in space. They have to be determined during a calibration. For more details on the photogrammetry technique, reference [59] provides the corresponding information and for more explanations about the development of the technique at AER-TUM, see the work of Beguin [18].

During the calibration, a plane (X,Y) marked with points is moved in the third perpendicular direction Z. A volume demarcated by $[X_{min} \ X_{max}, Y_{min} \ Y_{max}, Z_{min} \ Z_{max}]$ is calibrated, which

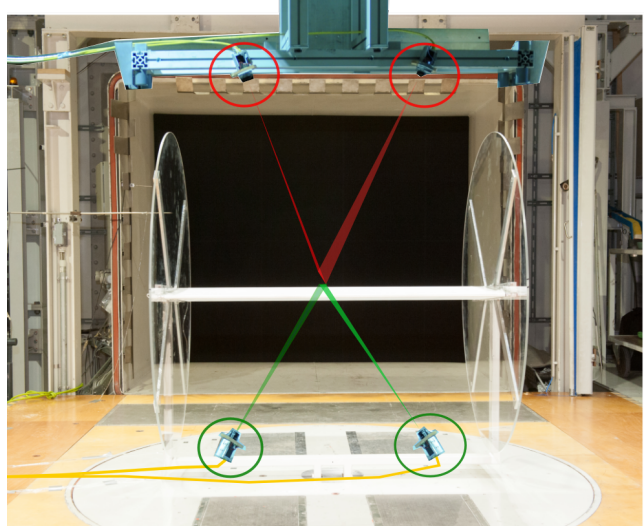
3.3. Experimental Setup

means that the coordinates of any points situated in the range of $[X_{min} \ X_{max}, Y_{min} \ Y_{max}, Z_{min} \ Z_{max}]$ can be reconstructed. During the calibration, an estimation of the average accuracy can be measured. In our case, the average accuracy is equal to 0.13 mm per pixel.

During the experiments, four cameras are set: two measure the deflection on the upper surface of the wing while the other two measure the deflection on the lower surface of the wing. Each camera takes a photo of a group of reflectors distributed on the complete wing surface. The reflectors define the points where the coordinates are reconstructed. Sometimes, one shot was not enough to record the complete wing surface. Therefore, a movement in the span or in the chord direction was necessary to make the measure on the complete wing. Afterwards, an interpolation is applied to combine the deflection in all directions. Figs. 3.13 and 3.12 illustrate the two pairs of cameras set in wind tunnel facilities for each model. One pair of cameras maps the marker distribution on the upper surface of the wing while the other pair detects it for the lower surface. The cameras used to conduct the tests are delivered by the firm Basler[®] [12]. They have a resolution of 2592 x 1944 pixels with a focal length of 16mm.



(a) WTB model.



(b) WTA model.

Figure 3.12: Photogrammetry measurement setup for the two-dimensional WTB and WTA models.

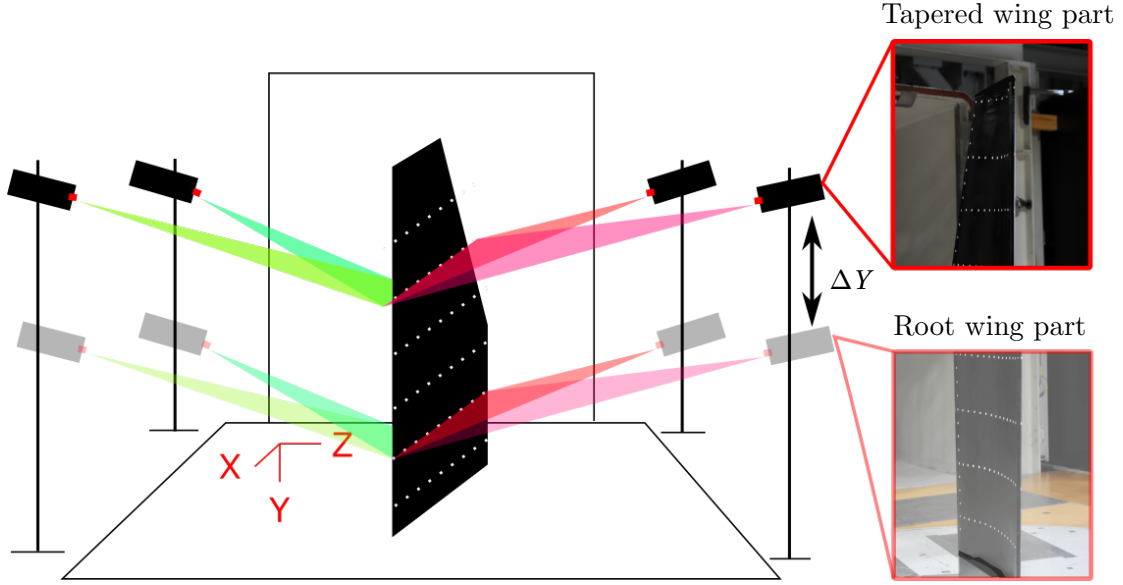


Figure 3.13: Sketch explaining the photogrammetry measurement for the three-dimensional WTA model.

3.3.3 Velocity Field Measurements

3.3.3.1 Hot-wire anemometry

The flow velocity field is measured with a hot wire anemometry system (HWA). The system utilizes probes, which are miniature crosswires made of platinum-plated tungsten with a diameter of $5\mu\text{m}$. The technique is based on a constant temperature anemometry technique, which consists in maintaining the wire at a constant temperature. The sensitive wire is part of a Wheatstone bridge whose resistance is variable. Adjusting the operating resistance allows to adjust the temperature of the wire. When the fluid speed increases, the temperature of the wire tends to cool down and its resistance decreases resulting in an imbalance of the bridge. Then, the system receives a signal which causes an augmentation of the temperature of the probe.

The probe calibration is based on a look-up table technique (cf. [22]): a calibration allows to generate a relationship between the hot-wire voltage and the flow velocity and the flow angle. One measurement is recorded during a time of $t_{meas} = 6.4\text{ s}$ with a sampling rate of $f_{meas} = 3000\text{ Hz}$, meaning that 19200 values are recorded and then averaged. A low-pass filter is applied to the bridge output voltages at $f_{lp} = 1400\text{ Hz}$ with respect to the Nyquist criterion.

For the present cases, the HWA is employed in the middle of the span for both two-dimensional WTB and WTA models and downstream of the WTB wing. The flow velocity field is measured

in the middle plane ($Y = 0$) on the upper-side of the wing (cf. Fig. 3.14), whereas the lower-side was excluded for concerns about the interference between the traversing unit and the wing. The crosswire probes measure two coordinates of the velocity vector. With the coordinate system shown in Fig. 3.14, the x -coordinate u and the z -coordinate w are the components of the velocity measured during the experiments. The traversing unit moves the crosswire probe within a grid resolution of $\Delta x, z = c_r/22$ in the x - and z -direction, respectively, and a refinement of $\Delta z = c_r/73$ near the membrane. Finally, the HWA is employed to measure the induced angle β behind the model ($X = X_{TE} - 0.1m$).

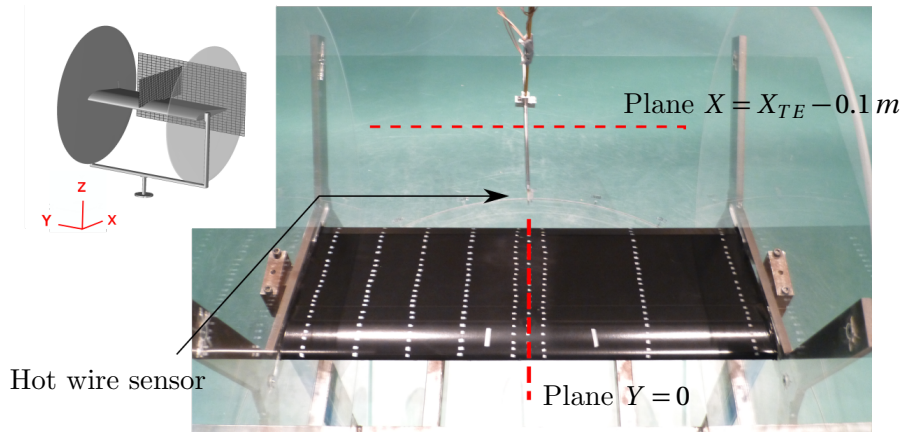


Figure 3.14: HWA measurement set up for the two-dimensional WTB and WTA models.

3.3.4 Test conditions

Table 3.1 summarizes the test conditions during the wind tunnel experiments for each model. Force and membrane deflection measurements are conducted for all models at various q_∞ . The flow velocity field is measured for both the 2.5D WTB and the 2.5D WTA model.

3.4 Numerical Setup

Two different meshes are necessary for the computations of the fluid state and the membrane deflection. Each mesh, designated as the CFD- and the FEM mesh, is of a structured type obtained with separate grid generators. The CFD mesh is generated with ICEM CFD [6] whereas, the FEM mesh is constructed with GiD [28]. For each experimental model presented in Sec. 3.2.2, a CFD and a FEM meshes have to be generated. In a first step, a two-dimensional analysis is considered

Model	Test conditions	Balance	Photogrammetry	HWA
2.5D WTB Model	U_∞ , m/s	20, 35	20, 35	20
	q_∞ , Pa	230, 690	230, 690	230
	$Re \times 10^5$	2.8, 5.0	2.8, 5.0	2.8
	α , °	0:2:20	0, 6, 10, 15	6, 15
2.5D WTA Model	U_∞ , m/s	22, 30	22, 30	22
	q_∞ , Pa	280, 520	280, 520	280
	$Re \times 10^5$	6.5, 1.0	6.5, 1.0	6.5
	α , °	-5:5:20	-5:5:15	0, 6, 15
3D WTA Model	U_∞ , m/s	15, 22, 30	15, 22, 30	-
	q_∞ , Pa	130, 280, 520	130, 280, 520	-
	$Re \times 10^5$	4.35, 6.67, 8.70	4.35, 6.67, 8.70	-
	α , °	-5:2:29	-5:5:15	-

Table 3.1: Test conditions considered in the experimental investigations.

to simplify the computations. Then, an extension to three-dimesional analysis is executed. In the following, the mesh generation and the setup in the computations are presented.

3.4.1 2D Models

3.4.1.1 Mesh Generation

- *CFD Meshes - WTB and WTA models*

Two distinct CFD meshes are created to model the flow around the WTB and the WTA geometries. The two CFD meshes are based on the same design. The flowfield is globally discretized with a C-topology mesh. Additionally, an O-topology is employed to refine the airfoil's nearfield, assuring a more accurate resolution of the boundary layer. It is not possible with ANSYS CFX or TAU to solve a pure two-dimensional plane problem. Therefore, the two meshes are constructed with an extrusion in the third direction, namely the y-direction (see Fig. 3.15a). The extrusion length is smaller than 2% of the chord length, which can be considered as negligible compared to the other lengths. Detailed views of the refinement around the two airfoils are depicted in Figs. 3.15b and 3.15c. A value of $y^+ = 1$ is used to construct the two meshes and assure an accurate resolution of the boundary layer. The latter induces that an off-body distance of $z = 0.016$ mm and $z = 0.017$ mm discretization is generated for the WTB and the WTA model, respectively.

Regarding the boundary conditions, they are set similarly for the two meshes. An inlet velocity is set on the surface forward of the airfoil while an opening boundary with a pressure difference

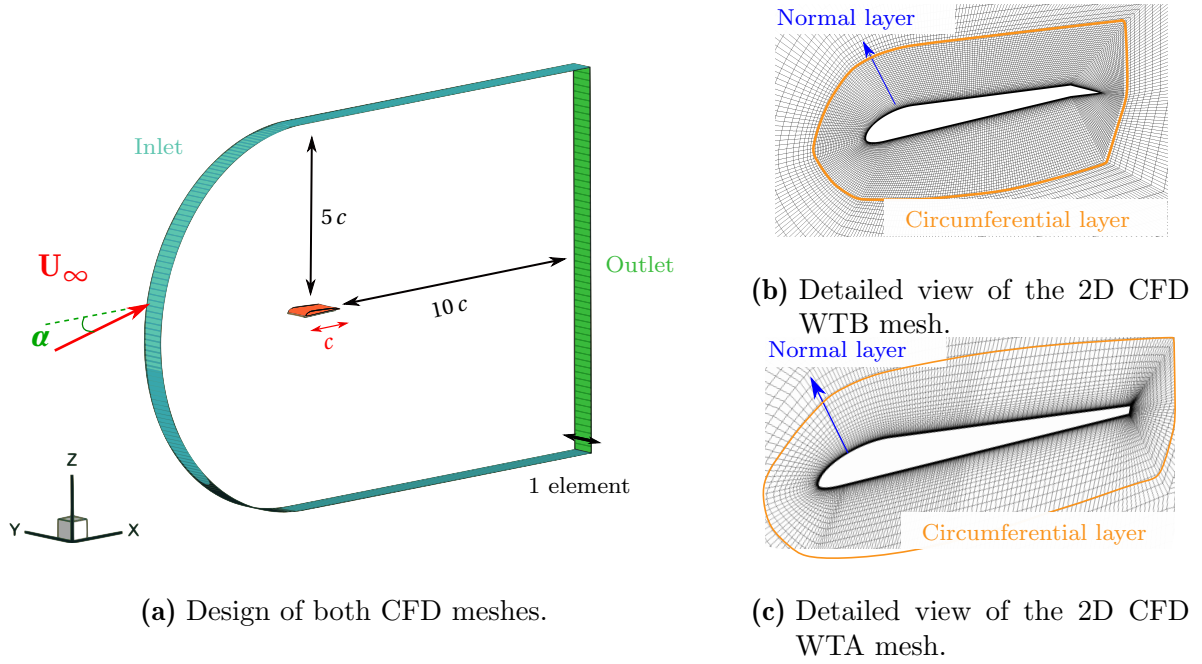


Figure 3.15: 2D CFD meshes.

to the atmospheric pressure equal to 0Pa is fixed to the surface backward of the airfoil. Then, two symmetry boundaries are applied to the surfaces which are positionned on both sides of the airfoils. Finally, the airfoils are considered as a viscous wall where no roughness influence is taken into account.

- **FEM Meshes - WTB and WTA models**

Two distinct FEM meshes are generated to model the WTB and the WTA airfoils as well. Both meshes are based on the same design. Both FEM meshes are structured and have rectangular elements. As the CFD meshes are extruded in the y -direction, the FEM meshes have to be extruded as well. It is crucial that CFD and FEM meshes are complementary to assure the feasibility of the computations. A same coordinate system is then mandatory to assure a correct information exchange between the two solvers. The FEM meshes are defined by the number of divisions on two symmetrical lines, depicted in Fig. 3.16.

Regarding the boundary conditions, they are set similarly for the two meshes. The elements on the LE and on the TE are fixed in all directions to maintain the shape of the geometries. All elements are fixed in the y -direction to ensure the two-dimensional characteristics of the analysis. The membrane is defined as an isotropic material with a Young's modulus taken equal to the

Young's modulus of the membrane in the weft direction, namely $E = 2.1$ MPa or $E = 4$ MPa depending on whether the WTB or the WTA model is considered. The membrane is assumed as an isotropic material for the computations to simplify the implementation of the FSI analysis. A Poisson coefficient of $\nu = 0.2$ is taken as a standard value for both membrane fabrics. Finally, initial pre-stresses are defined: for the WTB model and the WTA model, pre-stresses of $\sigma = 42.000$ Pa and $\sigma = 360.000$ Pa are set, respectively, as it is employed during the wind tunnel tests (cf. Sec. 3.2.2).

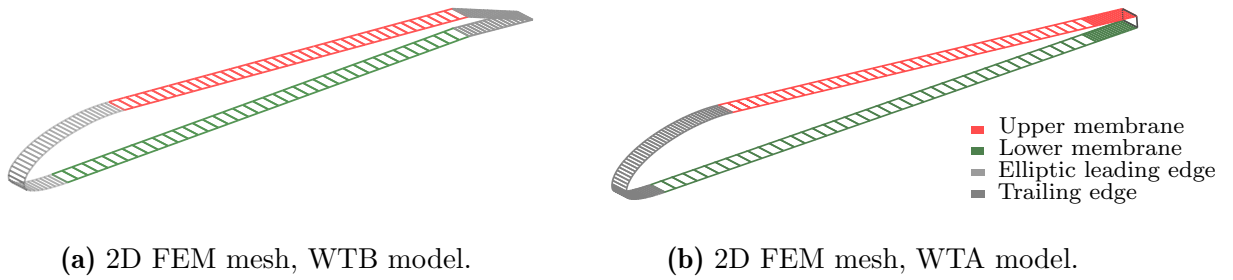


Figure 3.16: FEM meshes.

3.4.1.2 Grid Sensitivity Study

• *CFD Mesh - WTB model*

A grid sensitivity study is conducted to assure the results independency from the spatial discretization. Four distinct resolutions, whose characteristics are summarized in Tab. 3.2, are generated. The results of the grid sensitivity study are shown in Fig. 3.17, where the lift coefficient (C_l) is plotted for the four resolutions at $\alpha = 0^\circ$, 6° , 10° , and 15° . The results show that C_l are very similar for the four resolutions up to $\alpha = 10^\circ$. The biggest error is equal to 1% at $\alpha = 10^\circ$ when C_l is compared between the medium and the extra-fine resolutions. However, the results are more sensitive to the grid refinement at $\alpha = 15^\circ$. If the fine mesh is considered as a reference grid, the coarse resolution overestimates C_l by 7%, while the medium mesh underestimates C_l by 1.2% and the extra-fine mesh overestimates C_l by 1.5%. In order to enable the usage of the same mesh at all α , the fine grid is chosen to perform the numerical investigations. The mesh has the following characteristics: it is constructed with 126 682 hexahedrons, with 120 layers in the airfoil's normal direction and 2×128 layers in the parallel direction of the airfoil contour, also designed as circumferential direction. The normal and circumferential directions are depicted in

3.4. Numerical Setup

Figs. 3.15b and 3.15c.

Characteristics	Coarse	Medium	Fine	Extra-Fine
Total number of nodes	39,234	75,140	126,682	210,074
Normal layer nodes	62	90	120	150
Circumferential layer nodes	2 x 73	2 x 99	2 x 128	2 x 165

Table 3.2: Characteristics of the different resolutions of the 2D WTB CFD mesh.

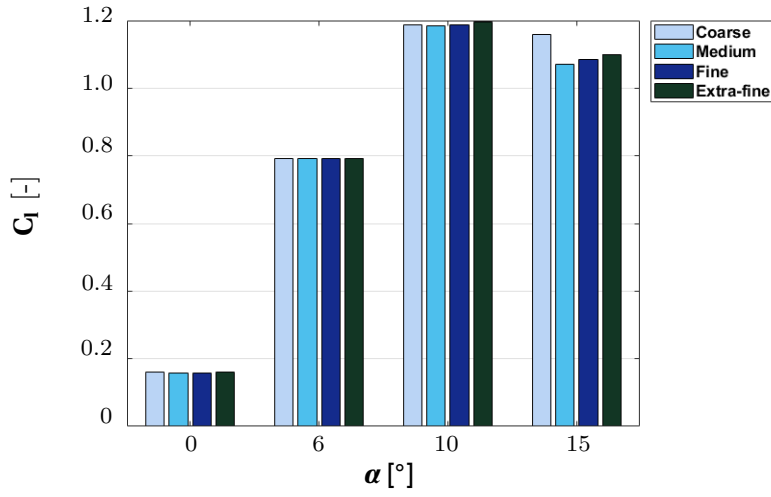


Figure 3.17: Results of the grid independency study for the 2D WTB CFD mesh.

- **CFD Mesh - WTA model**

A grid sensitivity study is conducted for the WTA CFD mesh as well. Four distinct resolutions are generated. Their characteristics are summarized in Tab. 3.3. The grid sensitivity analysis is performed at $\alpha = 0^\circ$, 4° , 12° and 16° . The resulting C_l is compared between the four resolutions in Fig. 3.21. The deviations in C_l are relatively small. The biggest difference is around 3% at $\alpha = 16^\circ$. Furthermore, C_l increases of 0.6% at $\alpha = 16^\circ$, when C_l is compared between the extra-fine and the fine resolution. Therefore, the medium resolution is chosen to carry out the computations. The mesh has the following characteristics: it is constructed with 114 796 hexahedrons, with 120 layers in the airfoil's normal direction and 2 x 210 layers in the circumferential direction.

- **FEM Meshes - WTB and WTA models**

A refinement study is performed for the FEM meshes as well. Several resolutions are generated

Characteristics	Coarse	Medium	Fine	Extra-Fine
Total number of nodes	53,056	114,796	213,116	456,466
Normal layer nodes	85	120	170	240
Circumferential layer nodes	2 x 140	2 x 210	2 x 275	2 x 420

Table 3.3: Characteristics of the different resolutions of the 2D WTA CFD mesh.

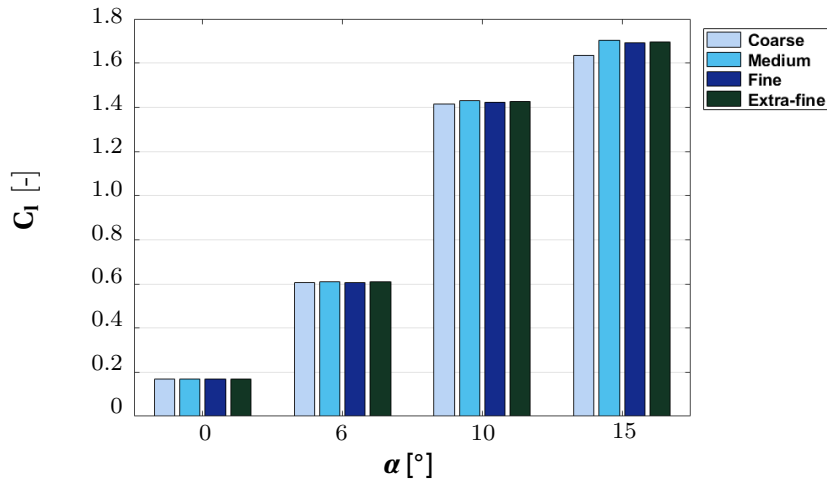


Figure 3.18: Results of the grid independency study for the 2D WTA CFD mesh.

by applying a pressure load to the membrane and their results are compared. The pressure is chosen of the same order of magnitude as the expected pressure loads when a flexible geometry is considered. The coarser the mesh is, the stiffer the membrane behaves. For the WTB and the WTA FEM meshes, both selected meshes have 456 nodes and present a relative error of 0.03% in comparison with the finest resolution.

In both cases, the mesh is refined at the LE and TE to capture the geometry accurately. Although these areas do not contribute to the structural loading, an accurate representation of the geometry is necessary to ensure the correct exchange of information between the FEM and the CFD mesh.

3.4.2 2.5D and 3D Model

3.4.2.1 Mesh Generation

- **2.5D and 3D CFD Meshes**

Two distinct meshes are generated to compute the flow around the entire 2.5D WTA and the 3D WTA models. The two meshes are based on the same construction steps described in the following.

The flowfield is globally discretized using a C-topology mesh with an O-topology to refine the wing's near field. Sketches of the two meshes are given in Figs. 3.19 and 3.20a. The two meshes are generated with a resolution of $y^+ < 1$ near the wing. The growth ratio of the cell in the wall-normal layer is lower than 1.2. A minimum cell angle of 30° is achieved to ensure a good quality of the two meshes. In both cases, the computational domain has a size of $20 \times c_{root}$ downstream the wing and $12 \times c_{root}$ in all other directions.

A velocity inlet and an opening boundary condition are applied at the inflow and the outflow, respectively. For the 2.5D WTA mesh, the endplates and the wing are set as turbulent walls, while the surfaces on the right and the left of the wing are defined as velocity inlet condition. For the 3D WTA mesh, the wall next to the wing is defined as turbulent wall, likewise the peniche and the wing.

- **2.5D and 3D FEM Meshes**

The FEM meshes representing the 2.5D and 3D wings are constructed as complementary surfaces of the wing of the CFD meshes. The two FEM meshes are structured and have rectangular elements. The elements of the LE and the TE are fixed in all directions. For the 3D WTA FEM mesh, the nodes at the tip and the root are fixed in all directions as well to represent the sealing between the membrane and the tip and root. For both models, a Young's modulus of $E = 4$ MPa is set while a Poisson coefficient of $\nu = 0.2$ is applied. Additionally, a pre-stress of $\sigma_{01} = 400.000$ Pa is set in the chord direction while a pre-stress $\sigma_{02} = 80.000$ Pa is defined in the span direction to avoid possible surface irregularities.

3.4.2.2 Grids Dependency Study

- **2.5D WTA CFD Mesh**

Three resolutions are investigated at $\alpha = 0^\circ, 5^\circ$ and 10° . Table 3.5 gives the different character-

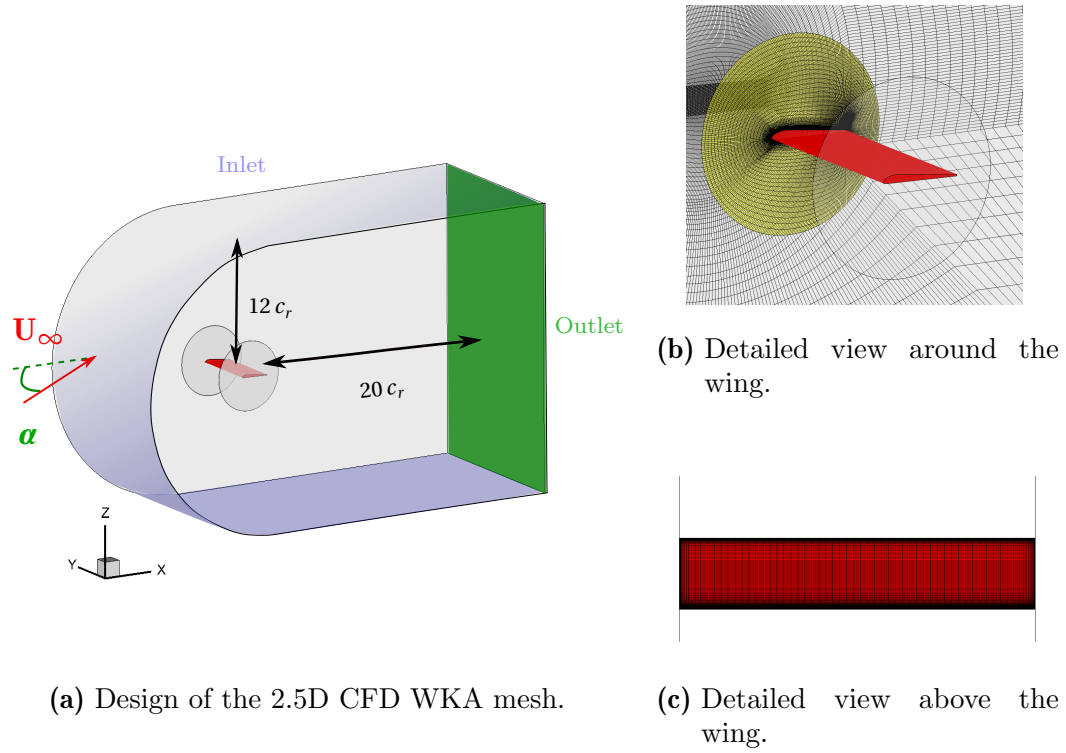


Figure 3.19: 2.5D CFD mesh.

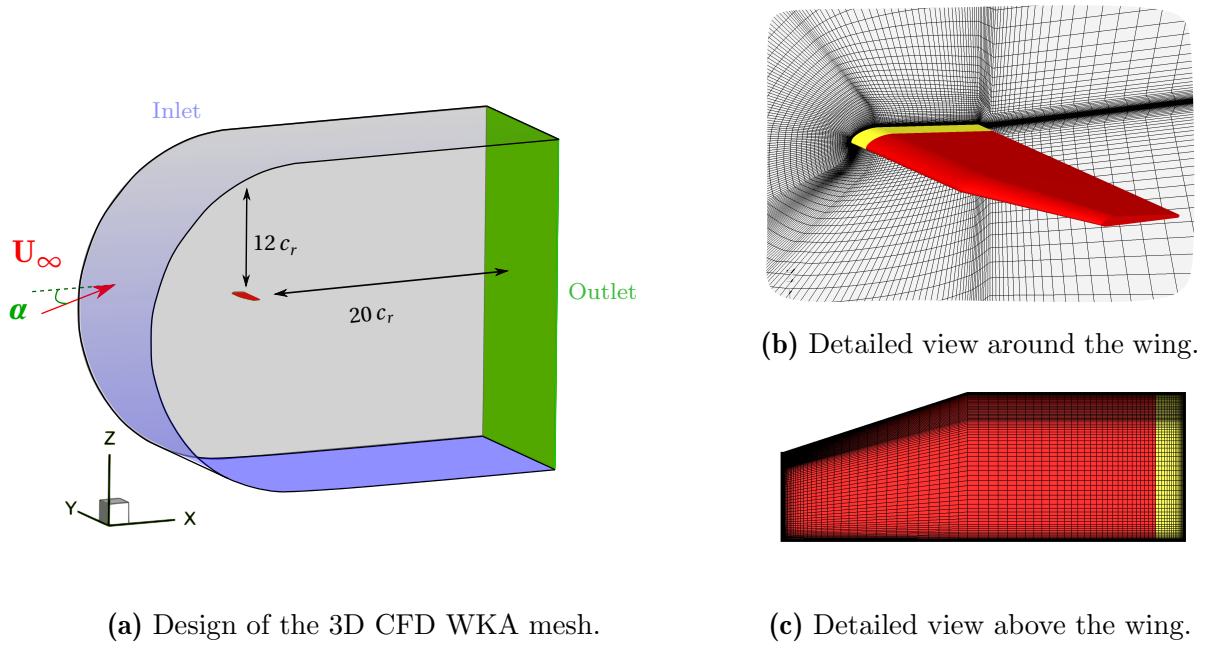


Figure 3.20: 3D CFD mesh.

istics of the resolutions, while Fig. 3.21 represents the values of C_L for the three resolutions at all α . The results show that the coarse mesh provides similar values of C_L than the medium mesh. The biggest deviation between the coarse and the medium mesh is for $\alpha = 10^\circ$, where $\Delta C_L = 0.8\%$. Nevertheless, the values of C_L obtained with the fine mesh are higher than for the two other resolutions. If the medium mesh is taken as a reference, the fine resolution overestimates C_L with deviations equal to 6.5%, 3% and 15% at $\alpha = 0^\circ, 5^\circ$ and 10° , respectively. It is decided to choose the medium resolution to perform the computations.

A time step sensitivity study is performed to be sure that the results are independent for the choice of the time step. The time step analysis is carried out by studying the response of the computations for $\delta t = 1\text{ ms}$, $\delta t = 5\text{ ms}$, $\delta t = 10\text{ ms}$ and $\delta t = 100\text{ ms}$. The results show that for $\delta t = 1\text{ ms}$, C_L and C_D do not converge in the time appropriate duration of the computations. For $\delta t = 100\text{ ms}$, C_L is around 13% higher than for the others computations. For $\delta t = 5\text{ ms}$ and $\delta t = 10\text{ ms}$, the results compute the same values for the aerodynamic coefficients. Consequently, the time step of $\delta t = 10\text{ ms}$ is chosen for the computations.

Characteristics	Coarse	Medium	Fine
Total numbers of nodes	4.6 Millions	8.9 Millions	12.3 Millions
Normal layer nodes	54	65	90
Circumferential layer nodes	244	244	244

Table 3.4: Characteristics of the different resolutions of the grids for the 2.5D WTA model.

- **3D WTA CFD Mesh**

Three distinct resolutions are investigated. Their characteristics are summarized in Table 3.5. Three angles of attack are investigated, namely $\alpha = 0^\circ, 5^\circ$ and 10° . The results are summarized in Fig. 3.22 where C_L is compared for the various resolutions. C_L fluctuates for the coarse mesh whereas it achieves a constant value for the two finer resolutions. The deviation of C_L between the medium and the fine CFD mesh is equal to 0.2 % at $\alpha = 5^\circ$ and to 0.1 % at $\alpha = 10^\circ$, the values for the medium mesh are used as references. As a compromise with respect to computational effort and accuracy enhancement, the medium resolution is chosen for the computations.

A time step sensitivity study is performed as well. The preliminary physical time step is equal to $\delta t = 300\mu s$. The time step analysis is performed by studying the response of the computations for the half and the double of $\delta t = 300\mu s$. The results show that for $\delta t = 300\mu s$ and $\delta t =$

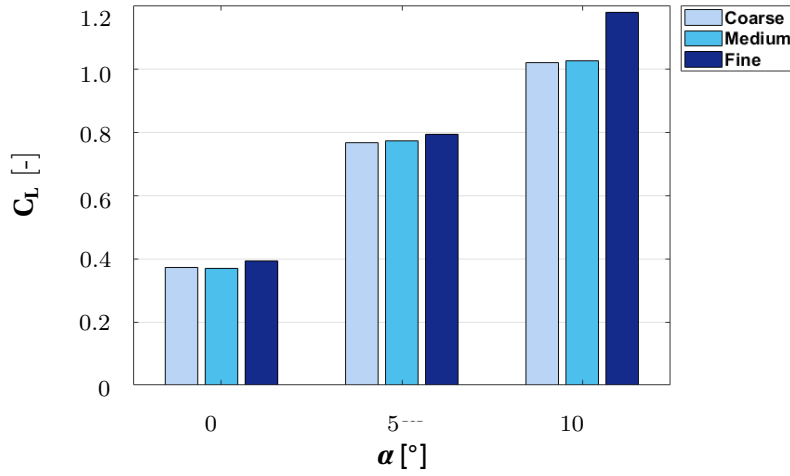


Figure 3.21: Results of the grid independency study for the 2.5D WTA CFD mesh.

$600\mu s$, C_L and C_D are the same. However, for $\delta t = 150\mu s$, undesired unsteady phenomena occur. Consequently, the time step of $\delta t = 600\mu s$ is chosen for the following computations.

Characteristics	Coarse	Medium	Fine
Total numbers of nodes	4.6 Millions	8.9 Millions	12.3 Millions
Normal layer nodes	54	65	90
Circumferential layer nodes	244	244	244

Table 3.5: Characteristics of the different resolutions of the grids for the 3D WTA model.

• 2.5D and 3D FEM Meshes

Four different resolutions are investigated for the 2.5D and the 3D FEM meshes. Between two resolutions, 10 nodes are added in each line of the chord direction. As the error between the resolutions does not exceed 0.1% for both models, the selected mesh is the one with 4100 nodes (20 nodes per line), which presents a relative error of 0.05% in comparison with the finest resolution. A finer mesh is generated at the LE and TE to capture the geometry accurately. As mentions previously, although these areas do not contribute to the structural loading, an accurate representation of the geometry is necessary to ensure the correct coupling between the CFD mesh and the FEM mesh.

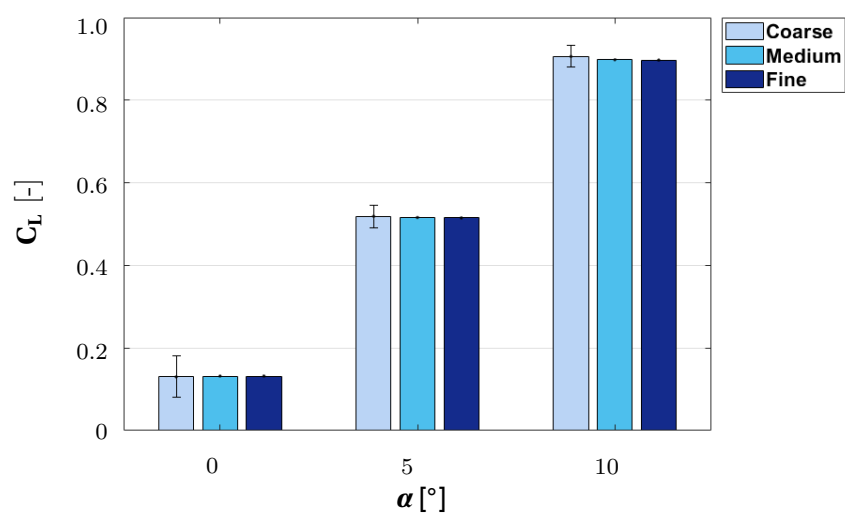


Figure 3.22: Results of the grid independency study for the 3D WTA CFD mesh.

Chapter 4 - Comparison of 2D FSI and Wind-Tunnel Data

The present chapter gives a comparison between 2D fluid structure interaction simulations and wind tunnel measurements. A juxtaposition of the two types of data is realized to estimate the accuracy of the computations. Only the numerical data for the 2D WTB and 2D WTA models are presented in this chapter. The comparative analysis starts with a comparison of the membrane deflection at various angles of attack for several dynamic pressures. Then, the comparison is continued with the analysis of the flow field, where two components of the velocity are analyzed, namely u/U_∞ and w/U_∞ . Finally, the aerodynamic properties are examined: the lift and the drag are plotted as functions of the angle of attack. Slight deviations are observed in the comparisons between numerical and experimental data. Therefore, the last subsection of each analysis for both models gives several experimental considerations, which have to be taken into account.

4.1 2D WTB Model

In this section, the comparison between numerical and experimental data is presented for the 2D WTB model. Note that the 2D WTB model is introduced in Sections 3.2.1.1 and 3.4.1. The FSI computations are conducted for a two-dimensional flow with the coupling between the CFD solver ANSYS CFX and the FEM solver ANSYS APDL. The numerical results are compared to the membrane deflection and the flow field velocity measured in the middle of the wingspan, where it is assumed that the flow features only two-dimensional characteristics. In order to facilitate a better comprehension of the analysis, a schematic explanation of the location where the experiments are conducted is given whenever a parameter is analyzed. The results presented in this section are based on the publication of Piquee et al. in the Aerospace Journal [67].

4.1.1 Membrane Deflection

The deflection of the membrane is measured at $\alpha = 0^\circ, 6^\circ, 10^\circ$ and 15° for $q_\infty = 230$ Pa and 690 Pa. Figs. 4.1 and 4.2 illustrate the membrane deflection obtained during the wind tunnel campaign and the deflection computed with FSI computations. Note that the wind tunnel data provide results for discrete points marked with red cross (x). The obtained data are afterwards interpolated with a spline.

In general, for the two q_∞ , the FSI computations overestimate the membrane deflection, see Figs. 4.1 and 4.2. For $q_\infty = 230$ Pa, the membrane deflection obtained with the FSI calculations can be characterized as close to the wind tunnel data, whereas for 690 Pa there is slight deviations. To evaluate the error between the two sets of data, the norm error L2 is calculated like the following:

$$\|e_2\| = \sqrt{\sum_{n=0}^N (\mathbf{x}_{n,\text{FSI}} - \mathbf{x}_{n,\text{W/T}})^2}, \quad (4.1)$$

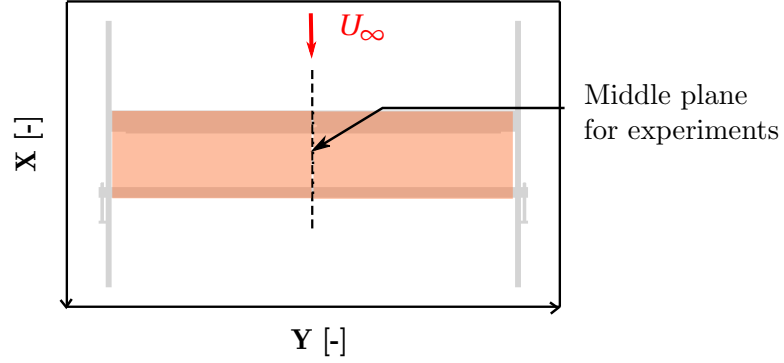
with e_2 the norm error L2, \mathbf{x}_{FSI} the vector of the deformation of the membrane obtained with FSI, and $\mathbf{x}_{\text{W/T}}$ the vector of the deformation of the membrane obtained in the wind tunnel.

For $q_\infty = 230$ Pa and $\alpha = 0^\circ$, the experiments are overestimated by 6% on the upper side surface and by 5% on the lower side surface of the wing. At $\alpha = 6^\circ$, the norm error L2 shows deviations of 5% on the upper side surface and of 6% on the lower side surface of the wing. Finally at $\alpha = 10^\circ$ and 15° , the error is under 6% for both sides.

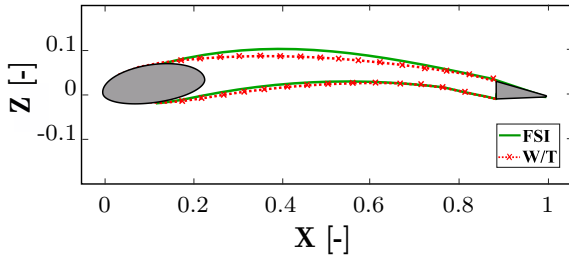
For $q_\infty = 690$ Pa and $\alpha = 0^\circ$, the membrane deflection is overestimated by 6.5% on the upper side surface, and by 4% on the lower side surface of the wing. For $\alpha = 6^\circ$, the overestimation is 8% and 5% for the upper and the lower side surfaces, respectively. When α increases, the error increases on the upper side surface as well, with 15% at $\alpha = 10^\circ$ and 15° , whereas it is less than 5% on the lower side surface. One explanation for the increase of the deviation is given in Sec. 4.1.4. It is shown that 3D effects play an important role at $q_\infty = 690$ Pa and the flow separation is over-estimated.

Although the deflection is overestimated, the FSI computations reproduce the expected behavior when α increases (see Fig. 4.3). Indeed, the abscissa $X_{Z_{\max}}$ where the maximal deflection occurs, is shifted upstream to the LE when α gets higher. The latter is barely observed for $q_\infty = 230$ Pa but more pronounced at $q_\infty = 690$ Pa. If the pressure distribution is observed, the phenomenon is explained with the progression of the separated flow starting from the TE and moving forward to

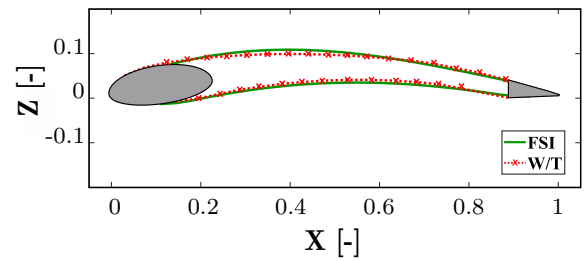
the LE. More details about this phenomenon is given in Sec. 5.



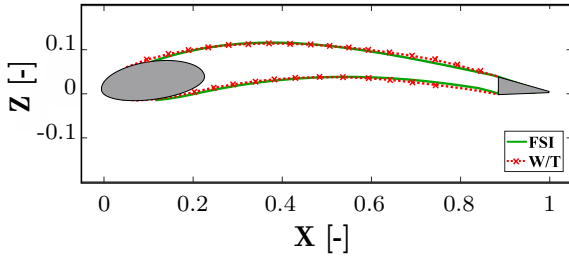
(a) Schema showing the plane where the experiments were conducted.



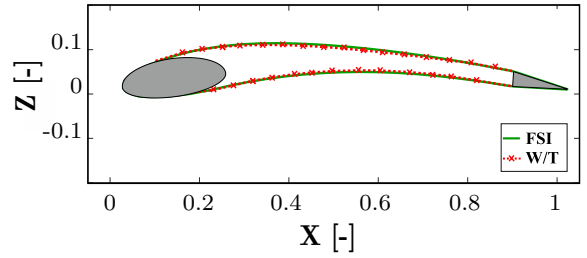
(b) $\alpha = 0^\circ$, $q_\infty = 230$ Pa.



(c) $\alpha = 6^\circ$, $q_\infty = 230$ Pa.



(d) $\alpha = 10^\circ$, $q_\infty = 230$ Pa.



(e) $\alpha = 15^\circ$, $q_\infty = 230$ Pa.

Figure 4.1: Comparison between FSI results and photogrammetry measurement data: Membrane deflection at $\alpha = 0^\circ, 6^\circ, 10^\circ$ and 15° at $q_\infty = 230$ Pa for the 2D and 2.5D WTB models. The deflection was measured in the middle of the wing span as shown in (a). (b)-(e) illustrate the deflection for the various α .

4.1.2 Flow Field Velocity

The flow field velocity is measured in the middle of the wingspan (cf. Fig. 4.4 (a)) with the HWA system at $\alpha = 6^\circ$, and 15° for $q_\infty = 230$ Pa. Two components of the velocity vector, namely the axial velocity u/U_∞ and the vertical velocity w/U_∞ are depicted in Figs. 4.4 and 4.5. The FSI

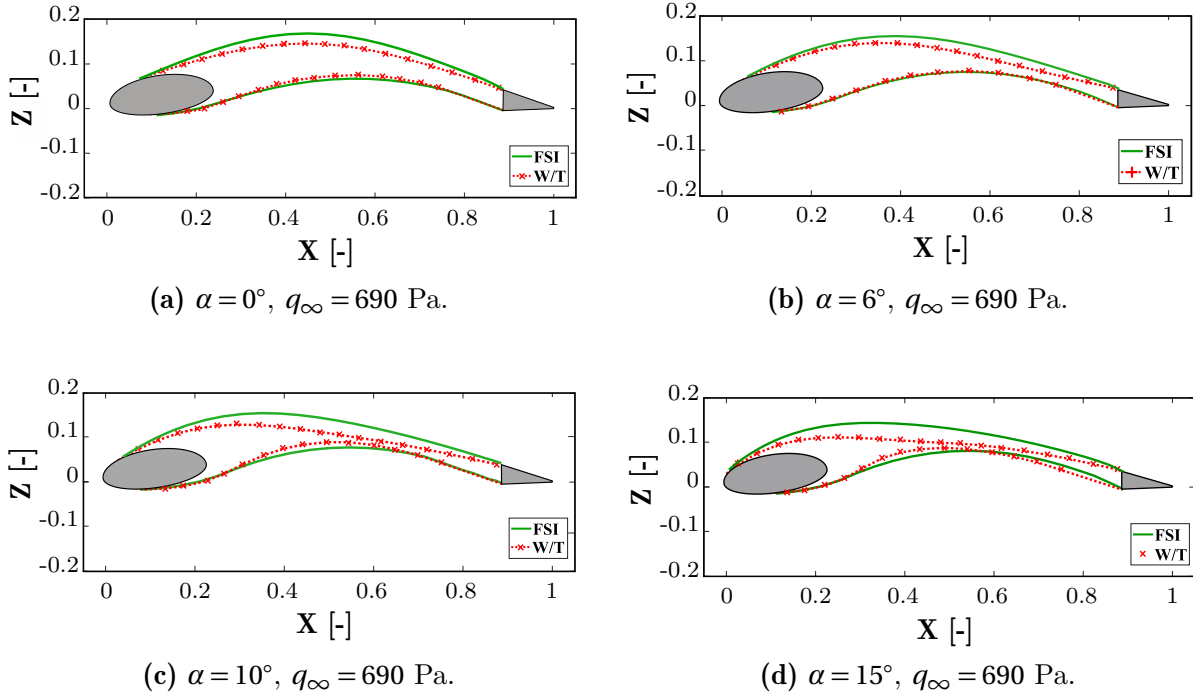


Figure 4.2: Comparison between FSI results and photogrammetry measurement data: Membrane deflection at $\alpha = 0^\circ, 6^\circ, 10^\circ$ and 15° at $q_\infty = 690$ Pa for the 2D and 2.5D WTB models. The deflection was measured in the middle of the wing span (see Fig. 4.1 (a)).

results are shown on the left side while the wind tunnel data are depicted on the right side. It has to be considered that the field close to the airfoil could not be measured because of the safety distance between the membrane and the sensor. Furthermore, only the velocity above the wing could be measured without disturbing the flow around the wing.

The results of the FSI computations are congruent with the flow measurements around the airfoil but some deviations are observed. When the computed velocity in the acceleration region on the upper surface and the velocity in the region near the TE are considered, they differ slightly from the wind tunnel data. The two regions are larger in the FSI computations. The observed phenomena can be explained as follows:

- The wake region is computed larger, which is attributed to 3D effects during the wind tunnel tests (cf. Section 4.1.4). The downwash flow produced by 3D effects decreases the local α , which results in a smaller wake region during the experiments. This reduction of the wake region is observed at $\alpha = 6^\circ$, but is even more pronounced at $\alpha = 15^\circ$.
- The region of the acceleration is computed larger because the camber of the profile is computed higher (cf. Section 4.1.1) and the effective angle of attack is lower. Even though

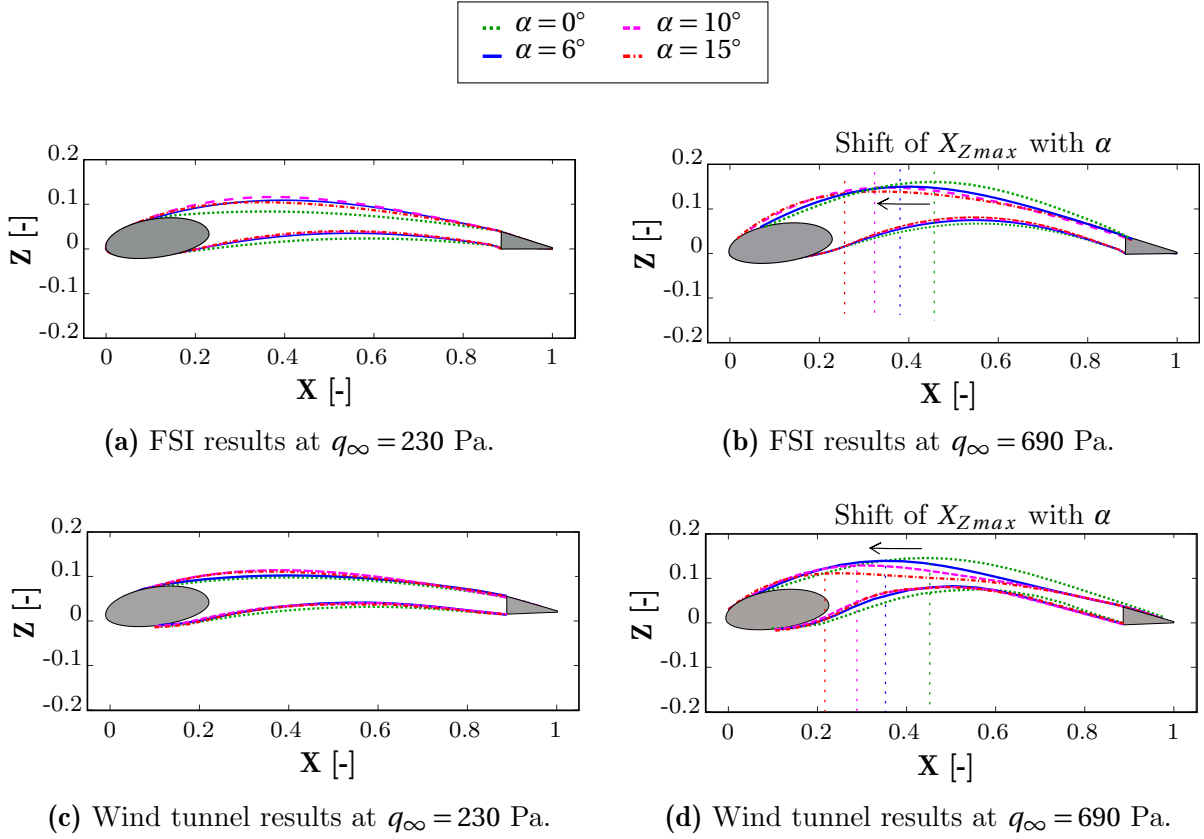
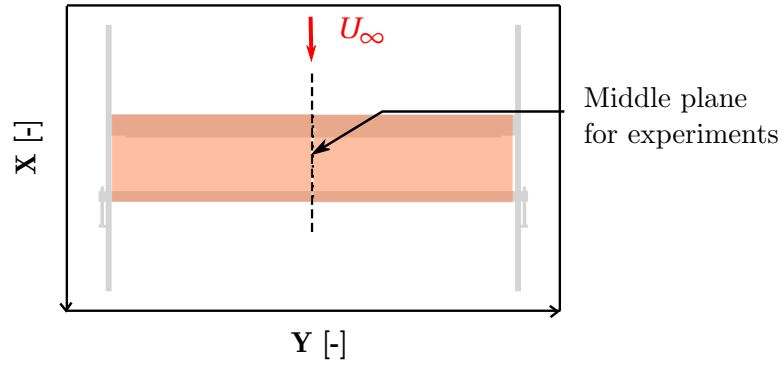


Figure 4.3: Comparison between FSI results and photogrammetry measurement data: Membrane deflection for the 2D and 2.5D WTB models at four α and $q_\infty = 230$, and 690 Pa. The deflection was measured in the middle of the wing span (see Fig. 4.1 (a))

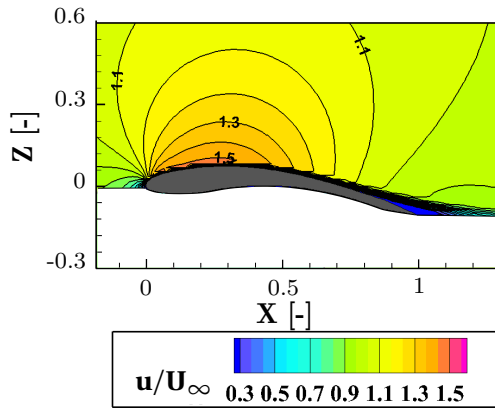
the deviations are small in the membrane deflection for the aforementioned α and q_∞ , they influence the velocity field. As the camber is computed higher at $\alpha = 6^\circ$, the flow accelerates over a longer distance along the upper side of the membrane and stays attached longer. The latter is clearly observed at $\alpha = 6^\circ$, whereas it is less obvious at $\alpha = 15^\circ$ because of the flow separation.

4.1.3 Lift and Drag

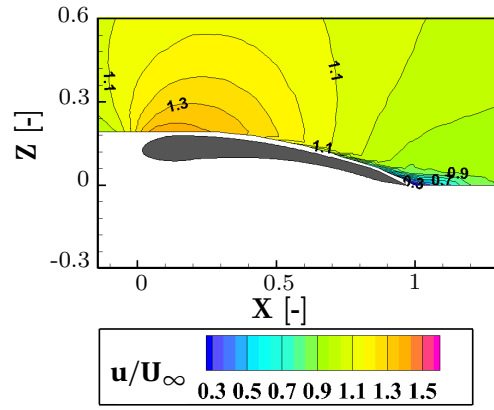
The following section presents C_l and C_d as functions of α from the wind tunnel experiments and the FSI computations. Various properties can be recognized with respect to the flexibility of the concept. Only a brief description of the advantages and the potential of a flexible membrane wing is given in the present chapter, as Chapter 5 presents more precisely the characteristics of a flexible membrane wing compared to its rigid counterpart.



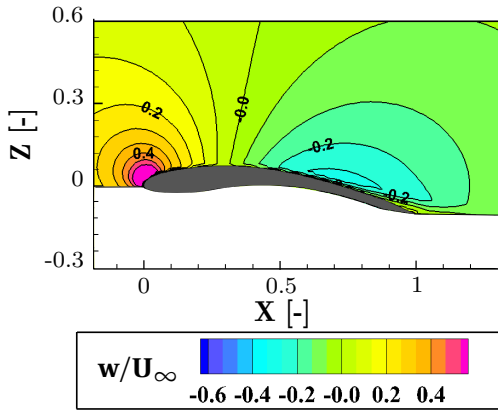
(a) Schema showing the plane where the experiments were conducted.



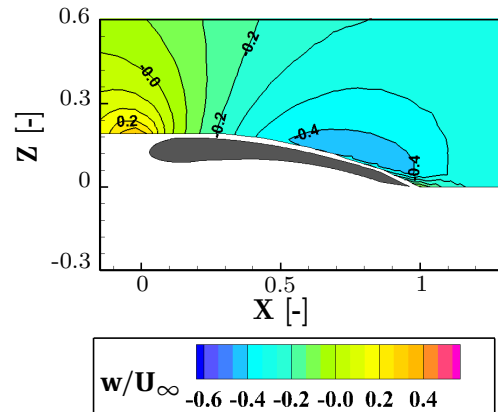
(b) FSI results, u/U_∞ .



(c) HWA measurements, u/U_∞ .

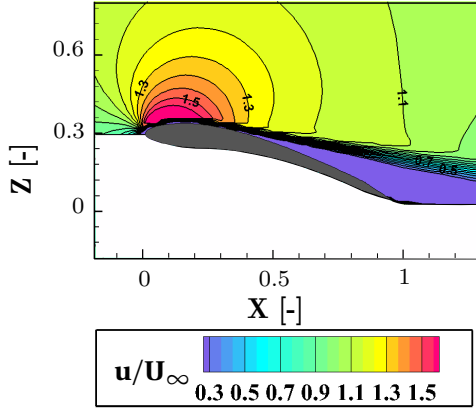


(d) FSI results, w/U_∞ .

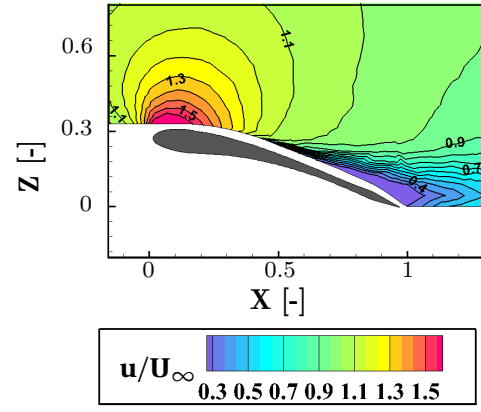


(e) HWA measurements, w/U_∞ .

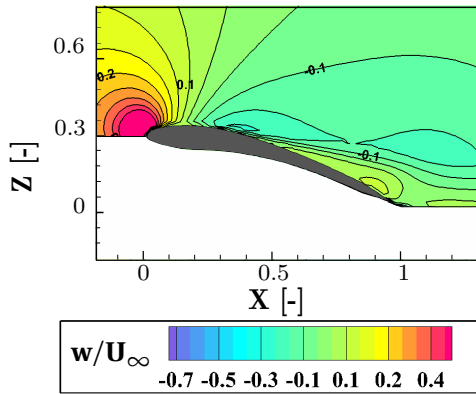
Figure 4.4: Comparison between FSI results and HWA data: Flow field velocity at $\alpha = 6^\circ$ at $q_\infty = 230$ Pa for the 2D and 2.5D WTB models. The velocity was measured in the middle of the wing span shown in (a).



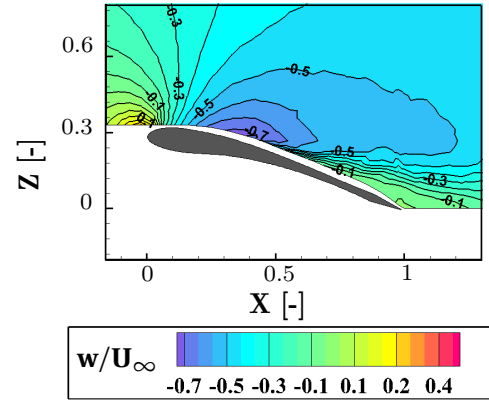
(a) FSI results, u/U_∞ .



(b) HWA measurements, u/U_∞ .



(c) FSI results, w/U_∞ .



(d) HWA measurements, w/U_∞ .

Figure 4.5: Comparison between FSI results and HWA data: Flow field velocity at $\alpha = 15^\circ$ at $q_\infty = 230$ Pa for the 2D and 2.5D WTB models. The velocity was measured in the middle of the wing span (see Fig. 4.4 (a)).

It is interesting to notice the general trend of C_l and C_d with α as it shows the particularities due to the flexibility of the model. When α becomes higher, the camber of the profile increases, permitting higher C_l until a maximum $C_{l,max}$ is achieved (see Fig. 4.6 at $\alpha = 12^\circ$). Then, instead of an abrupt decrease of C_l , it remains nearly constant for a range of α up to $\alpha = 16^\circ$. The onset of stall is delayed to higher angles of attack, while the abrupt decrease of C_l evolves gradually. The latter is related to the shift of the flow separation point towards the LE and the adaptivity of the membrane. The flexible membrane offers an enlargement of the flight envelope by mitigating and delaying the onset of stall to a larger region of α .

In the following, C_l and C_d are plotted for several α at $q_\infty = 230$ and 690 Pa and are discussed in relation with Sections. 4.1.1 and 4.1.2. The deviations observed between the FSI results and the wind tunnel data in the membrane deflection and the velocity field are also identified with the analysis of the polars (Fig. 4.6). Indeed, the lift and drag acting on the wing are directly influenced by the pressure distribution related to the velocity field and the geometry. Bearing in mind the overestimation of the upper side membrane deflection, the comparison can be described as follows.

- **Results for $q_\infty = 230$ Pa:** Beguin [18] noticed that the forces acting on a membrane wing varied for small angles of attack $-2^\circ < \alpha < 4^\circ$ during wind tunnel campaigns due to hysteresis phenomenon. In the present tests, the same phenomenon is observed (see Fig. 4.6). Repeated measurements are performed and the minimum and maximum values obtained in the wind tunnel are plotted on the curves for $q_\infty = 230$ Pa. The hysteresis phenomenon is more pronounced for small α .

At $\alpha = 0^\circ$, C_l is higher for the wind tunnel experiments than for the FSI computations. But considering the hysteresis phenomenon, the minimum of the experimental C_l value is close to the results of the computations. As the hysteresis effects are not taken into account in the numerical analysis, no conclusion can be drawn about the approximation of the aerodynamic properties at $\alpha = 0^\circ$.

At $\alpha = 6^\circ$, C_l is higher in the FSI computations than in the experiments. As noticed, the membrane deflection is overestimated on the upper side surface by the FSI. The latter results in a higher camber, which directly influences the pressure distribution and induces a higher C_l .

At $\alpha = 10^\circ$, and 15° , the membrane deflection is well estimated but slight higher C_l values are observed in the FSI computations. The latter is due to deviations of the flow field near the TE.

The region of the wake and the effective angle of attack are smaller in the wind tunnel tests, due to 3D effects, explaining the smaller C_l in the experiments.

Concerning C_d , the values obtained in the wind tunnel are clearly higher than the values obtained in the FSI computations. One explanation is directly related to the group support/end-plates described in Chapter 3. The drag of the group support/end-plates is around 80% of the global drag acting on the experimental model for $\alpha < 8^\circ$. During the dynamic calibration, a dummy wing is used to reproduce the features of the flow. However, as the drag is mostly produced by the group support/end-plates, the drag of the wing is difficult to determine. Nevertheless, the expected trend of C_d over α is reproduced: the abrupt increase of C_d is instead gradual when α increases, illustrating the capacity of the flexible membrane to mitigate and delay the onset of stall.

- **Results for $q_\infty = 690$ Pa:** The comparisons for C_l and C_d at $q_\infty = 690$ Pa between the FSI computations and the wind tunnel tests are depicted in Fig. 4.6. Note that the membrane deflection is overestimated (cf. Sec. 4.1.1) with a biggest norm error of 15% at $\alpha = 15^\circ$.

In Fig. 4.6, C_l is well approximated at $\alpha = 0^\circ$, 6° and 10° but underestimated at $\alpha = 15^\circ$ with a relative error of 8%. The results at $\alpha = 15^\circ$ are to be expected regarding the membrane deflection. The flow separates for smaller α in the FSI than in the wind tunnel tests. One explanation for the underestimation is that the membrane deflection is so high in the FSI computations that the flow after the abscissa X_{Zmax} can not stay attached. A high deflection related to a high camber results in a precipitated flow separation. Therefore, C_l starts dropping after $\alpha = 10^\circ$ in the computations whereas it still increases in the wind tunnel.

Regarding C_d , it evolves gradually as for the results at $q_\infty = 230$ Pa. The same comments can be made as the previous case, namely C_d is underestimated by the computations. The latter is also attributed to the drag being mostly due to the group support/end-plates as already mentioned.

4.1.4 Summary and Experimental Consideration

The present section has the purpose to summarize the comparison for the 2D WTB model and to give further considerations. As a summary of the validation of the data, the following remarks can be reported:

- **Results for $q_\infty = 230$ Pa:** although small deviations are observed, the agreement between FSI and wind tunnel data can be characterized as good. In general, the membrane deflection is

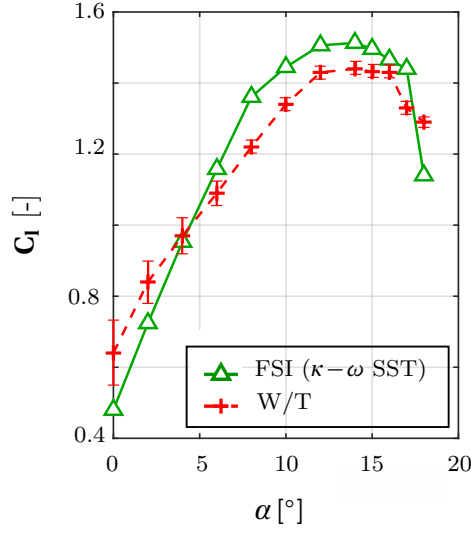
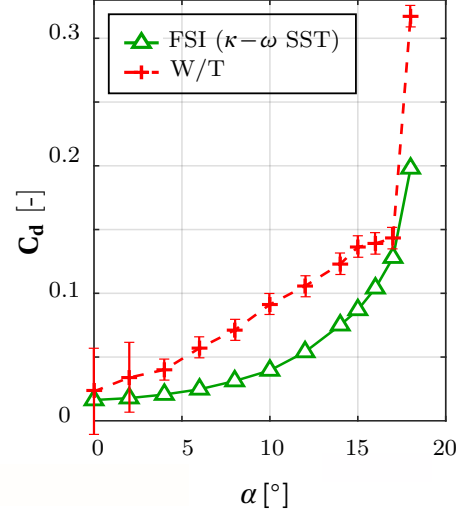
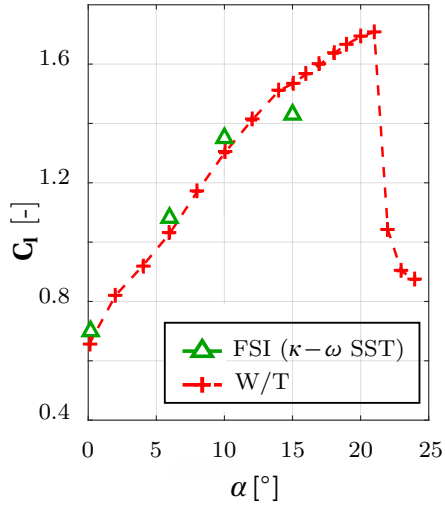
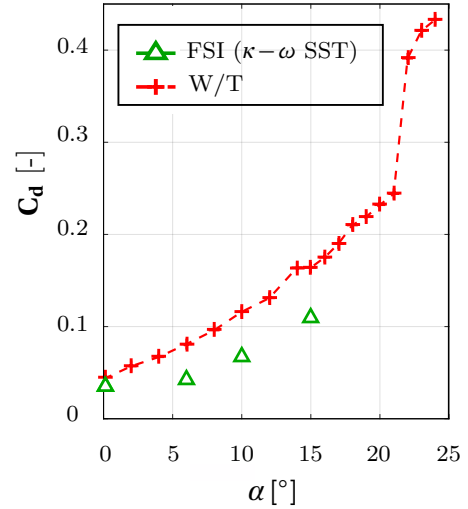

 (a) $q_\infty = 230$ Pa.

 (b) $q_\infty = 230$ Pa.

 (c) $q_\infty = 690$ Pa.

 (d) $q_\infty = 690$ Pa.

Figure 4.6: Comparison between FSI results and force measurement data: C_l - α and C_d - α curves at $q_\infty = 230$ and 690 Pa for the 2D and 2.5D WTB models.

slightly overestimated by the computations with a deviation under 6%. The overestimation results in higher C_l . Concerning C_d , it is underestimated by the computations as the group support/end-plates disturbs the measurements.

- **Results for $q_\infty = 690$ Pa:** the FSI computations estimate well the aerodynamic coefficients for $\alpha \leq 10^\circ$ and the membrane deflection is moderately overestimated. At $\alpha = 15^\circ$, C_l drops in the computations indicating that the flow separation started, whereas it is not the case in the wind tunnel. As the membrane deflection is overestimated by the FSI, one explanation is that the camber is too high in the computations and leads to a precipitation of the flow separation.

In general, the region of the wake is observed smaller in the measurements than in the computations. The latter is attributed to 3D effects during the wind tunnel campaign. Indeed, for further analysis, the induced angle β is measured behind the wing at a distance of one chord. The membrane deflection is measured as well on the upper surface of one half of the wing. The results are described in Figs. 4.7 and 4.8.

The induced angle β is depicted on Fig. 4.7 at $\alpha = 6^\circ$ for $q_\infty = 230$ and 690 Pa. At $q_\infty = 230$ Pa, the flow can be approximated by a 2D flow at $Y = 0$ as β is more or less homogeneous near the TE with Y . However, the measurements show clearly that 3D effects occur during the experiments at $q_\infty = 690$ Pa. β is not uniform any more with Y and obviously the end-plates influence the flow.

Concerning the membrane deflection measurement, it is easier to understand the parameter $\Delta Z(X, Y)$ defined in Sec. 2.2.2.3. Note that it corresponds to the difference between the deformed and the undeformed geometry at the respective X and Y coordinates. Near the LE and the TE, ΔZ narrows 0 as the membrane is hold by the two spars and follows their shape. The deflection occurs the most in the middle X -direction of the wing, and is expected uniform in the Y -direction.

The deflection is clearly not homogeneous in the wingspan at $\alpha = 6^\circ$ and $q_\infty = 690$ Pa (see Figs. 4.8). The end-plates disturb the flow on the wing and the membrane deflection along the wingspan. 3D effects influence the effective angle of attack, which explains why the wake and the membrane deflection are overestimated by the computations. The latter explains also why the flow stays attached longer and for higher α during the wind tunnel measurements.

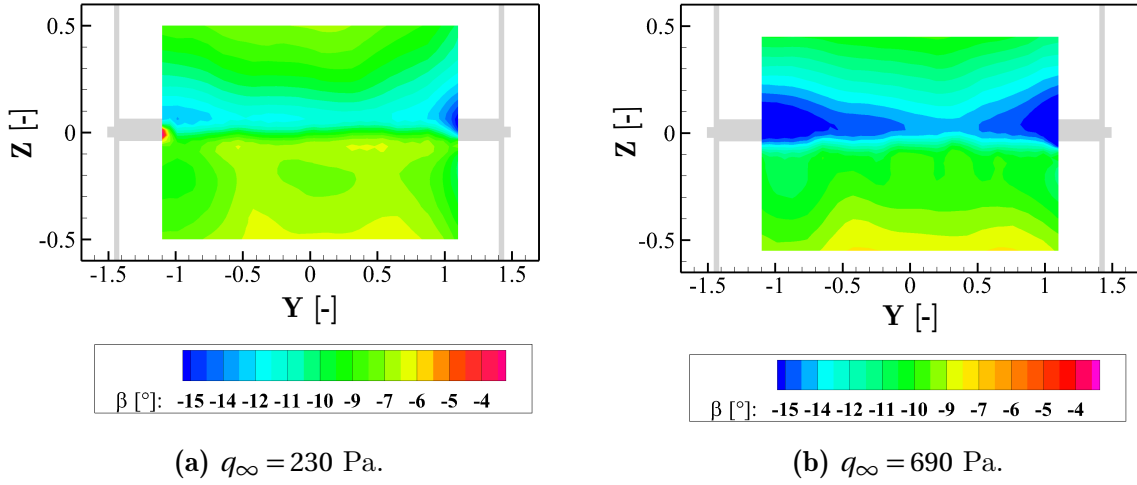


Figure 4.7: HWA measurement results: Downwash β [°] at $\alpha = 6^\circ$ behind the 2.5D WTB wing at $X = 1 \cdot c$.

4.2 2D WTA Model

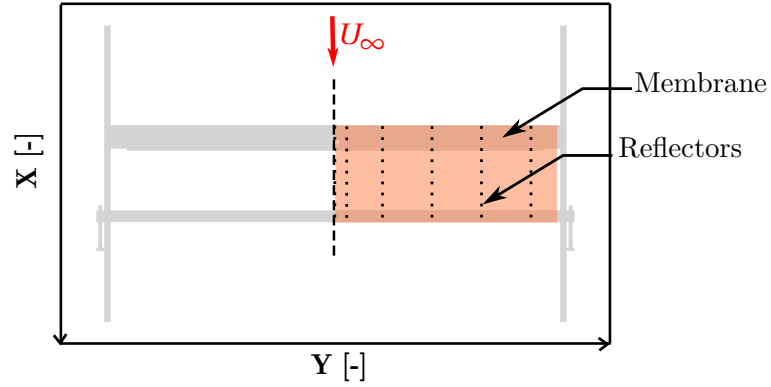
The comparison between FSI and experimental results are presented in the present section for the 2D WTA model. The 2D WTA model is introduced in Sections 3.2.1.1 and 3.4.1. The FSI computations are conducted for a two-dimensional flow within the coupling between the CFD solver TAU and the FEM solver Carat++. The results presented in this section are based on the presentation of Piquee et al. at the Applied Aerodynamics Conference 2018 (AIAA Aviation) [68].

4.2.1 Membrane Deflection

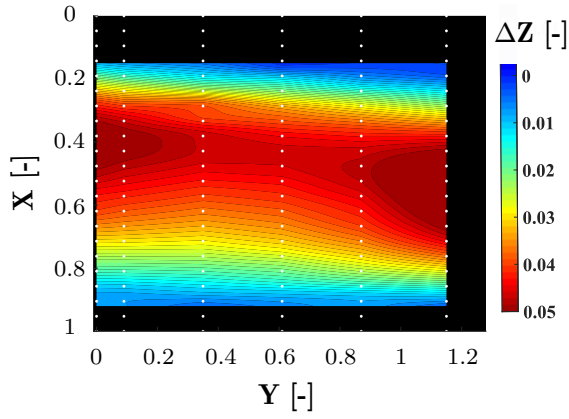
The membrane deflection is investigated for several α , namely 0° , 6° , 10° and 15° , at $q_\infty = 230$ Pa. Fig. 4.9 illustrates the comparison between the FSI results and the wind tunnel data. As previously, the experimental data is obtained for discrete points marked with red crosses (x). The norm error L2 is used to estimate the deviation.

At $\alpha = 0^\circ$, the norm error L2 is equal to 11% on the upper-side surface and 16% on the lower-side surface of the airfoil. It is observed that the FSI does not reproduce the membrane deflection to the positive z direction.

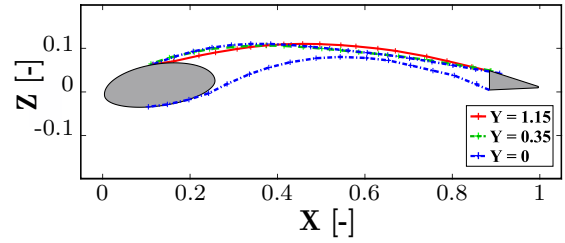
At $\alpha = 6^\circ$, the membrane deflection computed by the FSI is close to the experimental data. The norm error is equal to 7% on both the upper- and on the lower-side surfaces of the airfoil.



(a) Schema showing where the reflectors are placed on the upper side surface of the wing.



(b) $\alpha = 6^\circ$.



(c) $\alpha = 6^\circ$.

Figure 4.8: Photogrammetry measurement results for the 2.5D WTB model: the deflection was measured in the wingspan at $q_\infty = 690$ Pa. The variable ΔZ represents the difference between the deformed and the non-deformed geometry during the experiments.

At $\alpha = 10^\circ$ and 15° , the membrane deflection is overestimated by 17% and 22% on the upper-side surface of the airfoil, and by 8% and 12% for the lower-side surface, respectively. It is noticed that the membrane contour changes from a concave to a convex form near $X = 0.6$ at $\alpha = 10^\circ$, and $X = 0.4$ at $\alpha = 15^\circ$. The latter is related to the flow separation: the flow separation starts at the TE and is shifted to the LE of the wing with increasing α . When the flow is separated, the associated pressure is constant and lower than in a non separated flow. The membrane deflection becomes then lower and a change in the contour occurs (from a concave to a convex form). Chapter 6 gives more details about the change of contour on the upper side surface of the wing.

Regarding the present observations, it is assumed that the stall occurs for smaller angles of attack during the wind tunnel measurements in comparison to the FSI computations (cf. Section 4.2.3) and that a separated flow is expected at 15° for the wind tunnel data.

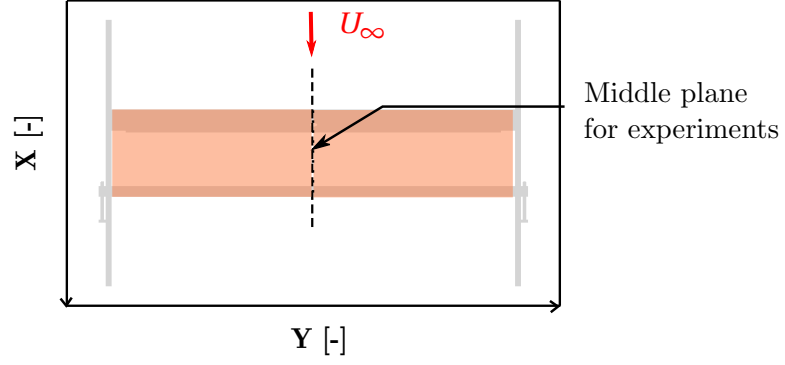
4.2.2 Flow Velocity Field

The flow field velocity is considered at $\alpha = 6^\circ$ and 15° for $q_\infty = 230$ Pa. u/U_∞ and w/U_∞ are depicted for the aforementioned α in Figs. 4.10 and 4.11. As previously, the velocity is measured in the middle of the wingspan, the region near the wing is not considered because of the safety distance between the sensor and the membrane, and only the velocity above the wing is measured.

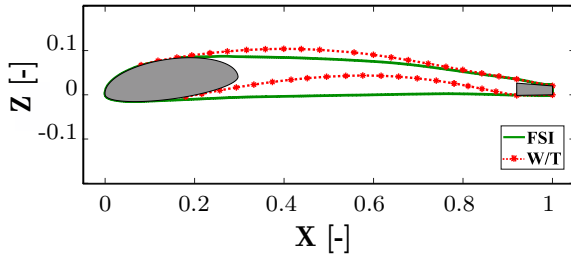
Generally, the predictions of the FSI are close the experimental data at $\alpha = 6^\circ$, whereas the deviations are bigger at 15° . However, for both α , the region of high u/U_∞ is predicted larger than in the wind tunnel experiments. At $\alpha = 6^\circ$, u/U_∞ is higher than 1.4 for $0 < X < 0.5$, whereas this region ends at $X \simeq 0.2$ during the experiments. The same phenomenon is noticed at $\alpha = 15^\circ$: u/U_∞ is predicted higher than 1.5 on the LE, whereas the maximum value is measured 1.4 in the wind tunnel.

Concerning w/U_∞ , the FSI computations predict more negative values in comparison to the wind tunnel tests. For both α , the FSI predict w/U_∞ reaching -0.3 over a large region above the wing, whereas w/U_∞ is observed mostly higher than -0.2 during the experiments.

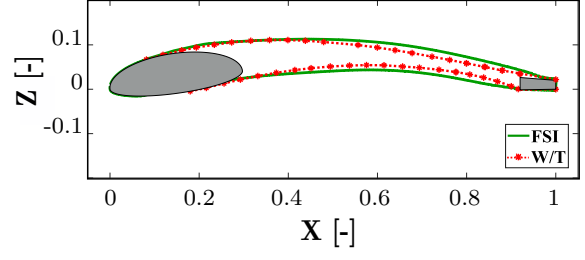
The same observations are commented in Sec. 4.1.2. As mentioned, a higher camber predicted by the FSI computations and 3D effects during the experiments can explain the deviations described at $\alpha = 6^\circ$ and 15° for $q_\infty = 230$ Pa.



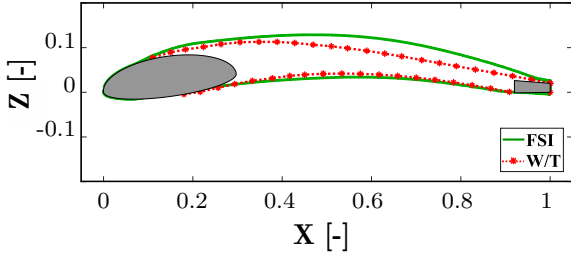
(a) Schema showing the plane where the experiments were conducted.



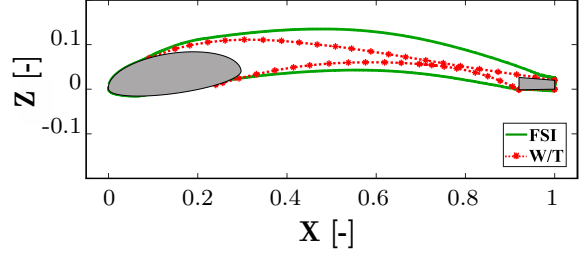
(b) $\alpha = 0^\circ$.



(c) $\alpha = 6^\circ$.

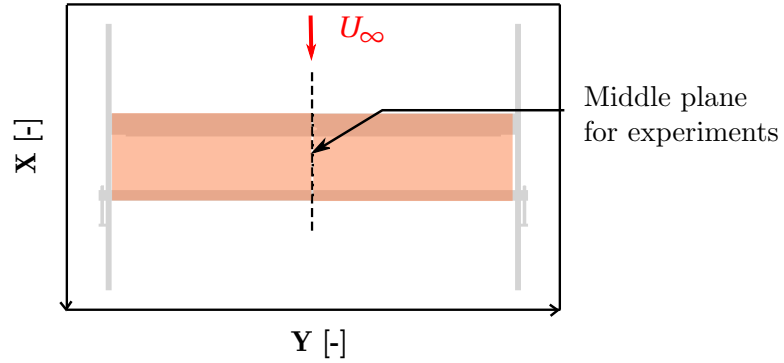


(d) $\alpha = 10^\circ$.

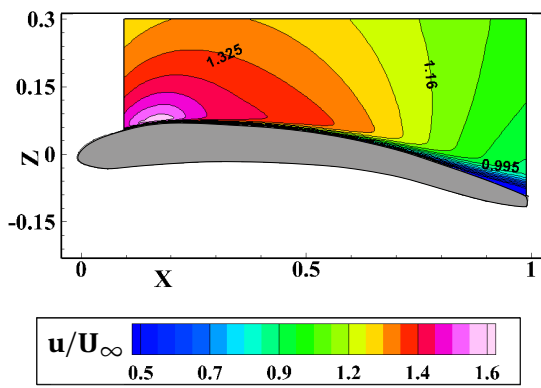


(e) $\alpha = 15^\circ$.

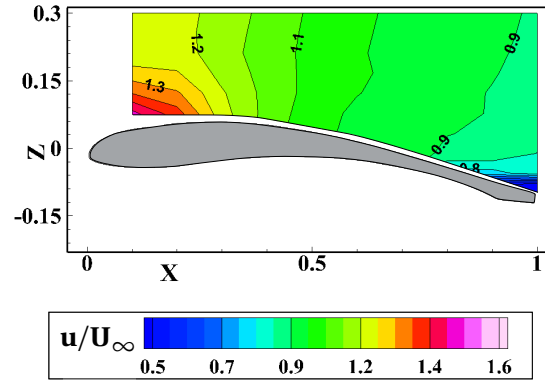
Figure 4.9: Comparison between FSI results and photogrammetry measurement data: Membrane deflection at $\alpha = 0^\circ, 6^\circ, 10^\circ$ and 15° at $q_\infty = 230$ Pa for the 2D and 2.5D WTA models. The deflection was measured in the middle of the wing span as shown in (a). (b)-(e) illustrate the deflection for the various α .



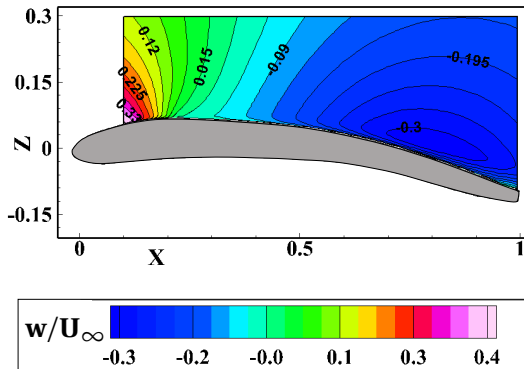
(a) Schema showing the plane where the experiments were conducted.



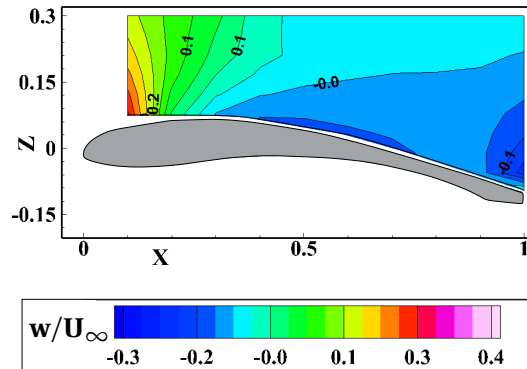
(b) FSI results, u/U_∞ .



(c) HWA measurements, u/U_∞ .



(d) FSI results, w/U_∞ .



(e) HWA measurements, w/U_∞ .

Figure 4.10: Comparison between FSI results and HWA data: Flow field velocity at $\alpha = 6^\circ$ at $q_\infty = 230$ Pa for the 2D and 2.5D WTA models. The velocity was measured in the middle of the wing span as shown in (a). (b)-(e) illustrate the two velocity components.

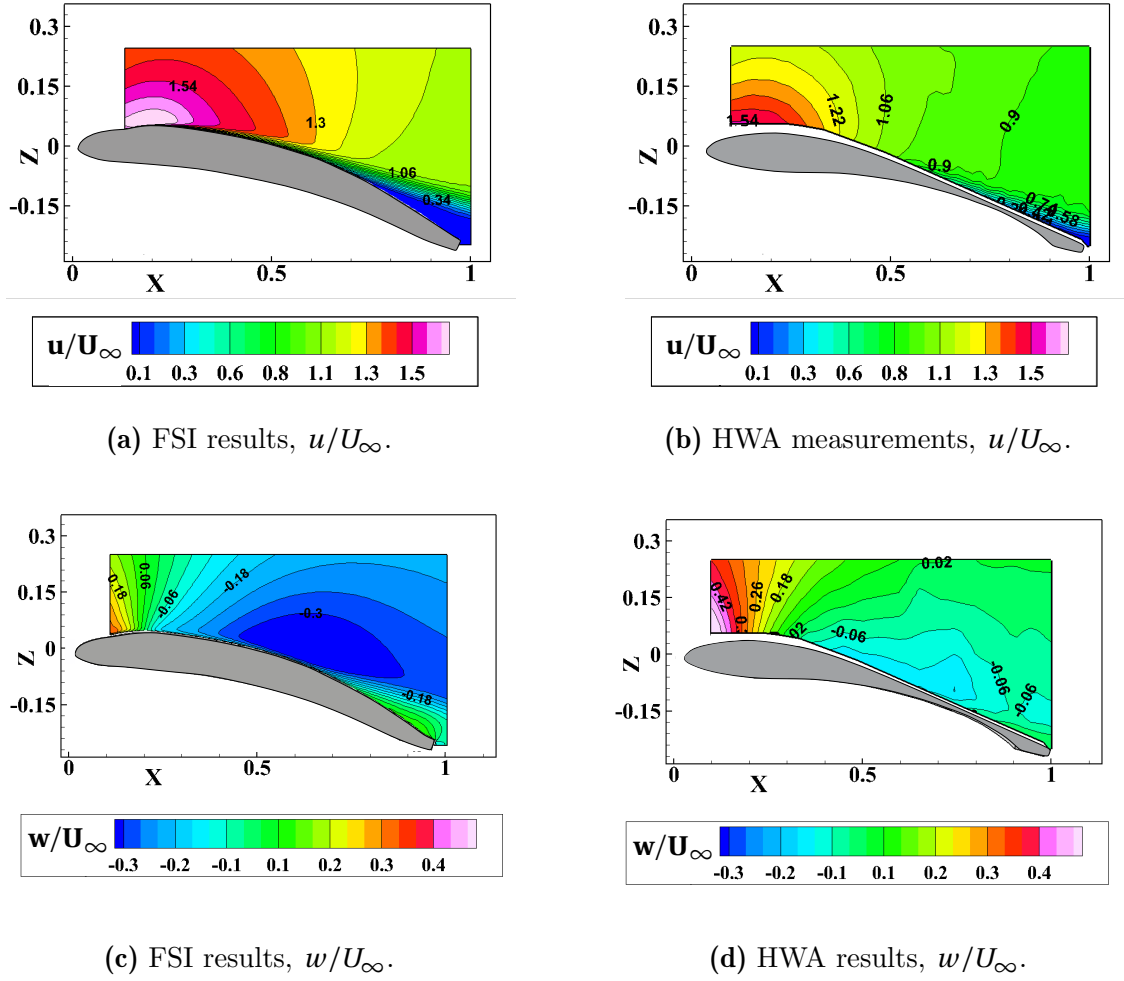


Figure 4.11: Comparison between FSI results and HWA data: Flow field velocity at $\alpha = 15^\circ$ at $q_\infty = 230$ Pa for the 2D and 2.5D WTA models. The velocity was measured in the middle of the wing span (see Fig. 4.10 (a)). (b)-(e) illustrate the two velocity components.

4.2.3 Lift and Drag

The aerodynamic forces are compared between the FSI computations and the experiments at various α , namely from -5° to 23° , for $q_\infty = 230$ Pa. Fig. 4.12 illustrates the curves C_l - and C_d over α . Like previously (Sec. 4.1.3), a hysteresis effect is observed during the measurements. This effect is reported on Fig. 4.12 with the error bars indicating the range of values obtained during the measurements. Afterwards, an average of C_l and C_d is calculated and plotted at each α .

At $\alpha = -5^\circ$, the FSI underestimate the wind tunnel data: they predict $C_l = -0.65$, whereas C_l is measured -0.23 .

At $\alpha = 0^\circ$, although Sec. 4.2.1 shows that the membrane deflection is not reproduced in the positive z -direction, C_l is well predicted in comparison with wind tunnel data. As the hysteresis effects are particularly intense around $\alpha = 0^\circ$, it is not clear how the FSI computations predict the state for this case.

At $\alpha = 6^\circ$, the membrane deflection and the flow field velocity are well approximated, which results in a good agreement in the C_l values.

For $\alpha \geq 10^\circ$, the computations overestimate C_l and the flow separation occurs at higher α ($\alpha \geq 17^\circ$ against $\alpha \geq 16^\circ$ in the wind tunnel). The latter was expected by analyzing the membrane deflection. Indeed, a change (from concave to convex) in the membrane contour is observed for $\alpha = 10^\circ$ and 15° in the experiments (cf. Sec. 5.1.2). This is related to the pressure distribution associated to a separated flow. On the curve C_l over α , it is noticed that $C_{l\alpha}$ starts decreasing at $\alpha = 10^\circ$, which is consistent with the flow separation hypothesis. The observations made for the membrane deflection (cf. Sec. 4.2.1) are congruent with the aerodynamic force results, namely the flow separation appears earlier, for smaller α , in the wind tunnel compared to the FSI computations.

Concerning C_d , the FSI computations predict well the values at small α , namely from -5° till 5° . For higher α , the value of C_d are higher during the experiments. However, as mentioned in Sec. 3.3, a dynamic calibration is performed in order to isolate the forces only acting on the wing. The drag of the group support/end-plates is found to be around 80% of the total drag of the complete model likewise for the 2D WTB model. The drag only acting on the wing is difficult to determine.

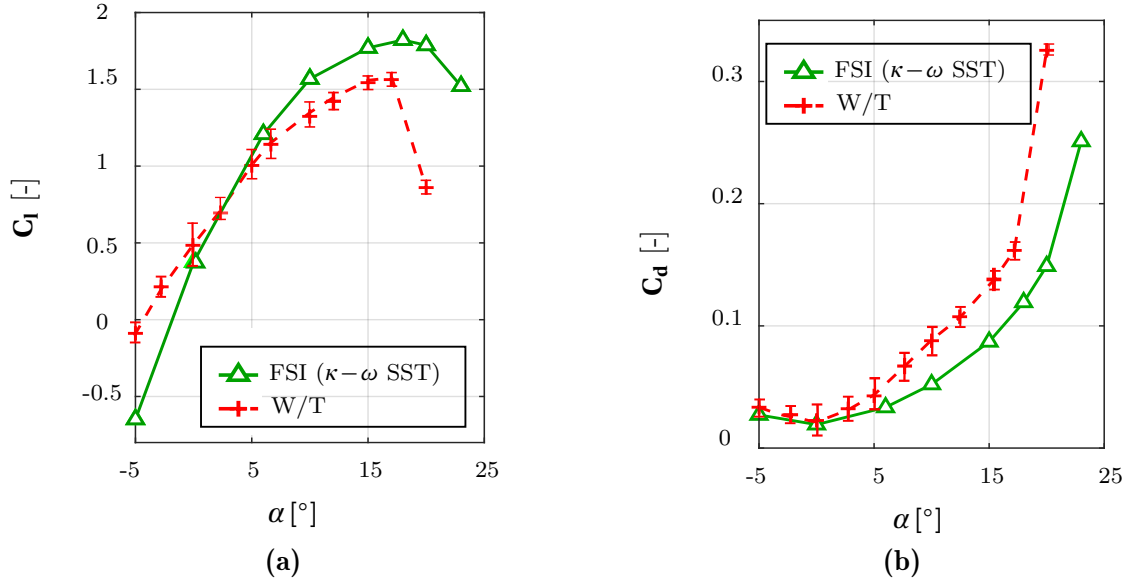


Figure 4.12: Comparison between FSI results and the force measurement data: C_l - α and C_d - α curves at $q_\infty = 230$ Pa for the 2D and 2.5D WTA models.

4.2.4 Summary and Experimental Consideration

The present section summarizes the comparison for the 2D WTA model and gives further considerations.

When the case $\alpha = 0^\circ$ is isolated, a fair agreement is found between the computations and the experimental data for small α (between $0^\circ < \alpha \leq 6^\circ$). C_l , C_d and the membrane deflection are well predicted although the flow velocity is slightly overestimated. Outer of the range $0^\circ < \alpha \leq 6^\circ$, the FSI computations overestimate the measurements.

In Sec. 4.1.3, 3D effects are noticed during the wind tunnel tests. It is also interesting to measure the deflection in the wingspan direction to obtain more information on the assumption of 2D flow features in the experiments of the 2D WTA model. The membrane deflection is measured a second time, but with a consideration in the entire wing (cf. Fig. 4.13 (a)), where several lines of reflectors are set in the wingspan direction. However, the region near the end-plates is not accessible because the end-plates made of Plexiglas[®] block the visibility of this region.

Fig. 4.13 shows ΔZ obtained in the wind tunnel on the upper side surface of the membrane for $\alpha = 0^\circ$, 5° and 10° at $q_\infty = 230$ Pa. Note that ΔZ is the difference between the deformed and the non-deformed geometry. It is directly proportional to the membrane deflection and mirrors its behavior. Near the LE and the TE, ΔZ narrows 0 as the membrane is hold by the two spars and

follows their shape. The deflection occurs the most in the middle of the X -direction of the wing, and is expected uniform in the Y -direction.

At $\alpha = 0^\circ$, it is noticed that ΔZ , i.e. the deflection, is not homogeneous in the Y -direction. Indeed, a maximal value of $\Delta Z = 0.03$ is only obtained in the middle left of the wingspan whereas $\Delta Z = 0.02$ in the other regions of the wing. The latter may explain why although the underestimation of the membrane deflection, C_l and C_d are still matching the wind tunnel data. The photogrammetry measurements from Sec. 4.2.1 are carried out in the middle plan of the wingspan ($Y = 0$). The deflection is at its highest in this region but it is not representative of the deflection on the entire wing. The resulting experimental C_l is then lower than expected.

For $\alpha = 5^\circ$ and 10° , the deflection is homogeneous in the Y -direction. The latter is consistent with the 2D flow assumption in the wind tunnel at the aforementioned α . Note that Sec. 4.2.1 shows a change of the membrane contour at $\alpha = 10^\circ$. As already mentioned, when the flow separates, the associated pressure is lower than in a non-separated flow, resulting in a lower deflection and a change in the membrane profile. In the results of the deflection on the entire wing, ΔZ reaches higher values and $X_{Z_{max}}$ is more downstream at $\alpha = 5^\circ$ compared to $\alpha = 10^\circ$. This is congruent with the progression of the flow separation assumption. The flow starts separating at the TE and is shifted towards the LE with increasing α , resulting in the observations commented previously.

It has to be mentioned that the pre-stress of the membrane is changed in the computations. Indeed, the first set of FSI computations performed with the pre-stress assumed in the experiments (cf. Sec. 3) leads to too small membrane deflections. Therefore, an adjusted pre-stress is utilized based on a Python script evaluating the pre-stress of the experiments. The several steps are the followings: the measured deflection obtained from the wind tunnel data is transformed as a CFD geometry to calculate the pressure distribution on the airfoil. Then, this pressure, the E -modulus and the Poisson coefficient ν_s of the membrane are exploited on the non-deformed geometry to test several pre-stresses. The tests end when the computed deflection matches the experimental data. The new pre-stress is used to compute the data presented in the present chapter. The new pre-stress is found lower than the one calculated in Sec. 3.

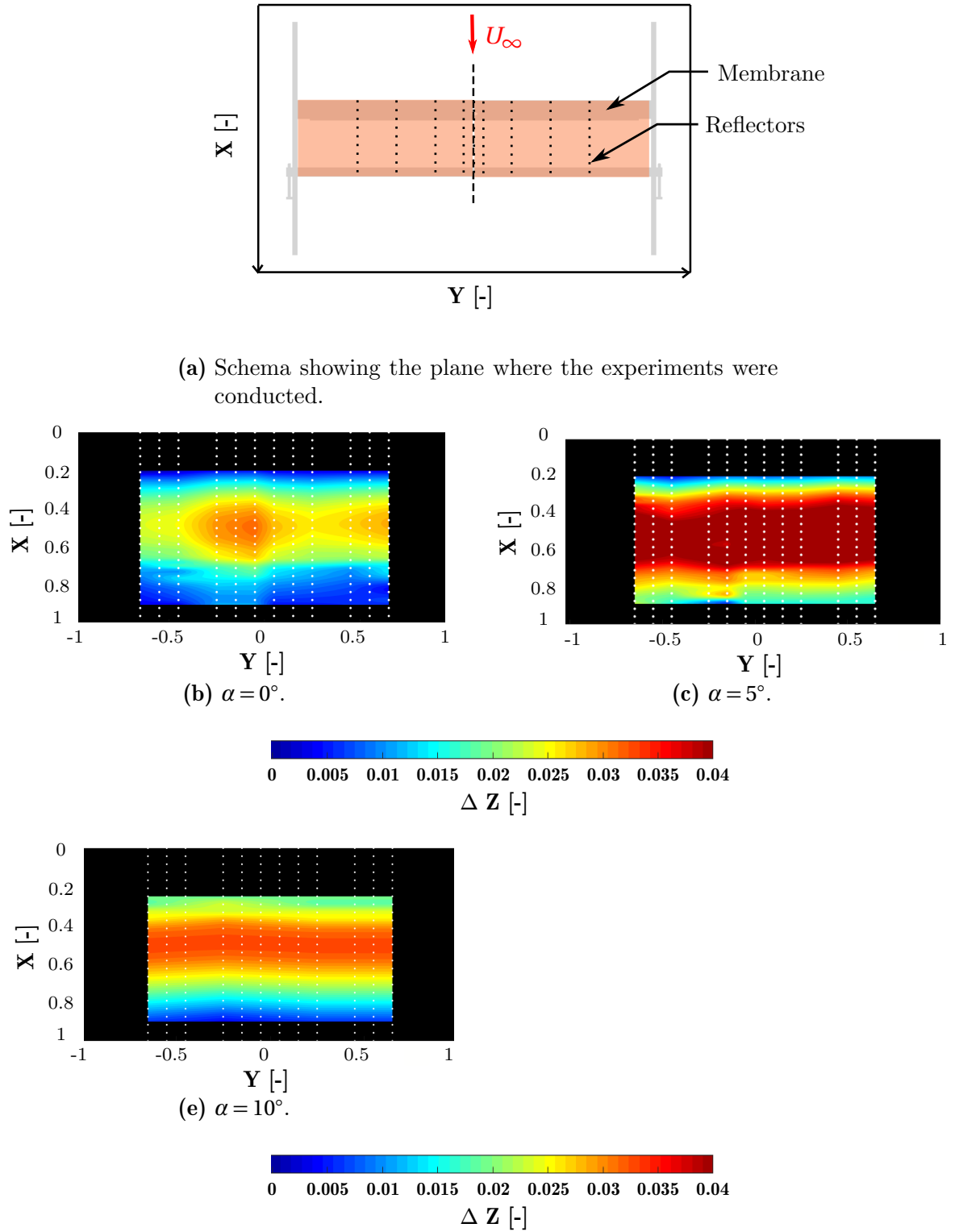


Figure 4.13: Photogrammetry measurement results for the 2.5D WTA model: the deflection was measured in the wingspan at $q_\infty = 230$ Pa. The variable ΔZ represents the difference between the geometry during the experiments and the undeformed one.

Chapter 5 - Aeroelastic Behavior of a Membrane Airfoil

The present chapter describes and explains the typical aerodynamic characteristics of an elasto-flexible membrane concept by studying the forces, the pressure distribution and the membrane deflection obtained by fluid structure interaction analysis. The FSI analysis are performed on the 2D WTB and the 2D WTA models analyzed in Chapter 4, as the accuracy of the computations is evaluated. The FSI results are compared to data for a rigid case to better understand the advantages of the flexibility and adaptivity brought by a membrane on an airfoil. The data for a rigid case is computed with the same fluid model and the same geometry as the fluid structure interaction but without any coupling to a FEM solver. They are characterized as rigid as they can be correlated to a wing using a membrane having an infinite stiffness. Then, the influence of various parameters is investigated to enlarge the panel of knowledge about the aerodynamics of an elasto-flexible membrane concept.

5.1 Baseline

The following section illustrates the characteristics of an elasto-flexible membrane geometry based on FSI results obtained for both the numerical 2D WTB and 2D WTA models. The section is entitled as baseline because the explanations given are meant to describe the typical aerodynamic behavior of the flexible membrane airfoil and serves as basis for Secs. 5.2 and 6.1.

5.1.1 Aerodynamic Forces

The graphs in Fig. 5.1 presents C_l and C_d over α for a flexible geometry and its rigid counterpart obtained by FSI and CFD computations. The computations are performed for a dynamic pressure of $q_\infty = 230$ Pa. The benefits of a flexible geometry can be drawn by comparing the aerodynamic polars between the two configurations, as the following:

- The absolute value of C_l is generally higher for the flexible geometry compared to its rigid counterpart. The flexibility and adaptivity of the membrane allow a deflection of the material, permitting a change in the airfoil's camber. For $\alpha = -5^\circ$, a deflection is created to the negative z -axis direction, whereas when $\alpha > 0^\circ$ a deflection is created to the positive z -axis direction. In both cases, the camber is amplified compared to the camber of the rigid geometry. A camber accentuated in the negative z -axis leads to smaller C_l , whereas a camber accentuated in the positive z -axis leads to higher C_l .
- For $\alpha > 10^\circ$, the flow separation starts as $C_{l\alpha}$ decreases (see Fig. 5.2). The stall of the rigid airfoil occurs abruptly at $\alpha = 15^\circ$, whereas the stall of the flexible geometry occurs smoothly between $\alpha = 15^\circ - 23^\circ$. In fact, as $C_{l\alpha}$ becomes shallower, C_l remains in the same range until $\alpha = 20^\circ$ ($C_l \simeq 1.7 - 1.8$) and then decreases. The onset of stall is delayed to higher angles of attack, while the abrupt decrease of C_l evolves in a gradual one. The latter has to be related to the shift of the separation point from the TE towards the LE (cf. Sec. 5.1.2).
- While the adaptivity of the membrane postpones the stall to higher angles of attack and changes the abruptness behavior of the stall, it leads to an increase in C_d in the linear range of C_d over α ($\alpha < 15^\circ$). For $\alpha > 15^\circ$, the inverse occurs: C_d becomes lower for the flexible geometry than for the rigid one.

The polars illustrate the capacity of the flexibility and adaptivity of the membrane to delay and mitigate the onset of stall shifting it to higher angles of attack. Furthermore, it shows that in terms of passive flow control, the flexible concept can offer a better C_l/C_d in the stall region.

5.1.2 Pressure Distribution

In order to understand the evolution of C_l and C_d with α summarized in the previous section, the pressure distribution on the airfoil has to be considered. Fig. 5.2 shows $-C_p$ on the upper- and the lower-side surfaces of the airfoil at various α for the flexible and the rigid geometries. The following has to be commented:

- The CFD data shows that the suction peak present on the upper-side surface of the rigid airfoil is composed of a plateau followed by an abrupt decrease of $-C_p$ at $X \approx 0.1$. This is related to the geometry of the airfoil. The decrease appears at the abscissa where the slope of the profile's curve $\frac{dZ(X)}{dX}$ changes its sign ($X \approx 0.1$). For the flexible concept, as the membrane deflects to positive

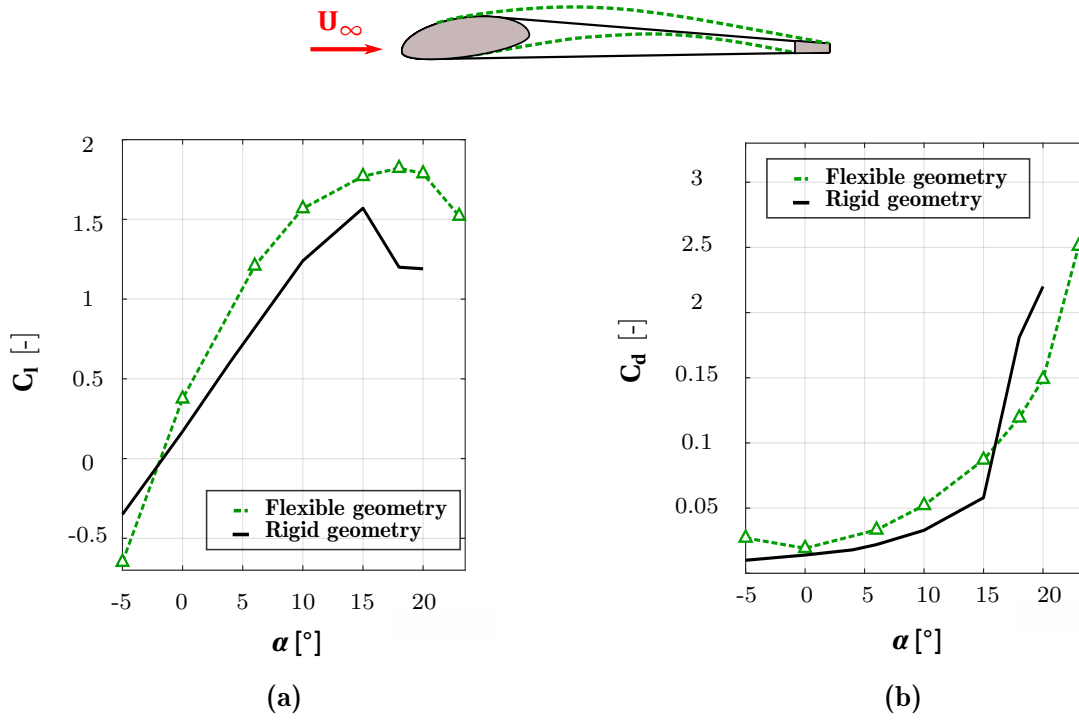


Figure 5.1: Comparison between flexible and rigid geometries: C_l - α and C_d - α curves at $q_\infty = 230$ Pa.

z-direction, the mentioned abscissa is downstream. It enables the flow to accelerate over a wider region of the wing inducing a higher $-C_p$ on a larger region and consequently a higher C_l .

- For the two concepts, the flow starts to separate at the TE. Indeed, the region on the upper-side surface of the wing where $-C_p$ is constant indicates a separated flow. Then, the abscissa where the flow separates (X_{sep}) moves upstream with increasing α for the two concepts. However, the shift of X_{sep} evolves slower for the flexible- than for the rigid geometry. The latter is due to the flexibility of the membrane. At $\alpha = 14^\circ$, the flow separates at $X = 0.2$ on the rigid airfoil whereas it occurs at $X = 0.5$ on the flexible geometry: around 80% of the flow is separated on the rigid airfoil, whereas only 50% of the flow is separated on the flexible geometry. The last observation is consistent with Fig. 5.1 indicating that the complete separation occurs after 15° for the rigid airfoil, whereas it occurs to higher α for the flexible geometry. Between $\alpha = 12^\circ - 18^\circ$, as X_{sep} moves slowly upstream from $X = 0.6$ to 0.1 , there is a delay in the onset of stall to higher α and a smooth evolution of C_l between $15^\circ - 20^\circ$ before C_l drops.

The progression of X_{sep} from the TE to the LE has to be connected to Sec. 4.1.1. The position of X_{Zmax} moves upstream to the LE with α because of the progression of the flow separation.

When the flow separates, $-C_p$ is not favorable on the wing and the membrane deflection decreases resulting in a change of curvature (from concave to convex) and a shift of X_{Zmax} upstream.

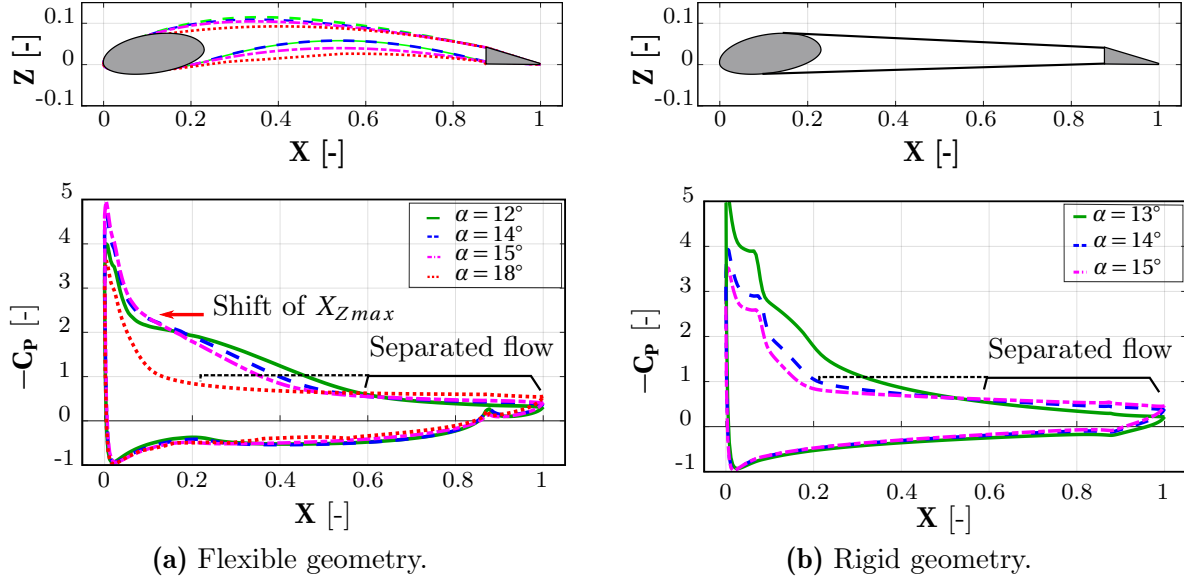


Figure 5.2: Comparison between flexible and rigid geometries: $-C_p$ distribution on the airfoil and the associated geometry at $q_\infty = 230$ Pa.

5.1.3 Membrane Deflection

The membrane deflection is associated to the pressure distribution. The membrane deflection is showed in Fig. 5.3 at various α . As observed in the previous chapter, the deflection is more intense at $q_\infty = 690$ Pa than at $q_\infty = 230$ Pa. Therefore, the explanations are given for $q_\infty = 690$ Pa. They can be summarized as the following:

- At $\alpha = 0^\circ$, a membrane deflection is observed in the positive direction of z -axis. Indeed, the geometry of the LE being rotated of 8° with the horizontal line, $C_{l,\alpha=0} \geq 0$ also without any membrane influence. The membrane induces an accentuation of the camber, resulting, for the aforementioned α in $C_{l,flexible} \geq C_{l,rigid}$.
- For increasing values of α , the membrane deflection increases as well, as consequence of the increase of the suction peak on the upper-side membrane surface. In Fig. 5.3, it is also observed that X_{Zmax} moves upstream to the LE for increasing values of α due to the progression of the flow separation to the LE. Furthermore, when the flow separation occurs,

the pressure gradient is less favorable for the deflection, explaining why the deflection is lower at $\alpha = 15^\circ$ than at $\alpha = 0^\circ, 5^\circ$ and 10° (cf. Fig. 5.3).

The adaptivity and flexibility of the membrane produce an accentuation of the airfoil's camber. In this case, as the flow separation starts at the TE and moves towards the LE for increasing α , X_{Zmax} moves to the LE till the deflection becomes lower ($\alpha = 15^\circ$).

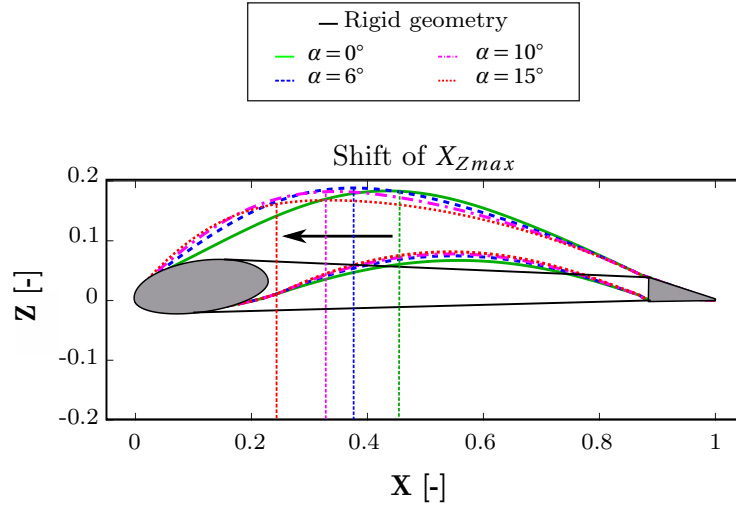


Figure 5.3: Comparison between flexible and rigid geometries: Geometry of the airfoil at $q_\infty = 690$ Pa.

5.2 Parameters Dependency Analysis

The present section gives an analysis of the influence of various important parameters on the aerodynamic behavior of an elasto-flexible membrane wing concept. The section has to be connected to the explanations from Section 5.1, whose purpose is to show the typical aerodynamic behavior of the concept. In the following section, three variables are varied, namely the dynamic pressure q_∞ , the turbulence model used in the FSI computations and gust conditions.

5.2.1 Influence of the Dynamic Pressure

The influence of q_∞ was already experimentally investigated by Béguin [18]. A brief review of the results found in [18] is given in order to understand whether the FSI computations performed in the present thesis generate reasonable results.

Note that the experimental model tested by Beguin in [18], is a half-model three-dimensional-tapered wing. It is found that the aerodynamic characteristics, namely the lift and the drag coefficients, have a pronounced dependency on q_∞ (cf. [18], Chapter 4). When q_∞ increases, the lift curves get steeper and non-linear as a results of the membrane deflection. Indeed, the camber increases resulting in the following: for positive angles of attack, the camber is accentuated in the positive z -direction causing higher lift with higher q_∞ , whereas for negative angles of attack, the camber is accentuated in the negative z -direction causing higher negative lift. Furthermore, the stall occurs more smoothly when q_∞ increases, due to the passive adaption of the membrane to the flow (cf. [18], Chapter 4).

In order to evaluate the effect of q_∞ on the aerodynamic behavior of a flexible membrane wing, several FSI computations are performed on the numerical 2D WTB model. Three q_∞ , namely $q_\infty = 230, 400$ and 690 Pa, are investigated at various α . The results are described by Fig. 5.5, where the evolution of C_l and C_d are depicted with α .

As expected, the polars show a pronounced dependency on q_∞ . If the curve C_l over α is considered at $q_\infty = 230$ Pa, C_l is linear from 0° to 8° . Afterwards, the flow starts separating being observed with a decrease of $C_{l,\alpha}$. For higher q_∞ , the slope $C_{l,\alpha}$ gets steeper for small α (for $q_\infty = 400$ Pa around $\alpha < 4^\circ - 6^\circ$, and for $q_\infty = 690$ Pa around $\alpha < 2^\circ - 4^\circ$), and afterwards becomes non-linear. The two comments are congruent with the results found in [18]. However, a main difference is observed. In [18], $C_{l,\alpha}$ increases with q_∞ for $0^\circ \leq \alpha \leq 30^\circ$, whereas in the present thesis, this phenomenon is only observed between the data at $q_\infty = 230$ and 400 Pa for $\alpha \leq 6^\circ$. Otherwise, $C_{l,\alpha}$ gets smaller when q_∞ increases. The latter is due to the flow separation. Indeed, one observation is unchanged between the present thesis and the results in [18], namely the membrane deflection becomes higher with q_∞ . But, the membrane deflection obtained in the present thesis by the FSI computations gets extremely high with increased q_∞ , which precipitates the flow separation unlike in [18]. The distribution of $-C_p$ is illustrated for various α in Fig. 5.4. At $\alpha = 8^\circ$ and $q_\infty = 400$ Pa, the flow separation occurs at $X = 0.63$, whereas it already occurs at $X = 0.5$ for $q_\infty = 690$ Pa, explaining why $C_{l,\alpha}$ gets smaller when q_∞ increases for high α .

Another phenomenon is consistent with [18]. The stall is smoother when q_∞ increases. This is the result of the smoother evolution of the onset of the separated flow towards the LE. The latter is illustrated in Fig. 5.4. At $\alpha = 8^\circ$, the flow starts separating at $X = 0.63$ for $q_\infty = 400$ Pa, whereas it already occurs at $X = 0.5$ for $q_\infty = 690$ Pa. At $\alpha = 15^\circ$, the flow separation occurs at $X = 0.4$ for

$q_\infty = 400$ Pa and for $q_\infty = 690$ Pa. The shift of X_{sep} to the LE develops smoother for $q_\infty = 690$ Pa, which results in a delay of the complete flow separation to higher α .

The smooth evolution with increasing q_∞ is further observed on Fig. 5.6 (a), where the evolution of the maximal camber f/c is plotted with α .

- On the one hand, f/c achieves higher values when q_∞ increases, expressing higher camber due to a higher suction peak.
- On the other hand, for all q_∞ , f/c increases for small α ($< 10^\circ$) and then decreases but with a different intensity: f/c evolves more gradually at $q_\infty = 690$ Pa than at 230 Pa. The increasing suction peak with q_∞ induces higher f/c till the flow separation occurs. When the flow separates, the pressure is less favorable inducing a decrease in f/c . But the progression of X_{sep} towards the LE, as shown previously, develops more progressively with high q_∞ .

Finally, a last remark has to be made concerning the evolution of the abscissa X_{Zmax} . In section 5.1.3, an explanation was found for the progression of X_{Zmax} to the LE when α increases. The results are supported with Fig. 5.6 (b). From 0° to 15° X_{Zmax} evolves downstream related to the shift of the flow separation to the LE. For higher α , X_{Zmax} is in the middle of the wing, as the flow being completely separated on the wing causes a less favorable pressure for the membrane deflection.

Concerning the drag of the wing, it is also profoundly dependent on q_∞ . Before the complete flow separation, C_d is higher when q_∞ is higher. Afterwards, the tendency is reversed, C_d becomes smaller for higher q_∞ . This phenomenon is also observed in [18]. Regarding the efficiency, the curve C_l with C_d shows that the flexible membrane wing concept has a better efficiency for low q_∞ . However, this is due to the precipitated flow separation on the wing. For a full model, it is expected that the flow separation appears at higher α , which suggest that the efficiency would increase with q_∞ (cf. Chapter 6).

The observations indicate that the aerodynamic behavior of a flexible membrane wing is deeply influenced by q_∞ . Higher q_∞ induces more accentuated membrane deflection, which is directly associated to a variation in the forces. Furthermore, the observations suggest a passive flow control in the stall region of the wing. The membrane passively adapts to the flow and induces a gradual evolution of the onset of stall. The membrane acts like a natural flow control system with q_∞ .

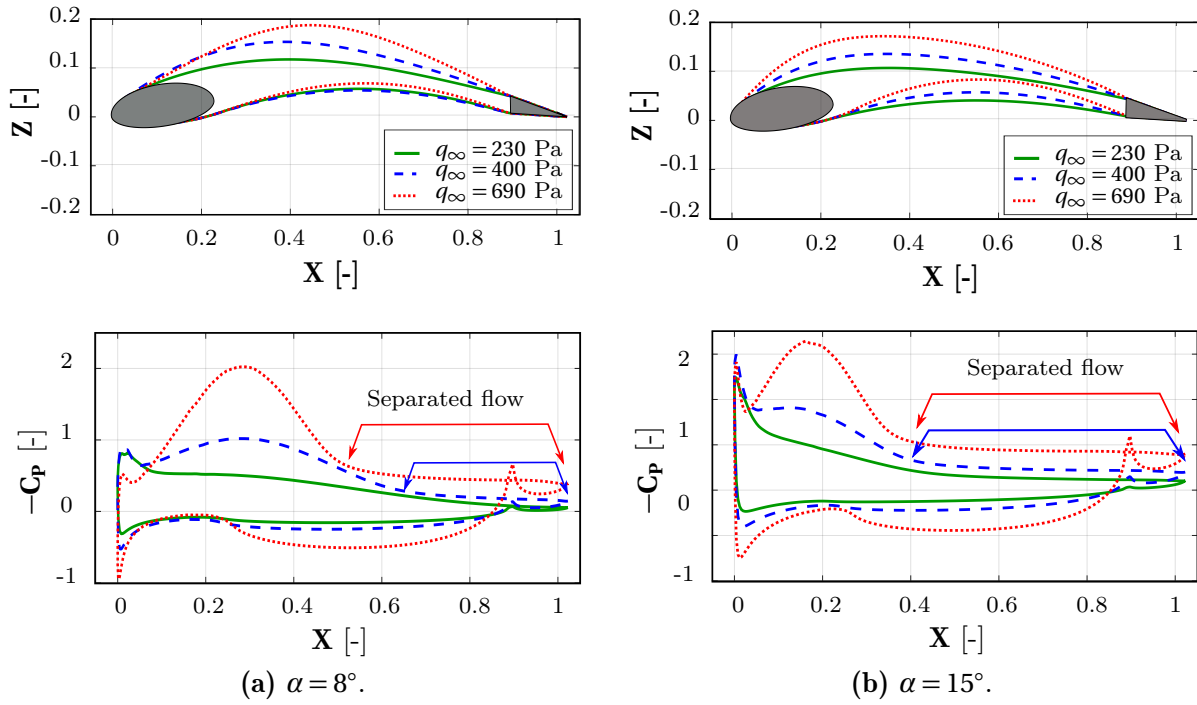


Figure 5.4: Comparison between FSI results: Membrane deflection and pressure distribution at $\alpha = 8^\circ$ and 15° at $q_\infty = 230$ Pa, 400 Pa and 690 Pa.

5.2.2 Influence of the Turbulence Model

The turbulence model has a significant impact on the numerical flow modeling. It affects the pressure distribution on the wing, which alters the aerodynamic properties. The effects of the boundary layer were already observed on a flexible membrane wing by Béguin [18], where free transition and forced transition were experimentally investigated. In the present thesis, it is noticed that the operative Re for the 2.5D WTB model is equal to 280,000. At this condition, an estimation of the relative percentage of laminar flow can be done following empirical correlations presented in [61]. The percentage of laminar flow is estimated to be more than 5% of the chord length of the 2.5D WTB model. Therefore, FSI computations taking into account the laminar-turbulent transition in the boundary layer are conducted on the numerical 2D WTB model. The laminar-turbulent transition is modeled with the $\gamma - Re_\theta$ transition model coupled to the $\kappa - \omega$ SST model [64, 54]. The following section shows the influence of the laminar-turbulent transition on the aerodynamics of a flexible membrane airfoil by comparing the FSI results obtained for two flow models, namely the $\gamma - Re_\theta$ transition model coupled to the $\kappa - \omega$ SST model and the $\kappa - \omega$ SST model for the fully turbulent flow.

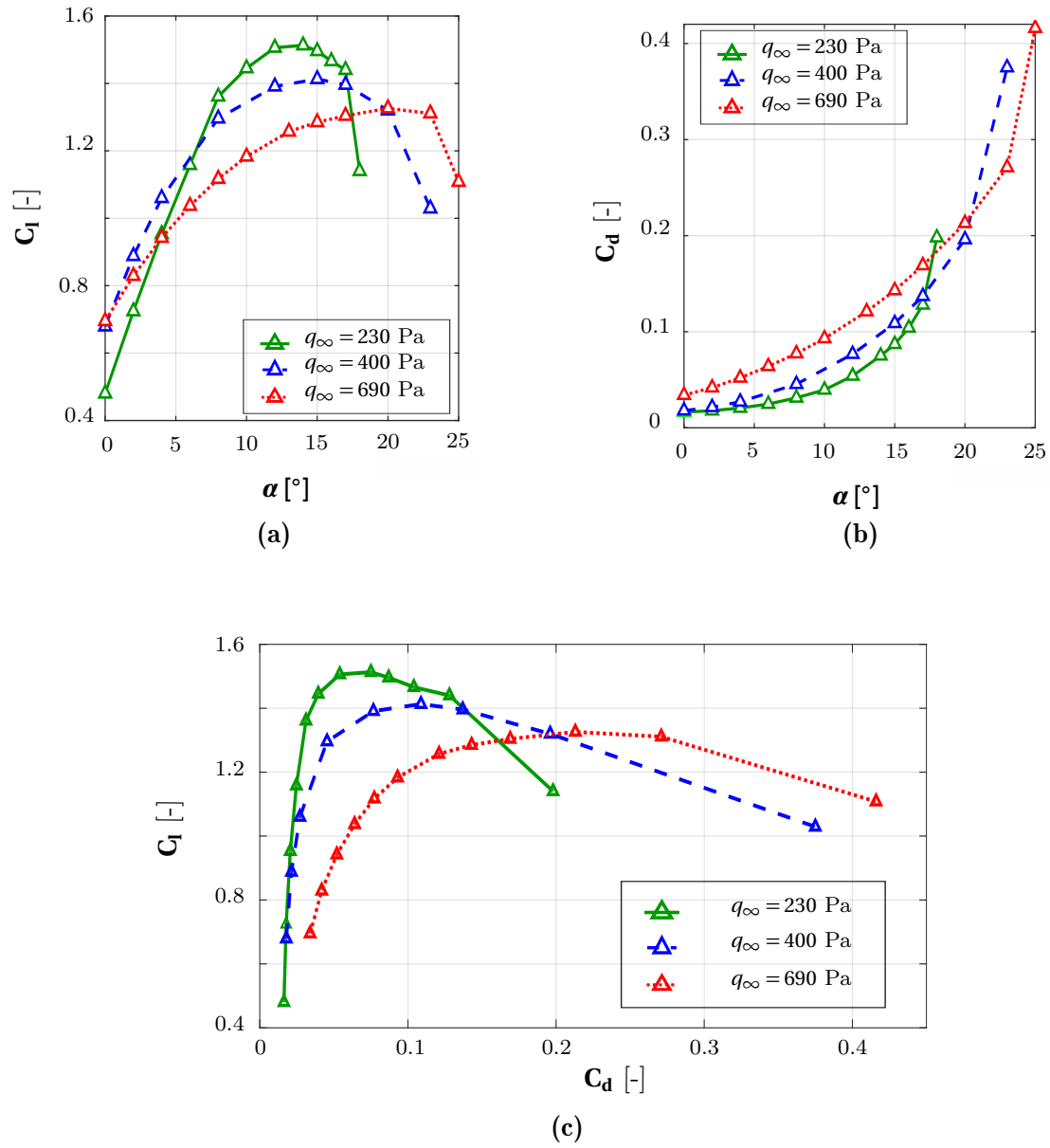


Figure 5.5: Comparison between FSI results: C_l - α , C_d - α and C_l - C_d at $q_\infty = 230$ Pa, 400 Pa and 690 Pa.

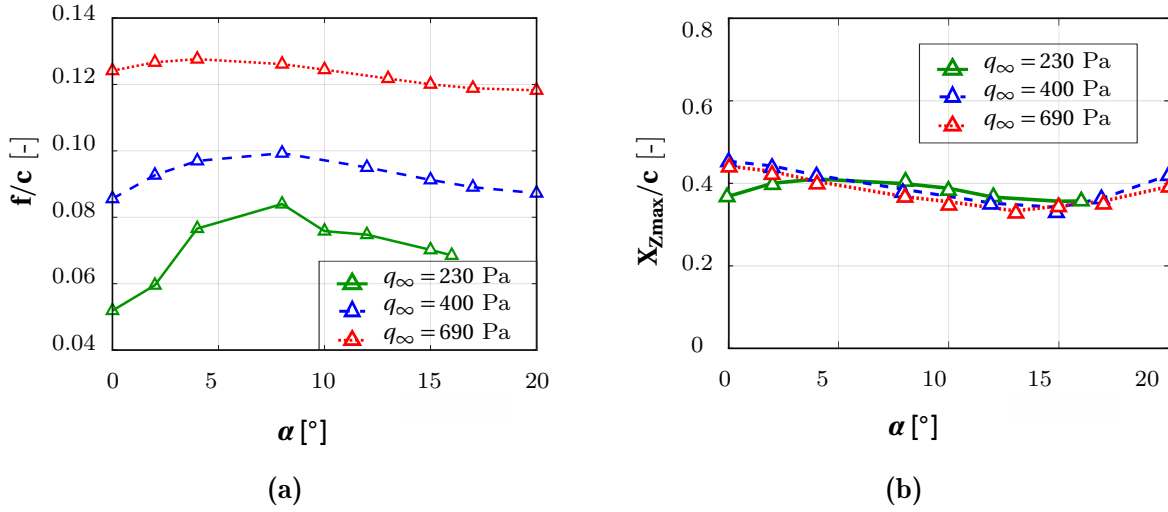


Figure 5.6: Comparison between FSI results: Evolution of the maximal camber f/c - α and X_{Zmax} - α at $q_\infty = 230$ Pa, 400 Pa and 690 Pa.

Note that the analysis in [18] is performed experimentally by using a half-model three-dimensional-tapered wing and numerically by using a coupling between an analytical formulation of the membrane equilibrium and the viscous/inviscid flow solver XFOIL (cf. [18] Chapter 4). The results show that the transition on the wing is caused by a laminar separation bubble, which is very sensitive to α and q_∞ . The transition takes place for small α , namely $\alpha \leq 10^\circ$, and causes a higher pressure distribution on the wing. Therefore, when transition takes place, the lift curve is steeper resulting in higher C_l . Then for $\alpha \geq 10^\circ$, the lift is similar for the free-transition and the forced-transition cases. Finally, the stall appears at higher α in a free-transition case compared to in a forced-transition. The geometry considered in this thesis is slightly different from the airfoil geometry used in [18], but similar results are expected.

In Fig. 5.7, C_l - and C_d over α are depicted for the $\gamma-Re_\theta$ transition model coupled to the $\kappa-\omega$ SST model and the $\kappa-\omega$ SST model at $q_\infty = 230$ Pa. Two significant comments can be made.

- Before the complete flow separation: between $0^\circ \leq \alpha \leq 12^\circ$, $C_{l\alpha}$ is steeper for the flow computed with the transition model than for the flow computed without transition modeling. This results in C_l being higher when the transition is considered. For $12^\circ \leq \alpha \leq 15^\circ$, the two curves are quite similar showing that the two models compute similar C_l . Both observations are consistent with the results of [18]. If C_d is considered, the two models compute similar values.
- After the complete flow separation: the onset of stall is shifted to higher α for the flow

computed without transition modeling, which differs from [18]. C_d is higher for the transition model.

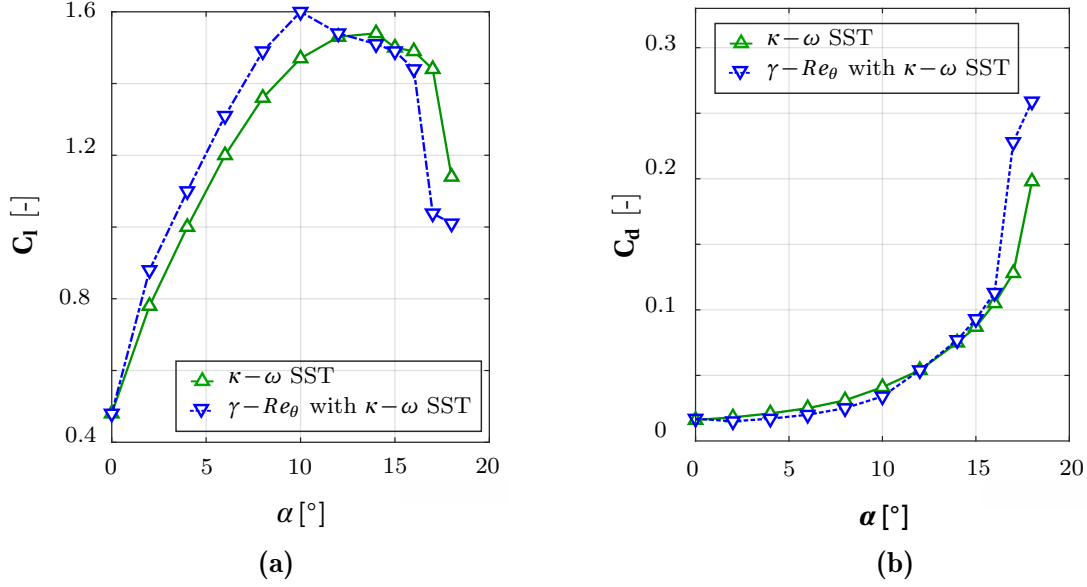


Figure 5.7: Comparison between FSI results: C_l - α and C_d - α curves at $q_\infty = 230$ Pa for two fluid models.

To explain the differences induced by the transition, the polars have to be correlated with the pressure distribution on the airfoil. The membrane deflection and the associated $-C_p$ are plotted in Figs. 5.8 and 5.9 at various α . The following can be commented:

- At $\alpha = 0^\circ$, the pressure distribution on the membrane is the same for the two flow models. This explains the similar C_l and C_d observed in the C_l - and C_d over α curves.
- At $\alpha = 6^\circ$ and 10° , the pressure distributions show that the suction is higher for the transition model on the upper-surface side of the wing. This explains why C_l is higher in a flow computed with the consideration of the transition (Fig. 5.7). For the aforementioned α , Figs. 5.9 illustrates a region ($0.4 < X < 0.6$) where $-C_p$ undergoes a plateau for the flow computed with the transition model. This is a characteristic of a laminar separation bubble. The laminar-turbulent transition for the present geometry is caused by a laminar separation bubble located on the upper-surface side of the wing like in [18]. An analysis of the friction coefficient (C_f) confirms the location of the transition bubble (see Fig. 5.9) and shows also a reattachment of a turbulent boundary layer. The laminar-turbulent transition can be observed on Figs. 5.10, 5.11 and 5.12 as well, where the turbulent intensity (Tu) is depicted

with an increasing α . At $\alpha = 6^\circ$, the turbulent boundary layer can be observed to start at $X = 0.55$ whereas at $\alpha = 10^\circ$, it starts at $X = 0.45$.

- At $\alpha = 15^\circ$, the pressure distribution on the membrane is the same for the two flow models and no laminar separation bubble can be observed. The boundary layers computed for both models appear to have the same nature (see Fig. 5.12). The latter explains the similar C_l for the two models observed in the C_l - α curve.
- For $\alpha \geq 16^\circ$, the shift of the onset of stall to higher α can be explained because the velocity gradient is steeper in a turbulent boundary layer.

The transition, in this case, is due to a laminar separation bubble, which is sensitive to α and more precisely to the suction peak at the LE. The laminar separation bubble is present between $\alpha = 2^\circ - 12^\circ$ and induces a higher suction on the upper-side surface of the airfoil compared to the results obtained with the fully turbulent computations. The latter results in higher values of C_l as seen in Fig. 5.7. It is observed as well that the separation bubble migrates upstream to the LE when α increases. When the separation bubble is located at the LE, the two models compute the same pressure distribution resulting in the same C_l . Finally, the complete separation appears for higher α for the fluid computed without the transition modeling.

5.2.3 Influence of Gust Conditions

As shown in section 5.1, the flexibility and adaptivity of the membrane permits to shift the stall to higher angles of attack and to mitigate it. An interesting topic results from the latter conclusion questioning whether an elasto-flexible membrane concept could mitigate the loads acting on a wing. As high loads can be induced by unsteady phenomena like gusts, it comes clear that an investigation of the flexible membrane concept under gust conditions is required. The present section has the purpose to illustrate the response of an elasto-flexible membrane geometry to various gust conditions. The present analysis is based on results obtained for the numerical 2D WTA model.

A gust can be defined as «a very strong discrete wind pulse, usually with a random and sudden character »[53]. Its numerical modeling is not simple and usually occurs in all the three dimensions. Nevertheless, the Federal Aviation Regulations for Transport (FART) provided examples for simplified modeling of a gust. The so-called 1-cosine law can be used to define a vertical gust acting in one dimension. If a vertical gust is considered for an aircraft, it can also be seen as a

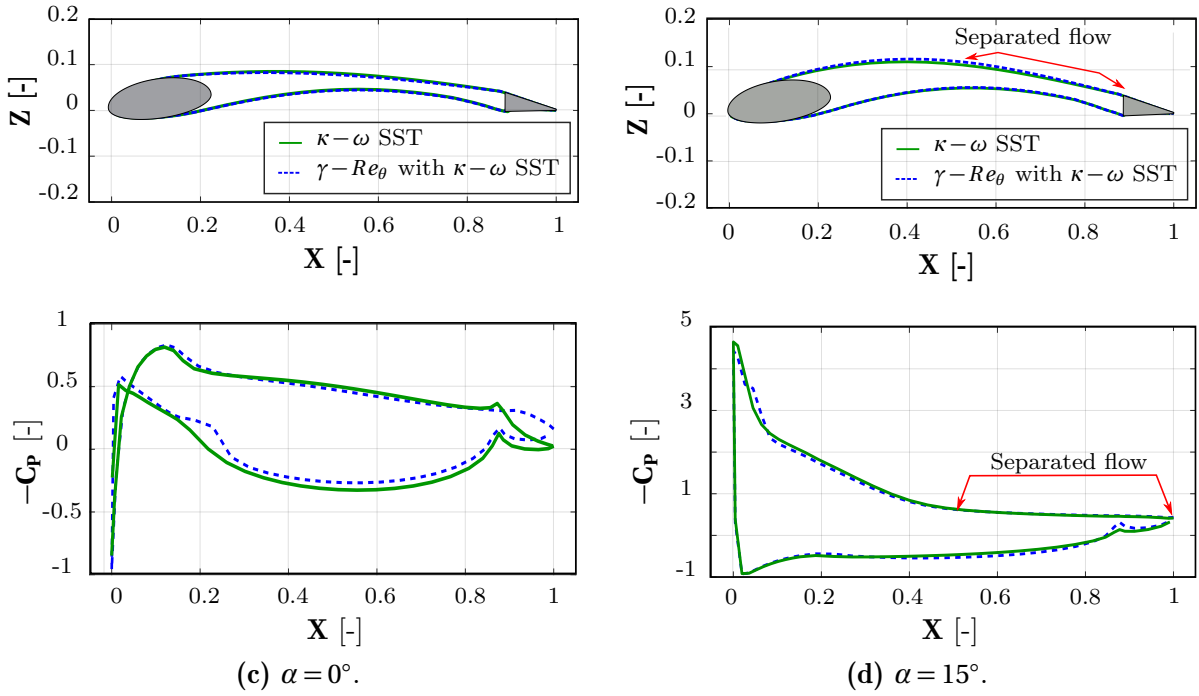


Figure 5.8: Comparison between fully turbulent and transition boundary layer: Membrane deflection and pressure distribution at $\alpha = 0^\circ$ and 15° at $q_\infty = 230$ Pa.

variation of the angle of attack ahead of the aircraft nose [71]. In the following, a 1-cosine law is employed to model gust conditions in the TAU code (see Eq. 5.1 and Fig. 5.13)

Different approaches are implemented in the TAU code to model a 1-cosine gust. The one used in the present thesis is defined as a Disturbance Velocity Approach (DVA) [43]. It consists of splitting gust and primary flow field conditions into two parts. The gust conditions are modeled as an independent domain which progresses with the time and the space. Then the two parts, namely the primary and the gust flows, are superposed to model a gust flow progressing to the geometry situated in the primary flow field. This approach permits to investigate the influence of the gust on the geometry but not the effect of the geometry on the gust, as the two domains are considered separately. To be able to analyze both sides, the Resolved Gust Approach (RGA) can be used [43]. In the following, the DVA is employed to investigate the response of a flexible membrane geometry to a gust; a variation of the angle of attack is included and various vertical amplitudes are computed as well.

The gust is modeled with a 1-cosine function described as the following:

$$g(x) = \frac{1}{2} g_0 \left[1 - \cos\left(\frac{2\pi x}{\lambda}\right) \right] \quad (5.1)$$

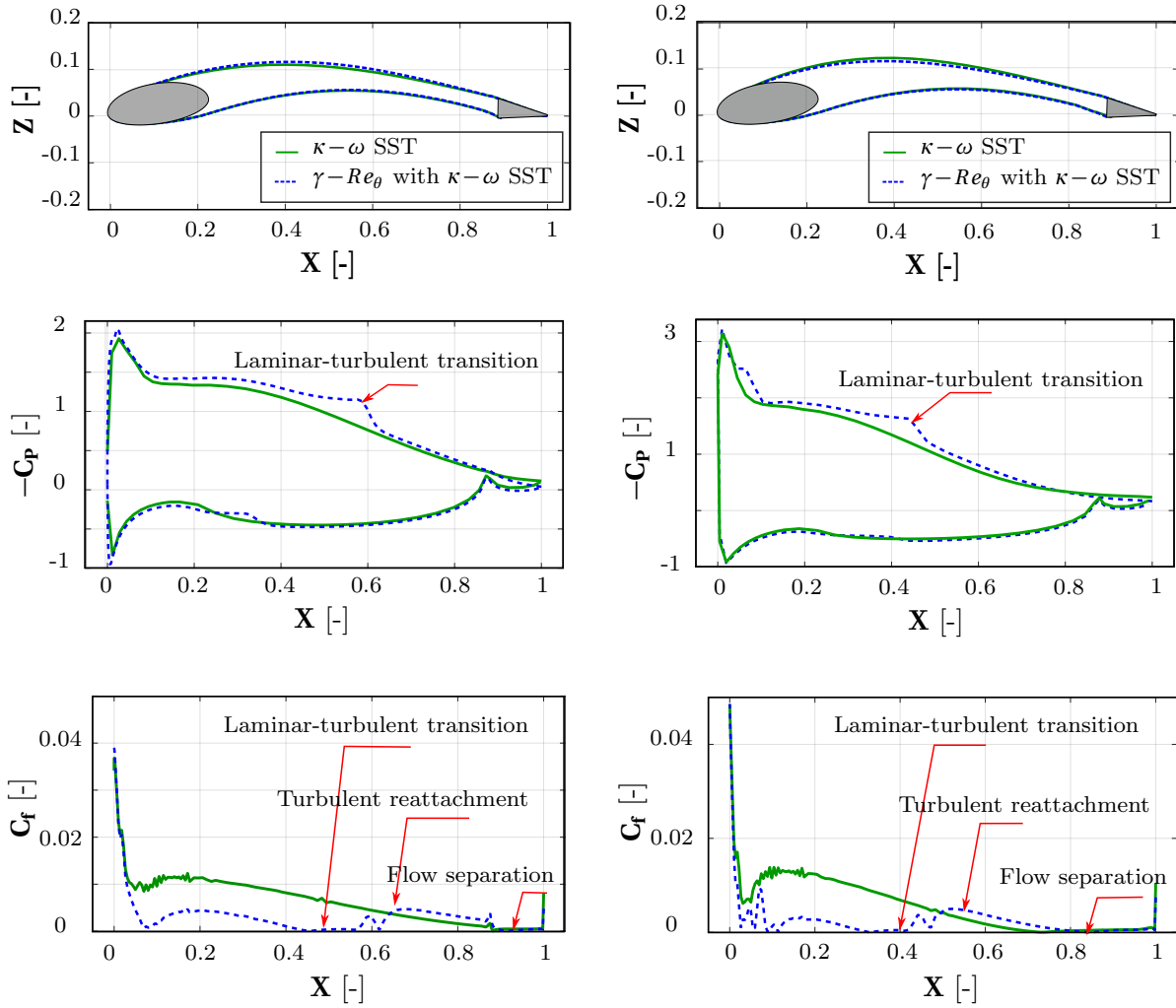


Figure 5.9: Comparison between fully turbulent and transition boundary layer: Membrane deflection, pressure distribution and C_f distribution at $\alpha = 6^\circ$ and 10° at $q_\infty = 230$ Pa.

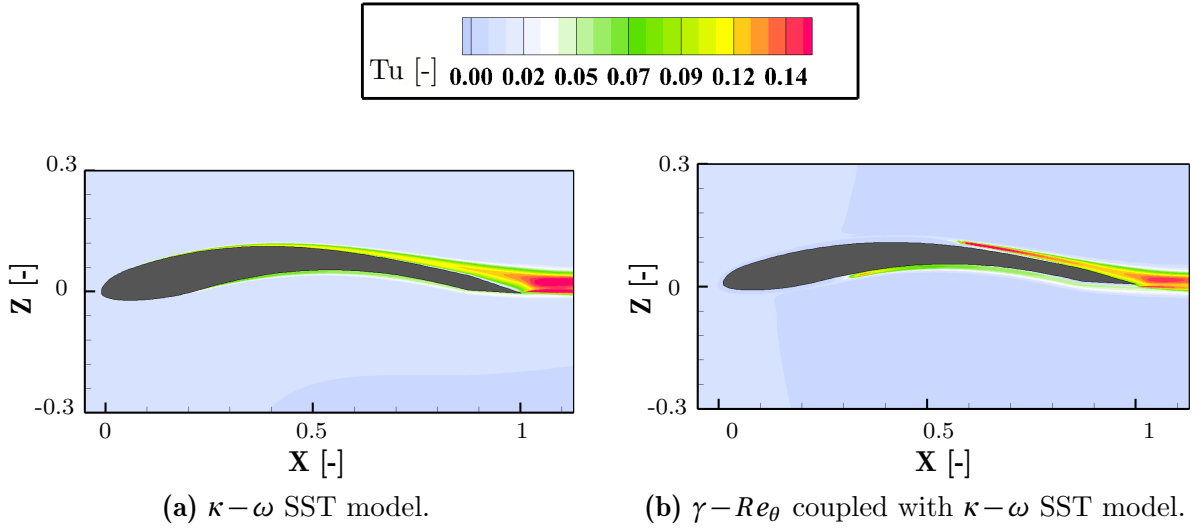


Figure 5.10: Comparison between fully turbulent and transitional boundary layer: turbulent intensity Tu at $\alpha = 6^\circ$ at $q_\infty = 230$ Pa.

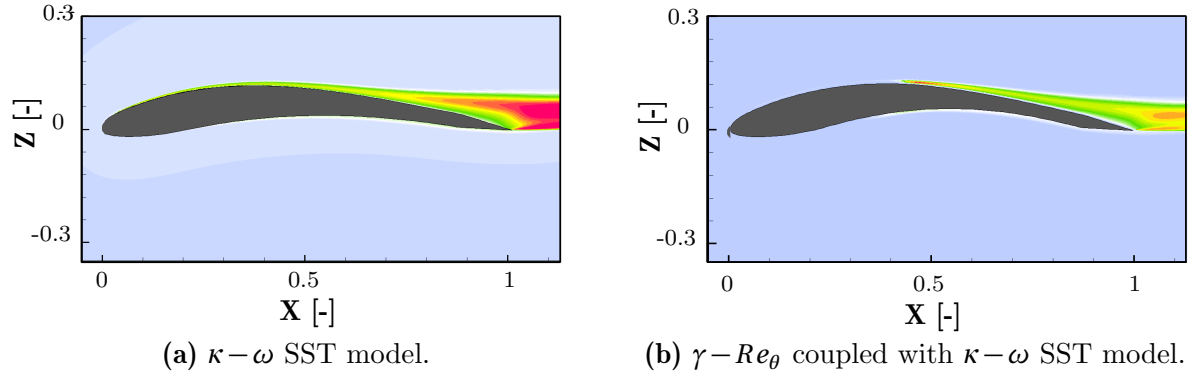


Figure 5.11: Comparison between fully turbulent and transitional boundary layer: Tu at $\alpha = 10^\circ$ at $q_\infty = 230$ Pa.

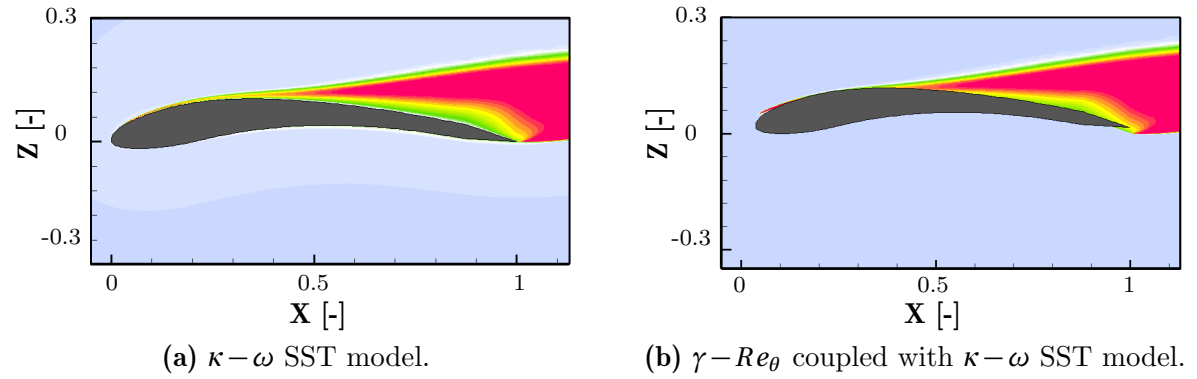


Figure 5.12: Comparison between fully turbulent and transitional boundary layer: Tu at $\alpha = 15^\circ$ at $q_\infty = 230$ Pa.

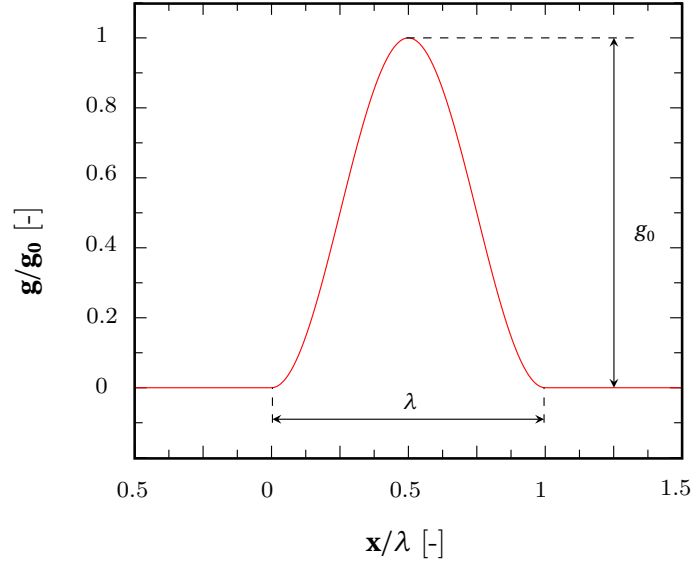


Figure 5.13: Shape of a “1-cosine” gust with g_0 as the amplitude and λ as the wave length.

with x the spatial coordinate, λ the gust wave length propagating through the flow domain and g_0 the gust amplitude. The vertical amplitude g_0 of the gust is set as a changing parameter, whereas the gust wave length is fixed to $\lambda = 2\text{m}$ and the translation speed to 5m/s in the chord direction. To facilitate the analyze of the progression of the gust, the convective time $t^* = U_\infty(t - t_0)/c$ is defined, with U_∞ [m/s] the freestream velocity of the primary flow field, c [m] the wing chord, t_0 [s] the physical time when the geometry enters in the gust and t the physical time [s]. Fig. 5.14 represents the progression of the gust with the convective time. The geometry enters and leaves the gust at $t^* = 0$ and $t^* = 20$, respectively. The gust peak is located at the LE at $t^* = 8$ and at the TE at $t^* = 12$.

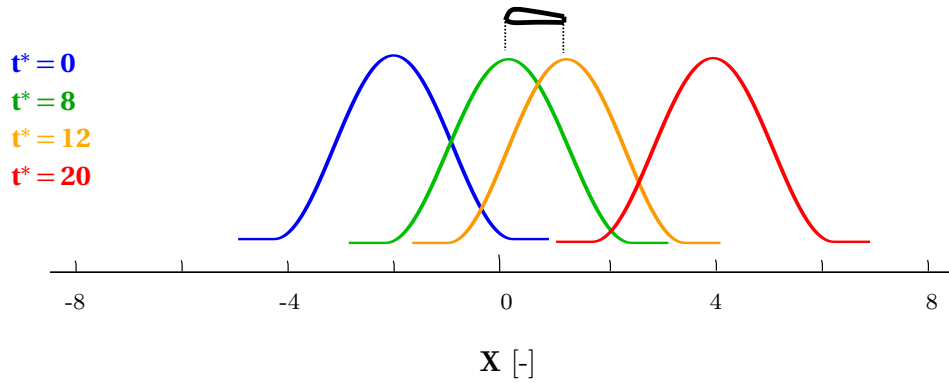


Figure 5.14: Schematic visualization of the convective time t^* and the progression of the gust, [53].

5.2.3.1 Response to a gust

The primary flow conditions of the FSI computations are set for $\alpha = 0^\circ$ and $q_\infty = 230$ Pa. The gust vertical amplitude is set to $g_0 = 10$ m/s. Fig. 5.17 shows the history of C_l and C_d , while Figs. 5.15 and 5.16 illustrate u/U_∞ along the wing for various convective times t^* . The coloured band under the pictures depicting u/U_∞ represents the progression of the gust in the X -direction as well as the dashed line showing $g(X)$. It has to be mentioned that each FSI computation starts from a converged solution as it observed on Fig. 5.17. The membrane is in equilibrium and C_l and C_d are equal to 0.2 and 0.02, respectively.

When the geometry enters the gust ($t^* > 0$), C_l and C_d start to change. Indeed, they mirror the sinusoidal gust shape by increasing until they reach a maximal value of $C_{lmax} = 2.2$ at $t^* = 11.2$ and $C_{dmax} = 0.52$ at $t^* = 12$. Between $8 < t^* < 12$, the peak of the gust is situated on the geometry. The upper-side membrane deflection is at its highest which explains the peak of C_l . Nevertheless, a flow separation region is observed on the backside of the geometry (Fig. 5.16). This is directly related to the abrupt decrease of C_l for $t^* > 11.2$ whereas C_d keeps increasing. While, the peak of the gust progresses downstream ($11.2 < t^* < 15$), the membrane deflection becomes lower as the dynamic pressure induced by the gust on the membrane becomes lower. It results in a reattachment of the flow linked with the plateau in the history of C_l observed on Fig. 5.17 around $t^* = 13$. Then, for $t^* > 15$, C_l and C_d decreases as the gust moves away and the dynamic pressure decreases. While the geometry leaves the gust ($t^* > 20$), the initial flow regime is newly established.

5.2.3.2 Variation of the gust vertical amplitude

The influence of the vertical amplitude of the gust is investigated when $\alpha = 0^\circ$ and $q_\infty = 230$ Pa are set in the primary flow field. Only g_0 changes, while the wave-length λ and the gust speed are kept as in Sec. 5.2.3.1. The amplitude g_0 varies from 1 m/s to 10 m/s. The histories of C_l and C_d are depicted on Fig. 5.17.

As each FSI computation start from an initial steady state at $\alpha = 0^\circ$ and $q_\infty = 230$ Pa, C_l and C_d are equal to 0.2 and 0.02 for each g_0 , respectively. As previously for $t^* > 0$, the geometry enters the gusts and disturbances are present in the primary flow: C_l and C_d start changing. They reproduce the gust sinusoidal shape for each g_0 . The general histories are very similar to those described in Sec. 5.2.3.1 for each vertical amplitude g_0 . Nevertheless, two comments can be made.

On the one hand, the higher g_0 is, the higher C_l and C_d values are reached. The latter is

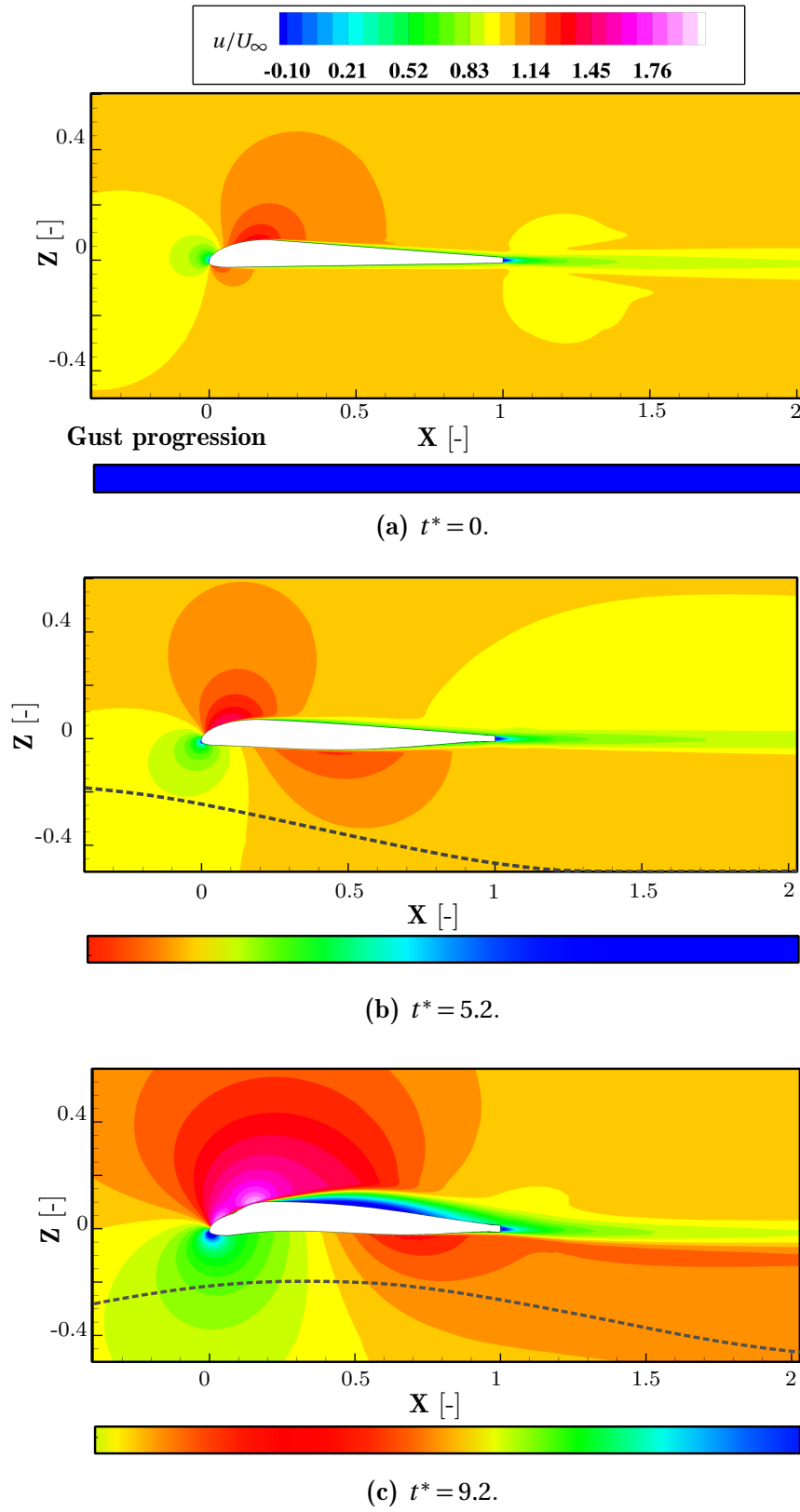
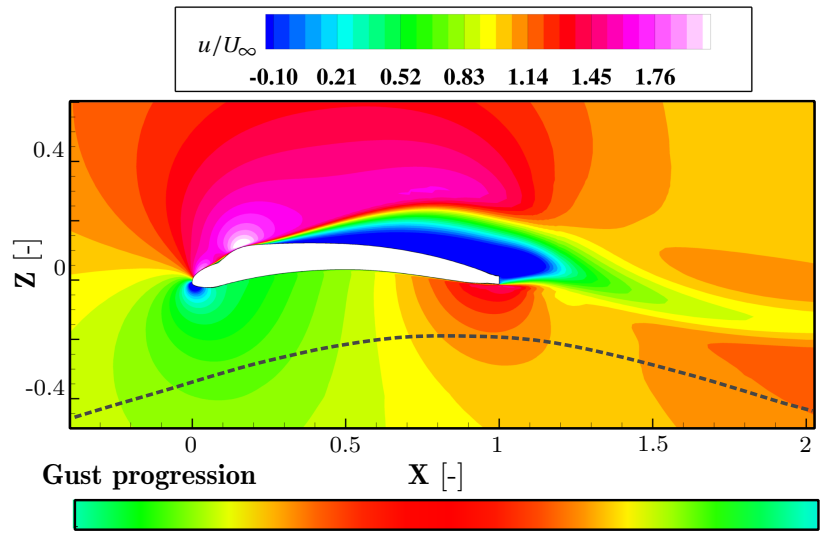
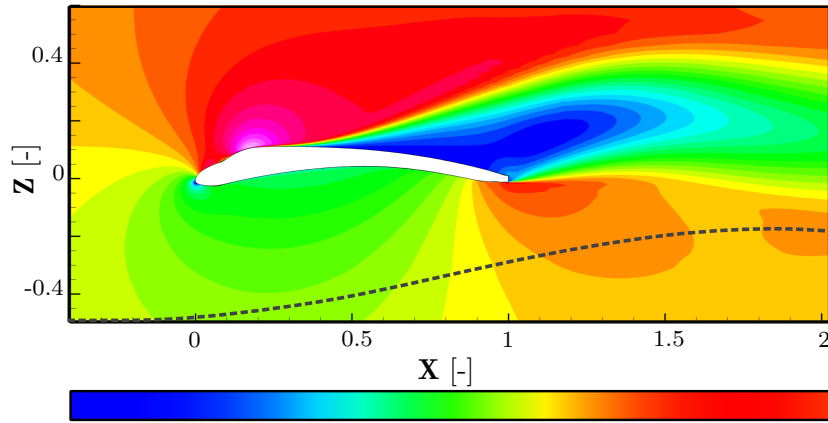


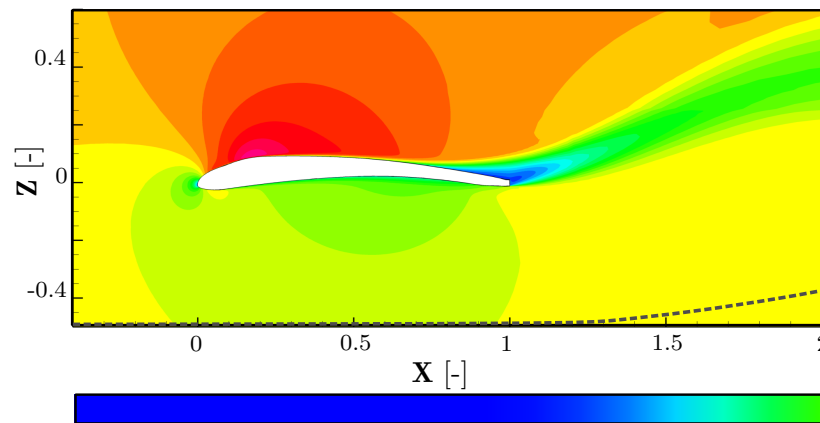
Figure 5.15: Illustration of the response to a "1-cosine" gust with $g_0 = 10 \text{ m/s}$: u/U_∞ at $\alpha = 0^\circ$ at $q_\infty = 230 \text{ Pa}$ for various convective time t^* .



(a) $t^* = 11.2$.



(b) $t^* = 15.2$.



(c) $t^* = 20$.

Figure 5.16: Illustration of the response to a “1-cosine” gust with $g_0 = 10\text{m/s}$: u/U_∞ at $\alpha = 0^\circ$ at $q_\infty = 230\text{ Pa}$ for various convective times t^* .

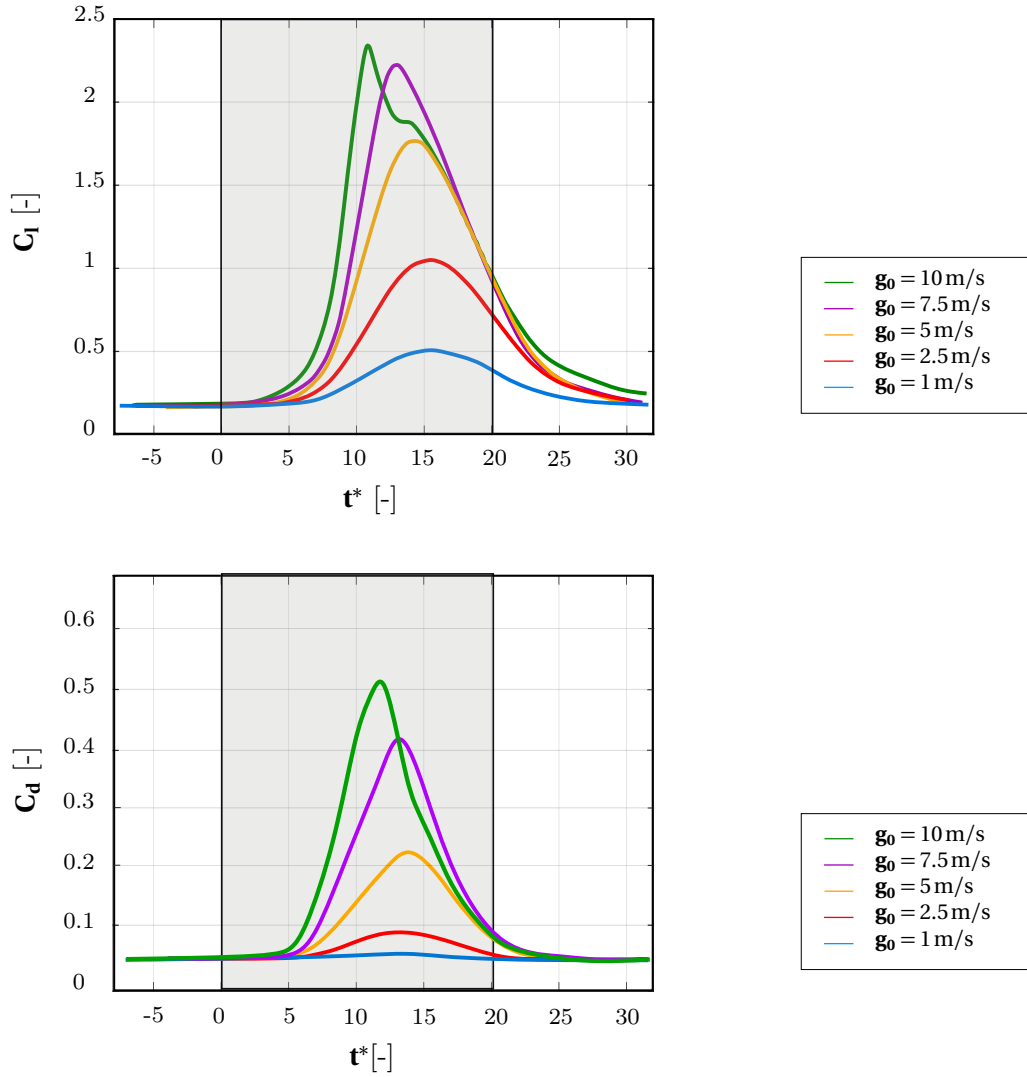


Figure 5.17: Illustration of the response to a “1-cosine” gust: Evolution of C_l and C_d at $\alpha = 0^\circ$ and $q_\infty = 230 \text{ Pa}$ as function of the convective time t^* .

directly related to the dynamic pressure induced by the gust. If the vertical amplitude of the gust increases, the dynamic pressure increases as well resulting in higher membrane deflection and higher camber. This induces and explains the higher C_l and C_d values.

On the other hand, C_l reaches a maximum value at different time when g_0 changes. The higher g_0 is, the earlier C_l reaches its maximum. The latter is related to the flow separation phenomenon. As already mentioned, a gust can be defined as a pulse of wind. The pulse of wind, or more precisely the vertical velocity, generates an induced angle of attack resulting in a change in the effective angle of attack. The effective angle of attack increases when a geometry encounters a vertical gust. Therefore, the higher g_0 is, the more likely it is to encounter a flow separation on the geometry. When the flow separates, C_l decreases giving the impression that C_{lmax} was reached for earlier convective times, whereas C_d keeps increasing. The phenomenon of flow separation at $g_0 = 10\text{m/s}$ is depicted in Figs. 5.15, 5.16 and 5.17, where C_l reaches its maximum but directly decreases afterwards while C_d keeps increasing.

5.2.3.3 Comparison with rigid wing

One of the expectations in using a flexible geometry is to mitigate the loads acting on it. Comparing rigid and flexible geometries to identify whether the loads can be influenced during gust conditions appears interesting. Nevertheless, an important issue has to be considered in finding a suitable rigid geometry to compare with the flexible case. If the undeformed geometry is used, the forces experienced by the flexible geometry are obviously amplified (see Section 5.1). Following this logic, it appears clear that the gust response are not alleviated but accentuated. Therefore, the comparison is not suitable and another idea is adopted. The response of the flexible geometry is compared to the response of a deformed geometry. The deformed geometry has the same deformation as the flexible concept in its steady state, but can not deform any more. In this logic, the aerodynamic forces can be appropriately compared as the deformed geometry has a camber, which also induces the same forces in the steady state as the flexible geometry. The results are depicted by Fig. 5.18, where the history of C_l and C_d are illustrated for various α .

The same observations as in Sec. 5.2.3.2 can be made. C_l and C_d reach higher values at different times when α increases. The two remarks are explained with the following: as the effective α is higher when α increases, a higher dynamic pressure is reached when the geometry enters the gust, and the flow separation appears earlier as well.

The main observation in Fig. 5.18 is connected to the peaks of C_l and C_d achieved by the flexible and the rigid geometries. For small α , namely 0° and 3° , the flexible concept has higher C_l and C_d than the rigid geometry. However, the trend is reversed for $\alpha = 6^\circ$ and 9° . According to this results, the assumption concerning the alleviation of loads appears promising. The flexible geometry can mitigate the lift during gust conditions at high α . But it is also observed that, at $\alpha = 9^\circ$, C_l oscillates. The membrane encounters a flutter phenomenon as long as the gust progresses from the middle of the geometry to the TE. Therefore the mechanical properties of the membrane should be further investigated under gust conditions to find a suitable material, which can mitigate the loads but also overcomes the fluttering.

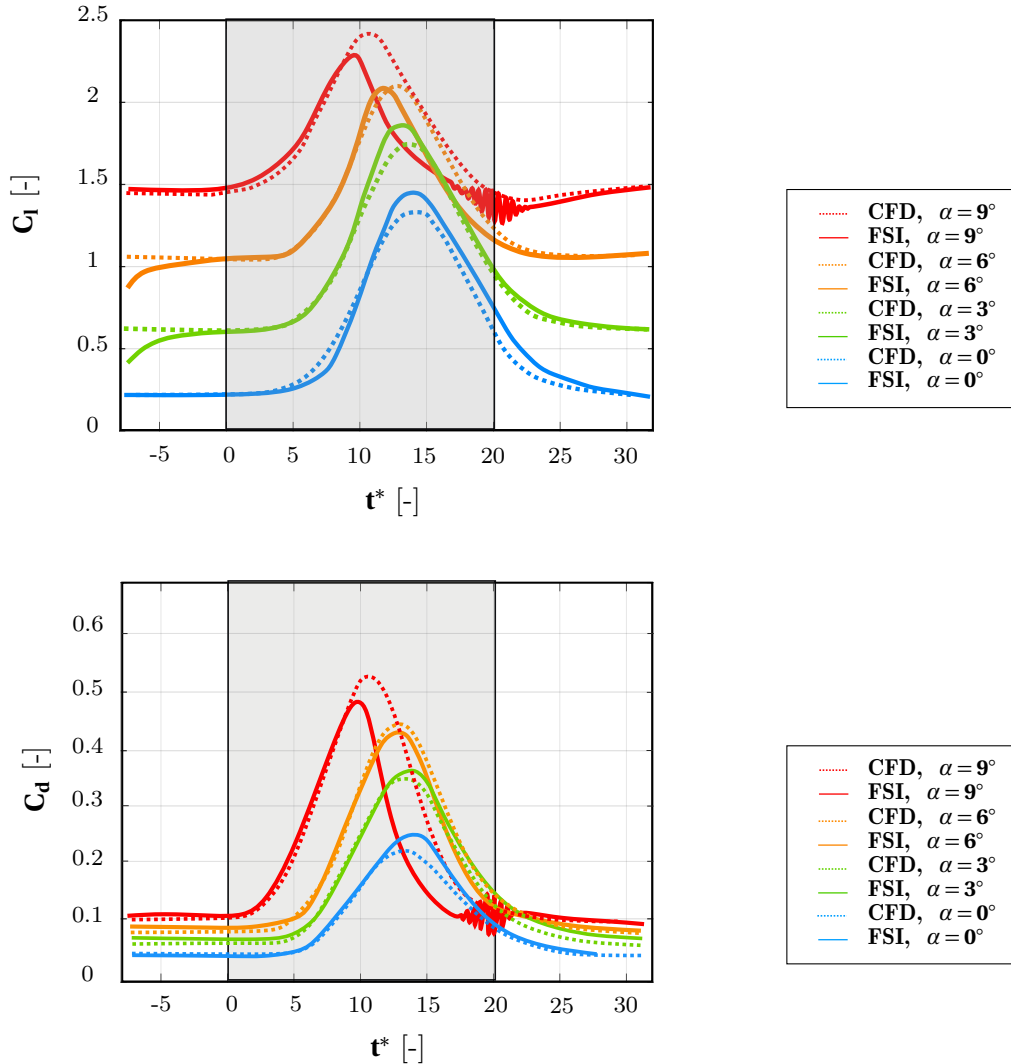


Figure 5.18: Comparison of the response to a “1-cosine” gust between a rigid and a flexible geometry: Evolution of C_l at various α and $q_\infty = 230$ Pa as function of the physical time t^* .

Chapter 6 - Aeroelastic Behavior of a Membrane Wing

The aerodynamic characteristics are promising regarding a two-dimensional model. An extension of the analyze in the span direction is therefore interesting to study. The present chapter has the purpose of extending the analysis to a quasi-two-dimensional wing, designated as the 2.5D WTA model, and to a three-dimensional tapered wing, designated as the 3D WTA model. The two models are presented experimentally and numerically in Chapter 3. The first part of this chapter presents the results obtained for the 2.5D WTA model, whereas the second part gives the results for the 3D WTA model. For the two cases, as in Chapter 4, the results of fluid-structure interaction computations are compared to results related to rigid counterparts. They are also compared to experimental data to evaluate the accuracy of the computations.

6.1 2.5D Model

The experimental and numerical 2.5D WTA models are introduced in the sections 3.2.2.2 and 3.4.2. They consist of an extrusion of the 2D WTA presented in Sec. 3.2.1.1. At each tip of the wing, an end-plate is fixed to support the development of a two-dimensional flow. In Chapter 5, the aerodynamic characteristics of a flexible airfoil are described and a study including the influence of the dynamic pressure, the turbulence model and the gust velocity conditions is given. Chapter 5 allows the possibility to build a baseline case for a flow around an airfoil and consequently for the 2.5D WTA wing.

The FSI computations for the 2.5D WTA model are presented in the following and compared to the experimental data to evaluate the accuracy of the computations. Section 6.1.2 ultimately gives a detailed comparison between the rigid and the flexible concepts by comparing the CFD and FSI results.

6.1.1 Comparison between FSI and Wind-Tunnel Data

6.1.1.1 Aerodynamic Forces

The aerodynamic coefficients, namely C_L and C_D , are plotted as a function of α in Fig. 6.1 for the FSI, the CFD computations and the experiments.

The FSI computations are performed like follows: five iterations are completed between the fluid and the structure at $\alpha = 0^\circ$ and $q_\infty = 230$ Pa. The relative errors between the two last iterations are under 5% for both C_L and C_D . The solution obtained at $\alpha = 0^\circ$ and $q_\infty = 230$ Pa is afterwards used as a first step for the next computations, namely $\alpha = 5^\circ$ and $\alpha = 10^\circ$ at $q_\infty = 230$ Pa. This permits to accelerate the convergence. In this case, the relative errors between the two last iterations are under 1% for both C_L and C_D .

The comparison between the FSI results and the experimental data can be summerized with the following:

- $\alpha = 0^\circ$: C_L and C_D are computed 0.526 and 0.031, respectively. In the wind tunnel, they are equal to 0.45 and 0.026, which results in a deviation of 16% for both C_L and C_D . Note that a relative error calculation is used.
- $\alpha = 5^\circ$: the FSI computations estimate $C_L = 0.914$ and $C_D = 0.057$ at $\alpha = 5^\circ$. During the measurements, C_L and C_D are measured as 0.83 and 0.062. Therefore, a relative error is equal to 10% and 8% for C_L and C_D , respectively.
- $\alpha = 10^\circ$: $C_L = 1.3$ and $C_D = 0.102$ are predicted at $\alpha = 10^\circ$ with FSI, whereas the wind tunnel tests measured $C_L = 1.16$ and $C_D = 0.115$ at $\alpha = 9.6^\circ$. The deviation between FSI computations and wind tunnel data are of 12% and 11% for C_L and C_D , respectively.

The FSI computations show a good agreement with the wind-tunnel data. A maximal relative error is found to be 16%. The moderate deviations obtained within C_L and C_D can be explained by analyzing the membrane deflection described in the following section.

6.1.1.2 Membrane Deflection

The membrane deflection for the 2.5D WTA model measured in the wing span are introduced in Sec. 4.2.4. This experimental data can be compared to the numerical results obtained with the FSI computations on the 2.5D WTA model. The comparison is illustrated in Figs. 6.2 and 6.3, where Z and ΔZ are plotted along the chord direction in the middle of the wing ($Y = 0$) and in

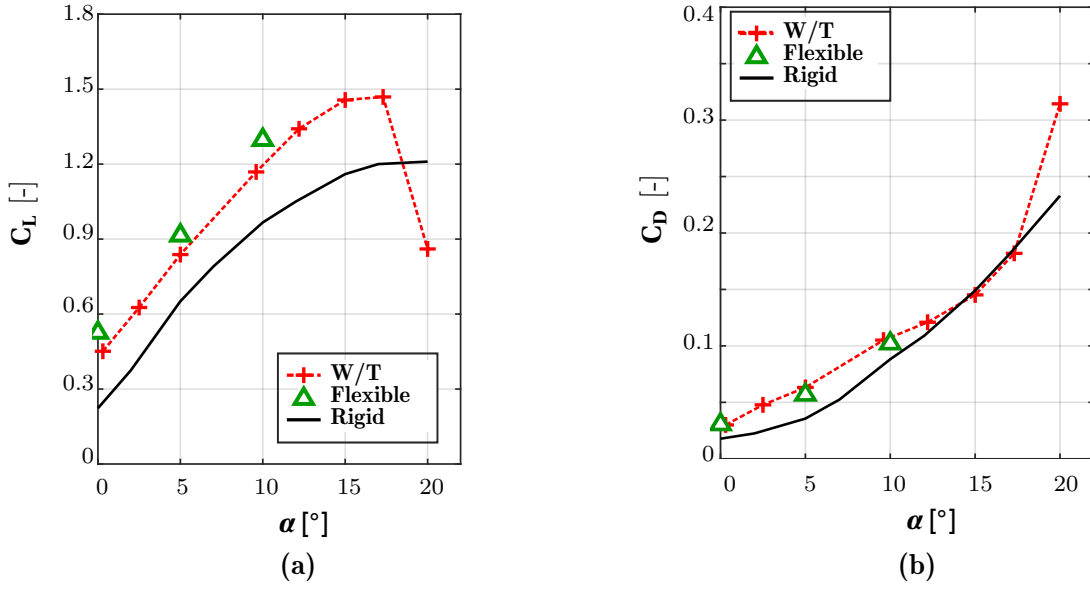


Figure 6.1: C_L - α and C_D - α curves obtained for the 2.5D WTA model during wind tunnel measurements, and for FSI and CFD computations at $q_\infty = 230$ Pa.

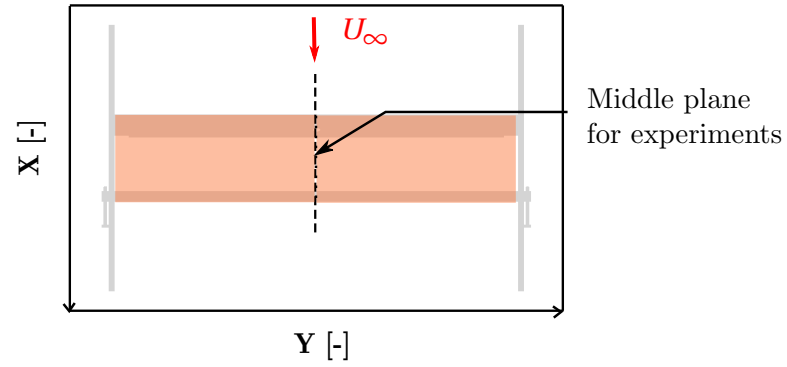
the wing span direction. Note that ΔZ represents the difference between the deformed and the non-deformed geometry. The following comments can be made concerning the comparison of the membrane deflection between FSI results and experimental data:

- $\alpha = 0^\circ$: as observed in Sec. 4.2.4, the deflection is not homogeneous in the wing span during the wind tunnel measurements (cf. Fig. 6.3). The latter may be explained with the high uncertainties due to the hysteresis phenomenon. If the numerical data is observed, the membrane deflection is almost uniform in the experimental region delimited with a rectangle (see Fig. 6.3) but not completely in the wing span direction. As the hysteresis is not taken into account in the computations, it results that the end-plates have an influence on the development of the flow. At $Y = 0$, the computations deviate with the experiments by overestimating the deflection by 11% and 10% on the upper and the lower surfaces, respectively. Note that a norm error L2 method is used to estimate the error.
- $\alpha = 5^\circ$: the FSI computations are initialized with the solution obtained at $\alpha = 0^\circ$. As observed in Sec. 4.2.4, the membrane deflection is homogeneous during the experiments. If the FSI computations are analyzed, the deflection appears also homogeneous in the measurement region, but not completely in the wing span direction. This confirms the conclusion about the end-plates influencing the flow. Furthermore, the FSI computations underestimate the

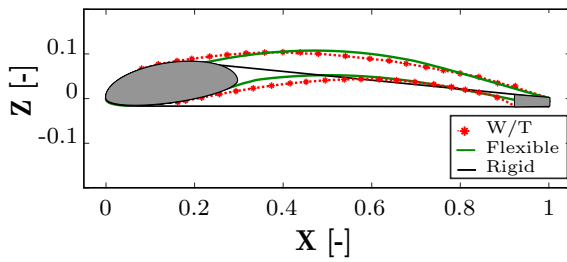
experimental deflection by 10% and 25% in the middle of the wing on the upper- and the lower-side surfaces, respectively. It can be noticed that the membrane deflection computed at $\alpha = 5^\circ$ is lower than at $\alpha = 0^\circ$, which is unexpected and does not agree with the data from the experiments.

- **$\alpha = 10^\circ$:** the membrane deflection is computed to be nearly uniform in the measurement region. This matches the experimental data showed in Fig. 6.3. However, the deflection increases until $X = 0.3$ in the experiments and then decreases linearly for $X \geq 0.4$ at $Y = 0$ (cf. Fig. 6.2). As explained in Sec. 5.1, this sudden change in the curvature is connected to the flow separation. It is assumed that the flow separates from $X = 0.4$ in the experiments for this model. However, the linear decrease of Z is not observed in the FSI computations. Note also that the abscissa X_{sep} , where the membrane detaches from the LE is located at $X = 0.2$ in the computations whereas it is around $X = 0.1$ in the experiments. The latter is due to the contact modeling in the numerical model: the FEM code Carat++ does not allow a real contact modeling. To solve this issue, the contact is approached with an artificial method: the abscissa X_{sep} is estimated in the experiments and reported in the simulations. However, it is not completely precise and it may explain why the abscissa where the maximal ΔZ occurs, X_{Zmax} , is situated around $X = 0.6$ for the computations, whereas it is located around $X = 0.5$ in the experiments (cf. Fig. 6.3).

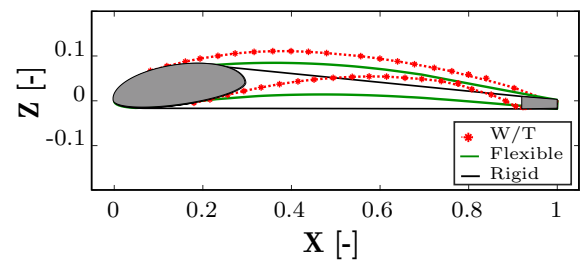
The FSI computations estimate the deflection to be nearly homogeneous in the measurement region. This matches the experiments except at $\alpha = 0^\circ$. The latter may be explained with the hysteresis phenomenon observed in the experiments and being strong at the aforementioned α . The comparison also points out that the absence of the contact between the LE and the membrane in the computations leads to deviations with a supposed incorrect estimation of the flow separation.



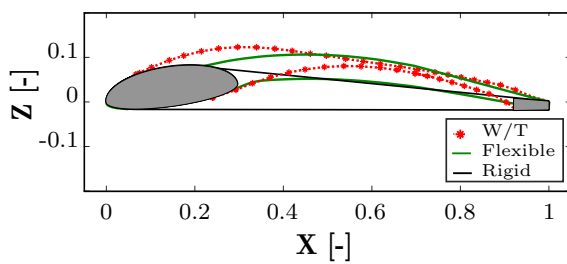
(a) Schema showing the plane where the FSI and the experiments were compared.



(b) $\alpha = 0^\circ$.



(c) $\alpha = 5^\circ$.



(d) $\alpha = 10^\circ$.

Figure 6.2: Comparison between the photogrammetry measurement data and the FSI and CFD results at $q_\infty = 230$ Pa in the middle of the wing for the 2.5D WTA model.

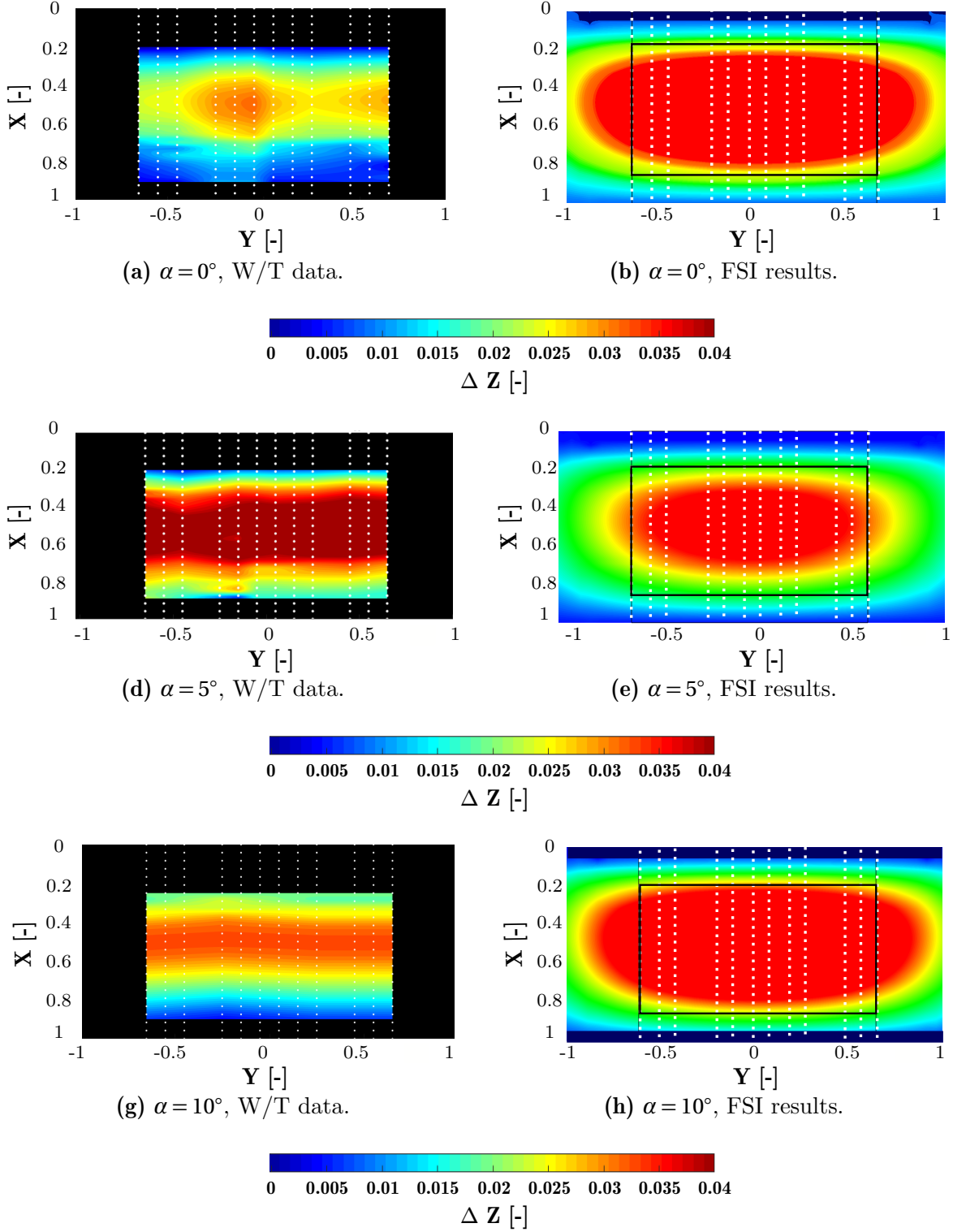


Figure 6.3: Comparison between photogrammetry measurement and FSI results: The deflection was measured in the wingspan at $q_\infty = 230$ Pa for the 2.5D WTA model. ΔZ represents the difference between the deformed and the non-deformed geometry.

6.1.2 Numerical Study

To continue the analysis on the 2.5D WTA model, it is interesting to study the computations in more detail in order to enlarge the understanding of the flexibility on the aerodynamics of the wing. In the present section, an extensive analysis of the pressure distribution and the flow topology is given for three α , namely 0° , 5° and 10° at $q_\infty = 230$ Pa. The benefits gained with the flexibility are highlighted by comparing the results of the FSI to its rigid counterpart. It is decided to split the next section for each α in order to clarify the advantages gained with the flexible concept.

6.1.2.1 Zero angle of attack ($\alpha = 0^\circ$)

The results obtained for the rigid and the flexible geometry are illustrated in Figs. 6.4, 6.7, 6.8 and 6.9. The flow velocity and the pressure distribution along the chord direction and in the span direction are plotted in order to allow a detailed analysis of the flow. For the zero angle of attack, the following remarks can be commented:

- The pressure coefficient $-C_p$ is plotted in the wing span at $Y = 0$, -0.5 and -1 and along the chord direction in Fig. 6.7. It is observed that the distribution varies in the wing span: $-C_p$ is higher in the middle of the wing (at $Y = 0$) than at the wing-tip next to the end-plates. This has to be related to the membrane deflection illustrated in Fig. 6.3, where the deflection is observed not completely homogeneous in the wing span. The hypothesis about the end-plates disturbing the flow is verified.
- A high difference in $-C_p$ is observed at $Y = 0$ between the rigid and the flexible concept, with $-C_p$ being higher for the flexible geometry. It is due to the capacity of the membrane to deform in the z -direction. The difference in $-C_p$ between both geometries becomes smaller near the end-plates. This results from the end-plates disturbing the flow and in ΔZ becoming lower as already observed in Fig. 6.3.

Both comments justify the results obtained for C_L and C_D (cf. Fig. 6.1 and Table 6.1). C_L is equal to 0.526 against 0.223 for the flexible and the rigid geometries, and C_D is higher for the flexible concept, namely 0.031 against 0.018. Finally, the efficiency is better for the flexible geometry with 17 against 12.4.

The two components of the flow velocity, namely the axial u/U_∞ and the vertical w/U_∞ components are illustrated in Fig. 6.4. Both components are illustrated for $Y = 0$ and $Y = 1$ in

the wing span above the wing. A classical development of the flow velocity is observed in Fig. 6.4. The flow accelerates on the upper-side surface of the wing with a region of acceleration being larger on the flexible than on the rigid geometry. This is directly associated to the higher suction level and the membrane deflection.

-	C_L	C_D	C_L/C_D
CFD, rigid	0.223	0.018	12.4
FSI, flexible	0.526	0.031	17.0

Table 6.1: Values of the aerodynamic coefficients obtained for the flexible and the rigid cases at $\alpha = 0^\circ$ and $q_\infty = 230$ Pa for the 2.5D WTA model.

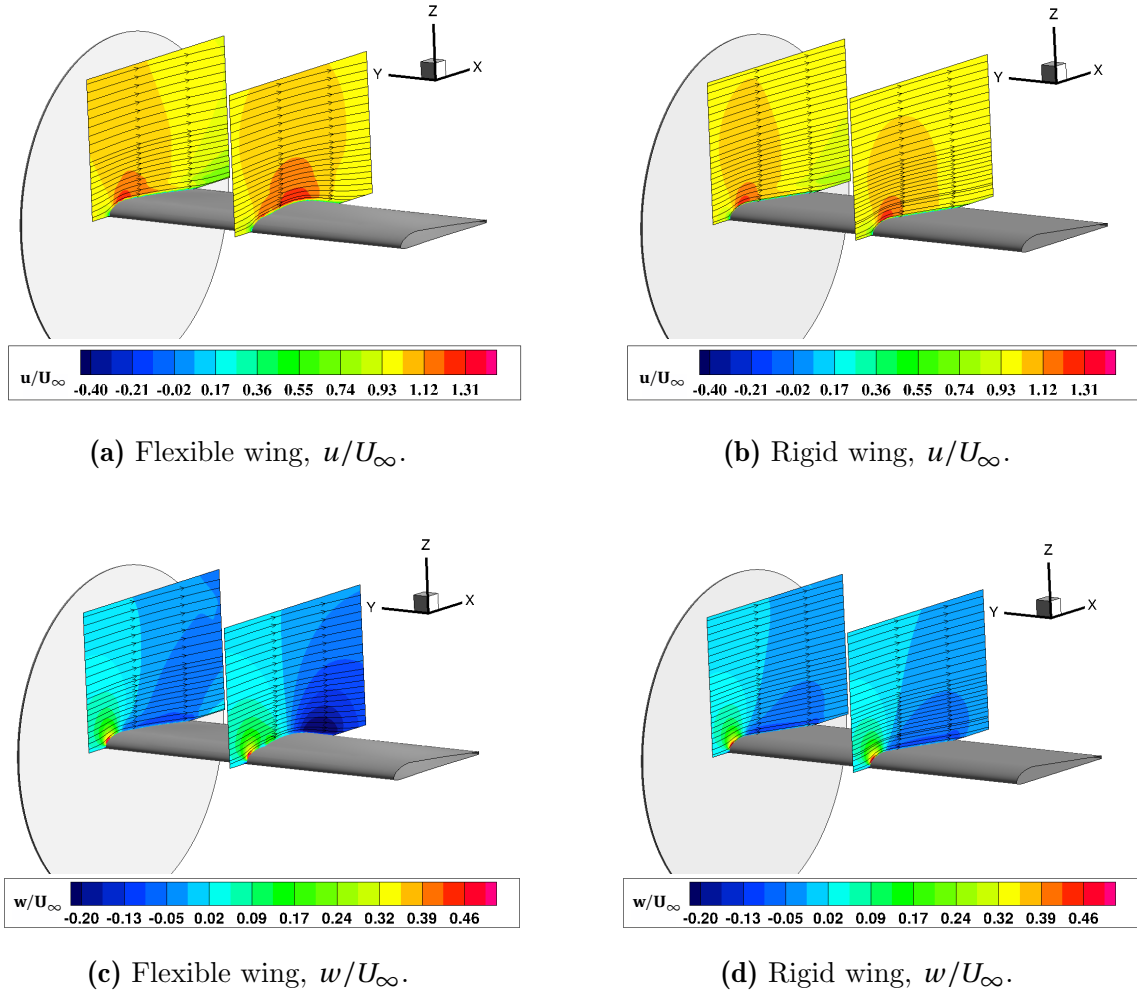


Figure 6.4: Comparison between flexible and rigid wings: Axial component u/U_∞ and vertical component w/U_∞ of the flow field velocity at $\alpha = 0^\circ$ at $q_\infty = 230$ Pa for the 2.5D WTA model.

6.1.2.2 Moderate angle of attack ($\alpha = 5^\circ$)

The results of the pressure distribution and the flow velocity are described for $\alpha = 5^\circ$ in Figs. 6.5, 6.7, 6.8 and 6.9.

As for the case $\alpha = 0^\circ$, $-C_p$ is plotted for $Y = 0, -0.5$ and -1 . The same comments can be made for $\alpha = 5^\circ$ as for the case $\alpha = 0^\circ$. $-C_p$ is not uniform in the wing span: it is higher in the middle of the wing than at the wing-tips next to the end-plates and $-C_p$ is higher for the flexible than for the rigid geometry.

The last comments explain the observations on the lift and drag (Fig. 6.3). Table 6.2 gives the values of C_L and C_D computed for the flexible and the rigid cases at $\alpha = 5^\circ$. C_L is equal to 0.914 against 0.651, result of the pressure distribution; C_D is equal to 0.057 against 0.036. One difference with the case $\alpha = 0^\circ$ is in the efficiency: C_L/C_D is higher for the rigid than for the flexible geometry.

Fig. 6.5 depicts the two components u and w of the flow velocity at $Y = 0$ and 1. Similar comments can be made as for the case $\alpha = 0^\circ$.

-	C_L	C_D	C_L/C_D
CFD, rigid	0.651	0.036	18.1
FSI, flexible	0.914	0.057	16.0

Table 6.2: Values of the aerodynamic coefficients obtained for the flexible and the rigid cases at $\alpha = 5^\circ$ and $q_\infty = 230$ Pa for the 2.5D WTA model.

6.1.2.3 High angle of attack ($\alpha = 10^\circ$)

The results obtained for $\alpha = 10^\circ$ are depicted in Figs. 6.6, 6.7, 6.8 and 6.9. As previously, the pressure distribution and the development of the flow velocity are depicted in the chord and the span wise directions. Similar comments can be made as in the cases at $\alpha = 0^\circ$ and 5° .

Regarding the flexible geometry, the membrane deflection is not completely uniform in the span wise direction like in the two other cases. In the middle of the wing ($Y = 0$), $-C_p$ is at its maximum explaining the maximal deflection at this location (cf. Figs. 6.3 and 6.7). At the tip ($Y = -1$), $-C_p$ decreases showing the influence of the end-plates. However, it is also observed that $-C_p$ decreases to stagnate to 0.5 on the upper-side surface of the wing. This phenomenon

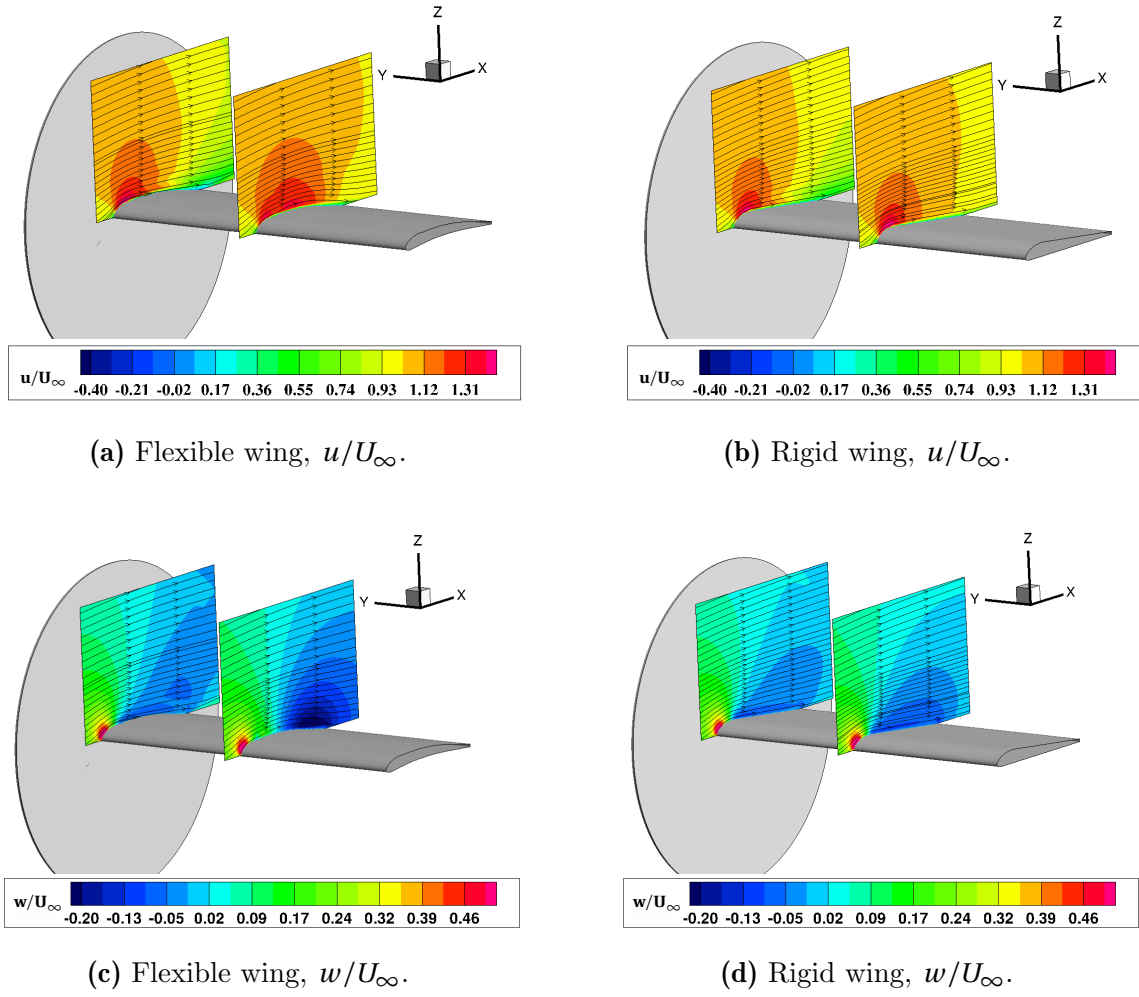


Figure 6.5: Comparison between flexible and rigid wings: Axial component u/U_∞ and vertical component w/U_∞ of the flow field velocity at $\alpha = 5^\circ$ at $q_\infty = 230$ Pa for the 2.5D WTA model.

appears for the flexible wing but also for the rigid one. In Fig. 6.8, tips vortices are depicted at the same location. The flow separates and the skin friction show the re-circulation domain. A very interesting phenomenon is that the vortices are much smaller in the flexible case than in the rigid one. The membrane deflection permits to minimize the tip vortices.

C_L is equal to 1.297 for the flexible geometry against 0.967 for the rigid one. C_D is still higher for the flexible geometry due to higher C_L , but the efficiency is better due to lower tip vortices on the flexible wing.

The axial u/U_∞ and vertical w/U_∞ flow velocity components are plotted in Fig. 6.6. The flow separation region is well observed near the end-plates with the streamlines depicted in black. The mitigation of the vortices is noticed as well as the region of the separated flow is much smaller for

the flexible than for the rigid geometry.

-	C_L	C_D	C_L/C_D
CFD, rigid	0.967	0.088	11.0
FSI, flexible	1.297	0.102	12.7

Table 6.3: Values of the aerodynamic coefficients obtained for the flexible and the rigid cases at $\alpha = 10^\circ$ and $q_\infty = 230$ Pa for the 2.5D WTA model.

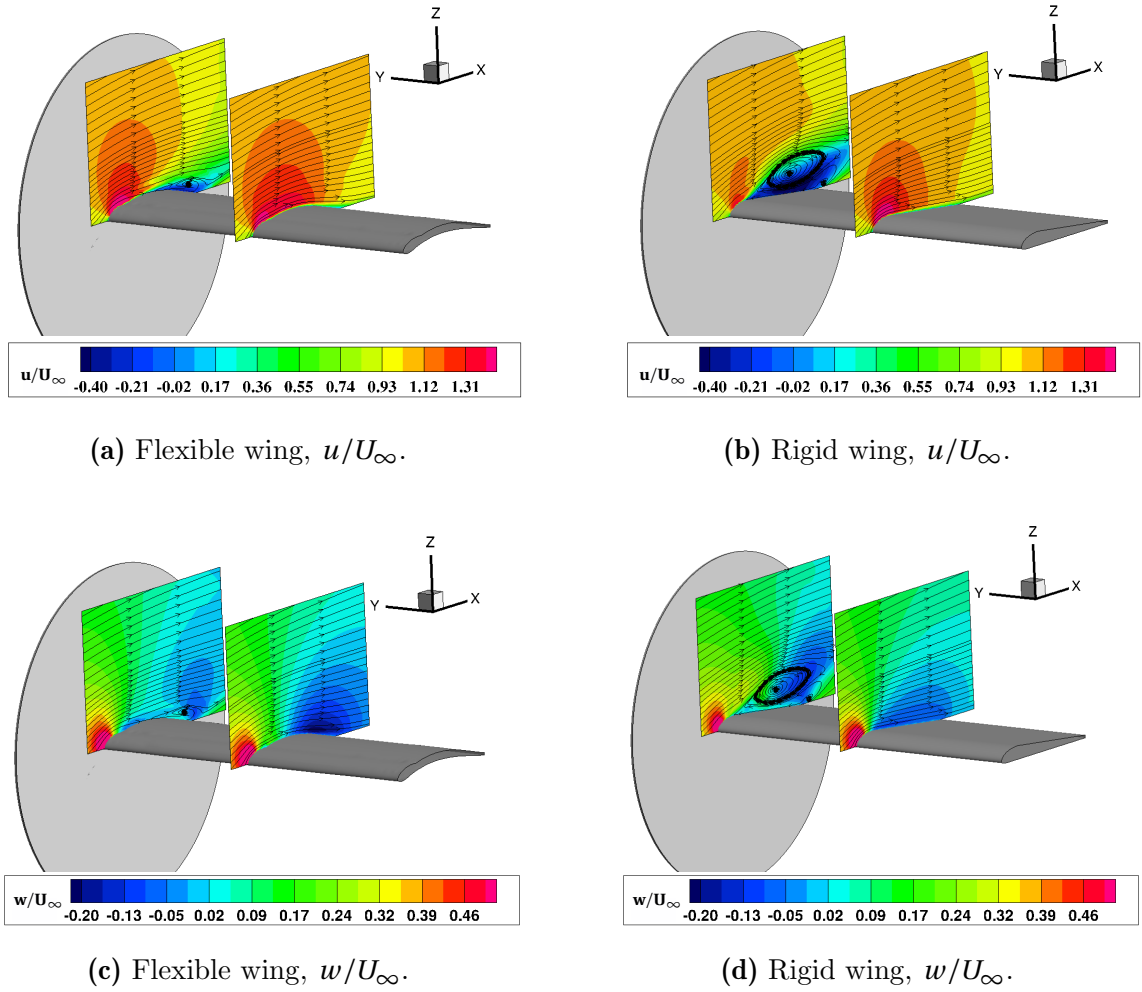


Figure 6.6: Comparison between flexible and rigid wings: Axial component u and vertical component w of the flow field velocity at $\alpha = 10^\circ$ at $q_\infty = 230$ Pa for the 2.5D WTA model.

Summary

As for the 2D case, the study of the FSI computations permits to understand that the membrane has the capacity to adapt itself to the incoming flow. The membrane deflects to positive z -direction

for positive values of α . The camber of the wing section is higher and the flow has a larger region to accelerate. It results in higher values of $-C_p$ and therefore in a better lifting capacity. However, the drag is higher as well. In the case of the 2.5D WTA, the end-plates have an influence on the flow at the tips. The pressure distribution is not completely uniform in the spanwise direction and the membrane deflection is not either. It seems that the end-plates induce a flow separation and vortices at the wing-tips for higher α . A very interesting phenomenon is that the membrane mitigate the vortices (and the flow separation, as it was also observed in Sec. 5.1), which is a promising characteristic of the wing flexibility.

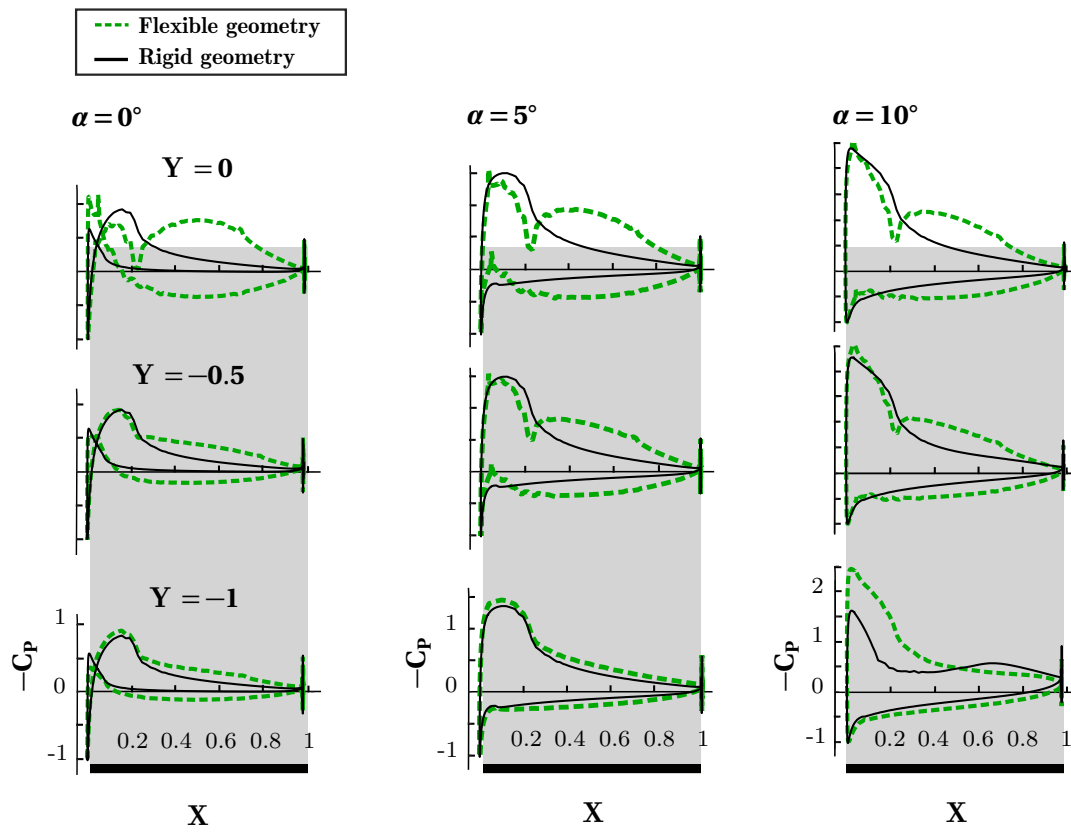


Figure 6.7: Comparison between flexible and rigid wings for the 2.5D WTA model: Evolution of $-C_p$ - X along the wing span at $\alpha = 0^\circ$, 5° and 10° for $q_\infty = 230$ Pa.

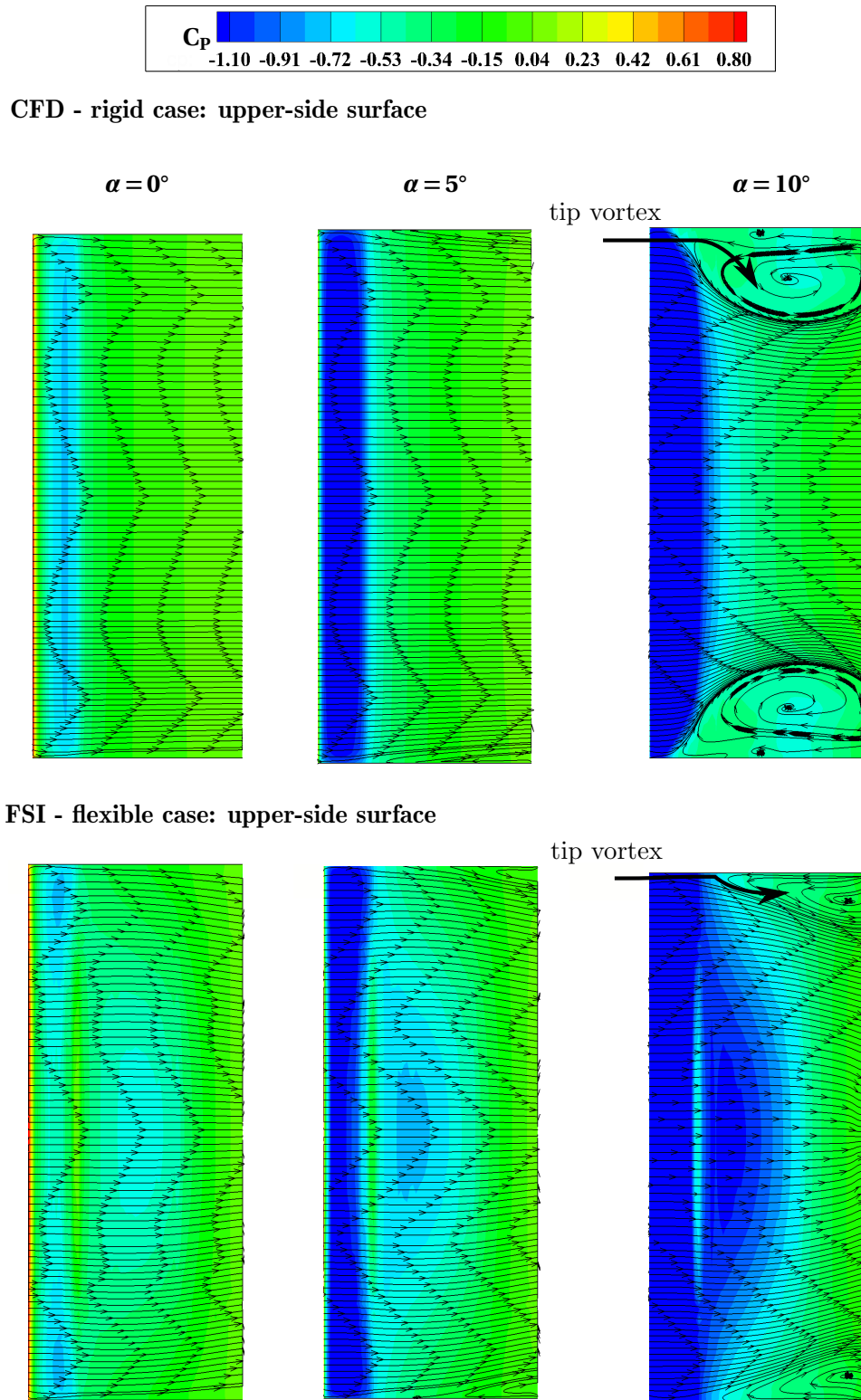


Figure 6.8: Comparison between flexible and rigid wings for the 2.5D model: Evolution of C_p -X along the wing span at $\alpha = 0^\circ$, 5° and 10° at $q_\infty = 230$ Pa and visualization of the skin friction lines.

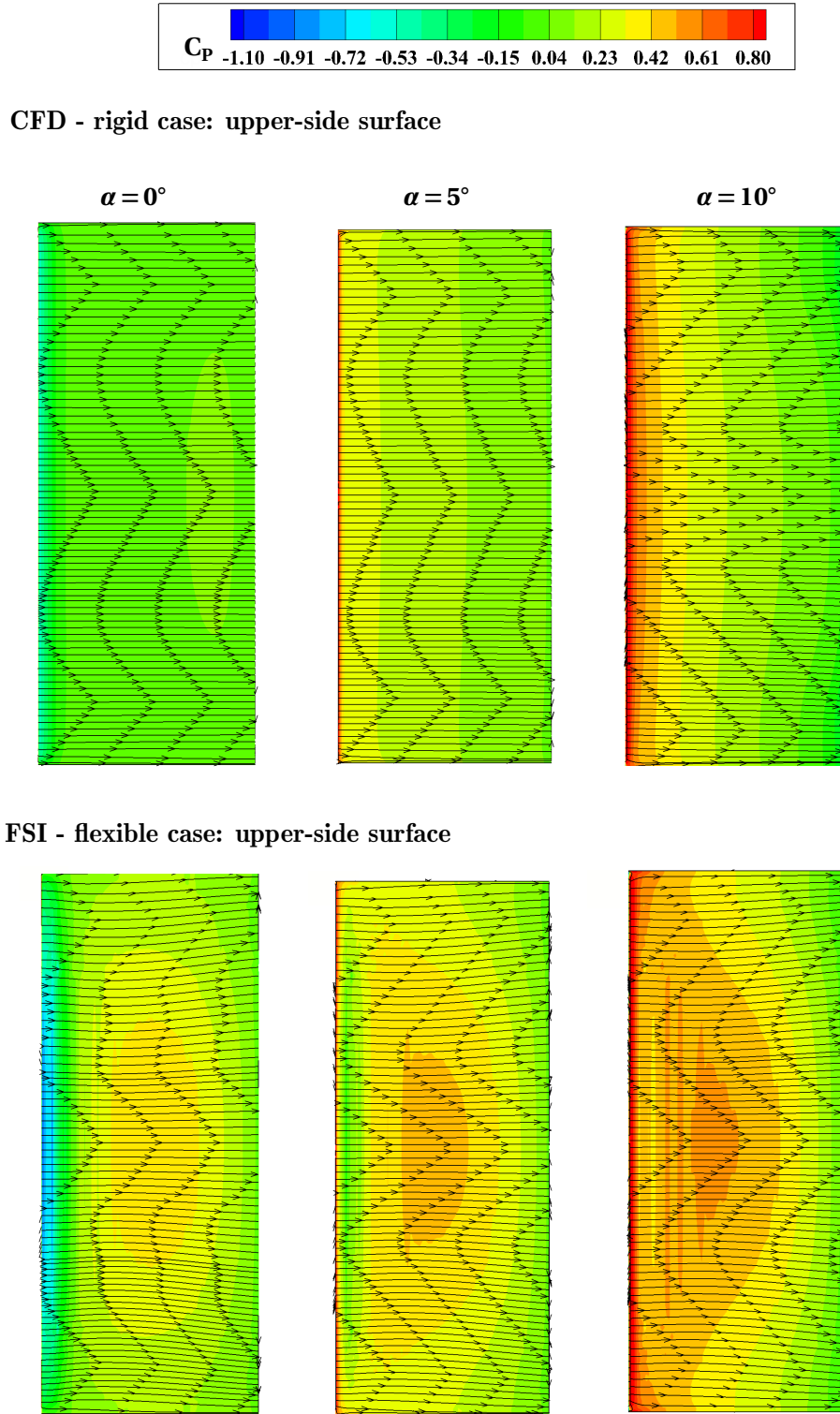


Figure 6.9: Comparison between flexible and rigid wings for the 2.5D WTA model: Evolution of C_p -X along the wing span at $\alpha = 0^\circ$, 5° and 10° at $q_\infty = 230$ Pa and visualization of the skin friction lines.

6.2 3D Model

The experimental and the numerical 3D WTA models are introduced in Sections 3.3.1.2 and 3.4.2. The wing is tapered and made without twist. The wing tip section was designed using a taper ratio of $\lambda = 0.6$ with a root chord length of $c_r = 0.5\text{m}$ and a tip chord length of $c_t = 0.3\text{m}$. The results presented in this section are based on the article published in the journal Advances in Aerodynamics [69]. The following section is organized into three main parts.

The first part gives experimental results. They permit to build a baseline case for the three-dimensional model. The aerodynamics forces obtained during wind tunnel campaigns are presented at various q_∞ and several α to extend the range of knowledge. Then, the membrane deflection is plotted along the wingspan for the same values of q_∞ and α . A relation and a comparison with Section 5.2 can be established.

In the second part, the FSI results are compared to experimental data. By this method, the accuracy of the computations can be estimated. The FSI are performed representing the entire three-dimensional tapered wing, which causes an extra complication in the wingspan direction in the computations of the structure compared to the previous case.

Finally, the last part gives a more detailed analysis of the flexible 3D WTA model by only considering the FSI computations. The pressure distribution and the flow field are examined to obtain a complete understanding of the aerodynamics of the 3D flexible wing. The data are compared to CFD results, representing a rigid wing, to understand the advantages of the flexible characteristics.

6.2.1 Baseline

6.2.1.1 Aerodynamic Forces

The experimental results obtained for C_L and C_D over α , and C_L over C_D are plotted for various values of q_∞ , namely 140 Pa, 310 Pa and 540 Pa, in Fig. 6.10. The following can be commented:

- For $q_\infty = 140\text{ Pa}$, C_L increases linearly with α until it reaches $C_{L-max} \simeq 1.3$ at $\alpha = 15^\circ$. Then, C_L decreases gradually suggesting the progression of the flow separation to the LE. The data at $q_\infty = 140\text{ Pa}$ are close to the values computed with a CFD method between $-5^\circ \leq \alpha \leq 8^\circ$. In Sec. 6.2.1.2, the membrane deflection is plotted for the various q_∞ and α . The membrane

deflection is observed quite small at $q_\infty = 140$ Pa, explaining the similar values of C_L with the CFD data. For $\alpha \geq 8^\circ$, a slight difference is observed between the curves representing the CFD and the FSI data suggesting that the pressure overcomes the structural forces and causes a membrane deflection.

- When q_∞ increases, $C_{L\alpha}$ becomes steeper between $-5^\circ \leq \alpha \leq 15^\circ$. This shows the pronounced dependency of the polars to q_∞ like it is noticed in Sec. 5.2. However, different effects are observed, which are closer to the results obtained by Beguin [18]. Instead of being shifted to higher angles of attack (right side of the curve) like in Sec. 5.2, the curve of C_L over α is shifted to higher values of C_L : the higher q_∞ is, the higher $C_{L\alpha}$ is. The latter is in opposition to the observations made in Sec. 5.2 but is in accordance with [18]. In Sec. 5.2, the membrane deflection is observed particularly high, resulting in a precipitation of the flow separation for smaller α . This results in lower $C_{L\alpha}$ at higher q_∞ . In the present section, it can be supposed that the flow separation does not appear for small α at high q_∞ explaining the tendency of $C_{L\alpha}$.
- As Beguin noticed in [18], the behavior of C_L with α becomes non-linear when q_∞ increases. The same phenomenon is visible between $-5^\circ \leq \alpha \leq 15^\circ$. The membrane deflection is higher with q_∞ (cf. Sec. 6.2.1.2), inducing higher cambers and leading to higher C_L . However, as the phenomenon is non-linear, C_L evolves non-linearly with α .
- Concerning C_D over α , C_D is higher for the flexible concept than the rigid one, due to higher C_L . C_L over C_D shows that the efficiency of the flexible concept is very similar to the rigid one between $-5^\circ \leq \alpha \leq 10^\circ$. However, the tendency is reversed for $\alpha > 15^\circ$. The latter suggests that the membrane allows a mitigation of the drag in the stall region of the wing. The membrane acts like a natural passive flow control.

6.2.1.2 Membrane Deformation

The membrane deflections measured during the wind tunnel campaigns are plotted in Figs. 6.13, 6.14 and 6.15. The figures illustrate the deflection for the same q_∞ values as previously and various α . The results have to be considered with the polars presented above. Figs. 6.13 and 6.14 represent the evolution of the deflection obtained at constant α with varying q_∞ , whereas Fig. 6.15 illustrates the evolution of the deflection at constant q_∞ with varying α .

Evolution with varying dynamic pressure q_∞ .

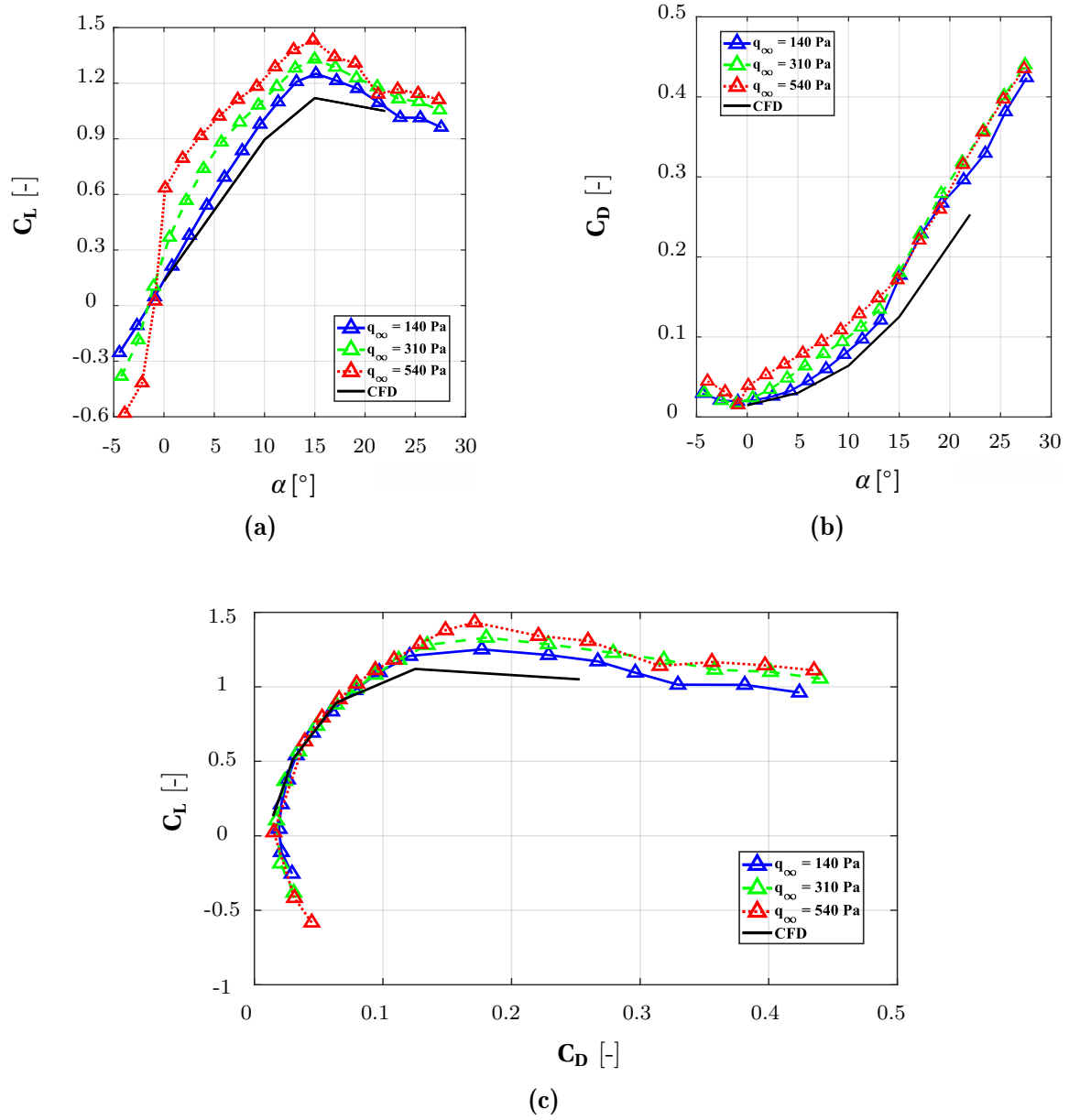


Figure 6.10: C_L - α and C_D - α and C_L - C_D for various q_∞ and for the CFD computations for the 3D WTA model.

The evolution of the membrane deflection is examined with varying q_∞ . The membrane deflection is plotted along the wing span at $Y = 0.96$, $Y = 0.59$ and $Y = 0.16$. The positions are chosen because they are representative of a three-dimensional flow. Indeed, the first position ($Y = 0.96$) represents the flow at the tip, the second position ($Y = 0.59$) the flow in the middle of the wing, and the last position ($Y = 0.16$) the flow at the root.

In general, the camber of each wing section is accentuated when q_∞ increases. Furthermore, the following observations can be made:

- As mentioned previously, the membrane deflection is small at $q_\infty = 140$ Pa compared to 310 Pa and 540 Pa. The membrane deflection is barely detected compared to the rigid geometry. The latter explains the similarity between the C_L and C_D values with the CFD data.
- If the deflection is considered along the wingspan, it is more pronounced in the middle and at the root of the wing, namely at $Y = 0.59$ and $Y = 0.16$, than at the tip ($Y = 0.96$). The deflection is small at the tip because of the compensation of the gradient of pressure.
- $\alpha = -5^\circ$: the deflection appears in the negative direction of z -direction in the middle and at the root of the wing. The negative camber induces a negative C_L value (cf. Fig. 6.10). The remark is valid for all the three values of q_∞ . Additionally, the higher q_∞ is, the more accentuated and negative the camber is. This induces higher values of C_L (cf. Fig. 6.10).
- $\alpha = 0^\circ$ and 5° : the deflection is in the positive direction of z -direction in the middle and at the root of the wing. The latter induces a positive C_L . The higher q_∞ is, the more accentuated and more positive the camber is, inducing values of C_L being more positive (cf. Fig. 6.10).
- $\alpha = 10^\circ$: the membrane deflects in the positive z -direction in the middle and at the root of the wing. However, the membrane deflection curvature changes from concave to convex near the TE. The second derivative of the contour $Z(X)$, d^2Z/dX^2 , is plotted with X in Fig. 6.11 in the middle and at the root of the wing, respectively at $Y = 0.59$ and $Y = 0.16$. The curvature's change occurs around $X = 0.8$, which is visible with the sign change of d^2Z/dX^2 . The phenomenon is more intense in the middle of the wing. This is related to the onset of the flow separation at the TE (cf. Sec. 5.1).
- $\alpha = 15^\circ$: the membrane deflects until $X = 0.4$ in the middle and at the root of the wing to positive z -direction and decreases linearly downstream. This is linked to the shift of the

flow separation to the LE (cf. Sec. 5.1). The linear decrease indicates that the onset of the flow separation starts around $X = 0.3$.

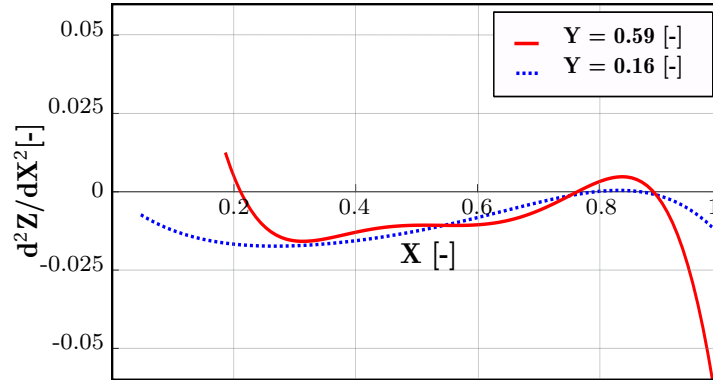


Figure 6.11: Curvature change at $q_\infty = 520$ Pa and $\alpha = 10^\circ$ for the 3D WTA model.

Evolution with varying angle of attack α .

The evolution of the membrane deflection is analyzed with varying α at constant q_∞ . The membrane deflection is plotted along the wing span at the same Y positions as previously. The following comments can be made:

- **$q_\infty = 140$ Pa:** the deflection of the membrane is small, which was already deduced from Fig. 6.10 and seen in Figs. 6.13 and 6.14. No difference can be detected in the deflection on the upper-side surface membrane and the rigid geometry between the various α . The pressure induced on the membrane is not sufficient with respect to the membrane tension to cause any dislocation. However, a difference is visible on the lower-side surface membrane. The deflection increases with α as it is expected.
- **$q_\infty = 310$ Pa:** the deflection is higher than at $q_\infty = 140$ Pa. At the wing root and in the middle of the wing, the deflection increases with α until 5° . At 10° , the deflection is lower than at 5° , which suggests that the flow separation already started. this is in accordance with Fig. 6.10 showing the slope $C_{L\alpha}$ decreasing after 7° . A change in the curvature is also observed in the middle and at the root of the wing (cf. Fig. 6.12). The upper-side surface section changes from concave to convex between $X = 0.6$ and $X = 0.8$, which is a sign that the flow separation appears near the TE between $X = 0.6$ and $X = 0.8$. At 15° , the deflection on the upper-side surface dropped and is completely lower than at 0° , 5° and 10° . The latter have to be considered with Fig. 6.10, where it is shown that C_{Lmax} is obtained for $\alpha = 15^\circ$. It can be deduced that the main part of the flow is separated at $\alpha = 15^\circ$, explaining the

deformation of the membrane, but not completely as C_L is at its maximum. At the wing tip, the membrane does deflect slightly due to the compensation of the pressure.

- $q_\infty = 540$ Pa: The camber of each section is clearly accentuated in the negative or the positive z -directions. This explains the more accentuated values of C_L in Fig. 6.10. The same comments as at $q_\infty = 310$ Pa can be made. Furthermore, the shift of $X_{Z_{max}}$ can be clearly observed to the LE with increasing α (cf. 5.1).

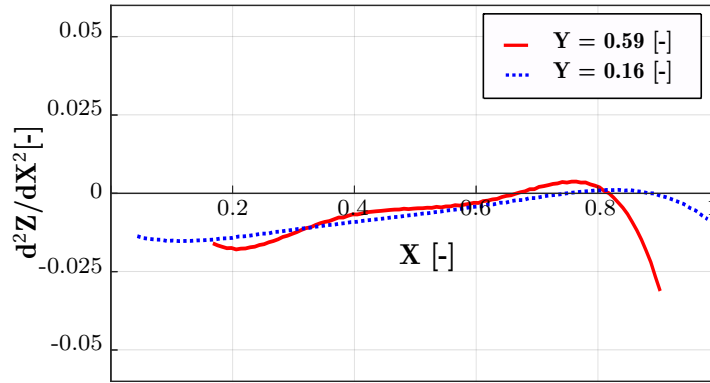


Figure 6.12: Curvature change at $q_\infty = 310$ Pa and $\alpha = 10^\circ$ for the 3D WTA model.

The wind tunnel campaigns conducted with the 3D WTA model show that the aerodynamics of the flexible wing are profoundly dependent of q_∞ . The latter is consistent with Sec. 5.2, where the same conclusion is made with FSI results on an airfoil. In the present section, the membrane flexibility permits a higher lifting capacity for higher q_∞ and a mitigation of the flow separation. C_L and C_D evolve gradually with α and q_∞ due to the passive adaptation of the membrane to the incoming flow. Although the results in the present section are different to the one obtained in Sec. 5.2, both sections indicate that the membrane acts like a natural passive flow control in the stall region of the wing.

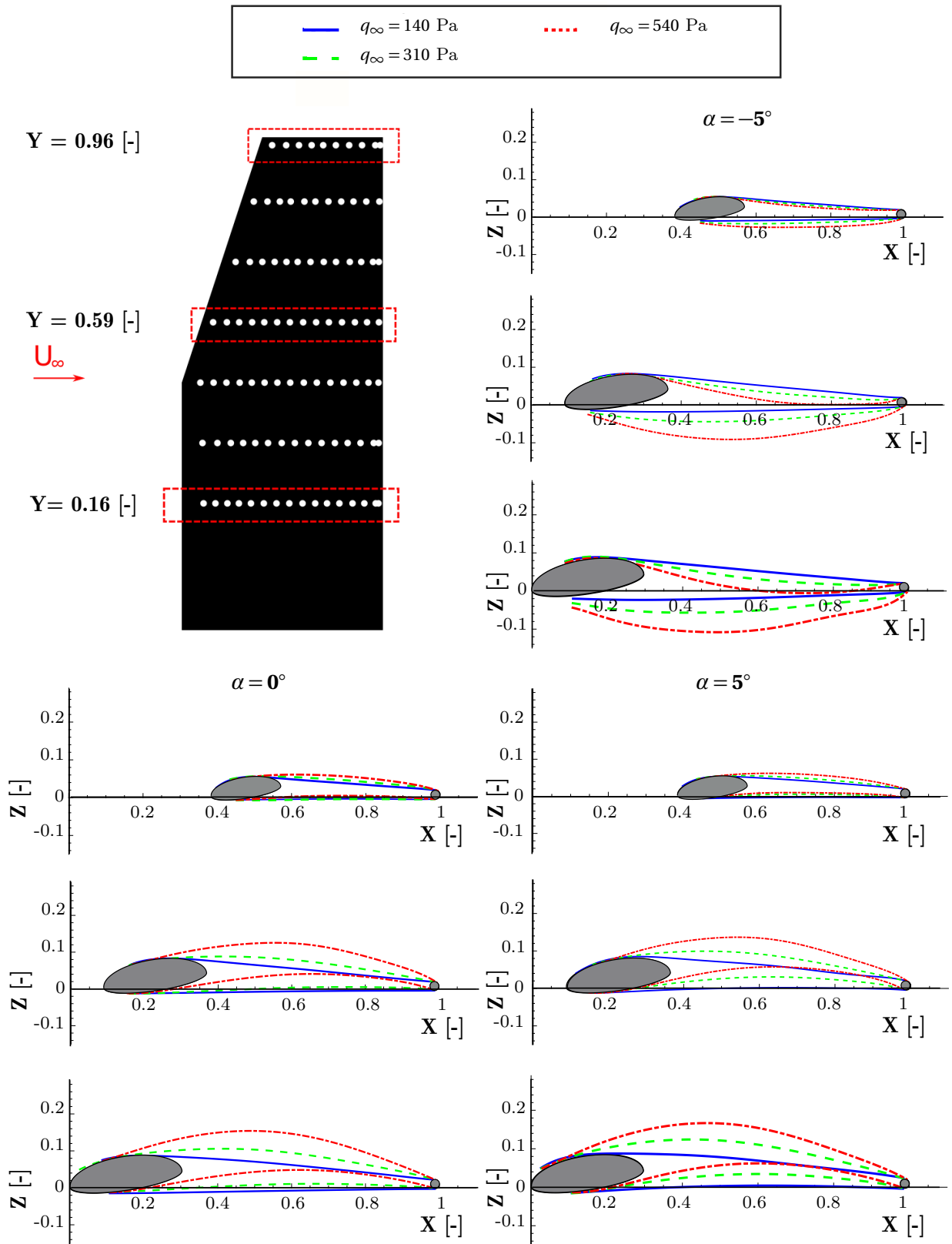


Figure 6.13: Comparison between the membrane deflection obtained for various q_∞ at $\alpha = -5^\circ, 0^\circ$ and 5° .

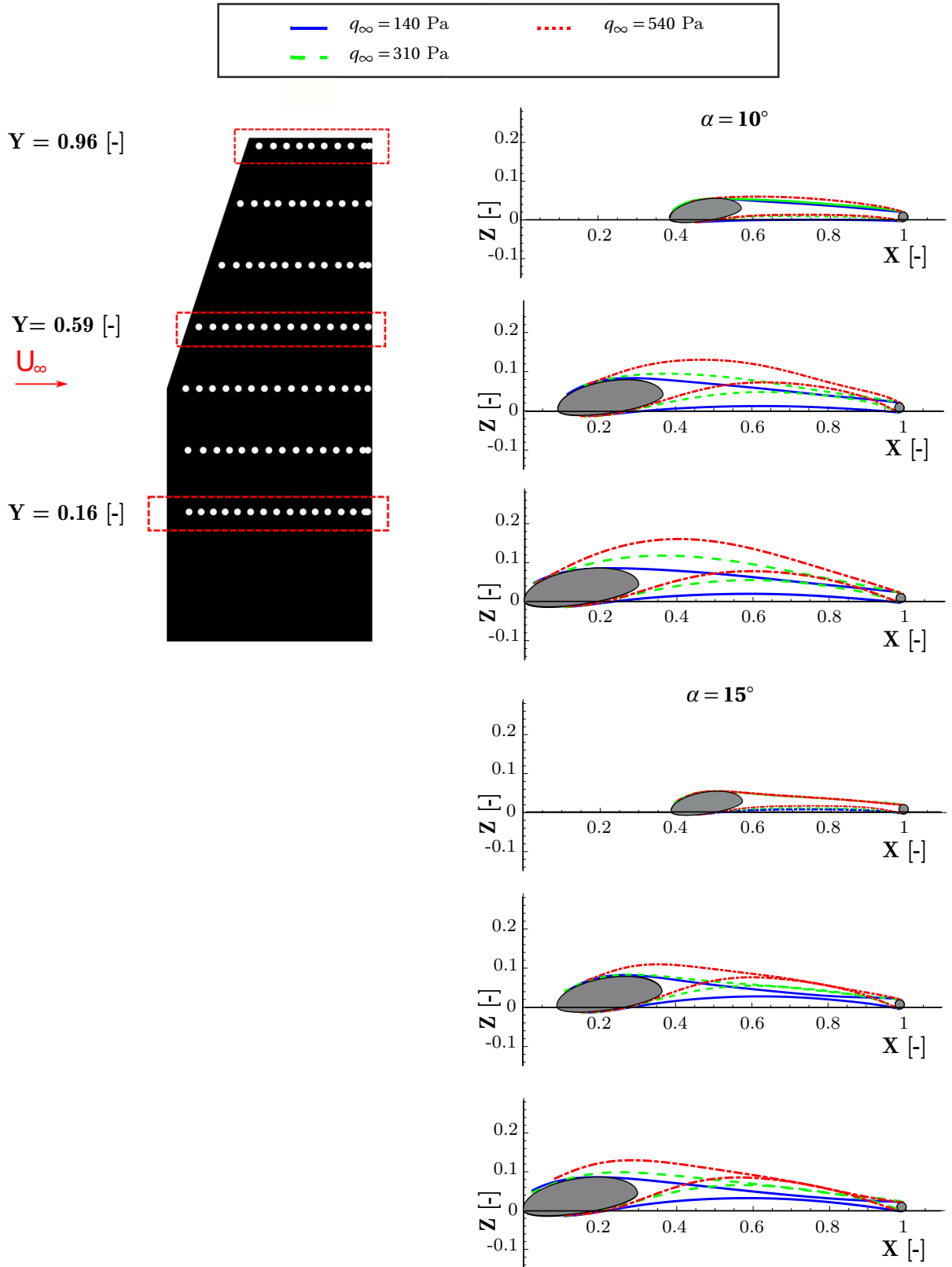


Figure 6.14: Comparison between the membrane deflection obtained for various q_∞ at $\alpha = 10^\circ$, and 15° .

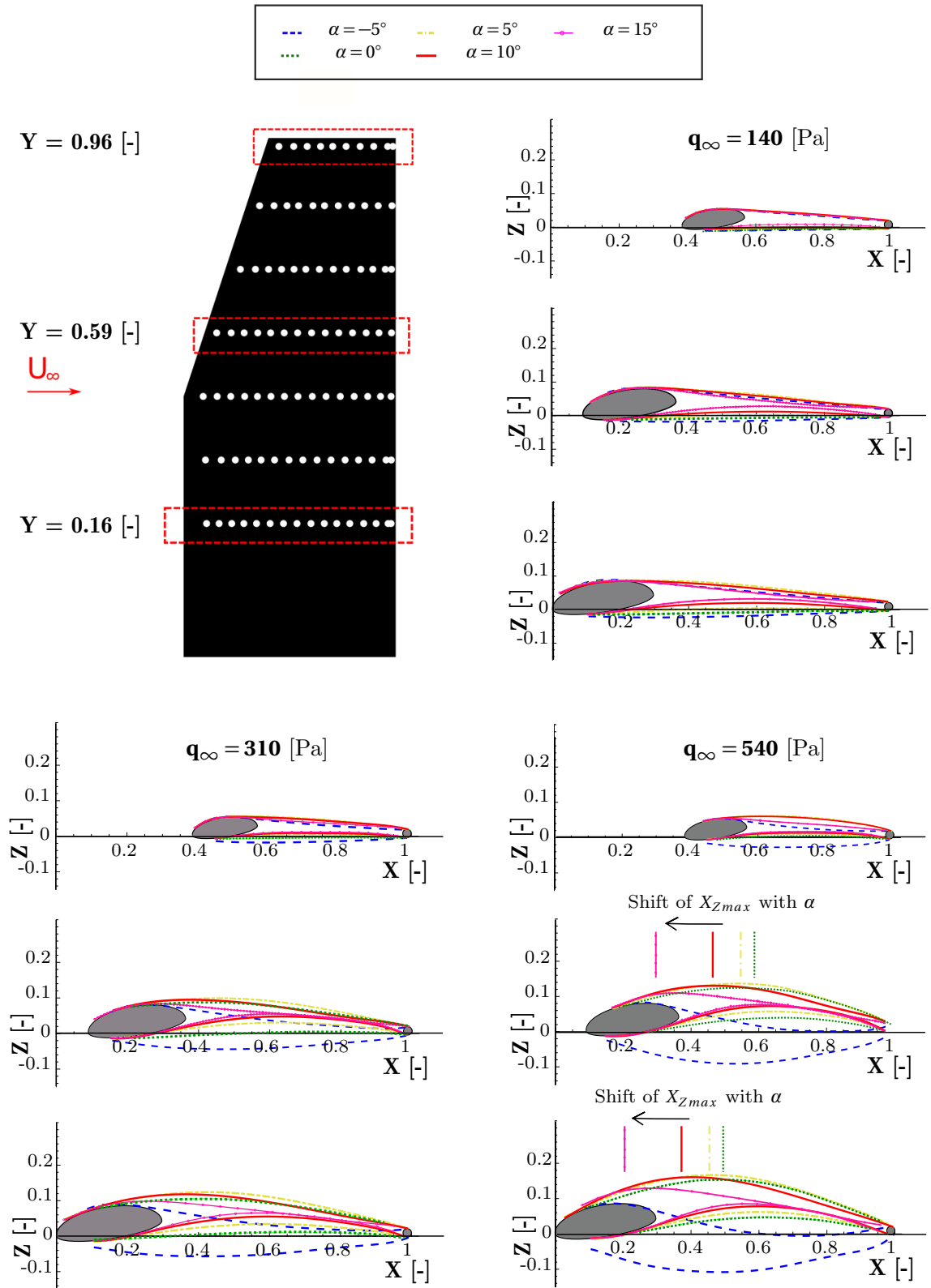


Figure 6.15: Comparison between the membrane deflection obtained for various q_∞ at several α .

6.2.2 Comparison between FSI and Wind-Tunnel Data

The results obtained with the computations are compared to experimental data for cross-evaluation. In the following, a comparison for $\alpha = 0^\circ, 5^\circ$ and 10° is performed at $q_\infty = 520$ Pa: firstly, C_L and C_D are compared as a function of α in Fig. 6.16 and secondly, the deflection of the membrane is plotted in Fig. 6.17.

6.2.2.1 Aerodynamic Forces

The FSI computations are performed as described in Section 3.4.2. The coupling is computed until the aerodynamic coefficients converge. The maximal error of C_L and C_D between the two latest iterations are equal to 0.35% and 0.4%, respectively. During the wind tunnel campaigns, a hysteresis phenomenon is observed. Repeated measurements are conducted and the maximum and the minimum values are reported on the polar. The following comments can be made concerning the comparison between both set of data:

- $\alpha = 0^\circ$: C_L and C_D are computed 0.51 and 0.034, respectively. As observed in Fig. 6.16, the hysteresis phenomenon is particularly strong at the aforementioned α . The average of the forces gives $C_L = 0.6$ and $C_D = 0.036$. The deviation between FSI computations and experiments is estimated to 17% and 6% for C_L and C_D , respectively, by using a relative error formula.
- $\alpha = 5^\circ$: the FSI computations estimate $C_L = 0.85$ and $C_D = 0.059$, whereas an average of $C_L = 0.92$ and $C_D = 0.079$ is measured. Therefore, a relative error of 7% and 25% for C_L and C_D is calculated between FSI computations and wind tunnel data.
- $\alpha = 10^\circ$: C_L and C_D are predicted = 1.18 and 0.124. The wind tunnel tests measured $C_L = 1.11$ and $C_D = 0.113$ at $\alpha = 9^\circ$ and $C_L = 1.18$ and $C_D = 0.130$ at $\alpha = 11^\circ$: the deviations between FSI computations and wind tunnel data are under 6.2% and 9% for C_L and C_D , respectively.

The FSI computations show a fair agreement with the wind-tunnel data. The deviations obtained within C_L and C_D can be explained by analyzing the membrane deflection described in the following section.

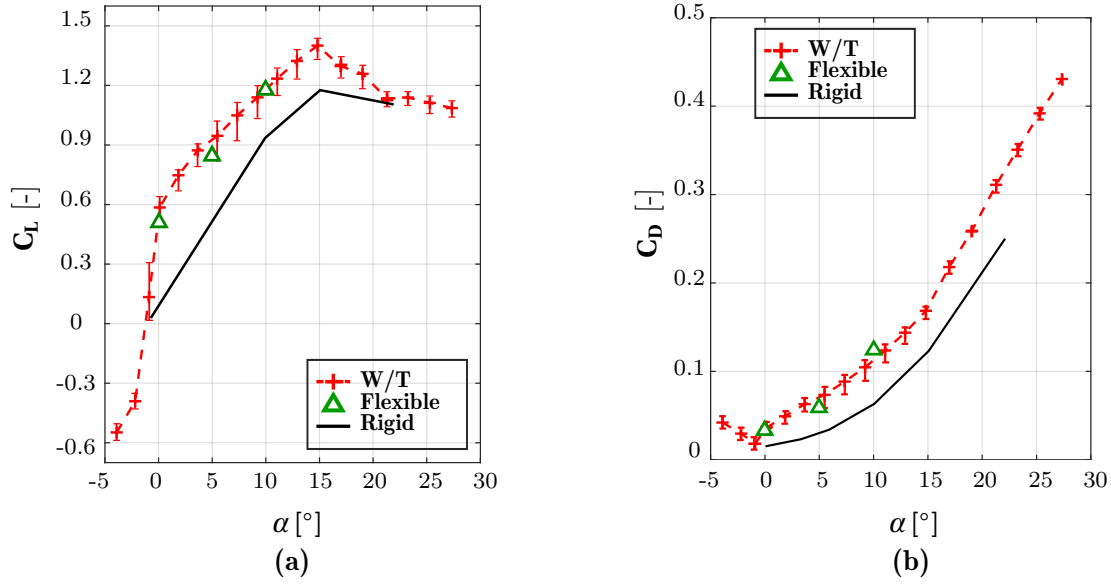


Figure 6.16: Comparison between the flexible case, the rigid case and the force measurement data: C_L - α and C_D - α curves at $q_\infty = 520$ Pa for the 3D WTA model.

6.2.2.2 Membrane Deflection

The membrane deflection is plotted in Fig. 6.17 for $\alpha = 0^\circ$, 5° and 10° at $q_\infty = 520$ Pa. The figure shows the membrane deflection for the FSI results and the experimental data at $Y = 0.96$, $Y = 0.59$ and $Y = 0.16$. The error norm L2 described by equation 4.1 is used to calculate the deviation. Table 6.4 recapitulates the values of the deviation with α on the upper- and lower-side surface of the membrane. The following can be commented:

- $\alpha = 0^\circ$: on the lower-side surface, the approximation of the deflection is good. The maximal error is equal to 7% at the tip of the wing.

On the upper-side surface, the maximal deviations are located at $Y = 0.16$ and $Y = 0.59$, with errors being between 16–17%. The main issue is that the FSI does not reproduce well the contour of the membrane around the LE at $X = 0.2$ – 0.3 . The reason is in the absence of contact modeling in the FEM solver. The contact between the LE and the membrane is not modeled, which disturb the estimation of the deflection at this location (like in Sec. 6.1.1). Even if an estimation of the abscissa where the deflection detaches the LE is conducted, the prediction of the membrane deflection on the LE (at $X = 0.2$ – 0.3) differ with the wind tunnel data. The latter can be a reason in the deviation between the values of C_L in Fig. 6.16.

- $\alpha = 5^\circ$: the membrane deflection is well estimated at $Y = 0.16$ on both surfaces. The maximal deviation is observed at $Y = 0.59$ where the norm error is equal to 14% and 16% on the upper- and the lower-side surface, respectively. At the wing tip, the error norm is equal to 13% and 10% on the upper- and the lower-side surface. In general, the FSI computations underestimate the membrane deflection along the wingspan explaining the deviation in C_L and C_D observed in Fig. 6.16.
- $\alpha = 10^\circ$: on the upper-side surface, the deflection is well estimated. A maximal deviation of 15% is reported at $Y = 0.16$. On the lower-side surface, the deviations are more important for this case than the two others. The error norm approaches 30% in the middle of the wing, which can not be explained at that time. Nevertheless, C_L and C_D are well predicted as observed in the polar.

α	surface side	$Y = 0.16$	$Y = 0.59$	$Y = 0.96$
0°	upper	16%	17%	7%
	lower	3%	5%	7%
5°	upper	10%	14%	13%
	lower	11%	16%	10%
10°	upper	15%	14%	13%
	lower	17%	29%	13%

Table 6.4: Estimation of the norm error L2 between the FSI and the photogrammetry data for the 3D WTA model.

Even if deviations are reported, the comparison shows a fair agreement on the membrane deflection obtained with the FSI computations and the experimental data. However, a comment has to be made. The absence of contact modeling between the membrane and the LE leads to uncertainties on the prediction of the abscissa where the membrane detaches the LE. The mentioned abscissa is more upstream in the experiments than in the computations.

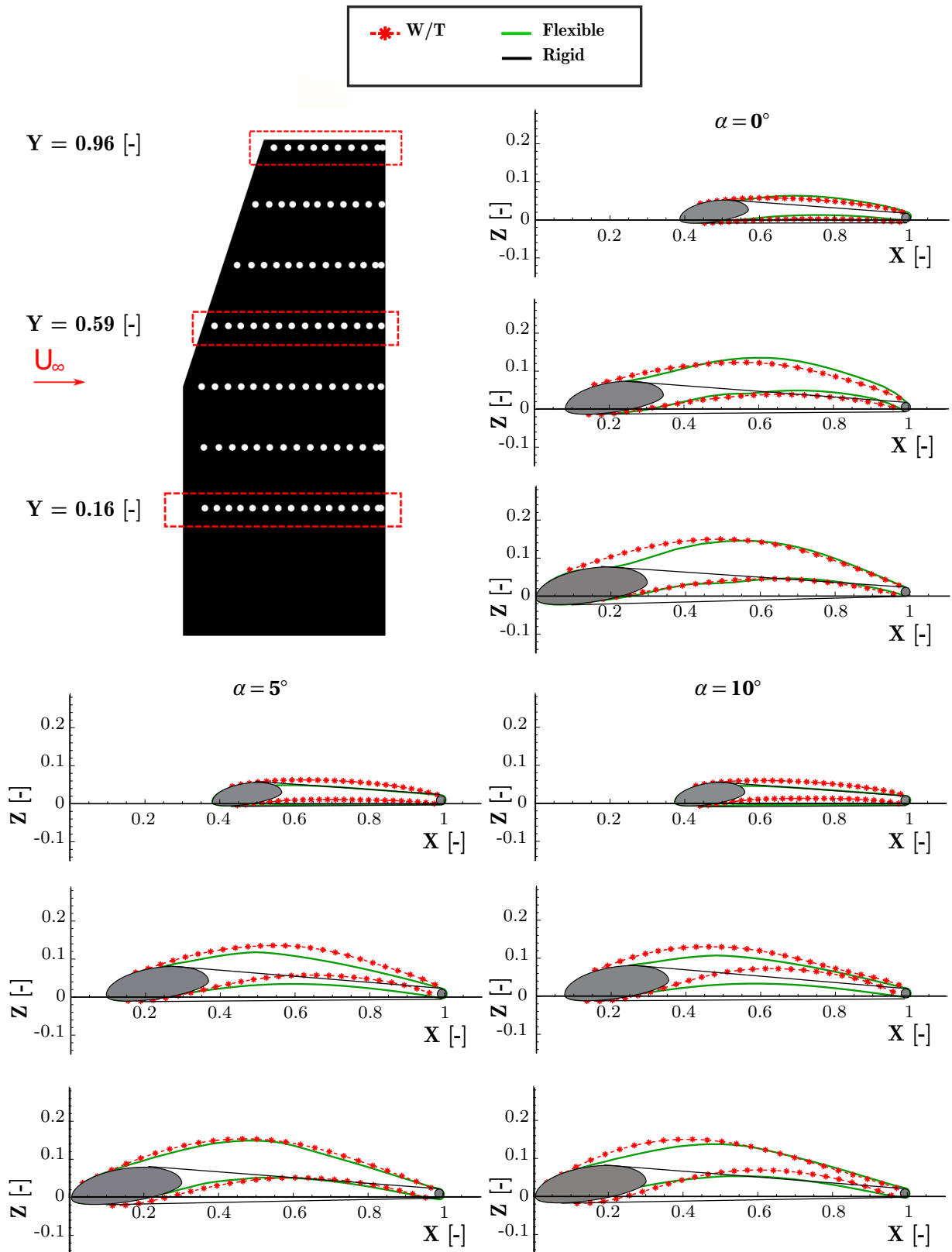


Figure 6.17: Comparison between FSI results and the photogrammetry measurement data at $\alpha = 0^\circ$, 5° and 10° and $q_\infty = 520$ Pa for the 3D WTA model.

6.2.3 Numerical Study

In order to extend the knowledge of the aerodynamics on flexible wings, a detailed analysis of the FSI on the 3D WTA model is proposed in the present section. Pressure measurements appear difficult to conduct without disturbing the flow in the wind tunnel, the computations are a good solution to analyze this parameter. Furthermore, a rigid experimental model is not available in the present thesis. Therefore, the computations show once more their advantages as it is simple to model a rigid case using CFD computations. The section is organized with the angles of attack as in Sec. 6.1.2.

6.2.3.1 Zero angle of attack ($\alpha = 0^\circ$)

The results obtained for the rigid and the flexible geometry at $\alpha = 0^\circ$ and $q_\infty = 520$ Pa are depicted in Figs. 6.18, 6.25, 6.26 and 6.27. The figures represent the pressure distribution, the local lift distribution and the skin friction lines along the wings.

In Figs. 6.25, 6.26 and 6.27, the pressure distribution is observed different along the wing span for both the rigid and the flexible geometries. At $Y = 0.16$ and 0.59 , $-C_p$ reaches values up to 1 on the upper-side surface of the flexible wing whereas it is significantly lower for the rigid geometry. The maximal values are furthermore achieved downstream for the flexible case around $X = 0.6$, whereas it is at $X = 0.2$ for the rigid case. As already mentioned, the membrane allows a deflection to the positive z -direction. The suction peak moves downstream inducing a higher camber and a higher acceleration region. At $Y = 0.96$, $-C_p$ is still higher on the suction side of the flexible geometry but the difference between $-C_p$ decreases due to the pressure compensation.

One remark has to be made concerning the evolution of $-C_p$. $-C_p$ is directly connected to the geometry obtained in Fig. 6.17. The contact between the LE and the membrane being not modeled, the location where the membrane detaches the LE is underestimated. This results in an unconventional contour between $0 \leq X \leq 0.3$ (Fig. 6.17) and consequently an unconventional evolution of $-C_p$.

In general, $-C_p$ reaches higher values on a bigger range of the wing for the flexible case in comparison to its rigid counterpart. One consequence is observed through the local lift coefficient along the wing span (cf. Fig. 6.18) being calculated according to Eq. 2.36. The values obtained for the flexible geometry are much higher than the values obtained for the rigid case. The latter

is due to the higher camber and the higher suction peak. Consequently, C_L is equal to 0.510 for the flexible geometry against 0.132 for the rigid one, which corresponds to ≈ 4 times higher. C_D is higher for the flexible case due to higher C_L , but the efficiency is equal to 15 for the flexible case against 8.8 for the rigid one.

The flow field, namely u/U_∞ and w/U_∞ , is represented in Fig. 6.19 with the description of the streamlines. In Fig. 6.19, the two components of the velocity vector are compared for the rigid and the flexible wing at $Y = 0.16$ and $Y = 0.71$. As the membrane deflects in the positive z -direction, each section of the flexible wing has a higher camber than the rigid wing and the flow can accelerate on a larger region. This is directly observed with u/U_∞ being ≥ 1.1 on a large region in the x -direction at $Y = 0.71$, whereas the same region is located near the LE for the rigid case. The latter has to be connected to the pressure distribution described in Fig. 6.25, where it is noticed that the maximum of $-C_p$ is reached for $X = 0.6$ in the flexible case against $X = 0.2$ in the rigid one.

Furthermore, w/U_∞ is more negative in the flexible than in the rigid case for $X \geq 0.2$. The latter is due to the contour Z of the membrane. dZ/dx being more negative in the flexible case, w/U_∞ has to be more negative.

If the skin friction lines are observed (cf. Figs. 6.26 and 6.27), they appear more deviated on both side of the flexible wing in comparison to the rigid geometry. The deviation is clearly visible to the inside of the wing on the upper-side surface, whereas it is clearly observed on the outside of the wing on the lower-side surface. The latter is due to the camber. As each section of the flexible wing is more cambered than the sections of the rigid one, the deviations of the skin friction lines are more accentuated for the flexible case.

-	C_L	C_D	C_L/C_D
CFD, rigid	0.132	0.015	8.80
FSI, flexible	0.510	0.034	15.00

Table 6.5: Values of the aerodynamic coefficients obtained for the flexible and the rigid cases at $\alpha = 0^\circ$ and $q_\infty = 520$ Pa for the 3D WTA model.

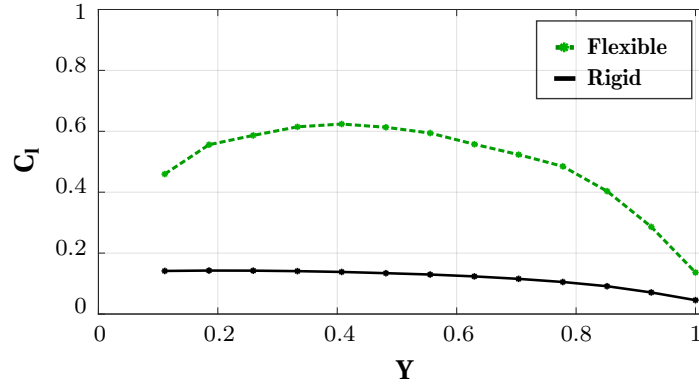


Figure 6.18: Comparison for the flexible and the rigid cases: Local lift distribution along the wing span at $\alpha = 0^\circ$ and $q_\infty = 520$ Pa.

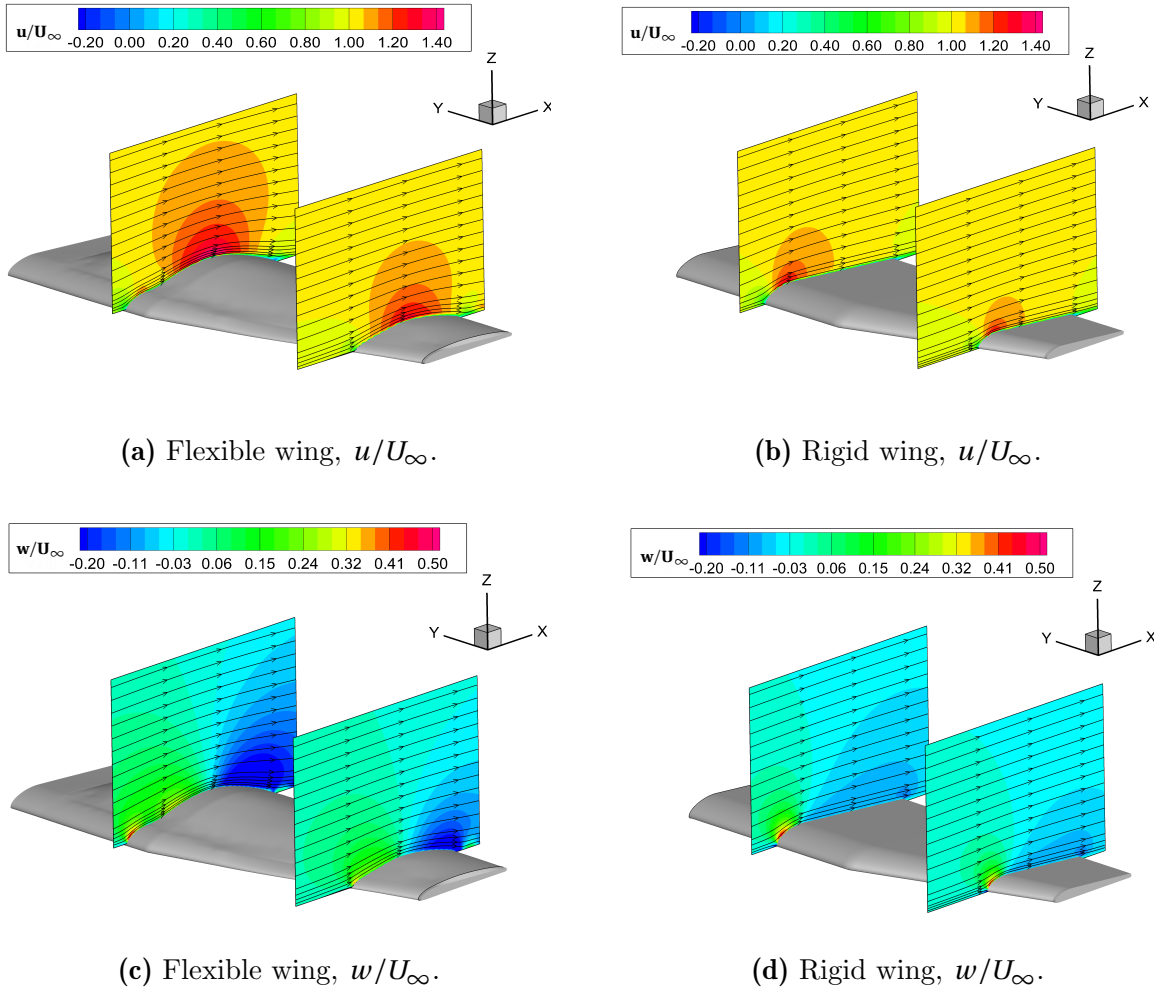


Figure 6.19: Comparison for the flexible and the rigid cases for the 3D WTA model: Axial component u and vertical component w of the flow field velocity at $\alpha = 0^\circ$ at $q_\infty = 520$ Pa.

6.2.3.2 Moderate angle of attack ($\alpha = 5^\circ$)

The results obtained for the rigid and the flexible geometry at $\alpha = 5^\circ$ and $q_\infty = 520$ Pa are depicted in Figs. 6.20, 6.25, 6.26 and 6.27. Like previously, the figures illustrate the evolution of the pressure distribution, the local lift and the skin friction lines along the wing span.

Similar comments can be made as for the case $\alpha = 0^\circ$:

- the suction is more intense and more downstream on the flexible than on the rigid wing.
- the local lift is higher for the flexible wing as for the rigid one. The flexible wing has a total C_L and C_D equal to 0.852 and 0.059, whereas they are equal to 0.514 and 0.03 for the rigid wing. However, one significant difference is that the efficiency becomes smaller for the flexible wing, as it is specified in Table 6.6. The efficiency is equal to 14.44 for the flexible case against 17.13 for the rigid case.
- u/U_∞ reaches higher values on a higher range of the flexible wing, whereas w/U_∞ is smaller.
- in Figs. 6.26 and 6.27, the skin friction lines are more deviated for the flexible wing. The skin friction lines show the creation of the tip vortex for both geometries more intense than at $\alpha = 0^\circ$. The evolution of the tip vortex is represented in Fig. 6.22, where the vorticity ($\omega_x c_r / U_\infty$) and the velocity vectors are plotted in two planes at $X = 1.5$ and $X = 3.5$ for the flexible and the rigid geometries.

-	C_L	C_D	C_L/C_D
CFD, rigid	0.514	0.030	17.13
FSI, flexible	0.852	0.059	14.44

Table 6.6: Values of the aerodynamic coefficients obtained for the flexible and the rigid cases at $\alpha = 5^\circ$ and $q_\infty = 520$ Pa for the 3D WTA model.

6.2.3.3 High angle of attack ($\alpha = 10^\circ$)

Figs. 6.25, 6.26 and 6.27 show the evolution of the pressure distribution in the chord direction along the wing span at $\alpha = 10^\circ$ and $q_\infty = 520$ Pa. The same remarks can be commented as for the cases $\alpha = 0^\circ$ and 5° . Only the difference with the two aforementioned cases are discussed in the following:

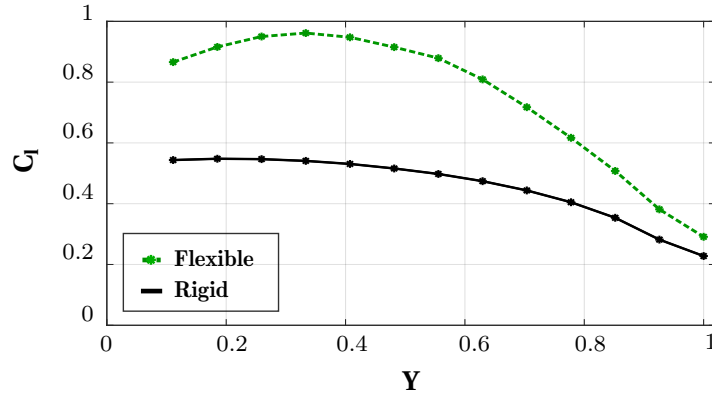


Figure 6.20: Comparison between flexible and rigid wings for the 3D WTA model: Local lift distribution along the wing span at $\alpha = 5^\circ$ and $q_\infty = 520$ Pa.

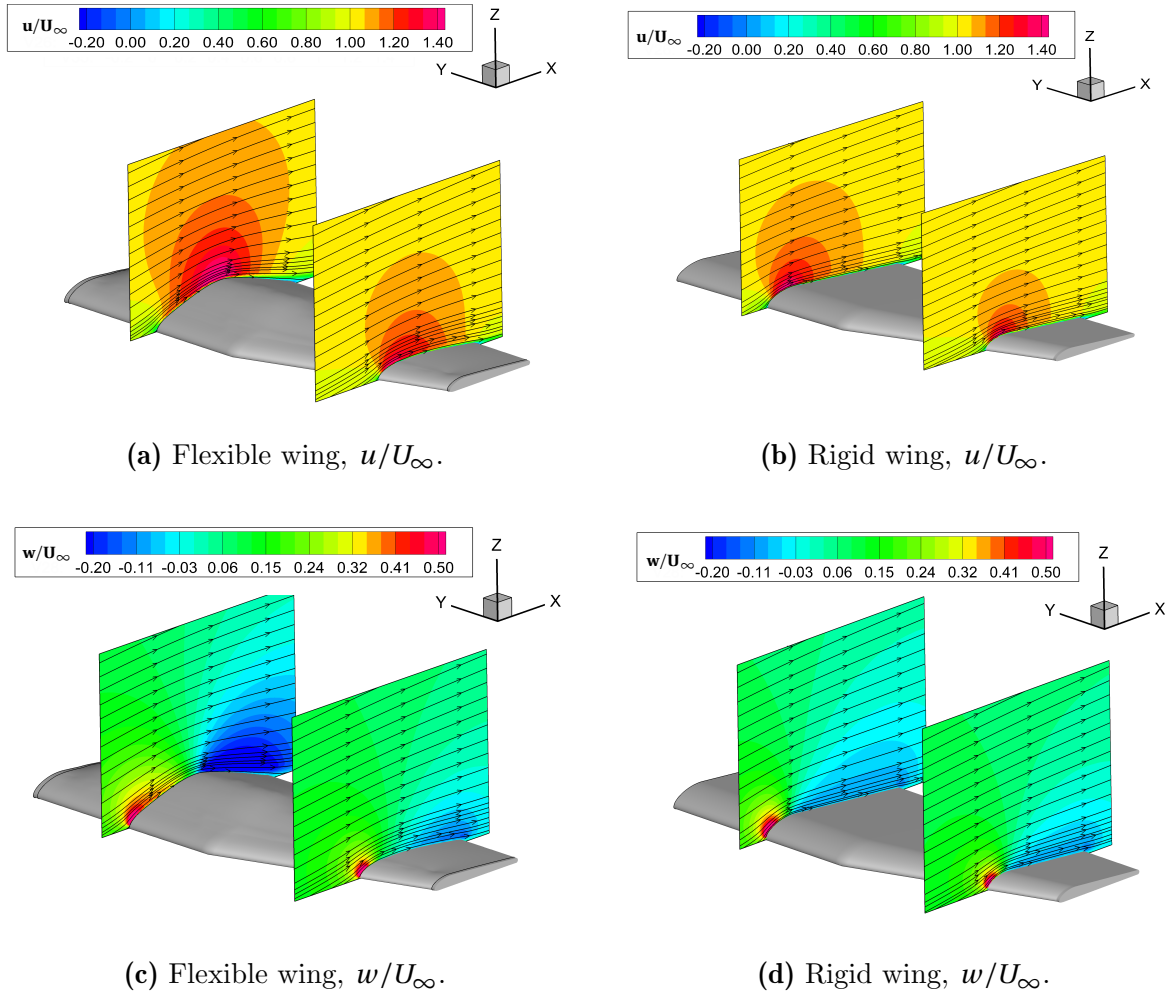


Figure 6.21: Comparison between flexible and rigid wings for the 3D WTA model: Axial component u and vertical component w of the flow field velocity at $\alpha = 5^\circ$ at $q_\infty = 230$ Pa.

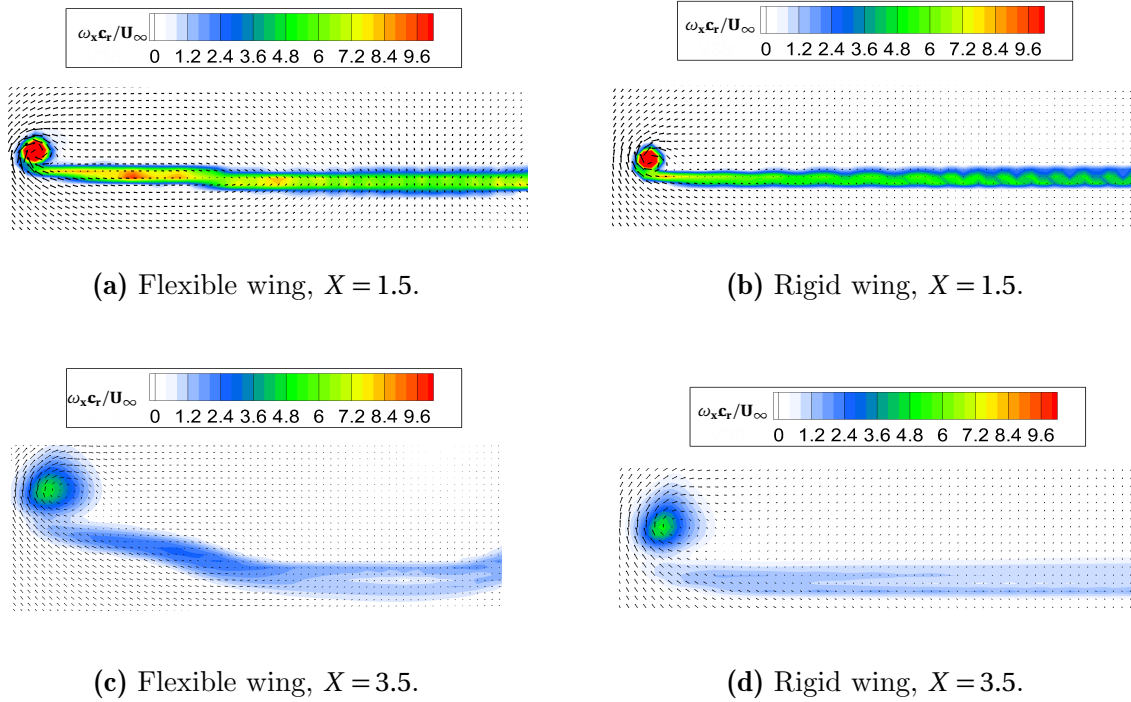


Figure 6.22: Comparison between flexible and rigid wings for the 3D WTA model: Vorticity $\omega_x \cdot c_r / U_\infty$ at $\alpha = 5^\circ$ at $q_\infty = 520$ Pa.

- Table 6.7 indicates that C_L and C_D are higher and the efficiency is smaller for the flexible wing. However, the loss of efficiency between the cases $\alpha = 5^\circ$ and 10° is smaller for the flexible than the rigid geometry. Indeed, the efficiency drops by approximately 66% for the flexible wing against approximately 80% for the rigid one.
- in Fig. 6.26, a recirculation region is observed where the skin friction lines converge on the upper-side surface of the flexible wing. The convergence of the lines is representative of a flow separation. In this case, it is assumed that the flow separation is the result of a too high membrane deflection as it does not occur for the rigid wing. The flow separation stays small as it is observed in Fig. 6.23 at $Y = 0.16$. The latter is consistent with the observations made in Sec. 5.2: a flow separation follows a too high-cambered geometry. Furthermore, the skin friction lines point out a more intense tip vortex than at $\alpha = 5^\circ$, which is described by the evolution of the vorticity ($\omega_x c_r / U_\infty$) in Fig. 6.24. The region of high vorticity is definitely larger at $\alpha = 10^\circ$ than at 5° .

-	C_L	C_D	C_L/C_D
CFD, rigid	0.895	0.064	13.4
FSI, flexible	1.182	0.124	9.53

Table 6.7: Values of the aerodynamic coefficients obtained for the flexible and the rigid cases at $\alpha = 10^\circ$ and $q_\infty = 520$ Pa for the 3D WTA model.

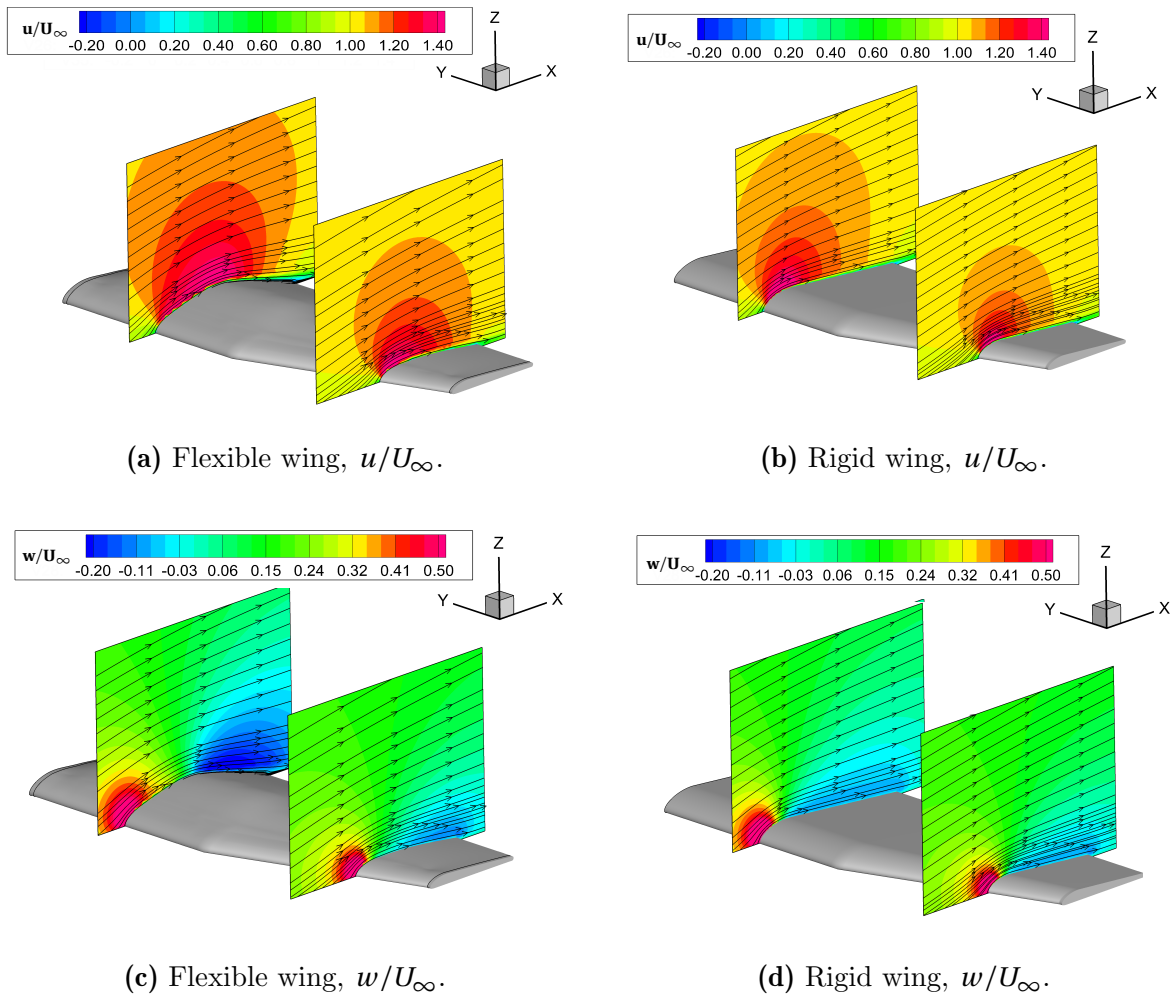


Figure 6.23: Comparison between flexible and rigid wings for the 3D WTA model: Axial component u and vertical component w of the flow field velocity at $\alpha = 10^\circ$ at $q_\infty = 230$ Pa.

Summary

The analysis of the FSI computations on the 3D flexible wing show similar conclusions than for the 2.5D wing. The flexibility of the membrane allows the sections of the wing to have a more accentuated camber. The flow can accelerate on a larger region on the upper-side surface of the

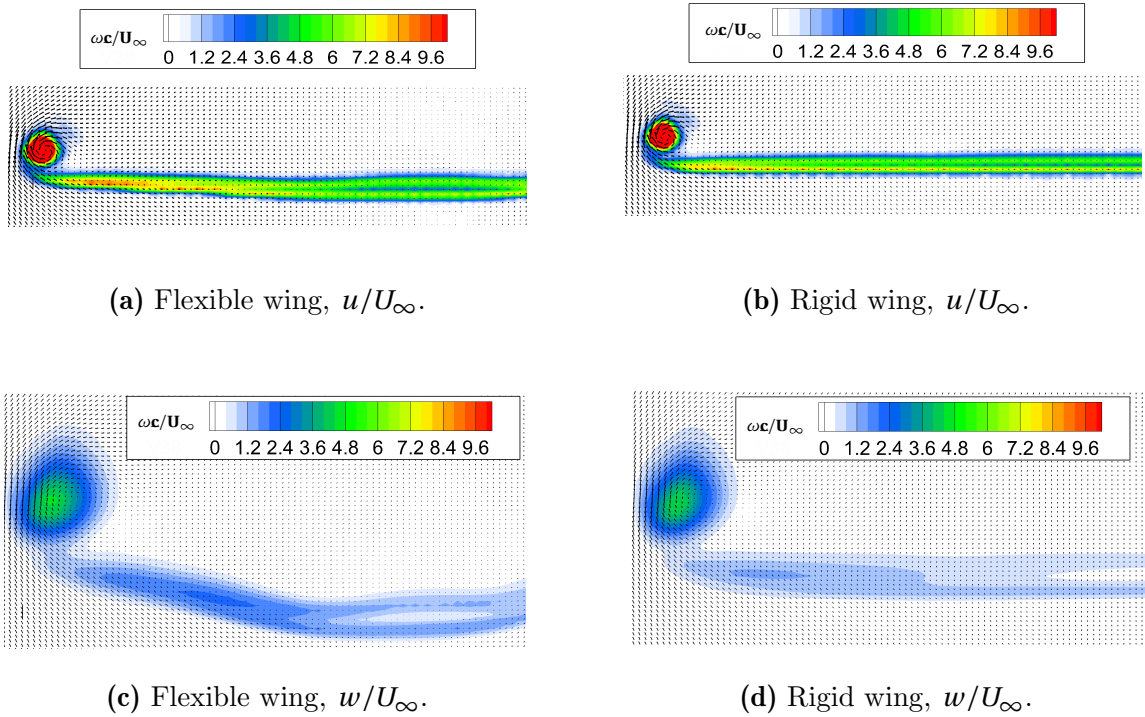


Figure 6.24: Comparison between flexible and rigid wings for the 3D WTA model: Vorticity $\omega_x \cdot c/U_\infty$ at $\alpha = 10^\circ$ at $q_\infty = 520$ Pa.

wing, which results in an increased suction level. At the tip of the 3D flexible wing, the deflection is low because of the compensation of the pressure gradient. This results in an enhancement of the lifting capacity. The present section allows also an interesting conclusion already suggested by Sec. 5.2. A flow separation follows a high deflection of the membrane. Therefore, the choice of the material and the pre-stress of the membrane has to be done carefully in order to keep the advantages of the flexible membrane mentioned in Sec. 5.1.

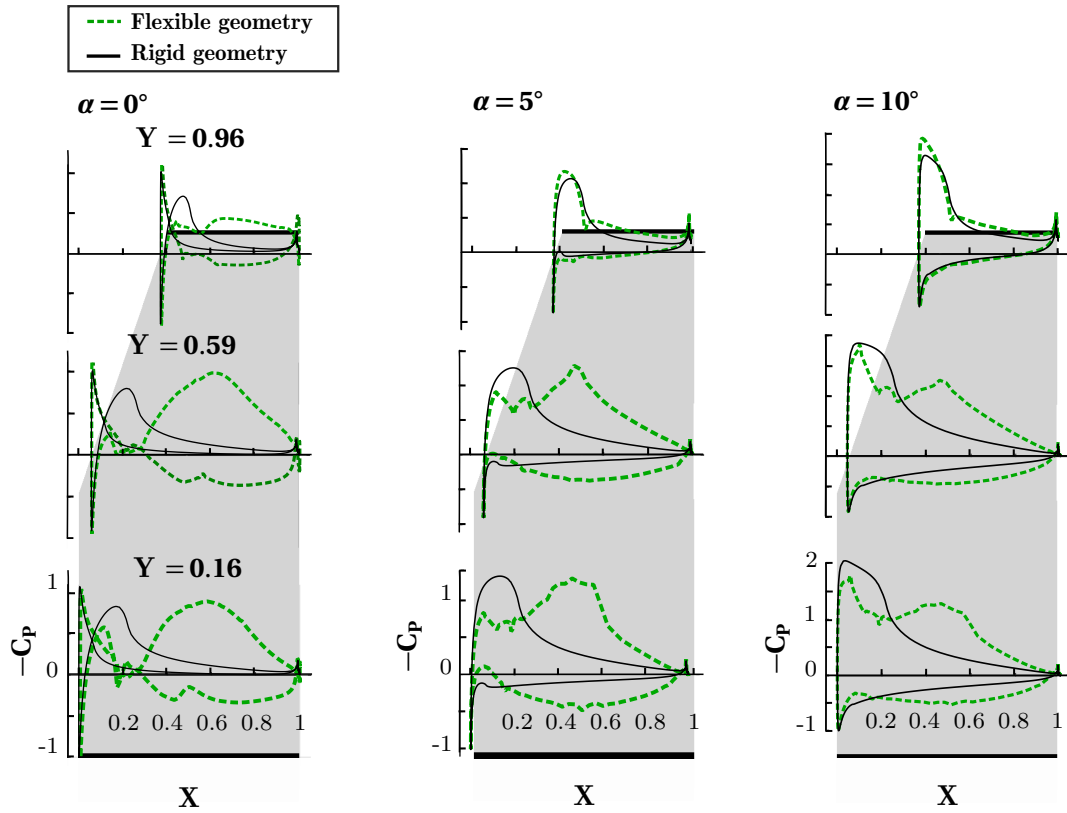


Figure 6.25: Comparison between flexible and rigid wings for the 3D WTA model: Evolution of $-C_p$ - X along the wing span at $\alpha = 0^\circ$, 5° and 10° and $q_\infty = 520$ Pa.

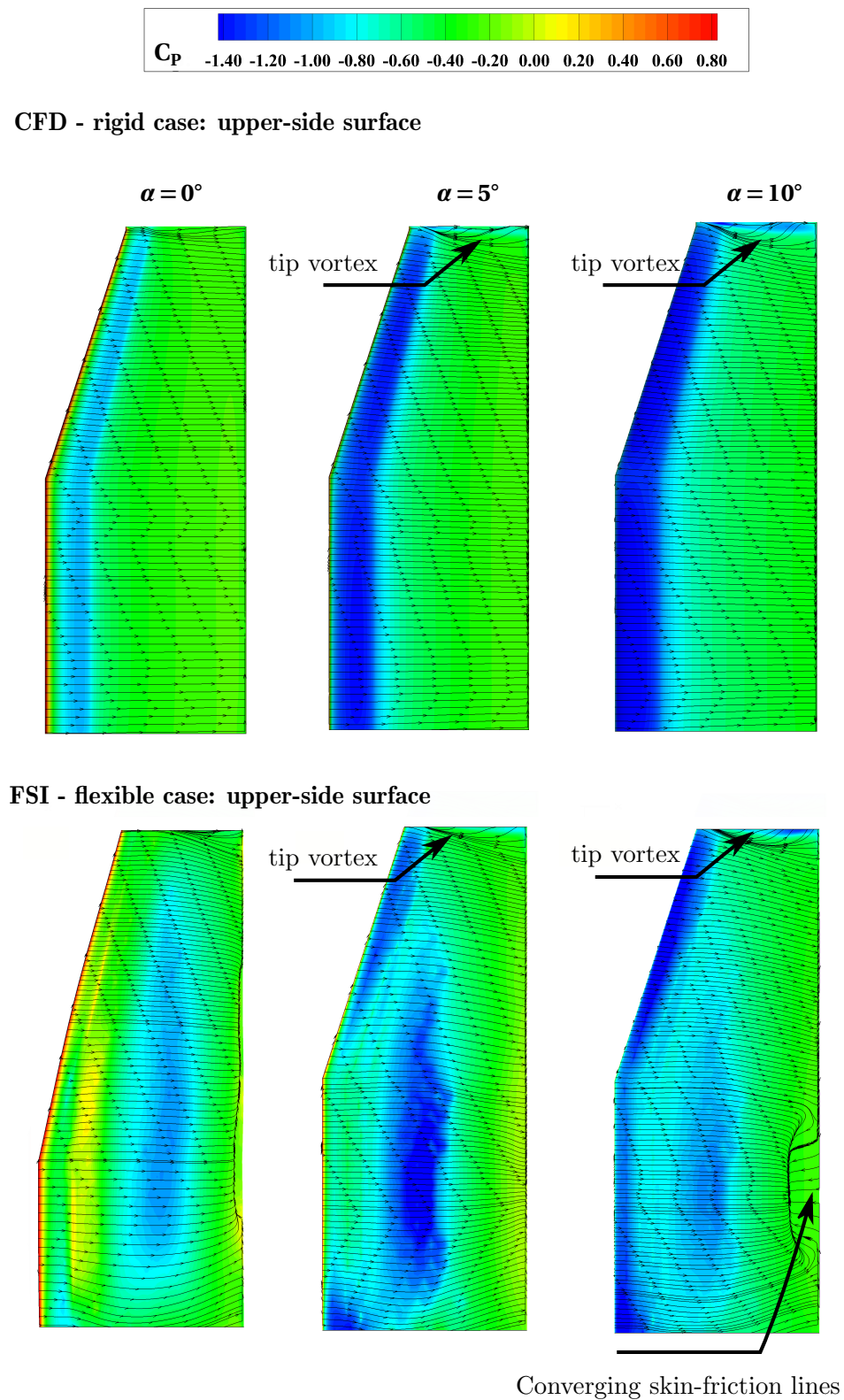


Figure 6.26: Comparison between flexible and rigid wings for the 3D WTA model: Evolution of C_p along the wing span at $\alpha = 0^\circ$, 5° and 10° at $q_\infty = 520$ Pa and visualization of the skin friction lines.

Chapter 7 - Conclusions and Outlook

The concept of wings made of an elasto-flexible membrane shows promising results to enlarge the flight envelope of a wing. The flexibility and the adaptivity of a membrane material as a lifting surface have been exploited by the Micro Air Vehicles domain since the last decade. The present dissertation focused on the analysis of such a wing on larger scale with numerical investigations. The motivation was to extend the concept for applications at higher Reynolds numbers like small flight vehicles or wind turbines and to conclude the benefits gained.

A detailed analysis on elasto-flexible concepts was conducted through numerical investigations involving Fluid-Structure Interaction (FSI) computations. As the deflection of the structure was important enough to alter the fluid flow, a two-way interaction had to be considered to model the reciprocity between the fluid and the structure. It was decided to take advantage of partitioned coupling techniques to develop the two-way interaction. Well developed solvers were chosen to separately solve the fluid and the structure states: on the one hand, the solvers ANSYS CFX and the TAU code and on the other hand, the solver ANSYS APDL and the code CARAT++. ANSYS CFX and the TAU Code use the Finite Volume Method approach and the Unsteady Reynolds Averaged Navier-Stokes turbulence modeling to solve the flow state, while ANSYS APDL and the CARAT++ Code exploit the Finite Element Method to calculate the structural displacement. In order to enable the exchange between the solvers, outer coupling tools were needed. The ANSYS MFX-MultiField was exploited to couple ANSYS CFX and ANSYS APDL, whereas EMPIRE linked the TAU and CARAT++ codes. The couplings were developed using the semi-implicit time stepping scheme and two mesh mapping approaches, namely the Nearest Element Interpolation Method and the Dual Mortar Mapping.

In total, four configurations were numerically analyzed from airfoils to tapered wings. Each configuration was designed similarly with an elasto-flexible membrane sewn on two spars, namely the leading- and the trailing edge. For each numerical investigation, a wind tunnel model was constructed and experiments were conducted. Force, membrane deflection and flow field velocity

measurements were conducted. The numerical results were compared to experimental data in order to assess the accuracy of the computations.

The first coupling to be realized modeled two-dimensional airfoils. This case allowed the understanding of the typical behavior of elasto-flexible concepts. The Fluid-Structure Interaction computations were compared to computational data representative of a rigid geometry. It could be concluded that the flexibility and the adaptivity of the membrane material enabled an adjustment of the airfoil shape to the incoming flow. The camber was accentuated whether in the positive or negative direction according to the angle of attack, resulting in an increase or decrease of the lifting capacity. Furthermore, the stall was found to be more gentle for a flexible geometry compared to its rigid counterpart. For this profile, in both the rigid and flexible cases, the onset of the flow separation started at the trailing edge and progressed to the leading edge with increasing angles of attack. However, instead of an abrupt decrease of the lift, the evolution of the flexible airfoil's lift was gradual with a slow decrease. The latter was due to the gentle progression of the separation point to the leading edge, whereas it progressed for a smaller range of angles of attack, in other words more abruptly, in the rigid case. One consequence was that the onset of the flow separation was delayed to higher angles of attack for the flexible concept. In terms of drag, smaller values were reported in the stall region for the flexible geometry. As a result, the use of a membrane material as a lifting surface showed promising characteristics to enlarge the flight performance by enabling a passive control on the aerodynamics and extending the range of angles of attack.

When the numerical results were compared to experimental data for the airfoil configurations, a fair agreement was found, which motivated further analysis. In order to enlarge the knowledge on elasto-flexible concepts, further numerical investigations were conducted with a variation of several parameters. The first parameter to be changed was the dynamic pressure. The aerodynamic behavior of the airfoil was analyzed for three different dynamic pressures. The lift and the drag coefficients were plotted as a function of the angle of attack. The polar showed a pronounced dependency on the dynamic pressure as it induced an accentuation in the membrane deflection. For a positive angle of attack, higher dynamic pressure would have caused a higher camber due to the increase in the suction peak. In this case, the increase of the camber was so high, that it precipitated the flow separation on the wing. Therefore, smaller lift coefficients were associated with higher dynamic pressure. However, the stall was observed more gentle with increasing dy-

dynamic pressure because the gradual progression of the separation point was even smoother. The membrane acted like a natural flow control by mitigating the aerodynamic loads.

The second parameter to be altered was the turbulence model of the fluid. The percentage of laminar flow was estimated to be not negligible and previous studies showed a dependency of the aerodynamics on the nature of the boundary layer. In this context, a transition between laminar and turbulent flow was modeled in the computations for the elasto-flexible airfoil. For this profile, the transition was due to a laminar separation bubble found to be very sensitive to the flow conditions. The presence of the transition was dependent on the suction peak and the angle of attack. When the transition occurred, the suction was higher on the upper-side surface of the wing resulting in higher lift for positive angles of attack. The laminar separation bubble migrated from the trailing- to the leading edge when the angle of attack increased. When the laminar separation bubble reached the leading edge, the boundary layer of the transition model had the same nature of the one without transition modeling. This results in the same values of lift. Finally, the stall appeared for smaller angles of attack when the transition was modeled.

The last parameter was linked to gust conditions. It was pointed out that the membrane permitted a mitigation of the aerodynamic loads. As high loads are induced from unsteady phenomena, an analysis of the response of the flexible concept to a gust became interesting. The flexible geometry was studied under the progression of a “1-cosine” law defining a one-dimensional vertical gust moving in the chord direction. Looking at the response, the lift and the drag mirrored the gust sinusoidal shape as expected. However, the most interesting part was to compare a rigid and a flexible case. When a cambered homologous geometry was considered, an alleviation of the aerodynamic loads was satisfied for high angles of attack. Nevertheless, a flutter phenomenon was observed, which implied an optimization of the membrane properties.

A second coupling approach was developed to model three-dimensional flexible wings. In total, two configurations were tested, a 2.5D and a 3D wing. Both configurations were designed with the idea to integrate them, as single or coupled parts, in a wind turbine blade. Altering the shape of the blade by means of a camber change allowed by the membrane, could be an interesting solution in the alleviation of aerodynamic loads or in the passive flow control. The study on the three-dimensional wings was divided into three parts. The first part provided a baseline using experimental analysis allowing the understanding of the aerodynamics of the wings. The second part compared the FSI computations to the experimental data to assess the accuracy of the numerical

analysis. The last part described in more detail the aerodynamics of the flexible configurations by analyzing parameters only available from the FSI computations. The aerodynamics of the flexible wing was also compared to the behavior of a rigid counterpart concept to highlight the advantages gained by the membrane.

For both the 2.5D and the 3D wings, the FSI computations approximated fairly the wind tunnel tests. The numerical analysis allowed an understanding that the capacity of the membrane to adapt itself to the incoming flow. The membrane accentuated the camber of the wing's sections. For a positive angle of attack, a higher camber related to a higher suction level permitted the flow to accelerate on a larger region. As a result, the lifting capacity of the wing was improved. The analysis showed also that an airfoil geometry featuring a high camber profile resulted in a pronounced flow separation. The latter indicated that the membrane material should be chosen carefully with respect to its needs, in order to avoid flutter or pronounced flow separation phenomena. Finally, the investigation also suggested that tip vortices could be moderated within the use of the membrane.

The wind energy field has been confronted to a significant expansion since the beginning of the 21st century. The expansion highlights the need to produce more efficient wind turbines. One solution has been investigated by means of increasing the wind turbine size. However, longer blades are associated to higher loads. As the membrane wing concept showed promising results in loads mitigation, a blade-shape change through a membrane material arouses interest. The idea would be to integrate sections of an elasto-flexible membrane wing into wind turbine blades. To achieve this, it is necessary to refine and improve the analysis provided by the present thesis.

In this context, it appears interesting to include the contact modeling between the leading edge and the membrane in the FSI computations. This will permit an improvement in the reliability of the flow separation phenomenon. Then, the rotation of the blade is also an important aspect in a wind turbine. The integration of a rotating frame in the computations has to be taken into account. The analysis of a rotating flexible membrane wing under a combination of a gust impact will give an important overview of possible advantages gained with a membrane. Finally, the choice of the membrane have to be particularly considered. The elasto-mechanical properties have to be chosen carefully to allow a deflection under varying free stream conditions but also to withstand the loads for a long time period. An algorithm could be developed to find the mechanical properties striking the best compromise between the aerodynamic efficiency and the loads cases.

Bibliography

- [1] Global Wind Statistics 2017, GWEC. https://gwec.net/wp-content/uploads/vip/GWEC_PRstats2017_EN-003_FINAL.pdf. Accessed: 2019-09-13. 8
- [2] LEXICO dictionary. <https://www.lexico.com/en>. Accessed: 2019-09-13. 2
- [3] S. Allmaras, F. Johnson, and P. Spalart. Modifications and clarifications for the implementation of the Spalart-Allmaras turbulence model. *Seventh International Conference on Computational Fluid Dynamics (ICCFD7)*, 2012. 28
- [4] J. D. Anderson. *Fundamentals of Aerodynamics*. McGraw-Hill series in Aeronautical and Aerospace engineering. McGraw-Hill Education Publishing, New York, NY, 6. edition, 2017. 22, 26, 27, 30
- [5] ANSYS. ANSYS CFX-Solver Manager User’s Guide 2011. http://read.pudn.com/downloads500/ebook/2077964/cfx_solv.pdf. Accessed: 2020-03-03. 45, 46
- [6] ANSYS. ANSYS ICEM CFD User Manual 2012. <https://pdfs.semanticscholar.org/c728/37a63921bbc47c83fa3d6bad8e2d9a86e2f7.pdf>. Accessed: 2020-02-11. 43, 63
- [7] ANSYS. ANSYS Mechanical APDL User Manual 2013. <https://de.scribd.com/document/233889393/ANSYS-Mechanical-Users-Guide>. Accessed: 2020-02-11. 45
- [8] B. Augier, J. Yan, A. Korobenko, J. Czarnowski, G. Ketterman, and Y. Bazilevs. Experimental and numerical FSI study of compliant hydrofoils. *Computational Mechanics*, 55(6):1079–1090, 2015. 10
- [9] C. Bak, M. Gaunaa, P. Andersen, T. Buhl, P. Hansen, K. Clemmensen, and R. Moeller. Wind Tunnel Test on Wind Turbine Airfoil with Adaptive Trailing Edge Geometry. *45th AIAA Aerospace Sciences Meeting and Exhibit*, 2007, Reno, Nevada. 8, 9
- [10] J. Baker, K. Standish, and C. P. van Dam. Two-Dimensional Wind Tunnel and Computational Investigation of a Microtab Modified S809 Airfoil. *43rd AIAA Aerospace Sciences Meeting and Exhibit*, 2005, Reno, Nevada. 8, 9

-
- [11] T. K. Barlas and G.A.M. van Kuik. Review of state of the art in smart rotor control research for wind turbines. *Progress in Aerospace Sciences*, 46(1):1–27, 2010. 8
- [12] Basler. https://www.baslerweb.com/de/produkte/?gclid=EAIaIQobChMIv_vo-9_e5AIVUP1RCh1bXgtSEAAAYASAAEgLcgPD_BwE. Accessed: 2019-09-20. 61
- [13] Y. Bazilevs, M.-C. Hsu, I. Akkerman, S. Wright, K. Takizawa, B. Henicke, T. Spielman, and T. E. Tezduyar. 3D simulation of wind turbine rotors at full scale. Part I: Geometry modeling and aerodynamics. *International Journal for Numerical Methods in Fluids*, 65(1-3):207–235, 2011. 10, 11
- [14] Y. Bazilevs, M.-C. Hsu, J. Kiendl, R. Wüchner, and K.-U. Bletzinger. 3D simulation of wind turbine rotors at full scale. Part II: Fluid-structure interaction modeling with composite blades. *International Journal for Numerical Methods in Fluids*, 65(1-3):236–253, 2011. 10, 11
- [15] Y. Bazilevs, M.-C. Hsu, Y. Zhang, W. Wang, X. Liang, T. Kvamsdal, R. Brekken, and J. G. Isaksen. A fully-coupled fluid-structure interaction simulation of cerebral aneurysms. *Computational Mechanics*, 46(1):3–16, 2010. 10
- [16] Y. Bazilevs, A. Korobenko, X. Deng, J. Yan, M. Kinzel, and J. O. Dabiri. Fluid-Structure Interaction Modeling of Vertical-Axis Wind Turbines. *Journal of Applied Mechanics*, 81(8):081006, 2014. 11
- [17] Y. Bazilevs, K. Takizawa, and T. E. Tezduyar. Challenges and Directions in Computational Fluid-Structure Interaction. *Mathematical Models and Methods in Applied Sciences*, 23(02):215–221, 2013. 9, 21
- [18] B. Béguin. *Development and analysis of an elasto-flexible morphing wing*. Dissertation, Technische Universität München, München, 2014. xv, 8, 12, 48, 49, 50, 51, 60, 82, 101, 102, 103, 104, 106, 107, 134
- [19] B. Béguin, C. Breitsamter, and N. Adams. Aerodynamic Investigations of a Morphing Membrane Wing. *AIAA Journal*, 50(11):2588–2599, 2012. 8, 12, 51
- [20] K. Bonnema and S. Smith. AFTI/F-111 Mission Adaptive Wing flight research program. *4th Flight Test Conference*, 1988, Reston, USA. 6
- [21] P-A. Breeze. *Power Generation Technologies*. Newnes Publishing, New York, 3. edition, 2019. 8

- [22] C. Breitsamter. *Turbulente Strömungsstrukturen an Flugzeugkonfigurationen mit Vorderkantenwirbeln*. Dissertation, Technische Universität München, München, Herbert Utz Verlag Wissenschaft, 1997. 62
- [23] H.-J. Bungartz and M. Schäfer. *Fluid-Structure Interaction*, volume 53. Springer Berlin Heidelberg, Berlin, Heidelberg, 2006. 9, 21
- [24] L. F. Campanile and D. Sachau. The Belt-Rib Concept: A Structronic Approach to Variable Camber. *Journal of Intelligent Material Systems and Structures*, 11(3):215–224, 2000. 7
- [25] Chair of Aerodynamics and Fluid mechanics, Technische Universität München. Wind tunnels of the Chair of Aerodynamics and Fluid mechanics,. 57
- [26] Chair of Structural Analysis, Technische Universität München. Carat++ 2018. <http://carat.st.bv.tum.de>. Accessed: 2020-03-03. 45
- [27] R. Chow and C.P. van Dam. Computational Investigations of Deploying Load Control Microtabs on a Wind Turbine Airfoil. *45th AIAA Aerospace Sciences Meeting and Exhibit*, 2007, Reno, Nevada. 8, 9
- [28] A. Coll, R. Ribó, M. Pasenau, E. Escolano, J.Suit. Perez, A. Melendo, A. Monros, and J. Gárate. GiD v.13 User Manual 2016. <https://www.gidhome.com/support/gid-manuals/>. Accessed: 2020-02-11. 44, 63
- [29] A. Da Ronch, L. Yongchao, L. Zhang, R. De Breuker, J. Kirn, S. Storm, D. Li, H. Peter Monner, and M. Kintscher. A Review of Modelling and Analysis of Morphing Wings. *Progress in Aerospace Sciences*, 100:46–62, 2018. 3
- [30] A. de Gaspari and S. Ricci. A Two-Level Approach for the Optimal Design of Morphing Wings Based On Compliant Structures. *Journal of Intelligent Material Systems and Structures*, 22(10):1091–1111, 2011. 10
- [31] J. Degroote, K.-J. Bathe, and J. Vierendeels. Performance of a new partitioned procedure versus a monolithic procedure in fluid-structure interaction. *Computers and Structures*, 87(11):793 – 801, 2009. 21
- [32] F. H. Dieringer. *Numerical Methods for the Design and Analysis of Tensile Structures*. Dissertation, Technische Universität München, München, 2014. 34
- [33] M. Drela and H. Youngren. Xfoil 6.9, General Description. http://web.mit.edu/aeroutil_v1.0/xfoil_doc.txt, 2001. 8, 10

-
- [34] C. A. Felippa. *Introduction to Finite Element Methods*. Department of Aerospace Engineering Sciences and Center for Aerospace Structures, University of Colorado. 2004. xv, 32, 33, 37, 38, 40
 - [35] J. Flanagan, R. Strutzenberg, R. Myers, and J. Rodrian. Development and Flight Testing of a Morphing Aircraft, the NextGen MFX-1. *48th AIAA/ASME/ASCE/AHS/ASC Structures, Structural Dynamics, and Materials Conference*, 2007, Honolulu, Hawai. xv, 6, 7
 - [36] M. Frémond. *Virtual Work and Shape Change in Solid Mechanics*, volume 7 of *Springer Series in Solid and Structural Mechanics*. Springer International Publishing, Cham and s.l., 2017. 37
 - [37] H. Garcia, M. Abdulrahim, and R. Lind. Roll Control for a Micro Air Vehicle Using Active Wing Morphing. *AIAA Guidance, Navigation and Control Conference and Exhibit*, 2003, Reston, USA. 4
 - [38] T. Gerhold. *Overview of the Hybrid RANS Code TAU, Notes on Numerical Fluid Mechanics and Multidisciplinary Design (NNFM)*. Springer-Verlag Berlin Heidelberg, Berlin, Heidelberg, 2005. 44
 - [39] Eschler Textile GmbH. <https://www.schoeller-textiles.com/de/geschaeftsbereiche/eschler-technical-textiles>. Accessed: 2019-09-18. 48
 - [40] D. Gross, J. Hauger, W. Schröder, and W. A. Wall. *Technische Mechanik 1: Statik*. Springer Verlag, Berlin and Heidelberg, 13. edition, 2016. 32, 33, 38
 - [41] D. Gross, W. Hauger, J. Schröder, and W. A. Wall. *Technische Mechanik 2: Elastostatik*. Springer Verlag, Berlin, 12. edition, 2014. 32, 33, 38
 - [42] M. Hansen. *Aerodynamics of Wind Turbines*. Routledge Publishing, 2015. 8
 - [43] R. Heinrich and L. Reimer. Comparison of different approaches for gust modeling in the CFD code Tau. *IFASD 2013 - International Forum on Aeroelasticity and Structural Dynamics*, 2013, Como, Italien. 109
 - [44] A. Hövelmann and C. Breitsamter. Leading-Edge Geometry Effects on the Vortex Formation of a Diamond-Wing Configuration. *Journal of Aircraft*, 52(5):1596–1610, 2015. 21, 44
 - [45] H. Hu, M. Tamai, and J. T. Murphy. Flexible-Membrane Airfoils at Low Reynolds Numbers. *Journal of Aircraft*, 45(5):1767–1778, 2008. xv, 4, 5, 6

- [46] W.-H. Hucho. *Aerodynamik der stumpfen Körper: Physikalische Grundlagen und Anwendungen in der Praxis*. Vieweg + Teubner Verlag, Wiesbaden, 2. edition, 2012. 58
- [47] P. Ifju, D. Jenkins, S. Ettinger, Y. Lian, W. Shyy, and M. Waszak. Flexible-wing-based micro air vehicles. *40th AIAA Aerospace Sciences Meeting and Exhibit*, 2002, Reston, USA. 4
- [48] T. Ivanco, R. Scott, M. Love, S. Zink, and T. Weisshaar. Validation of the Lockheed Martin Morphing Concept with Wind Tunnel Testing. *48th AIAA/ASME/ASCE/AHS/ASC Structures, Structural Dynamics, and Materials Conference*, 2007. 6
- [49] R. W. Johnson. *The handbook of fluid dynamics*. CRC Press Publishing, Boca Raton, 2. edition, 1998. 22, 26
- [50] S.J. Johnson, J.P. Baker, C.P. van Dam, and D. Berg. An overview of active load control techniques for wind turbines with an emphasis on microtabs. *Wind Energy*, 13(2-3):239–253, 2010. 9
- [51] J. N. Kudva. Overview of the DARPA Smart Wing Project. *Journal of Intelligent Material Systems and Structures*, 15(4):261–267, 2004. 6
- [52] X. Lachenal, S. Daynes, and P.M. Weaver. Review of morphing concepts and materials for wind turbine blade applications. *Wind Energy*, 16(2):283–307, 2013. 8
- [53] A. C. Laia. *Simulation of atmospheric effects with the DLR code TAU*. Master thesis, Universitat Politècnica de Catalunya, 2015. xvii, 108, 112
- [54] R. B. Langtry, F. R. Menter, S. R. Likki, Y. B. Suzen, P. G. Huang, and S. Völker. A Correlation-Based Transition Model Using Local Variables - Part II: Test Cases and Industrial Applications. *Journal of Turbomachinery*, 128(3):423–434, 2006. 104
- [55] R. J. LeVeque. *Finite volume methods for hyperbolic problems*. Cambridge texts in applied mathematics. Cambridge Univ. Press Publishing, Cambridge, reprinted edition, 2007. 26
- [56] Y. Lian and W. Shyy. Three-Dimensional Fluid-Structure Interactions of a Membrane Wing for Micro Air Vehicle Applications. *44th AIAA/ASME/ASCE/AHS/ASC Structures, Structural Dynamics and Materials Conference*, 2003, Reston, USA. 4, 10
- [57] Y. Lian and W. Shyy. Numerical Simulations of Membrane Wing Aerodynamics for Micro Air Vehicle Applications. *Journal of Aircraft*, 42(4):865–873, 2005. 4, 10

-
- [58] Y. Lian and W. Shyy. Laminar-Turbulent Transition of a Low Reynolds Number Rigid or Flexible Airfoil. *36th AIAA Fluid Dynamics Conference and Exhibit*, 2006. 4
- [59] T. Luhmann, S. Robson, S. Kyle, and I. Harley. *Close Range Photogrammetry*. Wittles Publishing, New York, 1. edition, 2006. 60
- [60] M. D. Maughmer. *Optimization and Characteristics of a Sailwing Windmill Rotor*. Ams report no. 1297, Princeton University, Department of Aerospace and Mechanical Science, 1976. 9
- [61] R. E. Mayle. The 1991 IGTI Scholar Lecture: The Role of Laminar-Turbulent Transition in Gas Turbine Engines. *Journal of Turbomachinery*, 113(4):509–536, 1991. 104
- [62] F. Menter. Zonal Two Equation k- ω Turbulence Models For Aerodynamic Flows. *23rd Fluid Dynamics, Plasmadynamics, and Lasers Conference*, 1993. 29
- [63] F. R. Menter. Two-equation eddy-viscosity turbulence models for engineering applications. *AIAA Journal*, 32(8):1598–1605, 1994. 29
- [64] F. R. Menter, R. B. Langtry, S. R. Likki, Y. B. Suzen, P. G. Huang, and S. Völker. A Correlation-Based Transition Model Using Local Variables - Part I: Model Formulation. *AIAA Journal*, 128(3):413, 2006. 104
- [65] H. Monner, M. Kintscher, T. Lorkowski, and S. Storm. Design of a Smart Droop Nose as Leading Edge High Lift System for Transportation Aircrafts. *Structures, Structural Dynamics, and Materials and Co-located Conferences*, 2009, Palm Springs, USA. 7
- [66] T. J. Mueller and D. DeLaurier. Aerodynamics of Small Vehicles. *Annual Review of Fluid Mechanics*, 35:89–111, 01 2003. 3
- [67] J. Piquee and C. Breitsamter. Numerical and Experimental Investigations of an Elasto-Flexible Membrane Wing at a Reynolds Number of 280,000. *Aerospace*, 4(3):39, 2017. 75
- [68] J. Piquee, I. López, C. Breitsamter, R. Wüchner, and K-U. Bletzinger. Aerodynamic Characteristics of an Elasto-Flexible Membrane Wing based on Experimental and Numerical Investigations. *2018 Applied Aerodynamics Conference, American Institute of Aeronautics and Astronautics*, 2018, Reston, USA. 86
- [69] J. Piquee, I. López Canalejo, C. Breitsamter, R. Wüchner, and K.-U. Bletzinger. Aerodynamic analysis of a generic wing featuring an elasto-flexible lifting surface. *Advances in Aerodynamics*, 1(20), 2019. 133

- [70] S. B. Pope. *Turbulent flows*. Cambridge Univ. Press Publishing, Cambridge, 12. edition, 2015. [27](#)
- [71] A. Prachař, P. Hospodář, and P. Vrchota. Gust Alleviation of Aeroelastic Aircraft Using CFD Simulation. *Transportation Research Procedia*, 29:366–375, 2018. [109](#)
- [72] T. Richter. *Fluid-structure Interactions: Models, Analysis and Finite Elements*, volume v.118 of *Lecture notes in computational science and engineering*. Springer International Publishing , Cham, 2017. [41](#)
- [73] A. Rodriguez. Morphing Aircraft Technology Survey. *45th AIAA Aerospace Sciences Meeting and Exhibit*, 2007, Reno, Nevada. [3](#)
- [74] M. Saeedi. *Multi-Fidelity Aeroelastic Analysis of Flexible Membrane Wind Turbine Blades*. Dissertation, Technische Universität München, München, 2017. [11](#), [12](#), [39](#)
- [75] M. Saeedi, K.-U. Bletzinger, and R. Wüchner. Multi-fidelity fluid-structure interaction analysis of a membrane blade concept in non-rotating, uniform flow condition. *Wind Energy Science*, 1(2):255–269, 2016. [11](#), [12](#)
- [76] M. Saeedi, K.-U. Bletzinger, and R. Wüchner. Investigation of Prestress-Dependent Aerodynamic Performance of a Double Membrane Sailwing. *Journal of Aircraft*, 54(3):980–994, 2017. [11](#), [12](#)
- [77] M. Saeedi, R. Wüchner, and K.-U. Bletzinger. Fluid-structure interaction analysis and performance evaluation of a membrane blade. *Journal of Physics: Conference Series*, 753:102009, 2016. [11](#), [12](#)
- [78] H. Schlichting and E. A. Truckenbrodt. *Grundlagen aus der Strömungstechnik Aerodynamik des Tragflügels (Teil I)*. Klassiker der Technik. Springer Verlag, Berlin and Heidelberg, 3. edition, 2001. [22](#), [26](#), [27](#), [30](#)
- [79] H. Schlichting and E. A. Truckenbrodt. *Aerodynamik des Tragflügels, des Rumpfes, der Flügel-Rumpf-Anordnung und der Leitwerke (Teil II)*. Klassiker der Technik. Springer Verlag, Berlin and Heidelberg, 3. edition, 2001. [22](#), [26](#), [30](#)
- [80] D. Schwamborn, T. Gerhold, and R. Heinrich. The DLR TAU-code: Recent applications in research and industry. *European Conference on Computational Fluid Dynamics, ECCOMAS CDF*, 2006. [44](#)

-
- [81] R. Schwarze. *CFD-Modellierung: Grundlagen und Anwendungen bei Strömungsprozessen*. Springer Verlag, Berlin and Heidelberg, 2013. 26
 - [82] R. Siddall, A. Ortega Ancel, and M. Kovac. Wind and water tunnel testing of a morphing aquatic micro air vehicle. *Interface focus*, 7(1):20160085, 2017. xv, 3, 4
 - [83] P. Spalart and S. Allmaras. A one-equation turbulence model for aerodynamic flows. *30th Aerospace Sciences Meeting and Exhibit*, 1992, Reston, USA. 28
 - [84] B. Stanford, R. Viieru, D. and Albertani, W. Shyy, and P. Ifju. A Numerical and Experimental Investigation of Flexible Micro Air Vehicle Wing Deformation. *44th AIAA Aerospace Sciences Meeting and Exhibit*, 2006, Reno, Nevada. 4, 10
 - [85] V.L. Streeter and B.E. Wylie. *Fluid mechanics*. International student edition. McGraw-Hill Publishing, New York, 7. edition, 1979. 24
 - [86] Morphing Aircraft Structures. *Defense Technology Objectives*. Dto 71, U.S. Department of Defense, U.S., 2003. 6
 - [87] T. E. Sweeney. *The princeton Windmill Program*. AMS Report No. 1093, Princeton University, Department of Aerospace and Mechanical Science, 1973. 9
 - [88] K. Takizawa, D. Montes, M. Fritze, S. MCintyre, J. Booben, and T.E. Tezduyar. Methods for FSI Modeling of Spacecraft parachute Dynamics and Cover Separation. *Mathematical Models and Methods in Applied Sciences*, 23(02):307–338, 2013. 10
 - [89] K. Takizawa, S. Wright, C. Moorman, and T. E. Tezduyar. Fluid-structure interaction modeling of parachute clusters. *International Journal for Numerical Methods in Fluids*, 65(1-3):286–307, 2011. 10
 - [90] N. Thouault. *Aerodynamic Investigations on Generic Fan-in-Wing Configurations*. Dissertation, Technische Universität München, München, 2010. 21, 44
 - [91] N. Trolborg. Computational Study of the Riso-B1-18 Airfoil with a Hinged Flap Providing Variable Trailing Edge Geometry. *Wind Engineering*, 29(2):89–113, 2005. 8, 9
 - [92] C.P. van Dam, D.E. Berg, and S.J. Johnson. Active load control techniques for wind turbines. *Sandia National Laboratories, SANDIA Report, SAND2008-4809*, 1973. 9
 - [93] H. K. Versteeg and W. Malalasekera. *An introduction to computational fluid dynamics: The finite volume method*. Pearson/Prentice Hall Publishing, Harlow, 2. edition, 2010. xv, 22, 23, 26, 44

- [94] T. Wang. *Development of Co-Simulation Environment and Mapping Algorithms*. Dissertation, Technische Universität München, München, 2016. [41](#), [46](#)
- [95] T. A. Weisshaar. Morphing Aircraft Systems: Historical Perspectives and Future Challenges. *Journal of Aircraft*, 50(2):337–353, 2013. [3](#)
- [96] P. C. Wölcken and M. Papadopoulos. *Smart Intelligent Aircraft Structures (SARISTU): Proceedings of the Final Project Conference*. Springer Verlag, Cham, 1st edition, 2015. [7](#)
- [97] B. K. S. Woods, I. Dayyani, and M. I. Friswell. Fluid/Structure-Interaction Analysis of the Fish-Bone-Active-Camber Morphing Concept. *Journal of Aircraft*, 52(1):307–319, 2014. [7](#), [10](#)
- [98] T. Yokozeiki, A. Sugiura, and Y. Hirano. Development of Variable Camber Morphing Airfoil Using Corrugated Structure. *Journal of Aircraft*, 51(3):1023–1029, 2014. [4](#), [7](#)
- [99] P. Zhang, L. Zhou, W. Cheng, and Q. Tao. Conceptual Design and Experimental Demonstration of a Distributedly Actuated Morphing Wing. *Journal of Aircraft*, 52(2):452–461, 2015. [7](#)
- [100] Z. Zhang, N. Martin, Wrist A., and J. P. Hubner. Geometry and Prestrain Effects on the Aerodynamic Characteristics of Batten-Reinforced Membrane Wings. *Journal of Aircraft*, 53(2):530–544, 2016. [xv](#), [5](#), [6](#)
- [101] O. C. Zienkiewicz, J. Z. Zhu, and R. L. Taylor. *The finite element method: Its basis and fundamentals*. Butterworth-Heinemann Publishing, Oxford, UK, 7. edition, 2013. [32](#), [38](#)